UNIVERSITÀ
DEGLI STUDI
DI CAGLIARI

Ph.D. DEGREE IN
Civil Engineering and Architecture
Cycle XXXVII

TITLE OF THE Ph.D. THESIS

Water resources planning and climate change adaptation strategies of Sardinian basins under water-limited conditions

Scientific Disciplinary Sector(s)

CEAR-01/B

Ph.D. Student: Serena Sirigu

Supervisor Prof. Ing. Nicola Montaldo

Co-Supervisor Prof. Gabriel G. Katul

Final exam. Academic Year 2023/2024
Thesis defence session: July 2025

"I can't carry it for you, but I can carry you"

Ai miei Samvise Gamgee

Acknowledgments

"My legs are so short and the way is so long,
I've no rest nor comfort, no comfort but song.
Sing to me, sing to me, lands far away,
Oh, rise up and guide me this wandering day.
Please promise to find me this wandering day.
At last comes their answer through cold and through frost,
That not all who wonder or wander are lost,
No matter the sorrow, no matter the cost,
That not all that wonder or wander are lost. . . "
[*This Wandering Day- The Rings of Power*]

Non posso certo affermare che questi tre anni siano stati come il viaggio di Frodo verso il monte Fato, certo è stato impegnativo, a volte fisicamente stancante, ci sono stati dei momenti impegnativi ma soprattutto è stato interessante e anche divertente.

Però come Frodo non ha affrontato il viaggio da solo neppure io l'ho fatto, per cui vorrei ringraziare tutte le persone che per una parte o sino alla fine, mi sono state vicine e hanno sostenuto e hanno avuto la pazienza di sopportare il mio caratteraccio.

Vorrei iniziare dal mio supervisore, Prof Nicola Montaldo, per avermi dato opportunità di intraprendere questo viaggio ed esserne stato la guida ...

Il compagno di sventure di tutto questo percorso, Roberto Corona, per avermi accompagnato e sostenuto durante tutti questi tre anni ...

Gaby e Sandra per avermi accolta e avermi fatto sentire a casa anche a centinaia di Km ...

Tutte le persone che hanno lavorato ai nostri progetti di ricerca: il nostro tecnico Antonio, Matteo, Sara, il mio "figlioccio" giovane Gaspa, Claudia e Riccardo, Damiano che hanno reso il lavoro, meno lavoro e più una bella avventura ...

Elena, Mara, Alice e Sara, che hanno ricoperto (senza compenso!) il ruolo di psicologhe, motivatrici e consigliere, grazie per esserci sempre state ...

Alessandro, che nell'ultimo anno ha avuto, non so se definirla fortuna per lui, di condividere l'ufficio con me, per me di sicuro una fortuna lo è stata, per esser essermi stato vicino nei momenti peggiori e anche in quelli migliori di questo ultimo anno ...

Simone Ferrari, per le chiacchiere, le risate e i caffè ...

A gli amici e colleghi del nostro gruppo di dipartimento allargato: Stefano, Silvia e Silvia, PG, Andrea, Malin, Avi, Tara, Luca e Peppe, grazie per i pranzi e le risate ...

E ultimi ma non per importanza, tutta la mia famiglia: mia madre Antonella, mio padre Luigi, mia sorella Alessia, mio fratello Mattia, mia cognata Cristina e le nostre cucciole Virgi e Ali, che più di tutti, negli anni, mi hanno sempre sostenuto e sopportato ...

Abstract

Sardinia, an island in the western Mediterranean Sea, is a natural laboratory to study the effects of climate change on ecosystems and water resources in water-limited environments. Long-term observations over the last century have revealed significant declines in winter precipitation, a halving of annual river runoff, and an increase of approximately 1 ° C in mean annual air temperature. To investigate ecosystem responses to contrasting precipitation regimes, two micrometeorological towers were installed: one in Orroli, a site characterized by shallow basaltic soils, herbaceous vegetation, and wild olive trees; and another in the Marganai forest, a denser holm oak (Quercus ilex) forest on steeper rocky slopes. Measurements of land surface energy fluxes, carbon dioxide fluxes, soil moisture, and tree transpiration highlight different ecohydrological behaviors: at Orroli, evapotranspiration (ET) closely follows seasonal rainfall patterns and vegetation dynamics, whereas at Marganai, ET remains more stable throughout the year, sustained by deep water sources accessed by the trees. Ecohydrological models, coupled with climate projections from IPCC global circulation models, predict that rising temperatures and decreasing precipitation will lead to further reductions in vegetation cover (with up to a 50% decrease in Leaf Area Index), tree transpiration, and water availability. Future scenarios for 2024–2100 forecast that irrigation demands will not be fully satisfied, with up to 74% of future years experiencing irrigation deficits, and an average deficit of up to 52%. Additionally, although annual runoff is expected to decrease, the severity of flood events may increase, highlighting a future that is both drier and more prone to extreme events. These findings underscore the vulnerability of Sardinian ecosystems and water resource systems to climate change, emphasizing the urgent need for adaptive water and land management strategies to ensure the island's environmental and economic sustainability under future climate conditions.

Contents

List of Figures

List of Tables

1 Introduction

The consequences of climate change are becoming increasingly evident in many parts of the world, but the Mediterranean basin represents one of the most critical areas, being defined as a global climate "hot spot" (Giorgi and Lionello, 2008; Lionello and Scarascia, 2018). This designation stems from the combination of two factors: on the one hand, a significant increase in average temperature, and on the other, a reduction in precipitation, especially during winter months, accompanied by a rise in the frequency and intensity of extreme events. These processes directly impact water availability, vegetation structure, ecosystem functioning, and the socio-economic stability of the region (Brunetti et al., 2002; Caloiero and Veltri, 2019).

In Sardinia, between 1922 and 2010, Montaldo and Sarigu (2017); Corona et al. (2018) observed a significant decrease in winter precipitation (Mann–Kendall τ up to -0.40) and an even more marked drop in runoff (τ up to -0.45), with a strong decline in the annual runoff coefficient (τ = -0.32; Montaldo and Sarigu (2017); Montaldo and Oren (2018)). These dynamics have led to the progressive deterioration of water reserves, directly affecting water management for agricultural, civil, and environmental uses.

In this context, runoff is considered a synthetic yet effective indicator of basin water availability and its resilience to climate change (García-Ruiz et al., 2011). The seasonal structure of the Mediterranean climate — with rainfall concentrated in autumn and winter followed by prolonged dry periods — further amplifies the vulnerability of the hydrological system. Spring and summer coincide with the peak of water demand (for irrigation, domestic use, and tourism) but also with the lowest actual availability of water in soils and surface water bodies (Tabari et al., 2012; Park Williams et al., 2013a).

In this climatic context, terrestrial ecosystems have evolved to cope with limited water availability and high climatic variability. In particular, the spread of discontinuous ecosystems is observed, where evergreen tree formations (e.g., Olea europaea var. sylvestris, Quercus ilex) are arranged in clumps separated by patches of seasonal herbaceous vegetation. This configuration, defined as a "patchy ecosystem", results from a dynamic balance between water competition mechanisms and facilitative interactions (Scholes and Archer, 1997; Sankaran et al., 2005; Breshears, 2006).

Tree clumps play a key role in supporting the overall functionality of the ecological mosaic, not only by accessing deep water reserves in the rocky substrate but also by contributing to the redistribution of moisture to the upper soil layers during the night (hydraulic lift) (Domec et al., 2010; Dohn et al., 2013). This process, known as hydraulic lift, has been widely documented in semi-arid ecosystems, where tree roots act as "passive pumps", moving water from deep fractures in the rock to the surface soil, where it can be used by shallower-rooted herbaceous species (Yu and D'Odorico, 2015).

Under these conditions, the coexistence between tree and herbaceous species takes on a functional dimension: herbaceous plants benefit from moisture released by trees in spring, while trees benefit from the lower transpiration activity of grasses in summer, thereby reducing water competition (McCole and Stern, 2007). This seasonal balance represents an example of interspecific cooperation mediated by hydrological mechanisms.

One of the most relevant and often underestimated hydrological features in semi-arid Mediterranean ecosystems is the capacity of fractured rock substrates to store and release water accessible to plants. This water compartment, known as rock moisture, represents a strategic reserve especially during the dry season, when surface soils are completely depleted and the residual moisture in rocks becomes the main water source for vegetation (Rempe and Dietrich, 2018a).

Unlike true groundwater, rock moisture does not move freely in saturated pores but is retained by capillarity and adhesion within the fractures and porosity of the substrate. The deep roots of many Mediterranean woody species are able to penetrate these lithological discontinuities, accessing these reserves through physiological mechanisms of active absorption (Estrada-Medina et al., 2013; Allen, 2009). Isotopic studies have confirmed that during summer months, when precipitation completely ceases, most of the water transported in the tree xylem comes from the rocky substrate rather than from the soil (McCole and Stern, 2007).

This dynamic has profound implications for the eco-hydrological and physiological functioning of the system. The ability to access rock moisture allows trees to maintain photosynthesis and transpiration even during the dry months, reducing leaf fall and sustaining a minimum level of net primary productivity. Furthermore, it reduces root competition with herbaceous plants, which are mostly confined to the upper soil layers and thus more exposed to seasonal water stress.

Combined with hydraulic lift, rock moisture represents a quintessential example of an "invisible" yet essential resource for the resilience of patchy ecosystems. In particular, the system's ability to support vegetation under chronically arid conditions largely depends on this deep water storage, which can account for up to 70–90% of total evapotranspiration. For this reason, a new challenge in ecohydrology has emerged: the "ecohydrology of roots in rocks" (Schwinning, 2010).

In this context, evapotranspiration (ET), a leading loss term in the root-zone water budget, which in semi-arid regions can annually equal precipitation, represents an excellent parameter for estimating ecosystem health and serves as a vital link in atmosphere–soil interactions. However, despite growing scientific interest, a general lack of knowledge persists about the relationship between ET and plant survival strategies among different functional types and crops under water stress.

This highlights the need for accurately quantifying ET through both field measurements and mathematical modeling that enables the extension of analyses to evaluate the response of these ecosystems to changing extremes in magnitude and frequency predicted under future climate change scenarios (e.g., Swart et al. (2019b)).

The most advanced technique for directly measuring evapotranspiration is undoubtedly the eddy covariance method (Baldocchi, 2003a), which measures energy and CO_2 fluxes with very high temporal resolution (20–10 Hz). However, this method is partially influenced by site heterogeneity, topography, and soil characteristics, making correction methodologies necessary — such as the "residual energy closure" method — and also requiring auxiliary measurements (e.g., sap flux sensors for transpiration components, and surface temperature sensors) for validating the flux partitioning estimated by eddy covariance.

Monitoring represents a fundamental step in understanding soil–atmosphere dynamics but also forms the basis for developing modeling tools capable of realistically simulating water balance processes coupled with vegetation dynamics.

In this framework, distributed ecohydrological models represent one of the most promising frontiers in research (Tague and Band, 2004; Fatichi et al., 2016), as they allow for the simultaneous simulation of:(i) water fluxes into and out of the system, (ii) changes in plant biomass, (iii) vegetation response to water stress, (iv) feedback interactions with the atmosphere (Rodriguez-Iturbe, 2000; Montaldo et al., 2004, 2013), (v) while representing the spatial heterogeneity of Mediterranean landscapes, where topographic, lithological, and vegetation variability is especially pronounced (Beven et al., 2021).

To simulate vegetation dynamics, many models rely on the Leaf Area Index (LAI), which describes the active leaf area per unit of surface, affecting intercepted radiation, transpiration, and thus water demand. In semi-arid contexts, models must also include vegetation responses to vapor pressure deficit (VPD), which induces stomatal closure and alters transpiration dynamics.

Beyond representing internal system dynamics, ecohydrological modeling must also be able to simulate the impact of future climate change scenarios. To do so, models are forced with climate projections, typically from global circulation models (GCMs) developed under IPCC programs (e.g., Swart et al. (2019b); Taylor et al. (2012).

Knowledge derived from the integration of experimental observations and distributed modeling has a direct impact on sustainable water resource management. In Mediterranean contexts, water scarcity is not only seasonal but a structural trend, expected to intensify with ongoing climate change

(Swart et al., 2019a).

In such scenarios, ecohydrological models are essential tools for supporting policy and management decisions, providing quantitative projections of water availability, vegetation needs, and system recharge capacity.

This thesis fits within this framework and stems from European research projects such as FLUXMED, SWATCH, and ALTOS, which aim to develop innovative methodologies to increase the social-ecological Water Use Efficiency of managed ecosystems along the Mediterranean biome and climate types in the face of drier and more extreme climates.

One of the main contributions is the analysis of ecohydrological dynamics in Mediterranean ecosystems, with particular attention to deep water access processes studied and measured in two experimental sites: Orroli (patchy ecosystem) and the Marganai State Forest (forest ecosystem representative of widespread Mediterranean species).

The most innovative aspect lies in extending a Land Surface Model (LSM) to a dynamic vegetation model commonly used for field-scale hydrological studies, and integrating into it the process of water uptake from fractured bedrock. This enhancement enables consideration of tree survival strategies and their contribution to the water balance.

Again, the choice of two case studies representative of typical Mediterranean hydrological basins — one entirely natural (Rio Fluminimaggiore), and the Flumendosa basin, characterized by an interconnected reservoir system — allows for the simulation of climate change effects on water resources available both to ecosystems (e.g., forest vegetation) and to users (agriculture, civil sector, etc.). When coupled with a water resource management model, the ecohydrological model becomes a powerful scenario-based tool for local authorities and planners, enabling simulation of different land-use strategies and their impact not only on water balance but also on associated ecosystem services (e.g., carbon sequestration, biodiversity conservation, erosion control).

Each chapter of this thesis was designed to progressively address the various phases of the research activity: from theoretical background to field experimentation, modeling, and final considerations.

- **Chapter 2 – On the Estimate of Evapotranspiration in Typical Mediterranean Ecosystems**

  This chapter presents the environmental and climatic characteristics of the two experimental sites, along with the instrumentation used for monitoring. Particular attention is given to the eddy covariance systems and auxiliary sensors, the soil–atmosphere dynamics, and the challenges related to flux measurement methodologies.

- **Chapter 3 – A New Spatially Distributed Ecohydrological Model for Water Resources Planning**

This chapter describes the development, calibration, and validation of the distributed ecohydrological model, emphasizing the integration of experimental data and the representation of the spatial heterogeneity of the Mediterranean landscape.

- **Chapter 4 – Impact of Future Climate Change Scenarios on Basin Water Resources**
  This chapter demonstrates the application of the model as a tool for forecasting the impacts of climate change on ecosystems (e.g., forest health conditions) and water resources (e.g., availability for different users, with a focus on agricultural irrigation).

- **Chapter 5 – Conclusions and Future Perspectives**
  This final chapter summarizes the main findings, discusses their scientific and practical relevance, and proposes potential future developments for ecohydrological research and its applications in the Mediterranean region.

2

On the estimate of the evapotranspiration in typical Mediterranean ecosystems

The eco-hydrologic monitoring of and ecosystem consists in the extimation of the water budget and carbon budget components in the site, and when because sometimes it is not possible easily measure directly this components, it will be possible measure the related energy needed to have this components so it is possible measure the energy budget components of the system.

The above-mentioned variables, particularly the energy fluxes, can be directly measured in situ using advanced instrumentation or indirectly estimated through empirical or semi-empirical equations based on more easily obtainable environmental variables, such as air temperature, surface temperature, and relative humidity. These formulations are widely employed in hydrological models, highlighting the crucial role of field monitoring not only in enhancing the understanding of physical processes occurring under specific meteorological or topographic conditions, but also in supporting hydrological modeling efforts. Such modeling enables long-term climate projections (see chapters 3 and 4), with observational data representing a fundamental input for both parameterization and calibration procedures.

2.1 Case studies

The identification of representative case studies is an essential step toward a deep understanding of the eco-hydrological dynamics that characterize Mediterranean ecosystems, and for the development of models and management strategies that can be transferred to other similar contexts. Mediterranean ecosystems are inherently complex and marked by a high degree of environmental heterogeneity, both in terms of landscape morphology and in vegetation cover and soil composition. This complexity, combined with strong climatic seasonality, underscores the need for an experimental approach based on observation sites that are ecologically and climatically emblematic of the regional context. Such case studies enable the high-resolution spatial and temporal analysis of key phenomena, including seasonal water balance, vegetation responses to recurrent water stress, and the dynamics of scalar fluxes such as the Evapotranspiration that reppresent the link between the energy balance and the water balance.

2.1.1 Orroli site

Study Site Description

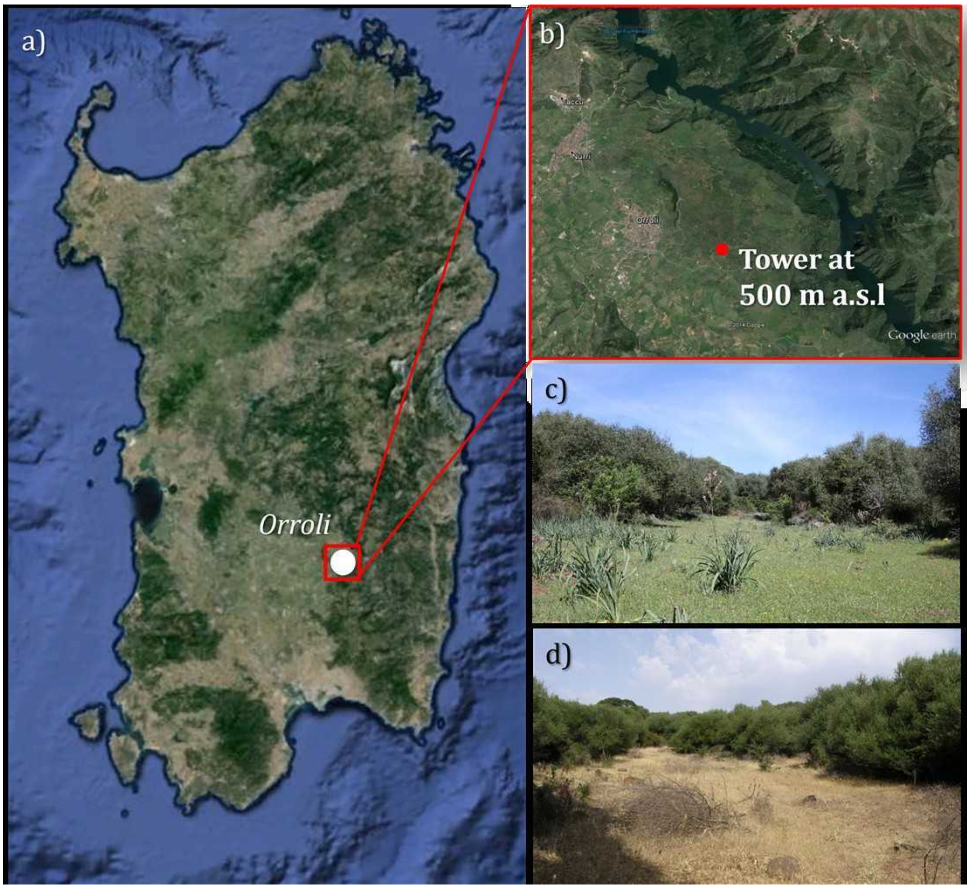

Figure 2.1: a) Geolocation of case study site 1; b) Aerial view of the site; c) site appearance in the Spring Season; d) Site appearance in the Summer Season

The field experiments are conducted near Orroli, in the Sarcidano area of east-central Sardinia (39°41'12.57" N, 9°16'30.34" E) (see Figure 2.1 a), at an elevation of approximately 500 m a.s.l. The site is located on a gently sloping basaltic plateau (slope ~3° from NW to SE) and represents a typical Mediterranean ecosystem, highly influenced by climatic conditions that determine landscape composition.

The area is characterized by a heterogeneous and patchy vegetation cover (Figure 2.1 c-d). Tree clumps, primarily composed of *Olea sylvestris* (wild olive) and scattered individuals of *Quercus suber*, occupy approximately 33% of the footprint area, with average tree heights around 4 m. Shrubs and climbing vines are commonly found in and around these tree patches. The interclump areas host herbaceous and grass species such as *Asphodelus microcarpus*, *Ferula communis*, *Bellium bellidioides*, *Scolymus hispanicus*, *Sonchus arvensis*, *Vicia sativa*, *Euphorbia characias*, *Daucus carota*, *Bellis perennis*, and monocotyledons like *Avena fatua* and *Hordeum murinum* which thrive during the wet season. These herbaceous species are strictly seasonal (Figure 2.1 c-d), depending on water availability during winter and spring. In the dry summer season, when precipitation is almost absent, these interclump areas transform into bare soil or dead vegetation, while only the more drought-resistant shrubs persist.

The climate is classified as maritime Mediterranean. The long-term mean annual precipitation (1924–2024) is 686 mm, with dry summers averaging just 12.5 mm in July and wet winter with a maximum monthly precipitation of about 101 mm in December (see Figure 2.2). The mean annual air temperature is 14.6°C, reaching a monthly average of 23.6°C in July.

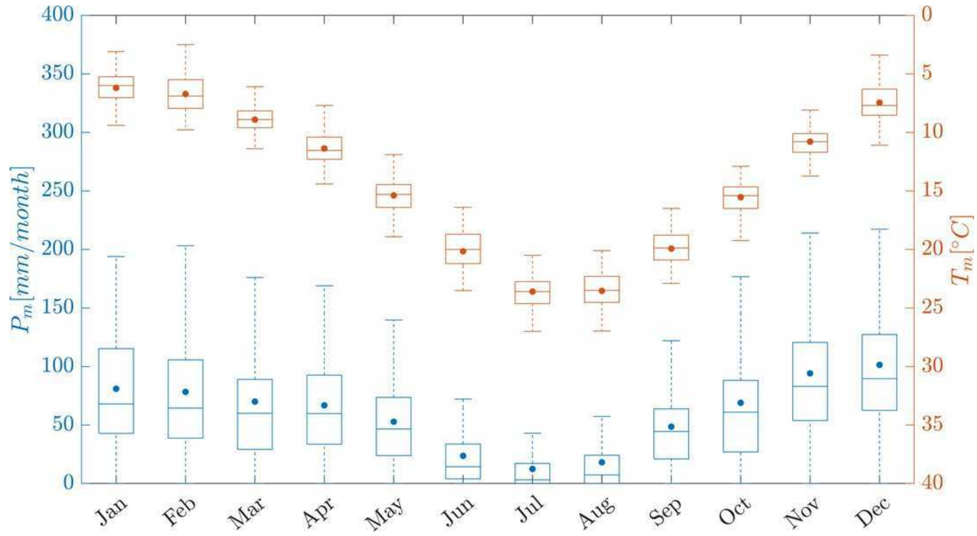

Figure 2.2: Historical climate in Orroli area, data since 1924; the central mark indicates the median, and the bottom and top edges of the box indicate the 25th and 75th percentiles, respectively and the whiskers extend to the most extreme data points, the dots indicate the average value, in blue is presented the monthly precipitation and in orange it's presented the mean air temperature.

Soil texture is classified as silt loam (19% sand, 76% silt, 5% clay), with a bulk density of $1.38 g/cm^3$ and porosity of 53%. Soil depth varies between 15 and 50 cm (average 17 ± 6 cm SD), limited by an underlying layer of fractured basalt that constrains root development.

Setup and Equipment

Figure 2.3: Orroli setup and equipment: a) micrometeorological tower, from the to to the bottom there are installed CSAT3B, LI-7500 and CNR-1, at about 7m height an bi-directional anemometer RMYoung 05103 and the SI111 that measure canopy surface temperature, at 2m height the HygroVue from Campbell Sci., at about 5m from the tower it's installed the raingauge PMB2 CAE; b) SI111 that measure grass/bare soil surface temperature and SQ-110; c) sapflow sensor; d) example of the installation of the Sentek Drill&Drop from the official internet site: Sentek; e) CS616 from Campbell Sci.

In May 2003, a micrometeorological measurement station was installed at this site (see Chapter 6 section 6.1 for the theory of the measurement). It remained in operation until November 2017, when it was removed, although the ground-based instrumentation was left in place. A new measurement station was installed in September 2020 as part of the European projects SWATCH, FLUXMED, and ALTOS. It consists of a 10-meter-high tower made of a modular tilting structure. On this tower, a CSAT3B 3D sonic anemometer from Campbell Scientific and a LI-7500 infrared gas analyzer from LI-COR (for CO_2 and H_2O) were installed. These instruments measure wind speed in three vector components, air temperature, and the concentration of the two gases at a frequency of 10 Hz. Using the eddy-covariance technique (Baldocchi, 2003b), the system estimates latent heat flux (LE) and sensible heat flux (H). The sampling frequency is 10 Hz, and the data are recorded every 30 minutes on a CR3000 datalogger from Campbell Scientific. The instrumentation was replaced in February 2023 with the SmartFlux system from LI-COR, which, with the addition of external memory, also allows storage of raw 10 Hz data. At the same height, a CNR-1 four-component radiometer (Kipp&Zonen) is installed, that provide both short wave and longwave incoming and outgoing radiation (Rsw_{in}, Rsw_{out}, Rlw_{in}, Rlw_{out}). About 5 meters from the tower, a SQ-110 quantum sensor from Apogee is used to measure photosynthetically active radiation (PAR). Precipitation is measured by a PMB2 CAE, air temperature (Ta) and relative humidity (RH) are measured using a HygroVue hygrometer from Campbell Scientific, and two SI111 infrared radiometers from Apogee measure the surface temperature of different components, grass/bare soil and tree, ($T_{sup,g}$ and $T_{sup,t}$). In the soil, there are two CS616 FDR probes from Campbell Scientific for measuring volumetric water content (θ), and a 30 cm Sentek Drill&Drop probe equipped with three sensors spaced 10 cm apart that provide soil moisture and temperature profiles. Additionally, four HFP01 heat flux plates (Huskeflux) are installed around the tower to measure ground heat flux (G). Between 2014 and 2018, various sensors for measuring sap flow were installed based on Granier (1987) technique (see Chapter 6 section 6.2 for the theory of the measurement). In the spring-summer of 2018, a variant of these sensors was installed in the roots: two complete bidirectional sensors and two that measure only direction. The complete bidirectional sensor consists of a symmetrical system of two pairs of reference probes centered around the heated probe. In this case, the needle length is either 2 or 1 cm, depending on the size of the monitored root.

The probes of the first pair are positioned approximately 10 cm to the right and left of the heated probe and are referred to as: proximal, the one closer to the trunk, and distal, the one farther from it. A second pair of reference sensors is placed approximately 7 mm upstream and downstream from the heated probe. The directional-only sensor is composed solely of the pair located 1 cm from the heated probe and measures only the direction of the flow, not its intensity. All data, except for those from the eddy-covariance system, are collected at half-hourly resolution using a CR3000 datalogger from Campbell Scientific. In the same season three water potential MPS2 sensors by Decagon Devices were also installed close to the directional root sapflow sensors.

Instrumental Data Overview

This section presents an overview of the time series data collected at the study site, with a focus on key meteorological and turbulent flux variables. The aim is to provide a preliminary understanding of the temporal dynamics observed throughout the measurement period. Soil moisture measurements in Figure 2.4 a) reflect the temporal evolution of water availability in the rooting zone, providing insights into drought stress and soil–plant interactions, soil water potential measurements in Figure 2.4 b) offer a more integrative view of water availability, capturing the energetic cost required for plants to extract water from the soil matrix and at least soil temperature dynamics in Figure 2.4 c) are closely linked to seasonal changes. All variables in Figure 2.4 are at daily timascale.

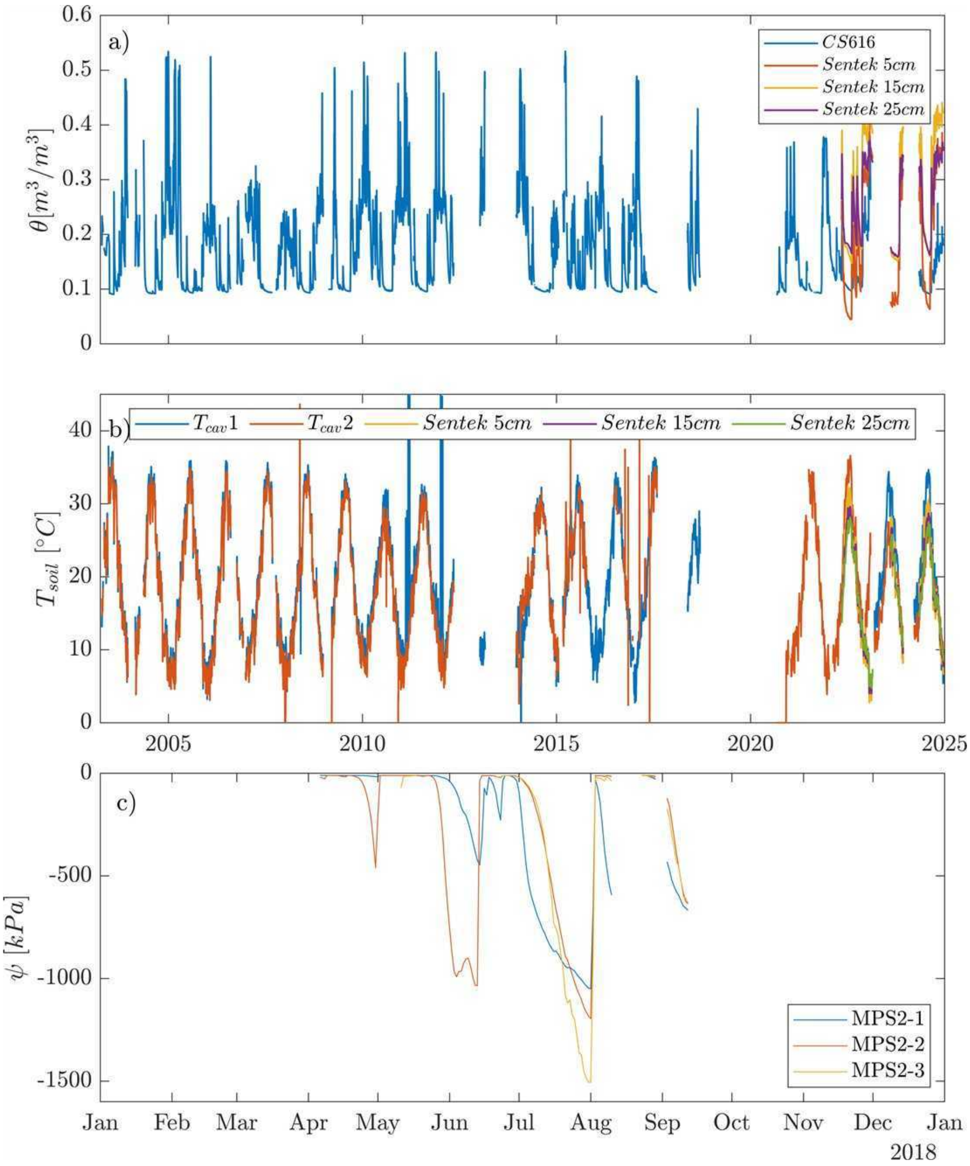

Figure 2.4: Soil related variable: a) soil moisture from two different soil moisture probes: FDR CS616 that is the mean of the 30cm soil layer in blue, soil moisture profile at three depth form the Sentek Drill and Drop in other colors; b) soil temperature in different position under the open patch: in blue and orange data from the thermocouple associated to the soil heat flux plate, in other colors soil temperature profile at three depth form the Sentek Drill and Drop; c)

The following is a list of the meteorological data that are the main drivers for the ecosystems: in Figure 2.5 a) it is presented precipitation that is a key forcing variable for both soil moisture and vegetation activity, air temperature T_a measured from the hygrometer at 2m height and from the CSAT3B at 10m height governs biological and physical processes (Figure 2.5 b), including evapotranspiration, photosyntesis and respiration rates; relative humidity in Figure 2.5 c) computed from the HygroVue at 2m height and from LI-7500 at 7m height, calculated from equation A21 from Garratt (1994); also VPD is derived from the same equation using T_a and RH of HydroVUE and the Eddy-Covariance system.

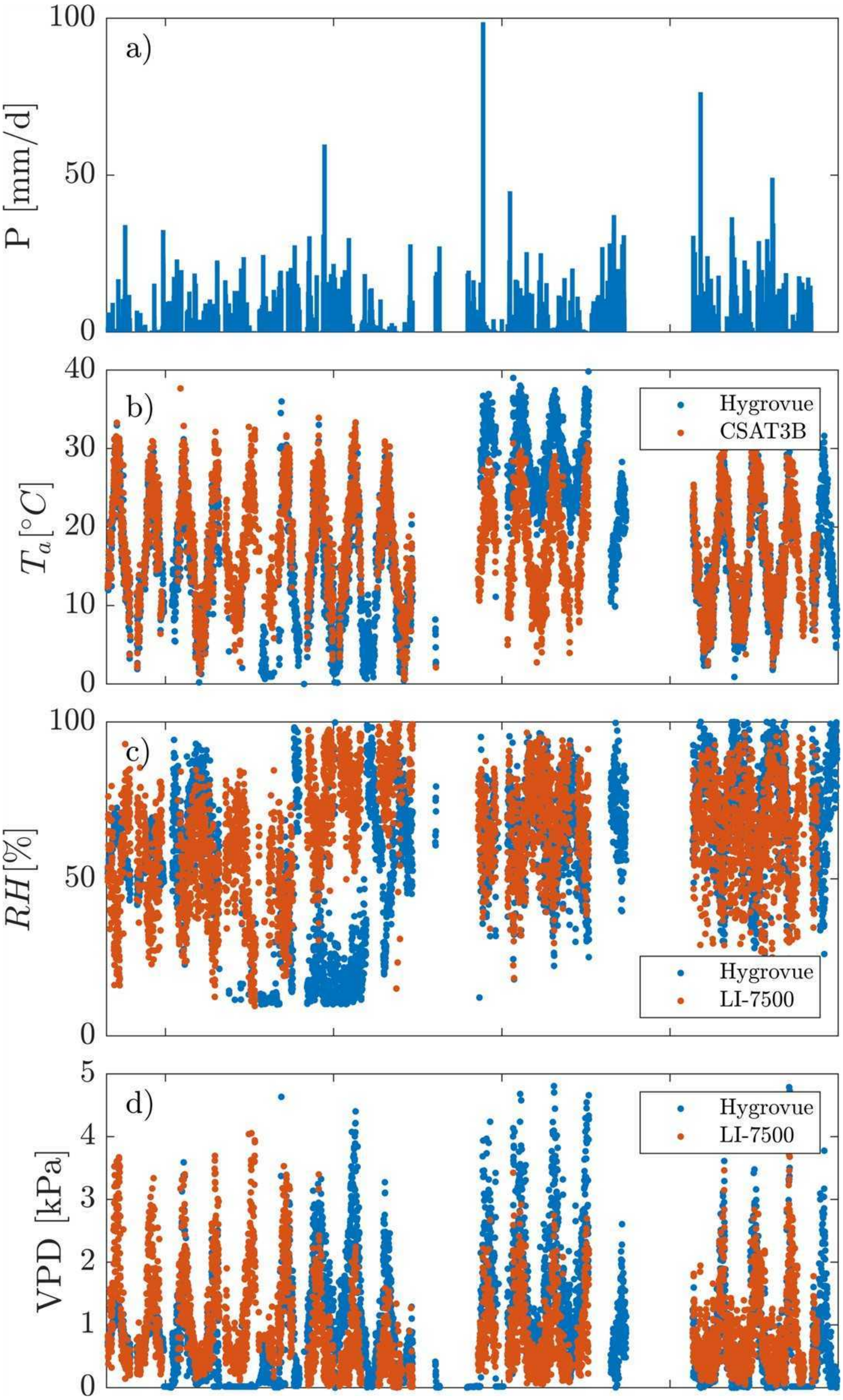

Figure 2.5: Meteorological data at daily timescale: a) precipitation; b) air temperature, in blue data from the HygroVue hydrometer at 2m height, in orange data from the sonic anemometer at 7m height; c) relative humidity, in blue data from the HygroVue hygrometer at 2m height, in orange data from the gas analyzer at 7m height; d) vapor pressure deficit, in blue data derived from T_a and RH from the hygrometer at 2m height, in orange data computed using the T_a from the sonic anemometer and RH derived from the gas analyzer.

With respect to vegetation, the raw data available consist of canopy, grass/bare soil or mixed surface temperature, sap flow measurements and total evapotranspiration. Canopy temperature, measured by the infrared radiometer SI111 (Figure 2.6 a), provides indirect information on energy balance, and stress levels under variable environmental conditions. Sapflow is measured using sensor based on (Granier, 1987), following Montaldo et al. (2020) and Ward et al. (2017) to estimate the baseline (Figure 2.6 b). It captures plant water uptake dynamics (f_d) and transpiration E_t.

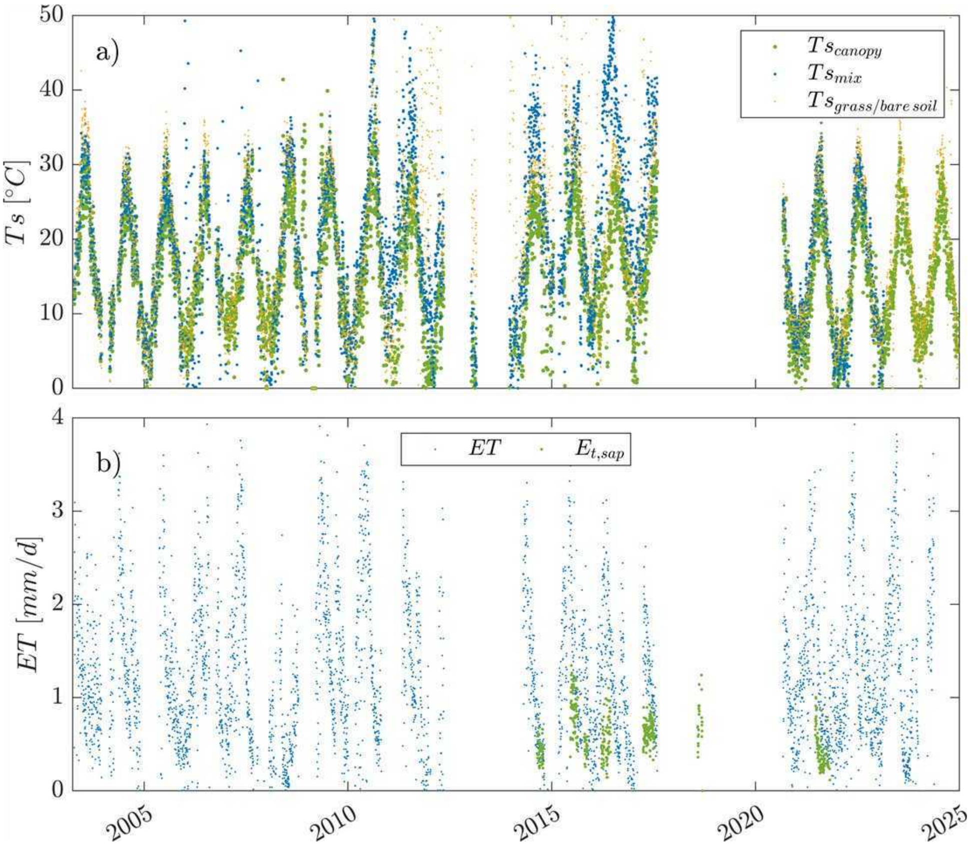

Figure 2.6: a) Surface temperature measured by the infrared radiometers; b)total evapotranspiration measured by the eddy-covariance system in blue and wild olive tree transpiration measured by the sapflow sensor in green.

Turbulent fluxes of carbon and energy provide integrative measures of ecosystem function, including carbon sequestration and water/energy exchange with the atmosphere. Four components of the radiation, measured by the CNR-1, Rsw_{in}, Rsw_{out}, Rlw_{in}, Rlw_{out}, at daily time scale are in Figure 2.7 a). Data from the Eddy-Covariance system are use to estimate the latent heat flux (LE) and the sensible heat flux (H)(see Figure 2.7 b) and the carbon flux (F_c) (Figure 2.7 d) the Webb-Pearman-Leuning adjustment was applied (Detto et al., 2006, 2008).

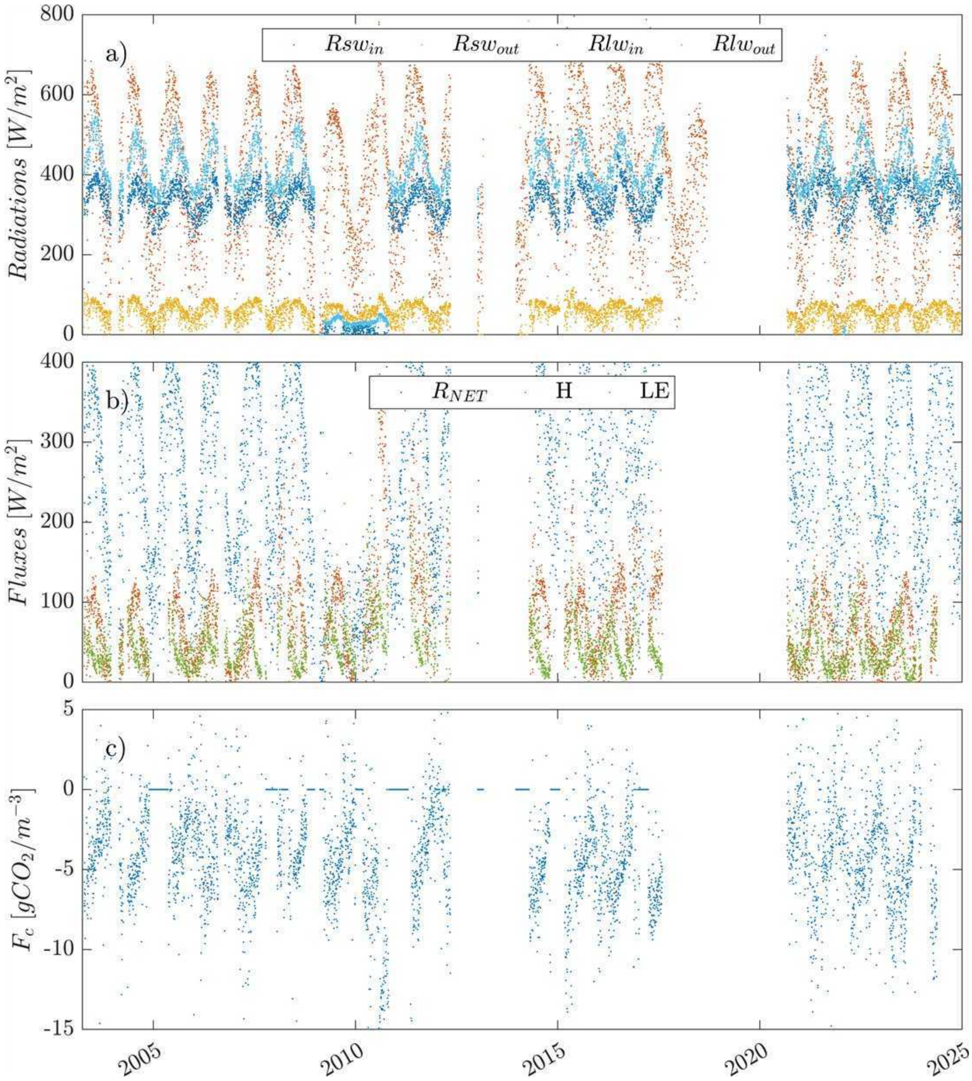

Figure 2.7: Daily fluxes: a) Four components of the radiation, dots are the observed data; b) Energy balance components; c)daily carbon flux measure by the Eddy-Covariance system.

Hydraulic redistribution

The hydraulic redistribution refers to the transport of water by roots from soil layers with higher water content to those with lower moisture levels (Rempe and Dietrich, 2018b; Eliades et al., 2018; Yan et al., 2019). This process is typical of arid and semi-arid climates, such as the Mediterranean one, in particular in patchy landscapes where tree clumps may reach for water extending roots not only into the rocky substrate below their canopies, but also horizontally into the soil and underlying rock of the surrounding areas covered with highly seasonal, shallow-rooted vegetation(Breshears, 2006; Breshears et al., 2009; House et al., 2003). , and can be divided into two distinct mechanisms: upward HR, also known as hydraulic lift, and downward HR (Luo et al., 2016). Montaldo et al. (2021), combined sap flux measured in trees across the eddy-covariance footprint with energy balance and eddy-covariance measurements to estimate ET and its components together with measured precipitation and soil moisture, and modeled flux components, to calculate a seasonal soil water balance and estimated of root water uptake from the rocky substratum of more then 50% of ET in spring and summer. As part of that study data from bidirectional root sapflux and soil water potential. In Figure 2.8 are presented the complete half-hourly timeseries of the two bidirecional rootsapflow sensors and the simplified ones. In the first panel the normalized signal of the sensors are plotted, showing the inversion of the flux during the night mainly of the sensor close to the stem (see the position of the sensors in 2.8 b). In pannels 2.8 b-c) it's plotted the sapflux in the root, in particular it's interesting to notice how the intensity of the negative flow (from the stem) increase from spring to July 2018.

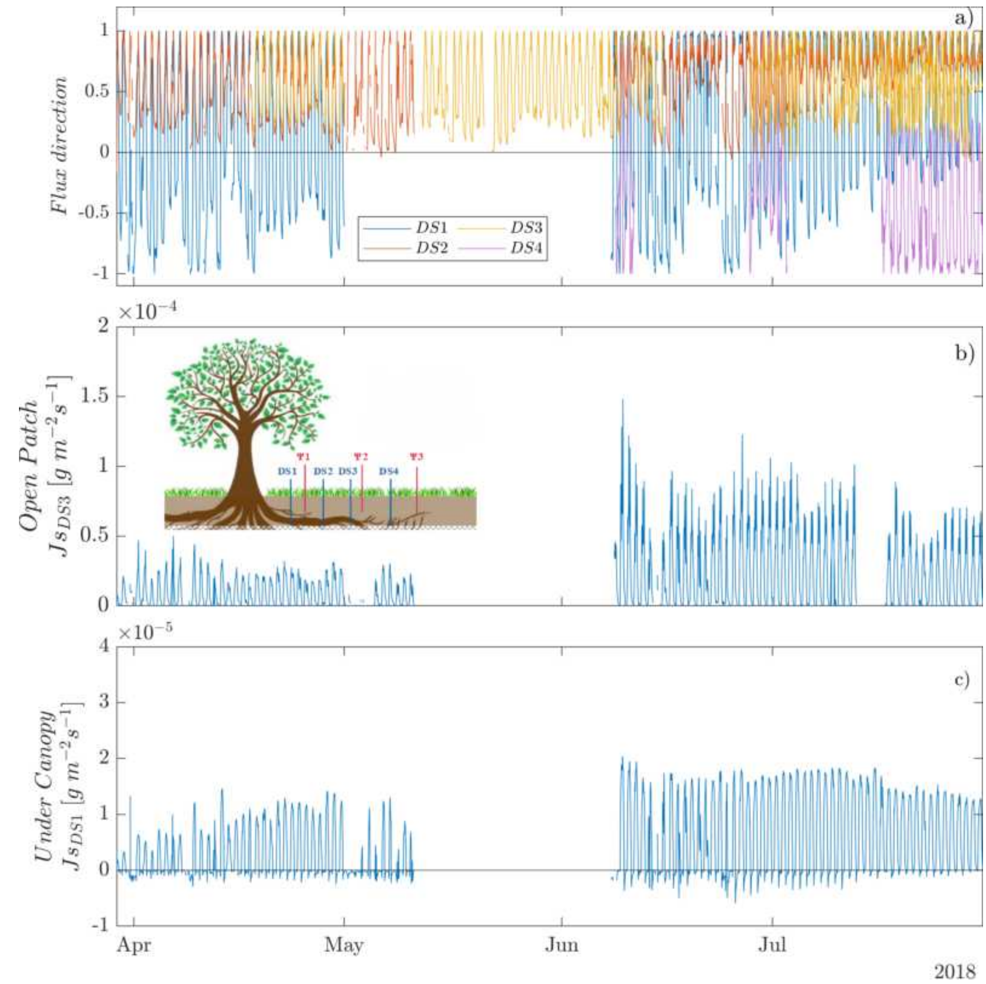

Figure 2.8: Time series of the root sapflux sensor: a) normalized signal of the directional sensors (probes at 1 cm to the heater); b) flux measured by the distal probe, in the pannel is also shown the position of the sapflux probes in the root and the water potential; c) flux measured by the proximal probe

Combining soil water potential and root sap flow measurements during July 2018, it was evaluated qualitatively the horizontal water flux between the area under the canopy and in the pasture, in the surface soil layer,and how it is supported by roots in the fractured rocks (Figure 4). July 2018 was a dry month following an unusually wet June, during which the soil saturated. Hence, ψ_s decreased from saturated to dry conditions both under the clump canopy and in the pasture, but at clearly different rates (Figure 2.9a). Under the canopy, water content decreased quickly due to tree water uptake; in the open, the senesced grass not only did not transpire, but may have slowed down evaporation; thus, a soil water potential gradient developed between the pasture area and tree clumps

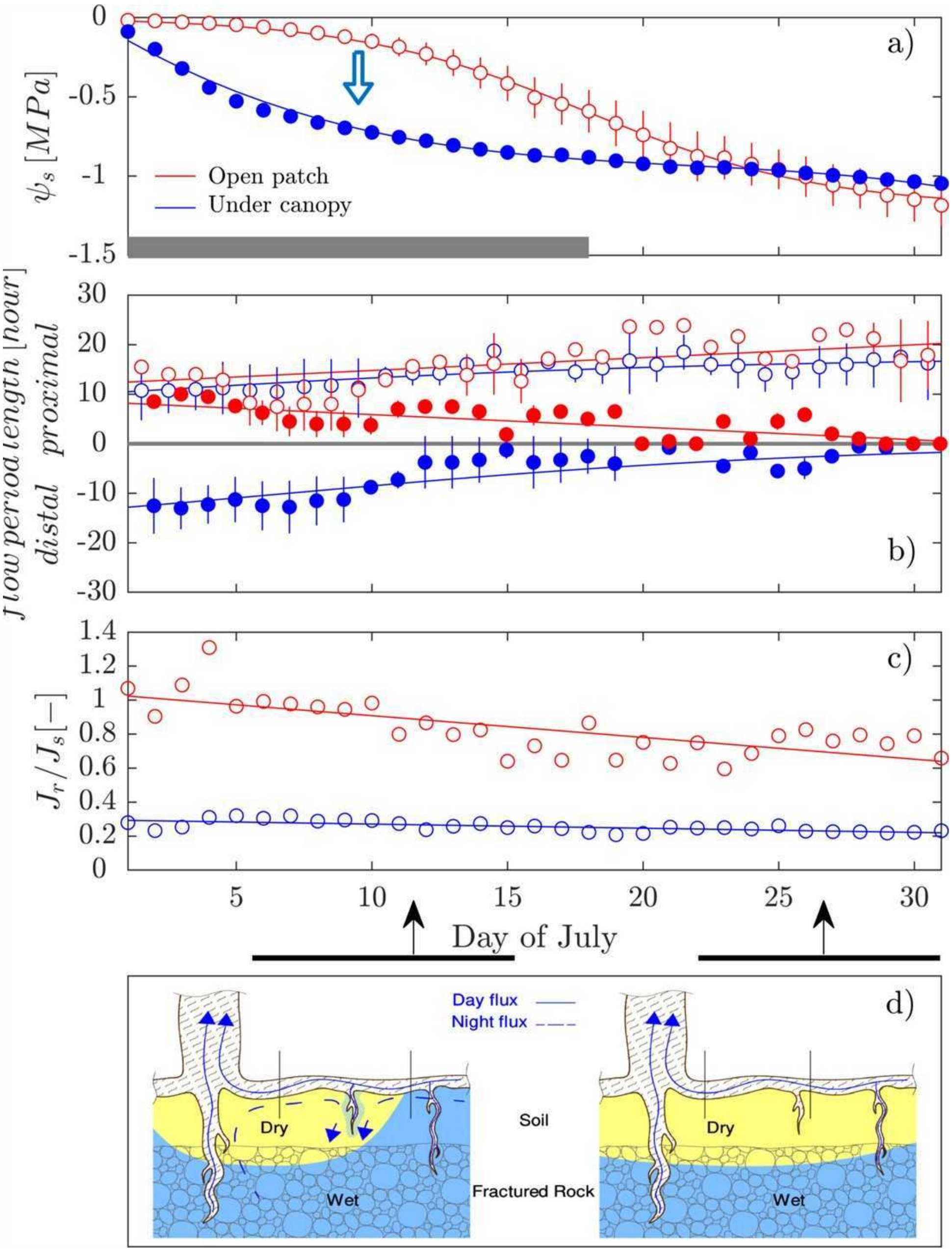

Figure 2.9: Over a drying cycle, a) a comparison between soil water potential (ψ) of a probe under the canopy and the mean of probes in the pasture area. The blue arrow indicates the direction of the force for water flow, and the horizontal gray line at the bottom indicates the days in which the two series are different($p < 0.05$, one sample t-test). b) The mean flow period length (in hours; proximal is toward the tree) of daytime (open points) and nighttime (filled points) of directional flow sensors under the canopy in the senesced grass-covered area . c) The ratios of root sap flow (Jr), one measured near the stem and the other in the grass-covered area (3 m from a tree clump) to mean (n = 6) stem sap flow (Js). d) Schematic representation of diurnal and nocturnal sap flux between trees and grass-covered area as soil drying progressed from near the tree clump; blue area represents moist soil and fractured rock

(Figure 2.9a;ψ_s gradient was significantly different from zero during the period represented by the horizontal bar; one sample t-test $p < 0.05$). This is consistent with the directional flow measurements, showing persistent proximal flow during both day and night from roots in the pasture(Figure 2.9b). Roots near the clumps showed proximal flow only in daytime, but distal flow at nighttime, likely from rock moisture recharging the overlaying soil near the clumps (Figure 2.9b and left panel of Figure 2.9d). Then, as the gradient decreased later in the month (Figure 2.9a), nighttime flow ceased, and unchanging soil moisture suggest that root-soil contact in the dry soil decreased and the proximal flow observed during most of the daytime hours in roots near and far from the clumps Figure (2.9b), was supplied by rock moisture uptake (right panel of Figure 2.9d). Sap flux of roots near clumps was low relative to that in stems, but nearly invariable (Figure 2.9c), while that of distant roots was similar to the stem sap flux, but decreased in relativeterms as the soil dried; this suggests that when the shallow soil dries, limits to water uptake are imposed by access to rock moisture only (Figure 2.9d).

The effect of the heterogeneus landscape on the flux measurament

Turbulent flows are presumed to have a spectrum of eddies of different sizes or time scales as determined by a decomposition of the velocity or scalar field into sinusoidal components of different wavelengths or frequencies (Wyngaard, 2010). The Eddy-Covariance instrumentation installed at Orroli since 2023 also enables the storage of high-frequency raw data ($10Hz$), allowing the implementation of spectral analysis on historical time series. Spectral analysis of high-frequency data is a technique used to study the distribution of energy or variance of measured signals as a function of frequency (see Chapter 6 section 6.3 for the theory). This methodology is particularly useful for analyzing turbulent phenomena that govern the exchange of mass and energy between the atmosphere and the land surface. Eddy-covariance stations are advanced instruments that record high-frequency data (usually in the order of 10–20 Hz) related to variables such as wind speed, temperature, humidity, and concentrations of gases like CO_2. Spectral analysis allows these signals to be decomposed into components at different temporal and spatial scales, enabling the identification of dominant physical processes. This technique helps to understand how turbulent energy is distributed among different scales of motion, from large eddies (low frequency) typical of the meso-scale phenomena,to small eddies (high frequency) more related to turbulent flow. This is crucial for describing how heat, moisture, and trace gas fluxes are transferred between the land surface and the atmosphere. Through spectral analysis, it is possible to identify which temporal (or spatial) scales are most relevant for the observed fluxes. These results can then be compared with theoretical predictions or ideal cases, as in our study, which involves a comparison with the Kansas case. The reference case for studying turbulent phenomena measured using the eddy-covariance technique is represented by the study conducted in Kansas in the 1970s, in a relatively flat and uniform agricultural area, ideal for investigating turbulence under quasi-homogeneous conditions.

The particularity of Orroli lies in the heterogeneity of the site's vegetation, which is more homogeneous in the distribution of trees in the South-East, while in the North-West there is a mix of seasonal herbaceous vegetation and olive trees. For this reason, the analysis was divided according to the two main wind directions (South-East and North-West) and the spring and summer seasons. The comparison between spectra calculated from Orroli's data and the results from the Kansas site (Wyngaard, 2010) thus allows for an estimate of the impact of this heterogeneity on energy fluxes into the atmosphere.

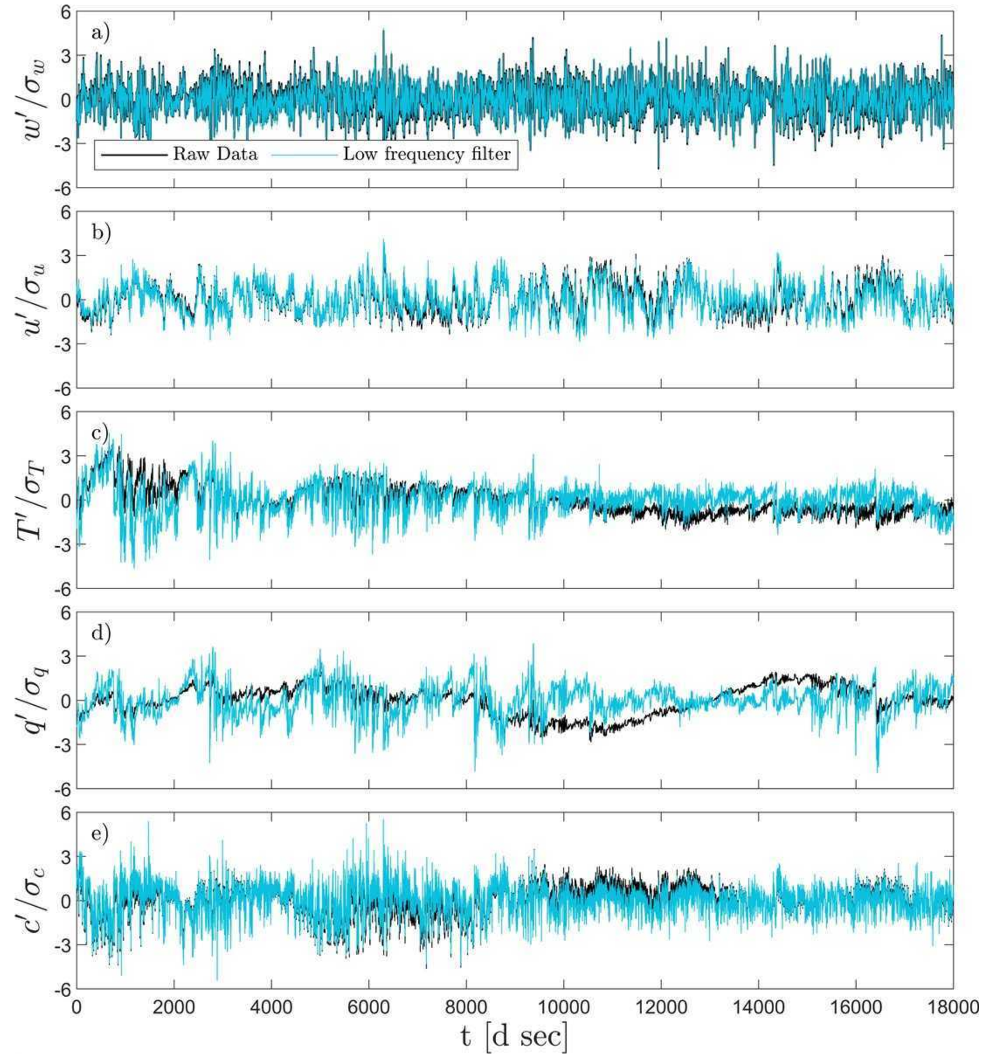

Figure 2.10: Example of the effect of the 5-min spectral filtering on the time series of turbulent vertical velocity with abscissa being time (in deciseconds) and ordinate being; a) w'/σ_w, b) longitudinal velocity u'/σ_u, c) temperature T'/σ_T, and d) water vapor concentration q'/σ_q and e) CO_2 concentration normalized by the standard deviation. The run featured here was collected on October 31^{st} (DOY=304, 14:30) for the NW wind direction. The black lines are the original and the blue lines are the filtered series. Note the appreciable effect of filtering on water vapor concentration.

Spectra were calculated from the fluctuations, and to evaluate the effects of non-turbulent motion on momentum and scalar exchanges (Figure 2.10), Fourier coefficients were computed for each flux variable over 30-minute intervals. All Fourier amplitudes associated with events with time scales longer than 5 minutes were set to zero. Then, an inverse Fourier transform was applied to reconstruct the time series of each flux variable without any low-frequency modulation.

Figure 2.11: The reduction in scalar variances due to low-frequency filtering (ordinate) compared to the original variance (abscissa) for different seasons and mean wind directions. The water vapor is most impacted by the spectral removal of low-frequency fluctuations. In each panel, the black dashed lines represent the regression lines forced to zero- intercept between the raw variable and the low-filtered one. The one-to-one solid lines are shown for reference. For the velocity components, the filtering had minor effects and is not shown.

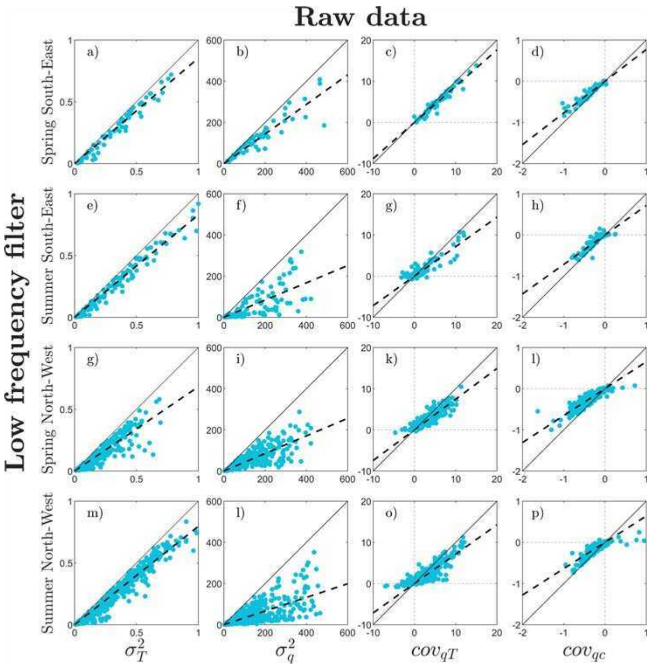

As it's shown in Figure 2.11 and Figure 2.11, the greatest impact of the filter is predominantly found on scalar variables, particularly on the variance of water vapor. Ratios between the scale of water vapor concentration and its variance, and between temperature scale and its variance, shown in Figure 2.12, are higher than the reference parameters reported by Kaimal and Finnigan (1994) (eq. 1.53). This suggests the presence of intense turbulent motions and vertical exchanges involving warmer and drier air, often associated with entrainment processes. These phenomena are particularly relevant during the summer season, which in Sardinia is typically hot and humid. These conditions may be influenced by the site's unique topography, located at the center of a Mediterranean island, relatively close to the sea (approximately 40 km to the South-East and about 70 km to the North-West) and near a mountainous region. Despite the filter removing the main mesoscale effects, low-frequency distortions remain (probably linked to entrainment phenomena). Comparing raw and filtered latent heat flux (LE) and sensible heat flux (H) fitting the data with $y = ax$ shape, the ratio $\frac{LE_{raw}}{LE_{filtered}} = 1.08$(goodness of fit: $R^2 = 0.93$, $rmse = 16.80W/m^2$, confidence interval=[1.069 1.091], significant level $\alpha = 0.05$) and the ratio $\frac{H_{raw}}{H_{filtered}} = 1.05$ (goodness of fit: $R^2 = 0.98$, $rmse = 13.62W/m^2$, confidence interval=[1.048 1.056] and significant level $\alpha = 0.05$),filtering has minimal impact on these fluxes but mainly influences variances.

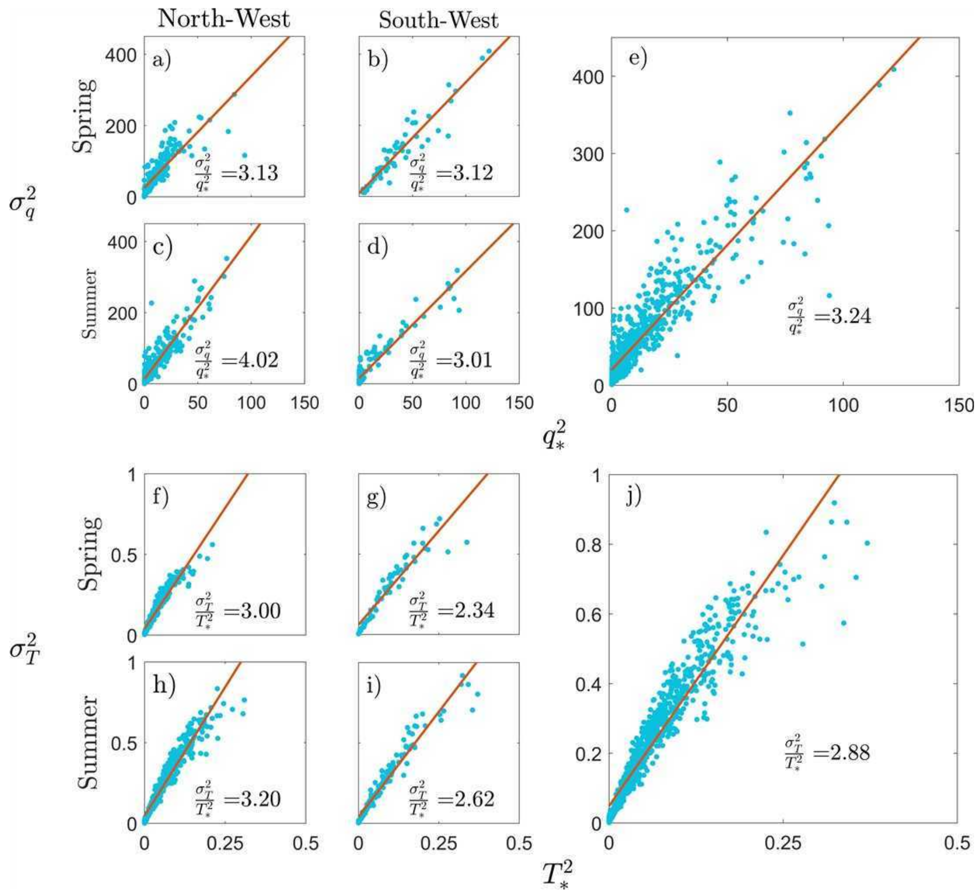

Figure 2.12: Comparison between scalar variances σ_s^2 and characteristic scalar scales S_*^2 for water vapor and heat where $S_* = \overline{w's'}/u_*$ and for the two seasons and wind directions. For the Kansas experiment, $\sigma_s^2 = 1.8(s_*)^2$, where $s_* = \overline{w's'}/u_*$. In panels a) to d) the relation between q_*^2 and σ_q^2 for each season and directions is shown. In panels f) to i) the relation between T_*^2 and σ_T^2 for each season and directions is shown. The last column (panels e) and j)) repeats the analysis without distinction between wind direction or season. In each panel, the orange solid line is the regression between the scaling variable (q_*^2 or T_*^2) and its scaler variance σ_q^2 and σ_T^2, the ratio presented in each plot is the slope of the regression line computed as a first degree polynomial.

	South-East		North-West		North-West$_{hc=0}$	
	Spring	Summer	Spring	Summer	Spring	Summer
$\frac{fS_w}{\sigma_w^2}$	0.25	0.20	0.40	0.40	0.63	0.63
$\frac{fS_w}{\sigma_w^2}_{kansas}$	0.50	0.50	0.50	0.50		
$\frac{fS_u}{\sigma_u^2}$	0.08	0.08	0.05	0.06	0.07	0.10
$\frac{fS_u}{\sigma_u^2}_{kansas}$	0.05	0.05	0.05	0.05		
$\frac{fC_{wu}}{\sigma_w\sigma_u}$	0.10	0.13	0.20	0.20	0.32	0.32
$\frac{fC_{wu}}{\sigma_w\sigma_u}_{kansas}$	0.08	0.08	0.08	0.08		
$\frac{fS_t}{\sigma_T^2}$	0.16	0.16	0.13	0.13	0.20	0.20
$\frac{fS_q}{\sigma_q^2}$	0.16	0.13	0.13	0.16	0.16	0.25
$\frac{fC_{wT}}{\sigma_w\sigma_T}$	0.16	0.16	0.25	0.25	0.40	0.40
$\frac{fC_{wq}}{\sigma_w\sigma_q}$	0.16	0.16	0.25	0.25	0.40	0.40
$\frac{fC_{wc}}{\sigma_w\sigma_c}$	0.16	0.16	0.25	0.32	0.40	0.50
$\frac{fC_{qT}}{\sigma_q\sigma_T}$	0.16	0.16	0.13	0.16	0.13	0.158
$\frac{fC_{qc}}{\sigma_q\sigma_c}$	0.16	0.13	0.10	0.25	0.20	0.25

Table 2.1: The location of the spectral and co-spectral peaks for the two dominant wind directions and two seasons as determined from the ensemble-averaged and filtered spectra and co-spectra.

	$\frac{fS_u}{\sigma_u^2}$	$\frac{fS_w}{\sigma_w^2}$	$\frac{fS_T}{\sigma_T^2}$	$\frac{fS_q}{\sigma_q^2}$	$\frac{fC_{wu}}{\sigma_w\sigma_u}$	$\frac{fC_{wT}}{\sigma_w\sigma_T}$	$\frac{fC_{wc}}{\sigma_w\sigma_c}$	$\frac{fC_{wq}}{\sigma_w\sigma_q}$	$\frac{fC_{qc}}{\sigma_q\sigma_c}$	$\frac{fC_{qT}}{\sigma_q\sigma_T}$
Spring South-East	-0.63	-0.50	-0.53	-0.66	-1.30	-0.73	-0.65	-0.86	-0.48	-0.94
Summer South-East	-0.61	-0.47	-0.53	-0.56	-1.22	-0.71	-0.50	-0.69	-0.50	-0.73
Spring North-West	-0.64	-0.51	-0.45	-0.65	-1.26	-0.75	-0.83	-0.83	-0.60	-0.79
Summer North-West	-0.64	-0.53	-0.47	-0.66	-1.25	-0.76	-0.80	-0.84	-0.66	-0.69
Mean South-East	-0.62	-0.49	-0.53	-0.61	-1.26	-0.72	-0.58	-0.77	-0.49	-0.84
Mean North-West	-0.64	-0.52	-0.46	-0.65	-1.26	-0.76	-0.81	-0.83	-0.63	-0.74
Mean all	-0.63	-0.51	-0.49	-0.63	-1.26	-0.74	-0.70	-0.80	-0.56	-0.79

Table 2.2: The slope of the linear regression of the high frequency (or inertial subrange) part of the spectra and co-spectra as evaluated for dimensionless frequencies higher than 0.7 but lower than 5 (just under a decade).

The computed spectra of the two velocity components and scalar quantities (temperature and water vapor) are shown in Figure 2.14. For the u' pre-multiplied spectra, an $f^{-2/3}$ scaling is observed (see Table 2.2, where slopes are tabulated) for eddies smaller than $(z-d)$ consistent with prior expectations for locally isotropic turbulence. at low frequencies for the w' and u' ensemble spectra, some distortions due to non-turbulent motion is observed in the u' spectra but not the w' spectra (Kolmogorov, 1991). In particular, the dimensionless frequencies associated with the peak spectra (i.e. the integral time scales) are shifted to low-frequency for the w' and to higher frequency for the u'. For the w', the peak frequency shift to low frequencies (or larger eddies) is more apparent along the SE direction. Along this direction, the flow experiences patchy vegetated canopy where the measurements may be within the roughness sublayer ($z/h_c = 2$). Thus, patch-scale heterogeneity commensurate with the separation distance between tree clumps (10 m), Kelvin-Helmholtz eddies commensurate with h_c (Katul et al., 1998), and attached eddies $(z-d)$ are contributing to the w' spectrum. The scalar spectra for heat and water vapor are impacted significantly by low-frequency (i.e. non-turbulent) motion. Even when filtering the non-turbulent motion, their shapes remain impacted by wind direction. The impact of such non-turbulent motion on the water vapor spectra is perhaps the most dominant feature when comparing Figure 2.14 in the low frequency range as already foreshadowed from Figure 2.11. Eddies that are two orders of magnitude larger than $z-d$ impact the spectra though this impact appears ameliorated for the spring in the SE direction. Plausible interpretations for these low frequency impacts often fall back to one or more of the following mechanisms: entrainment from the atmospheric boundary layer top, heterogeneity at the land-surface, marine influences through large-scale advection, or mesoscale-turbulence interaction causing non-stationarity. The 5-min filtering suppresses meso-scale motion (meso-scale times are measured in hours) but does not suppress entrainment processes. Thus, the filtered water vapor and temperature spectra reported here may be viewed as not dominated by meso-scale motion (or non-stationarity associated with it). Figure 2.14 shows that these large scale or low frequency effects may be related to entrained water vapor and temperature by eddies much larger than $z-d$. Partial support for this speculation is that for when expressing $S_q(k_x)$ and $S_t(k_x)$ by inertial layer scaling variables (u_* and z) and requiring independence from z at $k_x z < 1$, the dimensionless $S_q(k_x)$ and $S_t(k_x)$ may be written as (Katul et al., 1995; Kader and Yaglom, 1991)

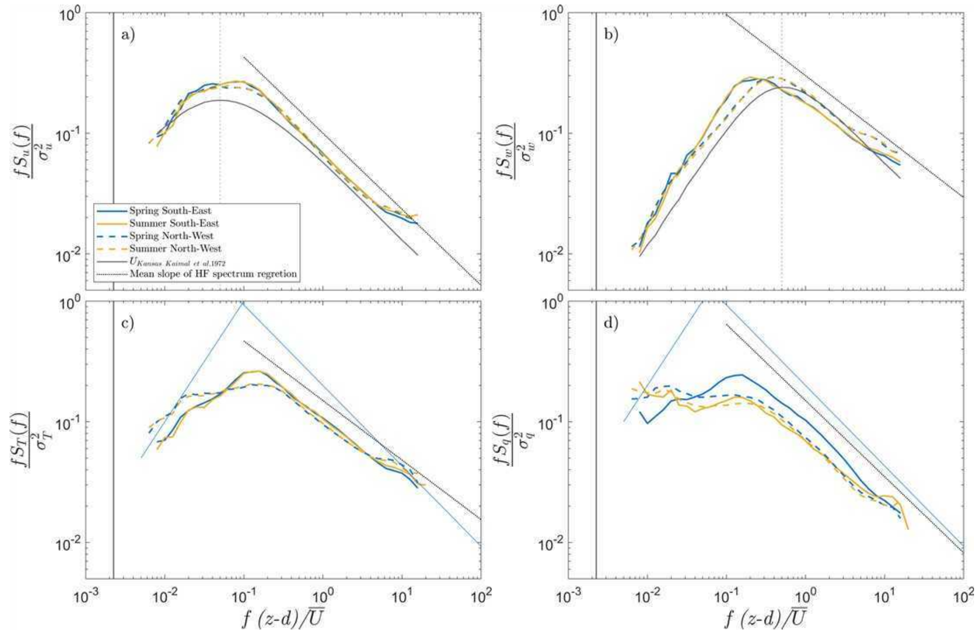

Figure 2.13: The ensemble-averaged pre-multiplied spectral variations with dimensionless frequency $f(z-d)/\overline{U}$ derived from the *filtered* time series for the two wind directions and the two seasons. Spectra are normalized to ensure unit variance so as to permit comparison. The normalized Kansas spectra are repeated for reference. Note that the water vapor spectra is consistent with turbulence theories compared to its original counterpart at low frequencies. In each panel, the black vertical lines represent the ensemble-averaged ABL height δ. In panels a) and b) the black dashed thin line represents the peak position of the Kansas spectra. In panels c) and d) the thin blue solid lines represent Kansas slopes for low frequency spectra (i.e. f^{+1}) and high frequency spectra (i.e. $f^{-2/3}$).

The spectral analysis is repeated for co-spectra of momentum, heat, water vapor, and carbon

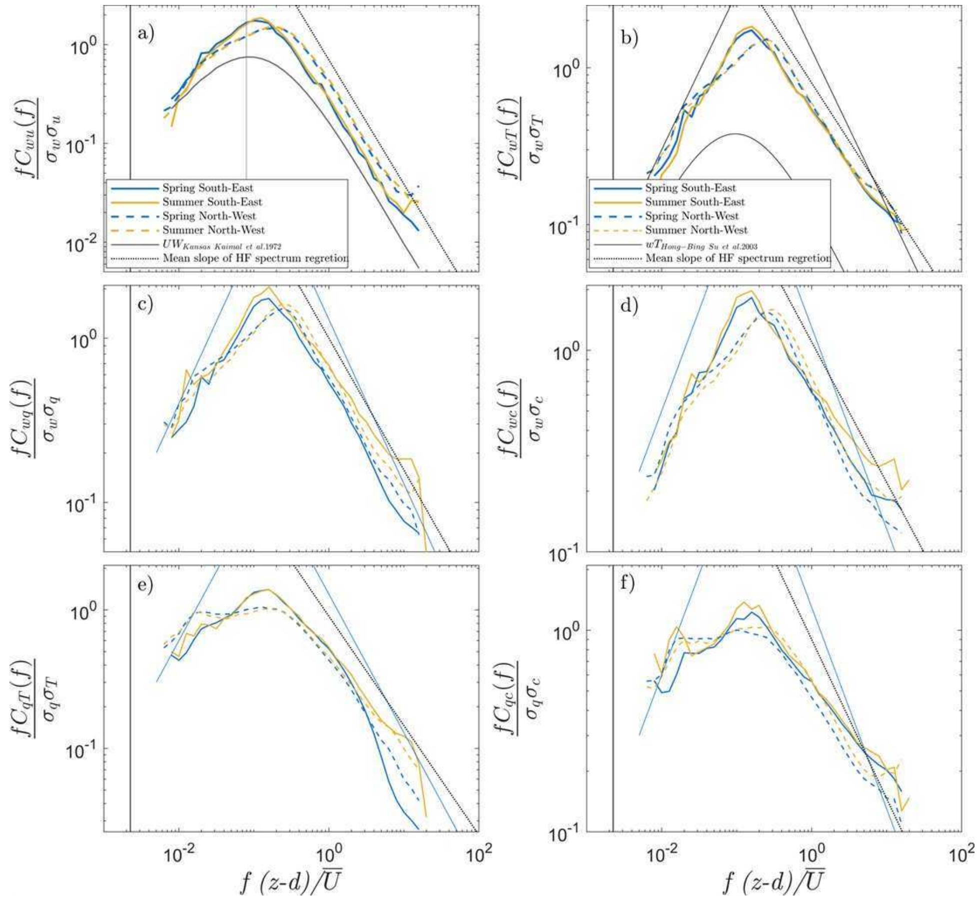

Figure 2.14: The ensemble-averaged pre-multiplied spectral variations with dimensionless frequency $f(z-d)/\overline{U}$ derived from the *filtered* time series for the two wind directions and the two seasons. Spectra are normalized to ensure unit variance so as to permit comparison. The normalized Kansas spectra are repeated for reference. Note that the water vapor spectra is consistent with turbulence theories compared to its original counterpart at low frequencies. In each panel, the black vertical lines represent the ensemble-averaged ABL height δ. In panels a) and b) the black dashed thin line represents the peak position of the Kansas spectra. In panels c) and d) the thin blue solid lines represent Kansas slopes for low frequency spectra (i.e. f^{+1}) and high frequency spectra (i.e. $f^{-2/3}$).

dioxide. Two additional co-spectra are also featured: the temperature-humidity and the carbon dioxide-humidity.

The co-spectra for momentum show peaks that are shifted to higher frequencies in the NW direction and less so in the SE direction. In the NW direction, these peaks occur at higher frequencies compared to those reported for the Kansas experiment perhaps due to some wake distortions as earlier noted. This is certainly the case for both filtered and original time series.

The sensible heat flux, latent heat flux, and carbon dioxide flux co-spectra also follow the same shapes as their momentum co-spectra (albeit noisier) suggesting that Reynolds' analogy holds for scalar and momentum vertical transport in near-neutral conditions. The effective eddy sizes dominating momentum and scalar transport are also similar - with the NW direction being at higher dimensionless frequencies compared to the SE direction. Uncertainties in zero-plane displacement alone cannot explain those differences.

The location of the maxima in the pre-multiplied co-spectra offers clues about the dominant eddy sizes contributing to momentum and scalar exchanges. For the momentum co-spectra, the peaks for the SE direction occur at lower dimensionless frequencies (larger eddies) than the peaks along the NW direction by a factor of 2. Likewise, the peaks in the co-spectra of heat, water vapor, and carbon dioxide fluxes follow the same trends as their momentum counterpart when contrasting the SE with the NW directions as in Table 2.1. While the pre-multiplied spectral peaks in the scalar co-spectra align well with the scalar spectra for the SE direction, they do not for the NW direction. The peaks in the pre-multiplied co-spectra of water vapor and temperature, and water vapor and carbon dioxide (i.e. scalar-scalar interaction) remain bounded between the spectral peaks in the longitudinal and vertical velocity pre-multiplied spectra. This means that the most efficient eddies causing scalar-scalar similarity are those associated by attached eddies between z and δ (Huang and Katul, 2022). The scalar-scalar peaks also align reasonably with the peaks in the pre-multiplied water vapor and temperature spectra. For the near-neutral flows considered here, the estimates of δ/z is on the order of 10-20.

At high frequencies, the scaling laws for the pre-multiplied co-spectra of $u'w'$ follow expectation for the inertial subrange (i.e. $f^{-4/3}$) as shown in Table 2.2. In the case of co-spectral analysis (see Figure 2.14, a notable change in high frequency slopes compared to the Kansas experiment is observed, particularly for turbulence coming from the North-East, suggesting the effect due to greater vegetation heterogeneity in that direction. The scalar pre-multiplied co-spectra all decay much slower than $f^{-4/3}$ and even slower than f^{-1} reported in other studies (Horst, 1997; Su et al., 2004; Bos et al., 2004) for the same inertial subrange where $F_{uw}(k_x)$ was shown to scale as $k_x^{-7/3}$. This finding cannot be explained by the fact that $F_{ww}(k_x) \sim k_x^{-1.5}$ and does not follow $k_x^{-1.67}$ expected from local isotropy consideration. As shown earlier, the co-spectra for momentum do obey an $f^{-4/3}$ (or $k_x^{-7/3}$). To offer one plausible explanation, the same type of co-spectral analysis employed for momentum can be used.

In this analysis, a relation between the scalar co-spectra and $F_{ww}(k_x)$ can be derived and is given by (Katul et al., 2014)

$$F_{wc}(k_x) = \frac{\tau_R(k_x)}{C_R}\left[(1-C_I)\frac{d\overline{S}}{dz}F_{ww}(k_x) + \frac{4}{3}\beta_o F_{Ts}(k_x)\right], \tag{2.1}$$

where $\beta_o = g/\overline{T}$ is the buoyancy parameter, g is the gravitational acceleration, and $F_{Ts}(k_x)$ is the cospectrum between temperature and scalar S (i.e. temperature, water vapor, or carbon dioxide). In the case where the scalar being analyzed is temperature, $F_{Ts}(k_x)$ becomes the temperature spectrum $F_{TT}(k_x)$, which is always present and positive even in near-neutral atmospheric conditions (i.e. $d\overline{T}/dz = 0$). Unlike momentum co-spectra, the scalar co-spectra are sensitive to the co-spectra between temperature and scalar S (i.e. scalar-scalar interaction). While $F_{ww}(k_x)$ is the same for all scalar and momentum co-spectra in equation 2.1, land surface heterogeneity may be sensed differently for momentum compared to scalars. This difference may be accommodated by $\tau_R(k_x)$ - which measures how effective is the pressure-scalar interaction is at de-correlating w' from u' or a scalar S. The largest impact of heterogeneity is likely to be in the water vapor scalar sources.

To sum up, Figure 2.15 presents a schematic summary of the main findings in terms of the impacts of removing low frequency (i.e. non-turbulent motion) and interrogating different heterogeneity (through wind direction selection) on variances, co-variances, and their energy distribution across scales (or frequencies). Deviations from the Kansas experiments are also presented in this Figure 2.15 with vertical and horizontal arrows used to indicate increases/decreases in energy content (vertical arrows) or shifts to larger/smaller scales (horizontal arrows). The effects of wind direction - with NW resembling a disturbed boundary layer and SE resembling a roughness sublayer - are presented in Figure 2.15 using different colors. Based on the analysis here and their schematized summary outcome in Figure **??**, the following conclusions can be drawn:

- The relation between velocity variances σ_u^2 and σ_w^2 and u_*^2 is robust to varying wind direction and seasonality despite apparent difference in land cover. Likewise, the normalized momentum roughness height $z_o/(z-d)$ inferred from a drag coefficient is also not appreciably impacted by wind direction and seasonality. Filtering low frequency events did not have any significant impact (i.e. less than 10%) on σ_u^2, σ_w^2, and $\overline{w'u'}$. These results are 'good news' for applying flux foot-print models that assume the velocity field is stationary and planar homogeneous (Detto et al., 2006).

- The impact of low frequency fluctuations on scalar variances is appreciable but not scalar turbulent fluxes. For temperature, the reduction in variance due to filtering scales reasonably with the variance magnitude. For water vapor, no such scaling exists and suggest external (or large scale) factors must be responsible. The impact of low-frequency motion and spatial patchiness

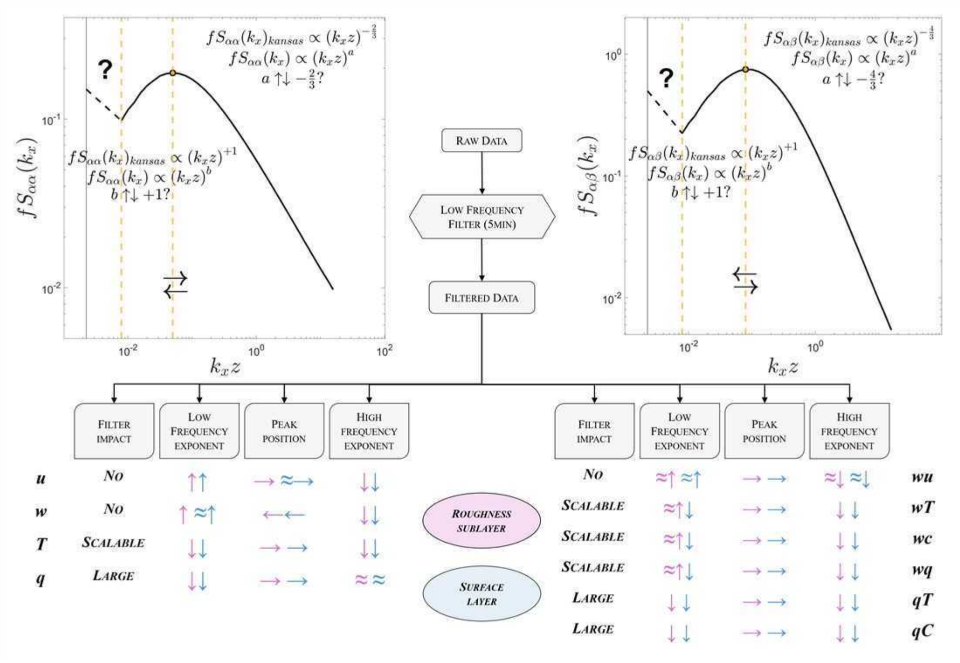

Figure 2.15: A summary of the key conclusions derived from the analysis when compared to the reference Kansas spectra and co-spectra. In this summary, the impact of the low-frequency filter, the peak spectral and co-spectral frequency location, scaling exponents of the spectra in the low-frequency and the high-frequency parts are qualitatively shown as increment or decrement relative to expectations from the Kansas shapes. Pink arrows are used to summarize results for the South-East direction and blue arrows are used for the North-West direction. The arrow direction indicates increases or decreases (vertical) or shift to the right or left (horizontal) compared to those reported for Kansas.

of the water vapor sources, especially during the summer months, weakens the relation between filtered and original σ_q^2. This finding implies that attempts to partition evapotranspiration into evaporation and transpiration using carbon dioxide and water vapor high frequency time series (Scanlon and Sahu, 2008; Scanlon and Kustas, 2010; Zahn et al., 2022) must be used with caution as entrainment effects are often not explicitly factored in.

- The normalized spectra of vertical velocity are insensitive to season, and the role of low frequency filtering had a minor effect on their shape when analyzed by season. This implies that attached eddies dominate the spectra between z and δ, which is well established from experiments and simulations for near-neutral canonical boundary layers (Kader and Yaglom, 1991; Katul and Chu, 1998; Drobinski et al., 2004; Huang and Katul, 2022).

- The co-spectra of the momentum fluxes were reasonably approximated by their Kansas counterpart with some modification to the frequency location of the peak momentum flux depending on wind direction. The scalar co-spectra, especially in the inertial subrange, deviated appreciably from local isotropy expectations. This deviation was explained by an interplay between two new mechanisms: the addition of a scalar-scalar cospectra in the scalar-cospectral budget, the pressure-scalar decorrelation time scale interacting with the advected source heterogeneity. The larger the source heterogeneity, the more random the pressure-scalar decorrelation time scale appears. This speculation explains the bounds on the scalar co-spectral exponents at frequencies within the inertial subrange.

2.1.2 Marganai site

Study Site Description

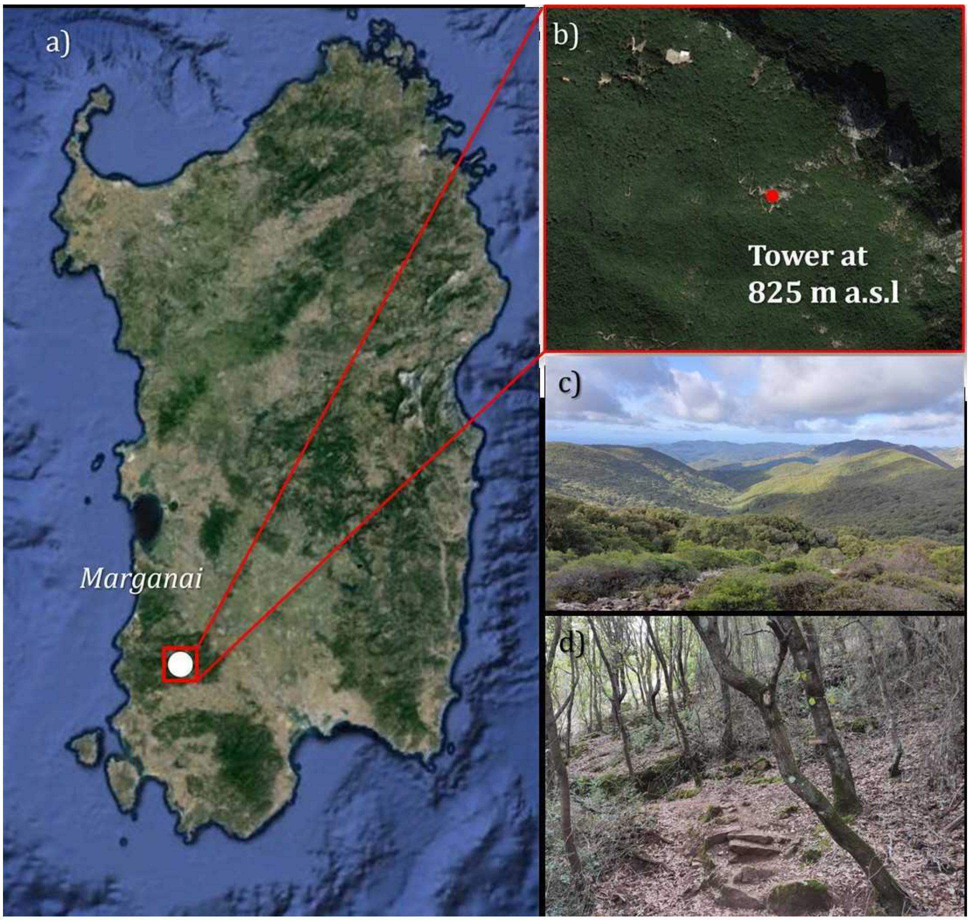

Figure 2.16: a) Geolocation of case study site 2 b) Aerial view of the site; c) site appearance from the tower point of view; d) under canopy area.

The field experiments are conducted near Iglesias, in the Sulcis-Iglesiente area of South-West Sardinia (39°20'54.63" N, 8°35'16.67" E) (see Figure 2.16 a), at an elevation of approximately 825 m a.s.l. The site is located on a mountain side (slope ~15° from W to E) and represents a typical Mediterranean forest ecosystem.

The Marganai forest is a Long – Term Ecosystem Research (LTER) Italian site and an European Site of Community Importance (Natura 2000), that includes five main forest management units managed bf Fo.Re.S.T.A.S.

The vegetation is mainly composed by *Quercus Ilex* (holm oak), *Quercus Sauber* (cork oak) and the typical species of Mediterranean maquis such as: *Arbutus Unendo, Philirea Latifoglia, Pistacia lentiscus and Erica arborea, etc...* (Figure 2.16 c-d).

The climate is classified as maritime Mediterranean. The long-term mean annual precipitation (1924–2024) is 782 mm, with dry summers averaging just 3 mm in July and wet winter with a maximum monthly precipitation of about 125 mm in December (see Figure 2.17). The mean annual air temperature is 16.3°C, reaching a monthly average of 24.3°C in August.

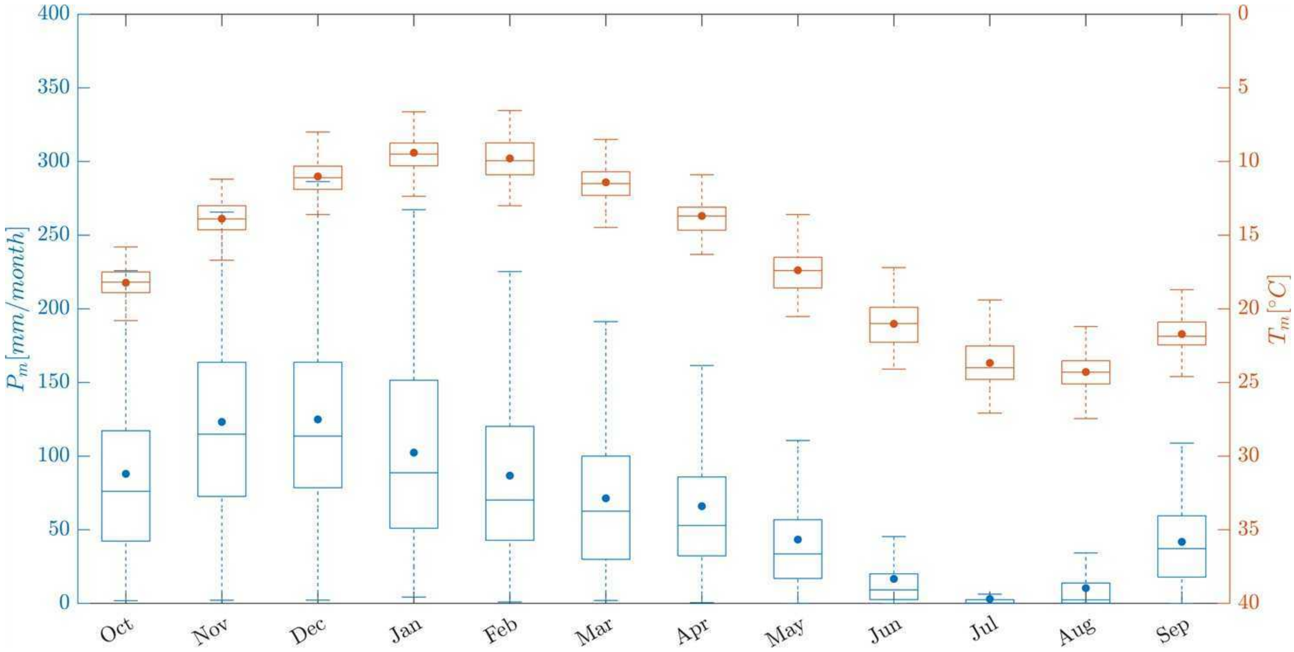

Figure 2.17: Historical climate in Marganai area, data since 1924 to 2024; the central mark indicates the median, and the bottom and top edges of the box indicate the 25th and 75th percentiles, respectively and the whiskers extend to the most extreme data points, the dots indicate the average value, in blue is presented the monthly precipitation and in orange it's presented the mean air temperature.

The area is characterized by rocky metamorphic layer with a shallow silty-clay soil in the valley part, and soil depth varies between 0 and 40 cm limited by an underlying layer of fractured metamorphic rock that constrains root development (see Figure 2.16 c-d).

Setup and Equipment

Figure 2.18: Marganai setup and equipment: a) micrometeorological tower, from the top to the bottom there are installed CSAT3B, LI-7500, NR-1 and the SI111 that measure canopy surface temperature. At about 5m height an bi-directional anemometer RMYoung 05103, and at 2m height the HygroVue from Campbell Sci., at about 5m from the tower it's installed the raingauge PMB2 CAE; b) Intallation of the sapflow sensor;c) ΔT theta probe d) installation of the MPS2.

In the end of November 2021, a micrometeorological measurement station was installed at this site, as part of the European projects SWATCH and FLUXMED. It consists of a 7-meter-high tower made of a modular tilting structure. On this tower, a CSAT3B 3D sonic anemometer from Campbell Scientific and a LI-7500 infrared gas analyzer from LI-COR (for CO_2 and H_2O) were installed. These instruments measure wind speed in three vector components, air temperature, and the concentration of the two gases at a frequency of 10 Hz. Using the eddy-covariance technique (Baldocchi, 2003b), the system estimates latent heat flux (LE) and sensible heat flux (H). At the same height, a NR-01 four-component radiometer (Huskeflux) and a SI111 infrared radiometers from Apogee. At about

5 meters from the tower a raingauge PMB2 (CAE) is installed, air temperature (Ta) and relative humidity (RH) are measured using a HygroVue hygrometer from Campbell Scientific at 2 m height. At about 20m from the tower, under the canopy there are installed a CS616 FDR probes from Campbell Scientific and a ΔT theta probe from ΔT for measuring volumetric water content (θ),. Additionally, two MPS-2 sensors (Decagon Device) that measure soil water potential (ψ) and soil temperature (T_{soil}), and from July 2022 to August 2023, six sapflow sensors (Granier, 1987) are installed in holm oak stems.

Instrumental Data Overview

To better characterize the functioning of the ecosystem and the prevailing environmental conditions, the temporal evolution of selected variables measured by the eddy covariance and auxiliary instruments is reported. These time series highlight seasonal patterns, climatic variability, and potential data anomalies.

Soil moisture measurements in Figure 2.19 a) reflect the temporal evolution of water availability in the rooting zone, providing insights into drought stress and soil–plant interactions, soil water potential measurements in Figure 2.19 b) offer a more integrative view of water availability, capturing the energetic cost required for plants to extract water from the soil matrix and at least soil temperature dynamics in Figure 2.19 c) are closely linked to seasonal changes. All variables in Figure 2.19 are at daily timascale.

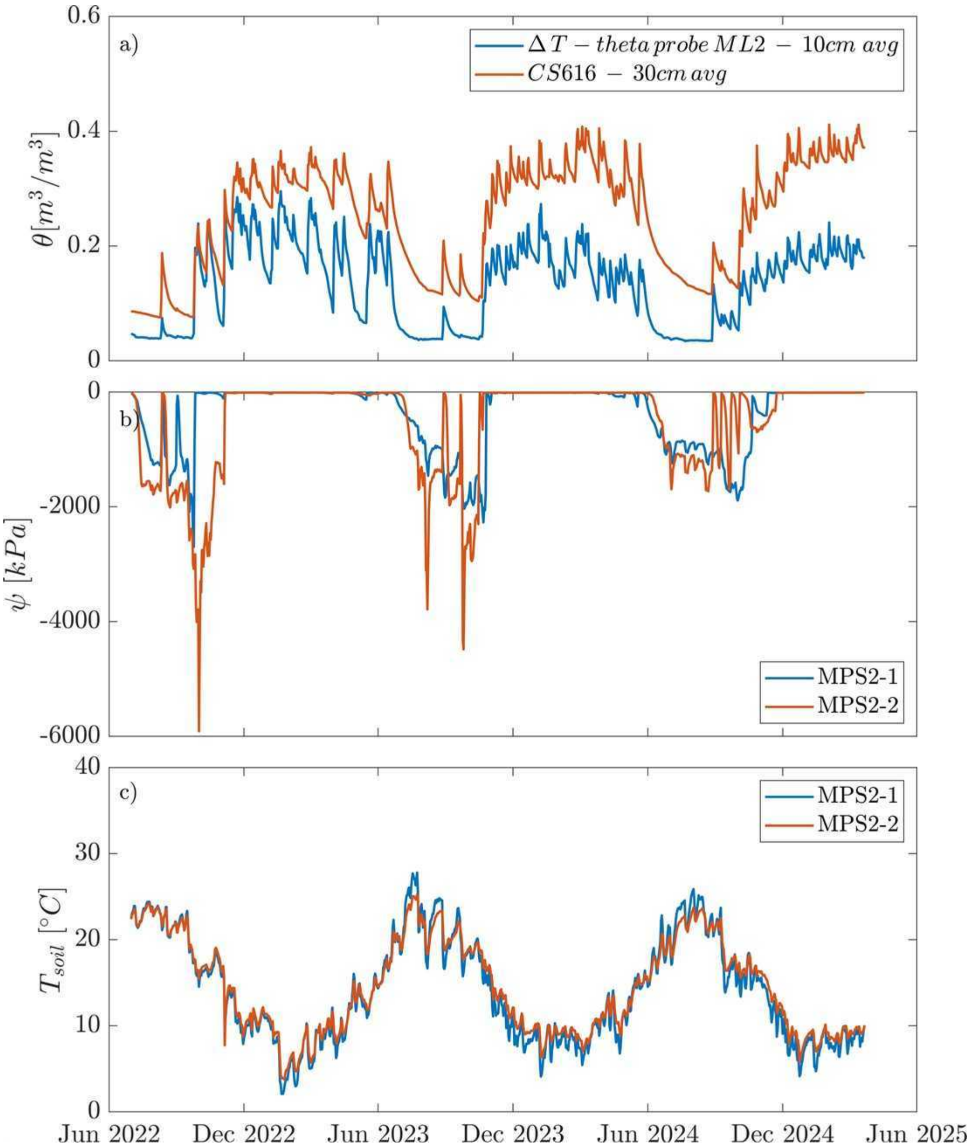

Figure 2.19: Soil related variable: a) soil moisture at two different mean depth of soil; b) soil water potential in two different position under canopy; c) soil temperature in two different position under canopy.

The following is a list of the meteorological data that are the main drivers for the ecosystems: in Figure 2.20 a) it is presented precipitation that is a key forcing variable for both soil moisture and vegetation activity, air temperature T_a measured from the hygrometer at 2m height and from the CSAT3B at 7m height governs biological and physical processes (Figure 2.20 b), including evapotranspiration, photosyntesis and respiration rates; relative humidity in Figure 2.20 c) computed from the HygroVue at 2m height and from LI-7500 at 7m height, calculated from equauation A21 from Garratt (1994); also VPD is derived from the same equation using T_a and RH of HydroVUE and the Eddy-Covariance system.

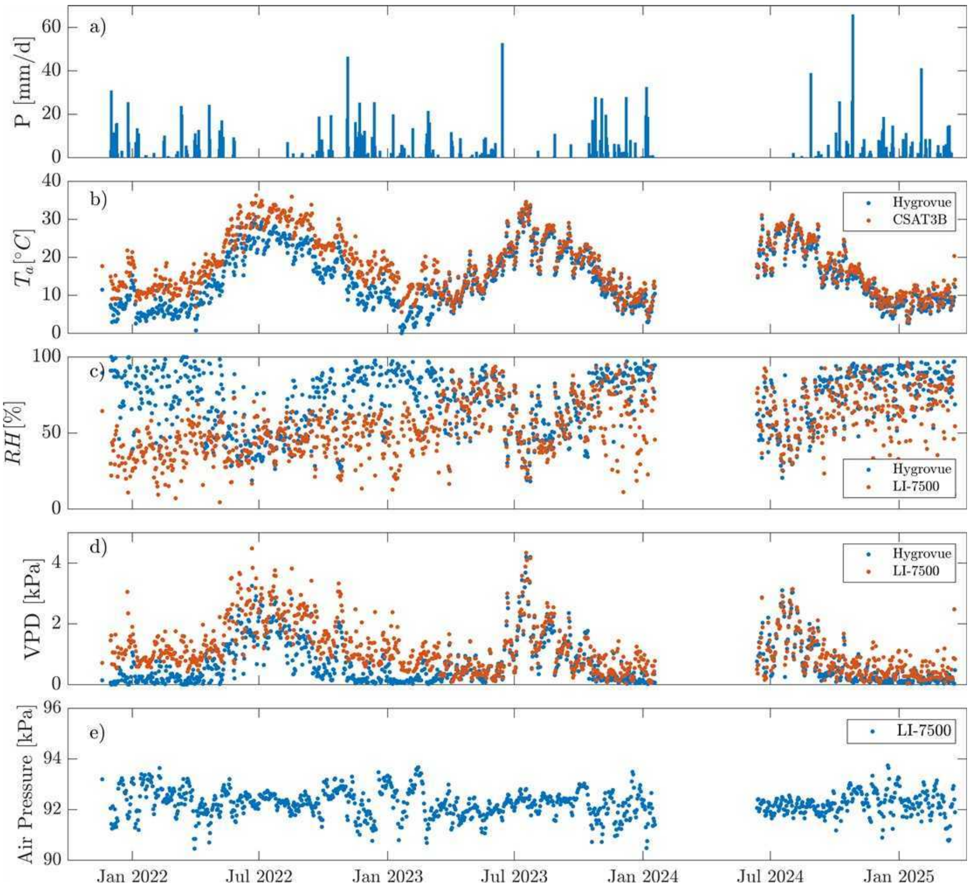

Figure 2.20: Meteorological data at daily timescale: a) precipitation; b) air temperature, in blue data from the HygroVue hydrometer at 2m height, in orange data from the sonic anemometer at 7m height; c) relative humidity, in blue data from the HygroVue hygrometer at 2m height, in orange data from the gas analyzer at 7m height; d) vapor pressure deficit, in blue data derived from T_a and RH from the hygrometer at 2m height, in orange data computed using the T_a from the sonic anemometer and RH derived from the gas analyzer.

With respect to vegetation, the raw data available consist of canopy surface temperature and sap flow measurements. Canopy temperature, measured by the infrared radiometer SI111 (Figure 2.21 a), provides indirect information on energy balance, and stress levels under variable environmental conditions. Sapflow is measured using sensor based on (Granier, 1987), following Montaldo et al. (2020) and Ward et al. (2017) to estimate the baseline (Figure 2.21 b). It captures plant water uptake dynamics (f_d) and transpiration E_t.

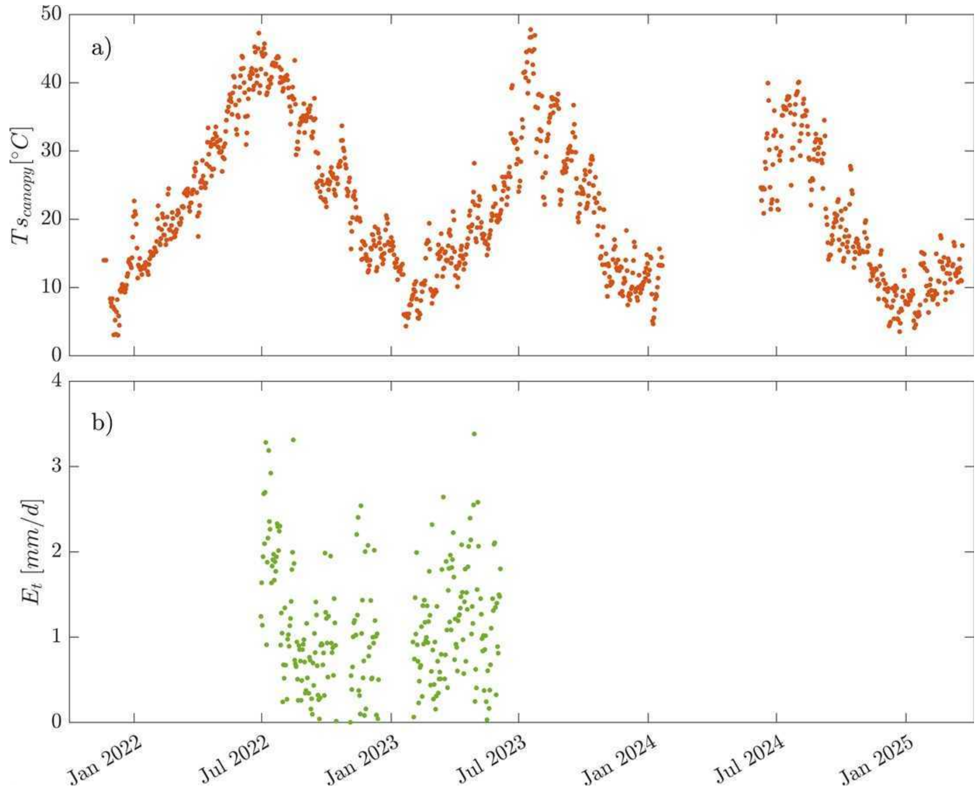

Figure 2.21: Canopy related variable: a) Surface mixed vegetation canopy temperature; b) Daily sapflux of holm oak.

Turbulent fluxes of carbon and energy provide integrative measures of ecosystem function, including carbon sequestration and water/energy exchange with the atmosphere. Four components of the radiation, measured by the NR-01, Rsw_{in}, Rsw_{out}, Rlw_{in}, Rlw_{out}, at daily time scale are in Figure 2.22 a), due to power supply issues, data from Genuary 18^{th} to end of June 2024 are missing or not physically based, and that period is gap-filed by ERA5-Land reanalysis data at 10 km resolution in 2.22 a) and are marked as '+'. Data from the Eddy-Covariance system are use to estimate the latent heat flux (LE) and the sensible heat flux (H)(see Figure 2.22 b-c) and the carbon flux (F_c) (Figure 2.22 d), the planar fit method is applied to try to reduce the site slope, and the Webb-Pearman-Leuning adjustment was applied (Detto et al., 2006, 2008).

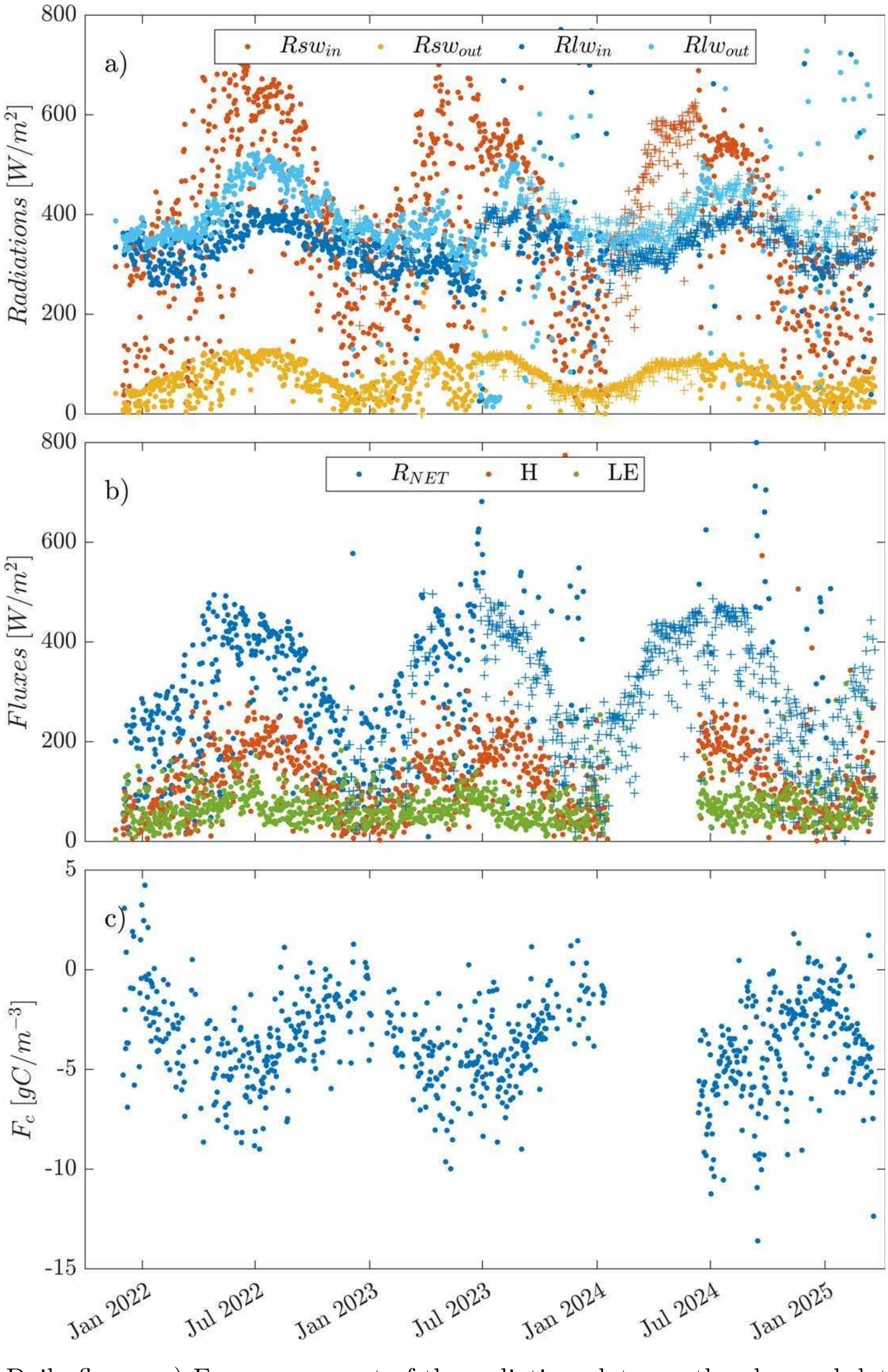

Figure 2.22: Daily fluxes: a) Four component of the radiation, dots are the observed data, + are the ERA5-Land data used to gap-fill the period; b) Energy balance components, + marks of the R_{NET} are the gap-filled data from ERA5-Land; daily carbon flux measure by the Eddy-Covariance system.

In the previous figure, the daily latent heat flux does not appear to differ from typical values reported in the literature (Pastorello et al., 2020); however, the half-hourly time series shows a particularly noisy pattern (see Figure 2.23), unlike the sensible heat flux (see Figure 2.24) and the CO_2 flux (see Figure 2.25). Due to this LE noisy signal, on March 16^{th} 2023 the system was changed with another that was installed in Orroli site, to understand if the problem was connected to the gas analyzer or to site morphology. As the Figure 2.23 b to d, with the new gas analyzer, the signal is still noisy. The next paragraph is going deep on that topic showing the connection to the topography of the site.

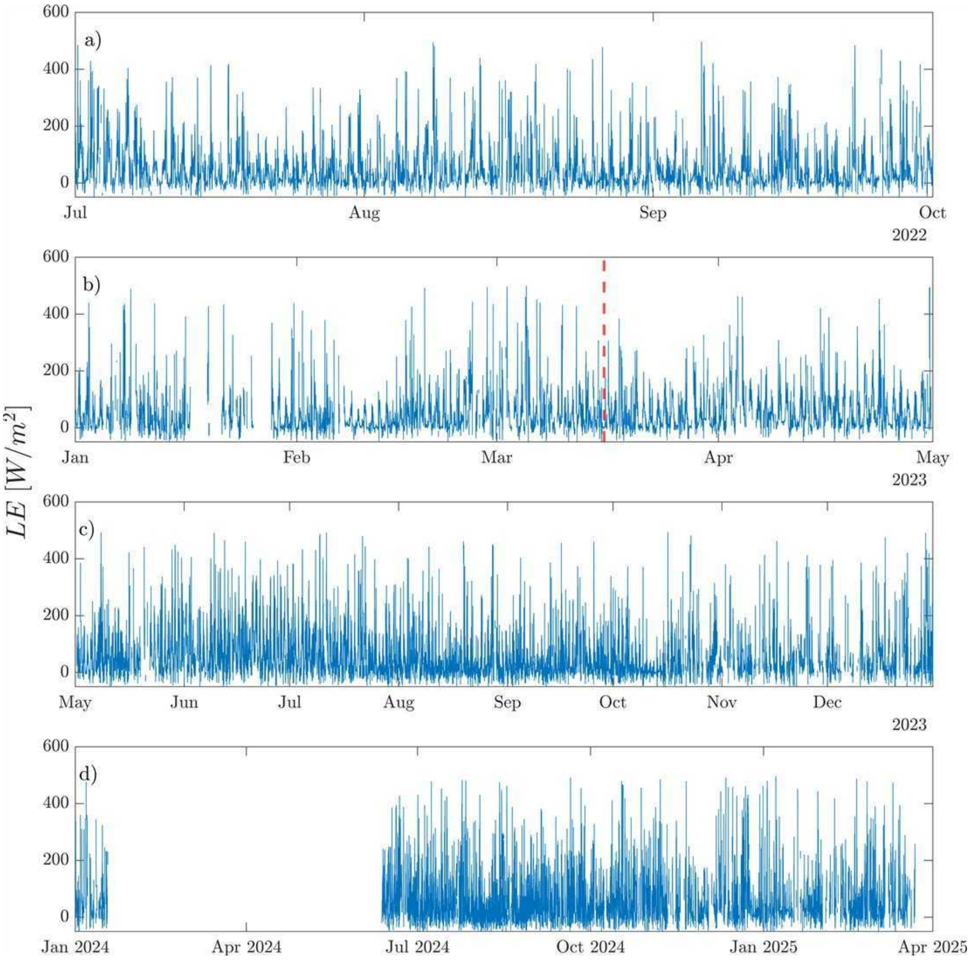

Figure 2.23: Complete LE half-hourly timeseries, the vertical dashed line indicates the day of change the Eddy-Covariance system

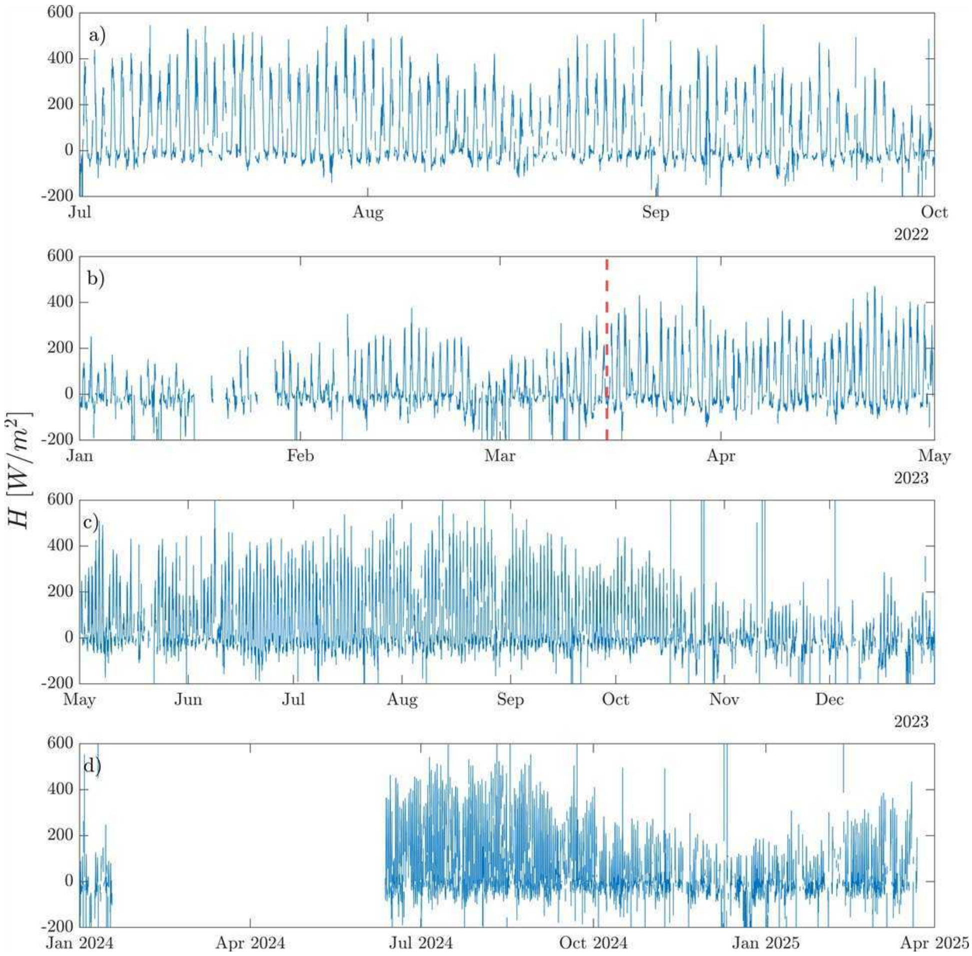

Figure 2.24: Complete H half-hourly timeseries , the vertical dashed line indicates the day of change the Eddy-Covariance system

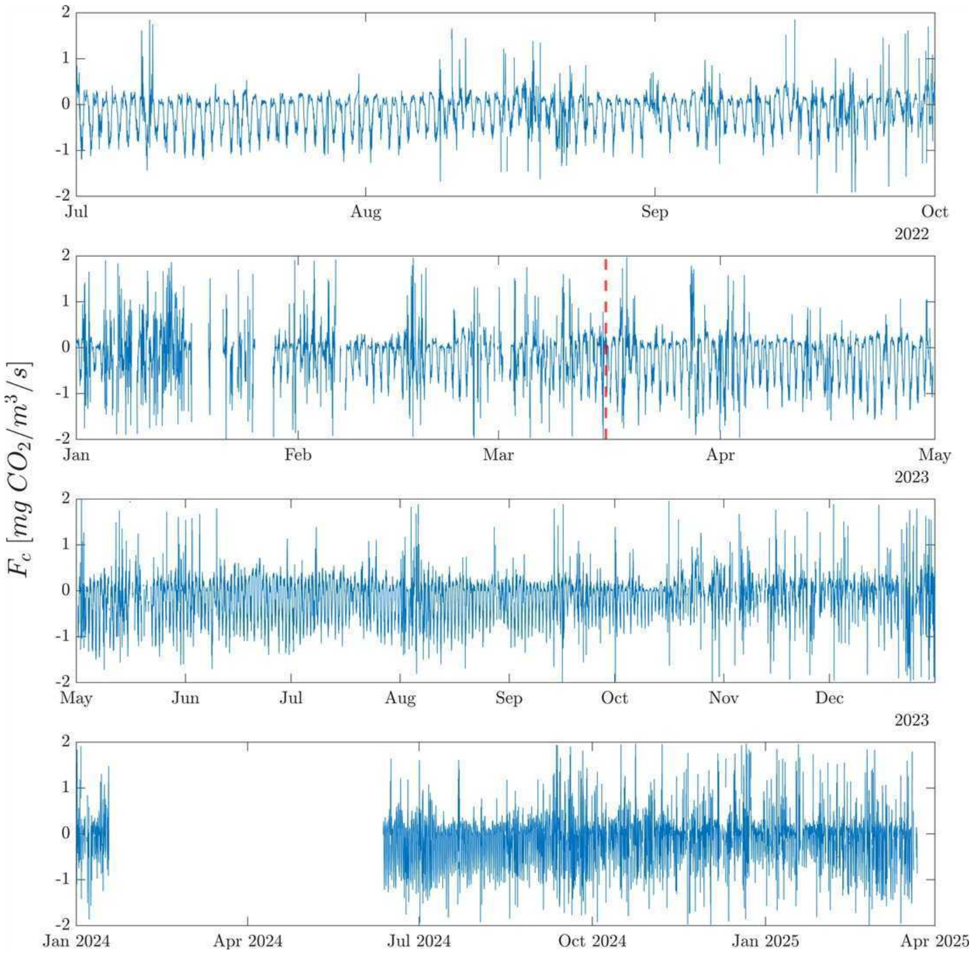

Figure 2.25: Complete F_c half-hourly timeseries, the vertical dashed line indicates the day of change the Eddy-Covariance system

The effect of the topography

The overarching goal was to explore how the velocity and scalar statistics are impacted by terrain variability and what are the consequences of such terrain variability on similarity arguments and the energy balance closure (EBc).

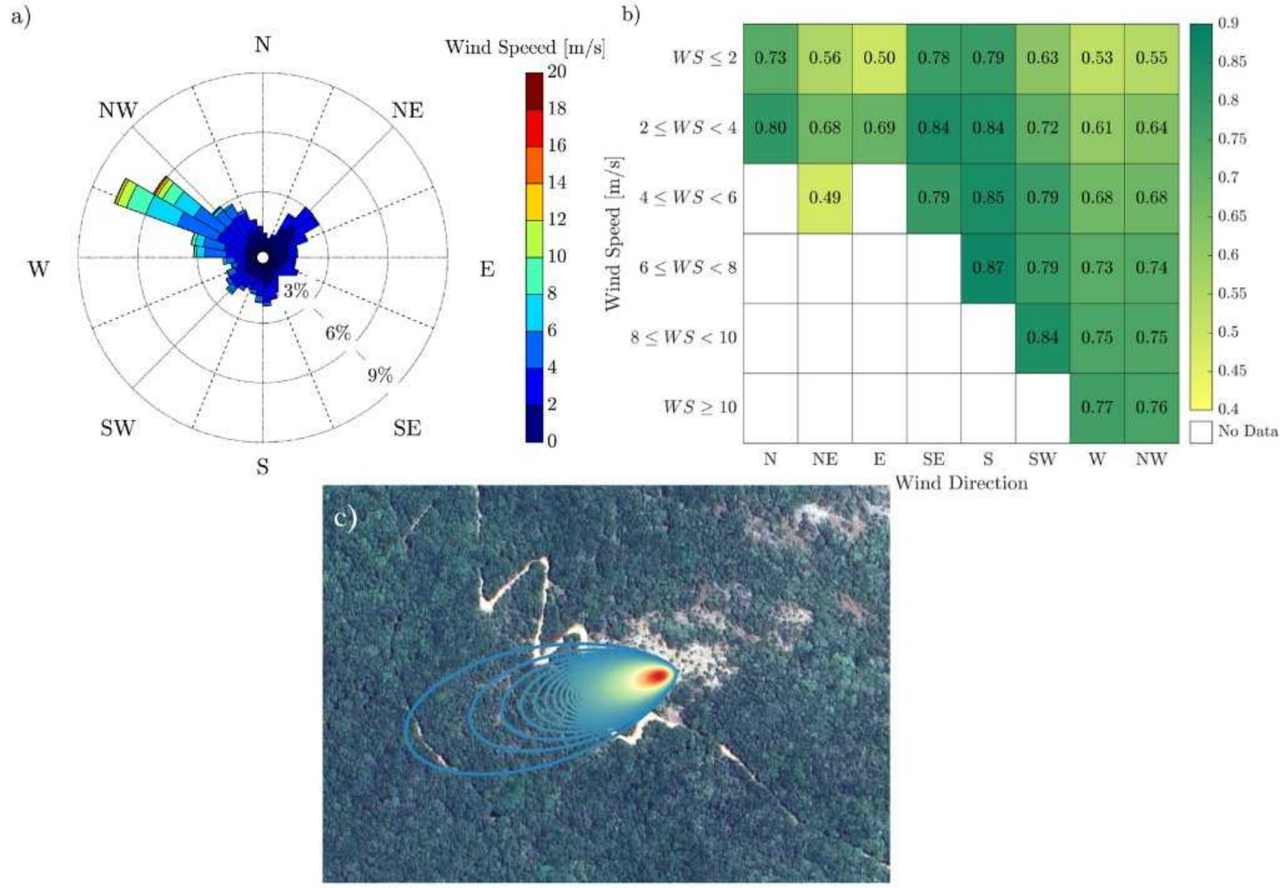

Figure 2.26: a) Wind Rose from more then three year dataset, b) mean footprint from each direction and wind speed interval, c) example of the contributing area, color from red to blue the maximum to minimum energy concentration.

From the wind rose obtained from the full dataset (Figure 2.26 a), it is evident that the prevailing wind direction is North-West, followed by West. Given the homogeneity of the data across the other 10° sectors, it was decided to use the eight cardinal directions associated with the main wind types. From the footprint analysis, following the approach by (Detto et al., 2006), it is instead possible to identify the contributing source area for the instrument's measurements, as it shows in Figure 2.26 b-c).

The data were first separated by different wind sectors and analysed for near-neutral conditions where the contributing area is bigger. The normalized relation between vertical velocity standard deviation (σ_w) and friction velocity (u_*) was insensitive to the mean wind direction (i.e. $\sigma_w/u_*= A_{ww}^{1/2}$ - a constant around 1.1-1.2). The heat flux similarity relations were investigated in two ways: the first uses a conventional flux-variance form whereby the turbulent vertical heat flux $\overline{w'T'}$ was related to u_* and temperature standard deviation (σ_T) using a similarity coefficient (i.e. $\overline{w'T'} = C_1\sigma_T u_*$). The second evaluates the much less studied relation between the horizontal heat flux $\overline{u'T'}$ and $\overline{w'T'}$ (i.e. $\overline{u'T'} = -C_2\overline{w'T'}$), where C_2 was previously reported to vary between 2 and 4 for 'flat-world' near-neutral conditions (Wyngaard, 2010). The findings suggest that C_1 was close to expectations from flat-world studies but C_2 was smaller in magnitude yet independent of mean wind direction.

When repeating the same analysis for water vapor concentration fluctuations (i.e. $\overline{w'q'} = C_3\sigma_q u_*$ and $\overline{u'q'} = -C_4\overline{w'q'}$), similarity theory failed on both accounts for almost all mean wind directions. In fact, for some wind direction sectors, including the upwind sector, no relation between $\overline{u'q'}$ and $\overline{w'q'}$ was found.

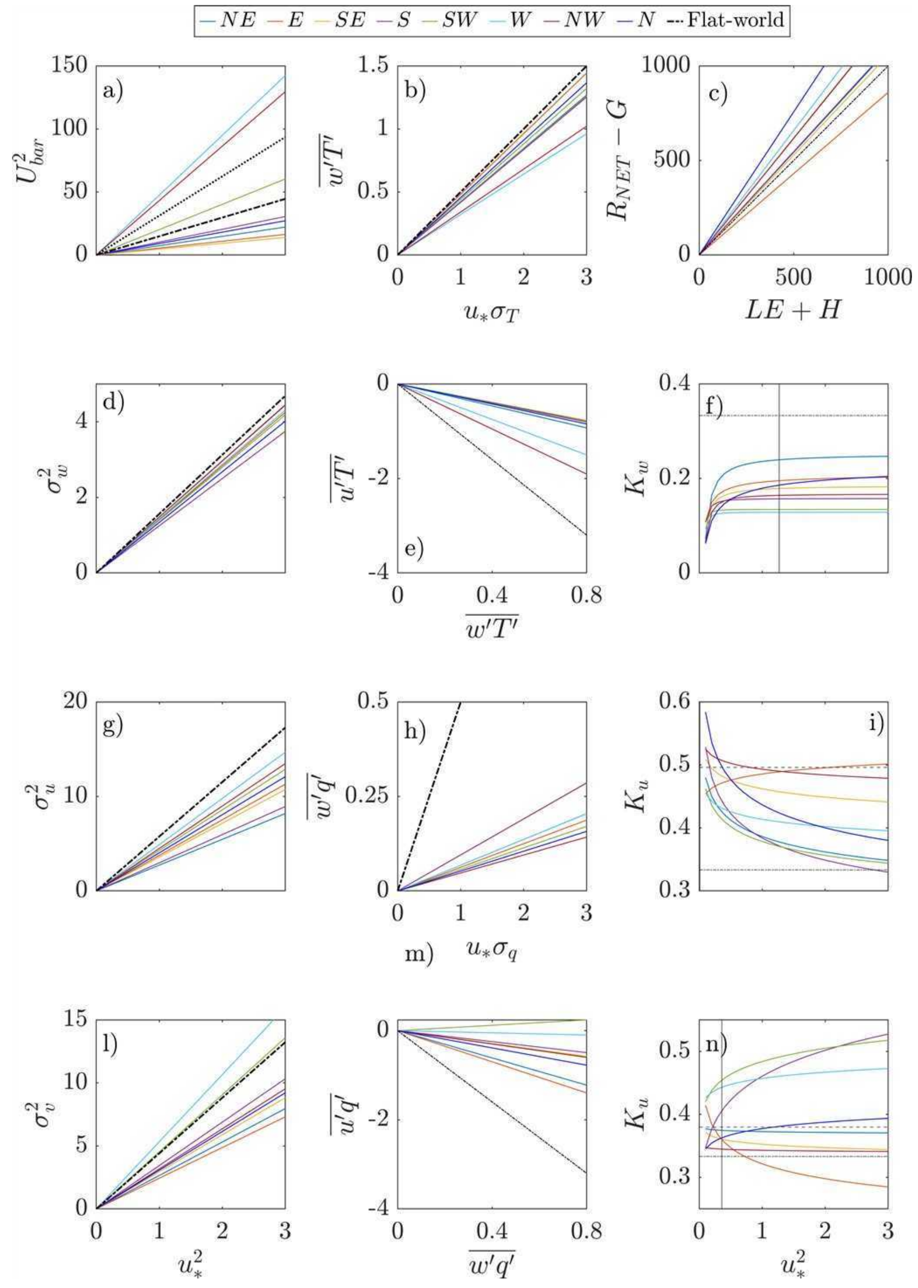

Figure 2.27: Similarity relation coefficient for each direction compared to the reference Kansas experiment: a) drag coefficient, black dotted line is the references for '$\frac{1}{C_D} = (\frac{1}{k}\ln(\frac{z_m - d_0}{0.05 h_{canopy}}))^2$', dashed and dotted black line is the reference for $\frac{1}{C_D} = (\frac{1}{k}\ln(\frac{z_m - d_0}{0.1 h_{canopy}}))^2$; b) C_1 coefficient, black dashed and dotted line is the reference where $C_1 = 0.5$, derived from Kaimal and Finnigan (1994) equation 1.53; c) slope of the fitting of the Energy Balance Closure, black line is the 1:1 slope;d) similarity coefficient $A_w w$, reference for flat world in black line is $A^{1/2}_{ww} = 1.2$; e) C_2 coefficient, black dashed and dotted line is the reference where $C_2 = 4$;f) TKE partitioning in the z axis, dash-dotted line is the 1/3 reference for the isotropy turbolence, the dashed line is the reference value $K_w = 0.124$ for the flat world in near neutral condition derived using $A^{1/2}_{ww} = 1.2$,$A^{1/2}_{uu} = 2.4$ and $A^{1/2}_{vv} = 2.1$; g) similarity coefficient $A_u u$, reference for flat world in black line is $A^{1/2}_{uu} = 2.4$; h) C_3 coefficient, black dashed and dotted line is the reference where $C_3 = 0.5$, derived from Kaimal and Finnigan (1994) equation 1.53; i) TKE partitioning in the x axis, dash-dotted line is the 1/3 reference for the isotropy turbolence, the dashed line is the reference value $K_u = 0.496$ for the flat world in near neutral condition derived using $A^{1/2}_{ww} = 1.2$,$A^{1/2}_{uu} = 2.4$; l) similarity coefficient $A_w w$, reference for flat world in black line is $A^{1/2}_{vv} = 2.1$; m) C_4 coefficient, black dashed and dotted line is the reference where $C_4 = 4$; TKE partitioning in the y axis, dash-dotted line is the 1/3 reference for the isotropy turbolence, the dashed line is the reference value $K_w = 0.380$ for the flat world in near neutral condition derived using $A^{1/2}_{ww} = 1.2$,$A^{1/2}_{uu} = 2.4$ and $A^{1/2}_{vv} = 2.1$.

Guided by recent findings about a connection between the anisotropy in the Reynolds stress tensor and deviations in flux-variance similarity relations, following the tensor invariant analysis by Choi and Lumpley (2001), the two isotropic parameter are computed:

$$F = 1 + 27III + 9II \tag{2.2}$$

$$X_B = B_1 + \frac{1}{2}B_3 \tag{2.3}$$

$$Y_B = \frac{\sqrt{3}}{2}B_3 \tag{2.4}$$

where if $\boldsymbol{\lambda} = (\lambda_1, \lambda_2, \lambda_3)$ is the vector of eigenvalues of the non-dimensionalized stress tensor $\mathbf{K}$, and the invariants are computed as:$I = tr(\mathbf{K})$, $II = \lambda_1 \cdot \lambda_2 + \lambda_2 \cdot \lambda_3 + \lambda_2 \cdot \lambda_3$, $III = \lambda_1 \cdot \lambda_2 \cdot \lambda_3$,$B_1 = \lambda_1 - \lambda_3$, $B_1 = 2(\lambda_2 - \lambda_3)$ and $B_3 = 3\lambda_3 + 1$.

As Choi and Lumpley (2001) demonstrates, F vanishes whenever turbulence becomes two-dimensional, and it becomes unity when turbulence enters a three-dimensional isotropic state, $\mathbf{Y_B}$ has same behavior, in Figure 2.28 are plotted the two isotropic condition parameters and it shows that going down-slope the tendency toward anisotropy increases.

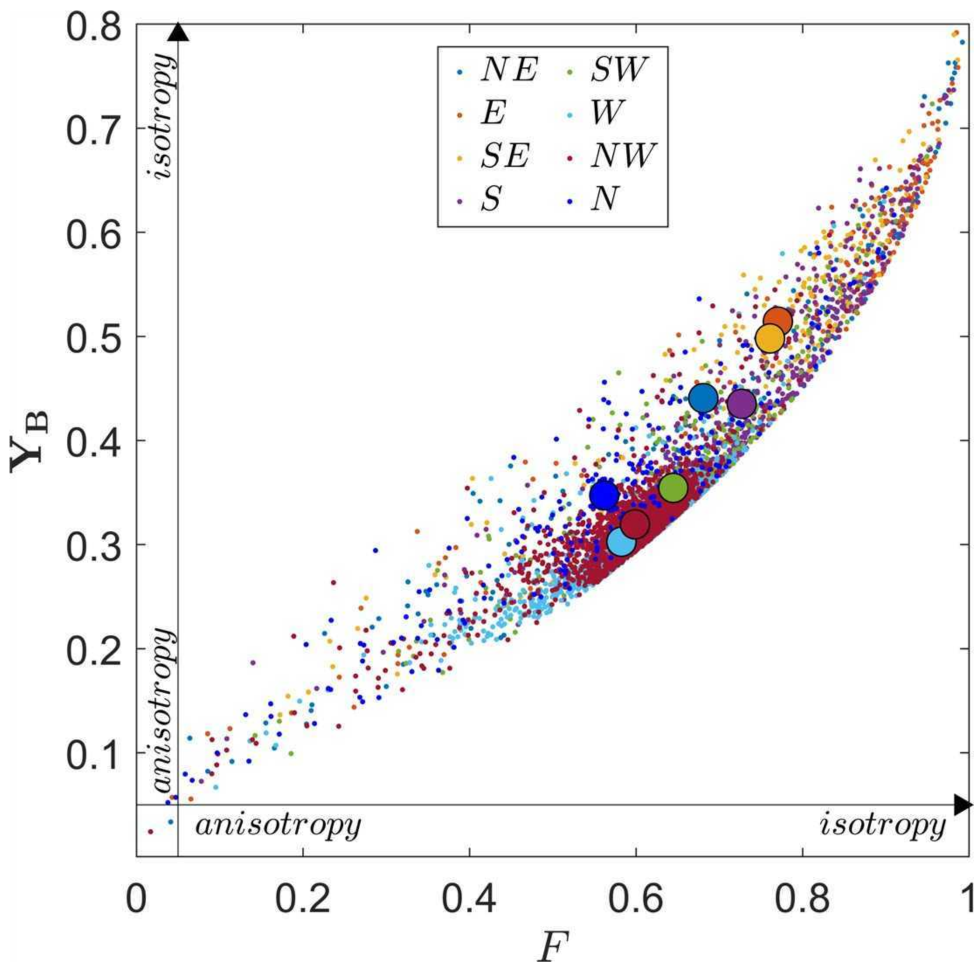

Figure 2.28: Anisotropy parameters for each direction, dots are the raw data and filled circles are the means

Stiperski et al. (2019, 2021) use a modified Lumley Triangle (Lumley, 1979) which allows for the representation of any realizable state of turbulence in a 2D map (Figure2.29). In the Figure2.29 are plotted, for each direction, the nonlinear maps, from panels d) to h) it can be seen that moving from south to northwest, or downward, the eddies increasingly exhibit a 2D axis-type anisotropy, known as 'pancake' anisotropy. These turbulences are represented by flattened structure which mainly expand in the two horizontal directions (bi direcional advecion), likely due to the steep terrain that distorts the flow with horizontal components, while the vertical component is often more limited due to the flow's stability near the surface.

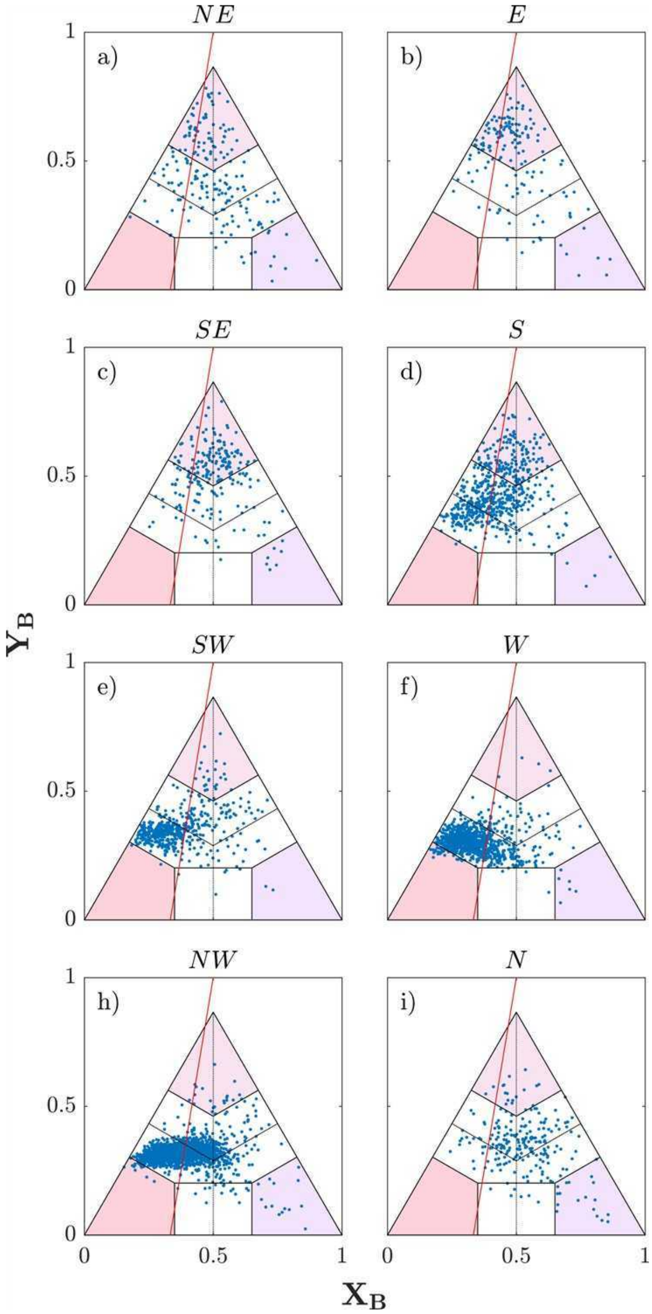

Figure 2.29: Barycentric Lumley Triangleas for each wind direction, as function of the anisotropy stress tensor eigenvalues and represented through the linearized coordinates X_B and Y_B, The shading indicates regions of the triangle that were selected as pure limiting states of anisotropy. The upper area represents the isotropic state, the left shaded area is the 2-component axisymetric state, the right shaded area is the 1-component axisymetric state. The red solid line represents the state in which at least one eigenvalue is zero and corresponds to plane-strain limit (PSL).

From the perspective of latent heat measurements, this implies an underestimation of the flux and thus of the evapotranspiration, requiring post-processing corrections from the energy balance closure.

2.2 Comparison between the two sites

The two study sites, located on opposite sides of the island of Sardinia, are representative of typical natural Mediterranean ecosystems. As illustrated in Figures 2.2 and 2.17, both areas experience similar meteorological conditions, thus offering an optimal opportunity for comparative analysis of micrometeorological fluxes.

Considering the years with complete datasets (2022 and 2023), Figure 2.30 highlights some notable differences: the Marganai site generally receives more precipitation than Orroli, particularly during the summer months. Conversely, air temperatures are higher in Marganai than in Orroli, especially during 2022. In contrast, vapor pressure deficit (VPD) values are higher in Orroli than in Marganai but values are comparable.

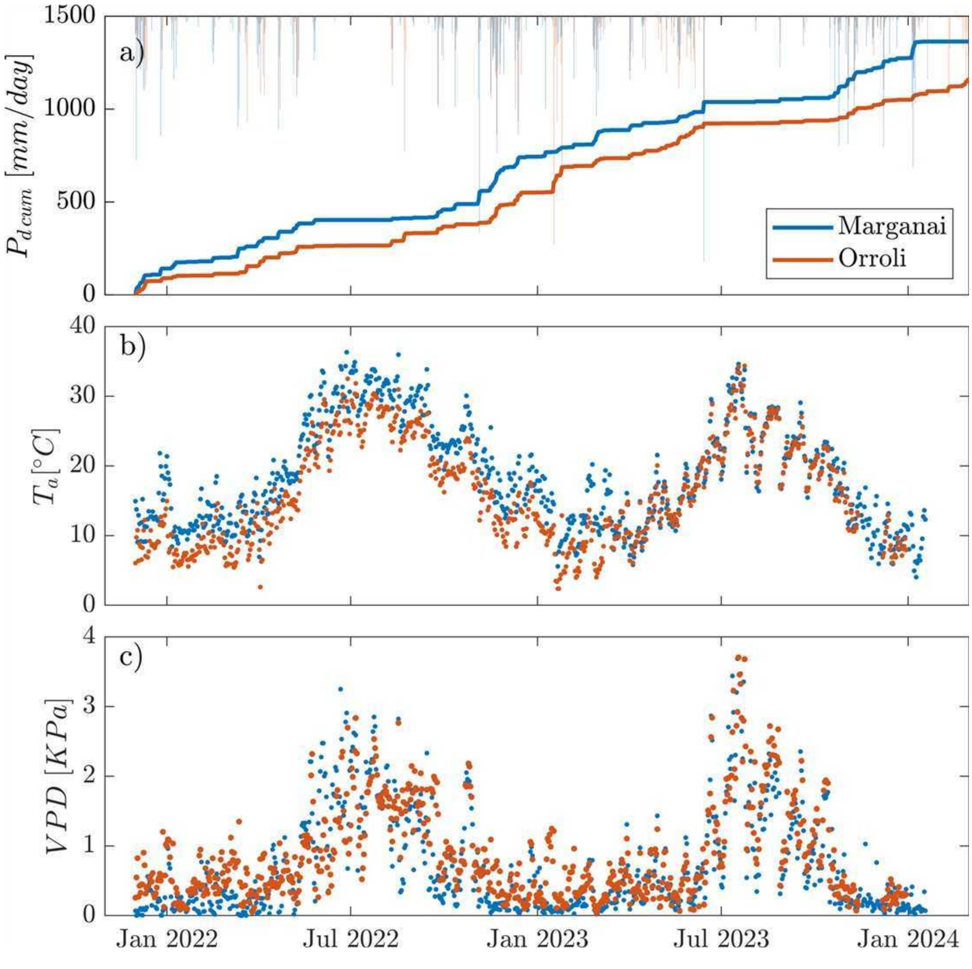

Figure 2.30: Comparison of meteorological variables at daily timescale: a) cumulative daily precipitation with daily values shown as stem plots; b) mean air temperature; c) mean vapor pressure deficit.

Regarding surface energy fluxes, both sites exhibit similar net radiation and potential evapotranspiration rates (Figures 2.31 d-e). However, more pronounced differences emerge in the partitioning of energy: latent heat flux (LE) is generally higher in Marganai, whereas sensible heat flux (H) dominates in Orroli.

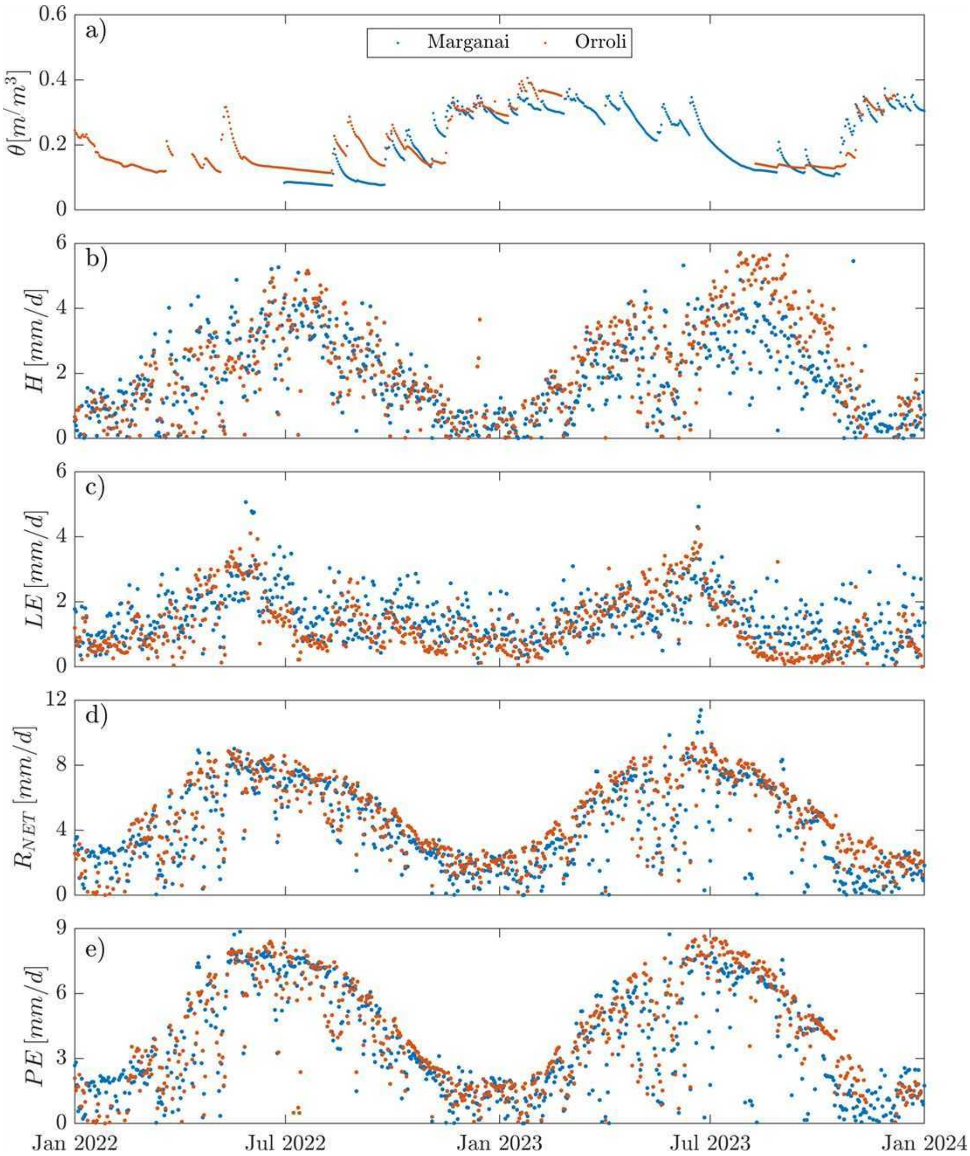

Figure 2.31: Comparison of surface energy fluxes and potential evapotranspiration between the two sites.

Focusing on total evaporation (i.e., LE) across the two years (Figure 2.32), both ecosystems exhibit substantial transpiration during the summer, underscoring the crucial role of deep root water uptake from fractured bedrock—especially relevant in the rocky terrain. Despite differences in tree species (*Olea sylvestris* in Orroli vs. *Quercus ilex* in Marganai), the results indicate comparable transpiration rates.

The similar evapotranspiration rates observed in Orroli during spring and early summer are partly attributed to the contribution of herbaceous vegetation. This vegetation remains active longer into the season due to hydraulic redistribution mechanisms facilitated by the wild olive trees, as discussed by Montaldo et al. (2021).

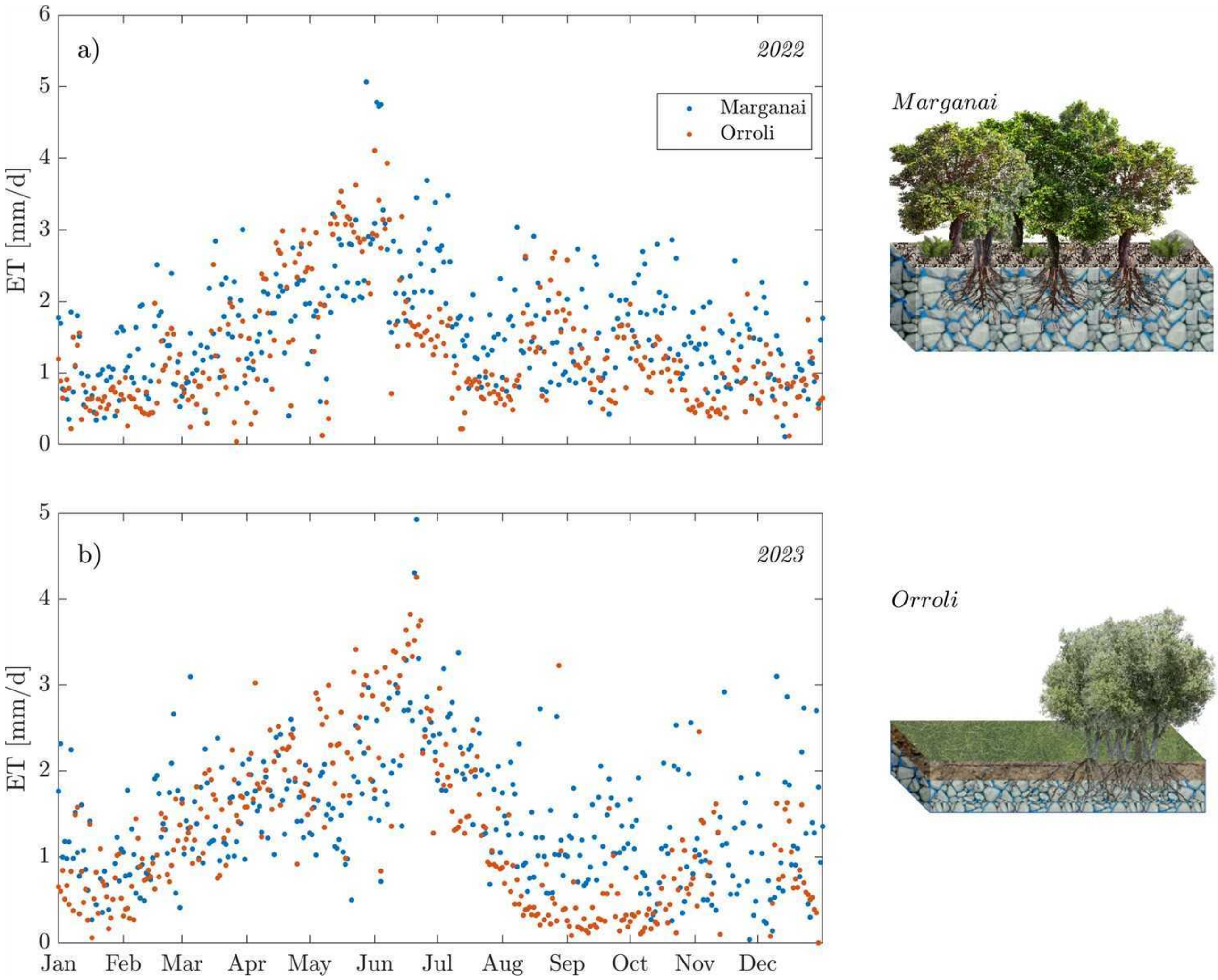

Figure 2.32: Comparison of latent heat flux (evapotranspiration) for the two ecosystems over the years 2022 and 2023.

3

A new spatially distributed ecohydrological model for water resources planning

Ecohydrological models are a key tool for predicting climate change impacts on water and vegetation resources, through the coupling of hydrologic and vegetation dynamics models.With the growth of computational power, ecohydrological models have increased in complexity through the inclusion of more processes, controlling variables and parameterization (Montaldo et al., 2005, 2003; Franks et al., 1997). These parameter additions are justified on the basis that the inclusion of additional controlling mechanisms should both improve the predictive skill and make the parameter values easier to estimate based on physiological characteristics or measurements, but the uncertainty of the parameterization has increased (Montaldo et al., 2005, 2003; Bashford et al., 2002; Beven et al., 2021).

Hence, there is a need for models with parsimonious parametrization that are still able to accurately predict the main drivers of the processes, with a low computational load, becoming key requirements when long databases are simulated. We propose an eco-hydrological model for both hydrological and vegetation dynamics modeling under water-limited conditions, which respond to the need for:

1. long-term (e.g., hundreds of years) hydrologic balance predictions;
2. the inclusion of vegetation dynamics;
3. the inclusion of the hydraulic redistribution by tree roots from deep to surface soil layers, an important contribution in water-limited forested ecosystems;
4. a spatially distributed approach that is able to capture
5. parsimonious model parameterization and a low computational load.

With these objectives, daily or monthly model time scales can be adequate for water balance and vegetation dynamics predictions (Deng et al., 2018; Wood et al., 2002; Zégre et al., 2010). We started from the basin-scale distributed hydrologic model of Montaldo et al. (2007) and the plot-scale ecohydrological model of Montaldo et al. (2008) and Montaldo et al. (2013), which couples a land surface model and a vegetation dynamic model. At a daily time scale, the Hortonian overland flow (Arnau-Rosalén et al., 2008; Chow, 1971; Li et al., 2011), typical of Mediterranean basins with steep hillslopes in semi-arid climate conditions, can be predicted using the Soil Conservation Service (SCS) method (Chow, 1971; Ponce, 1989; Service, 1986), which is widely used for surface runoff estimation (e.g., Arnold et al. (2000); Montaldo et al. (2004)). For the recharge of the shallow soil by tree roots through the hydraulic redistribution, recently, Montaldo et al. (2021) successfully developed a simplified approach, which we adapted in our proposed model. We used the vegetation dynamic model of Montaldo et al. (2008), running at a daily time scale and already tested in a Sardinian ecosystem for LAI predictions, which is parsimonious in model parameterization (Montaldo et al., 2005).

3.1 The distributed Eco-hydrological model

The proposed numerical model is a spatially distributed ecohydrological model (Figures 2 and 3), which couples a hydrologic model and a vegetation dynamic model. The model runs at a daily timescale and 200 m spatial scale. Three principal components can be identified in the model (Figure 3.1):

1. the soil water balance model (SWBM) that computes soil moisture, water balance, surface runoff and subsurface water flux;
2. the vegetation dynamic model (VDM) that computes biomass budgets and LAI;
3. the simplified overland flow and base flow computations.

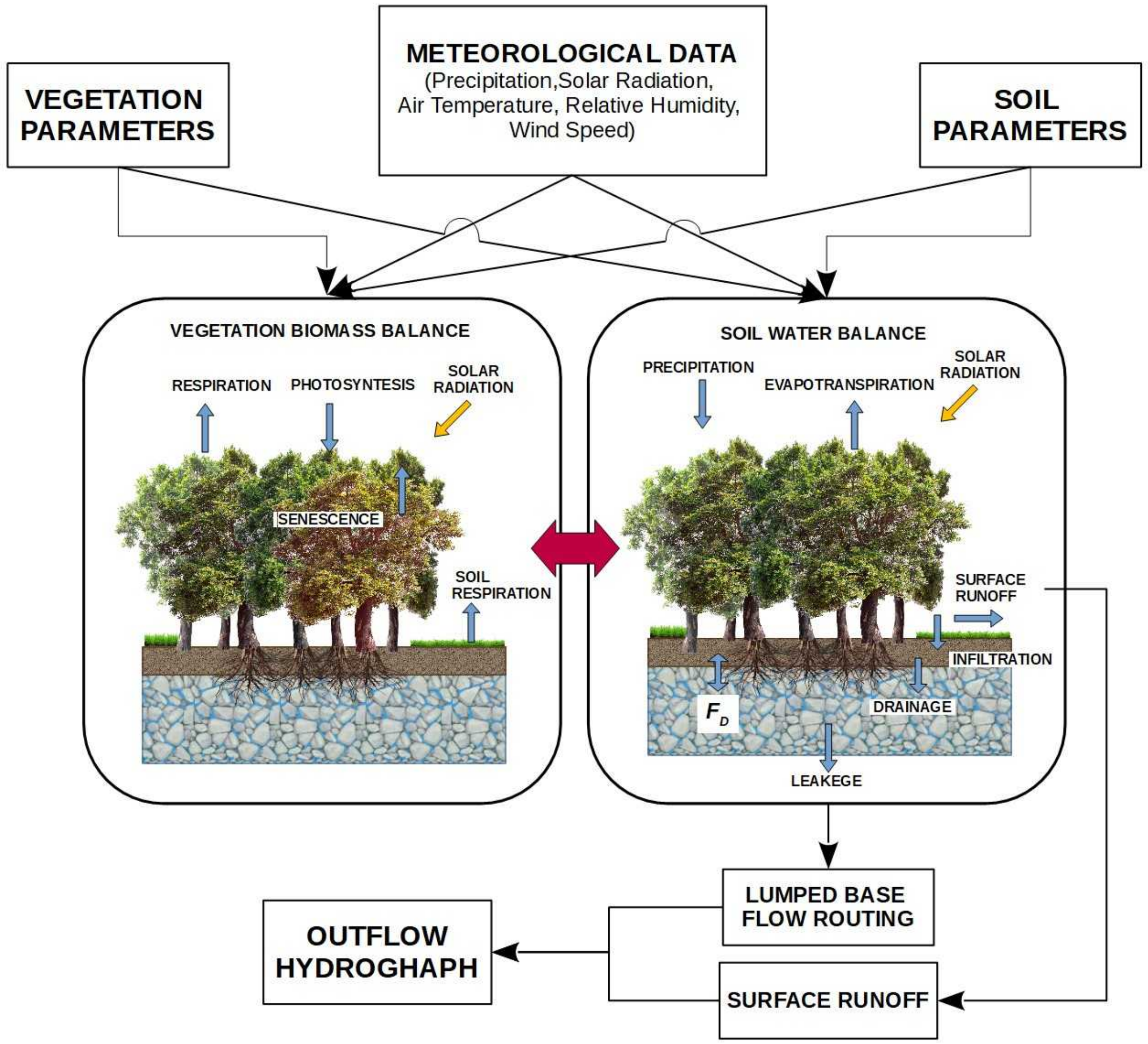

Figure 3.1: Struture of the distributed eco-hydrological model

In the first component, the soil water budget is computed at each cell of the basin. From this model component, the surface runoff and drainage are predicted, and these are used by the third component of the model for computing runoff at the basin scale. The second component, the vegetation dynamic model, provides the LAI at each cell, which is used by the SWBM for computing the evapotranspiration (ET) and rain interception (E_w). Meteorological model inputs are: precipitation (P), air temperature (T_a), wind speed (WS), relative humidity (RH), incoming short wave solar radiation (Rsw) and photosyn-thetically active radiation (PAR).

3.1.1 The Soil Water Balance Model (SWBM)

The SWBM predicts land surface fluxes and soil moisture evolutions for each grid cell. It is derived from the models of Montaldo et al. (2013) and Montaldo et al. (2021), and includes three land surface components for each cell: bare soil, grass and trees.

The model includes two layers vertically, a surficial soil of variable depth (d_s) according to the soil depth of the cell, and an underlying active fractured rock depth (d_r) for modeling root zone soil moisture. The model simulates the water balance of the two layers for each cell:

$$d_s \frac{\partial \theta_s}{\partial t} = P - E_w - Q_{sup} - f_{bs} E_{bs} - f_g E_g - \xi_t f_t E_{t,s} + f_d - D_r \tag{3.1}$$

$$d_r \frac{\partial \theta_r}{\partial t} = D_r - f_d - (1 - \xi_t) f_t E_{t,r} - L_e \tag{3.2}$$

where θ_s is the moisture of the upper soil layer, θ_r is the moisture of the underlying rocky layer, P is the precipitation, Q_{sup} is the surface runoff, E_w is the wet evaporation, which is equal to the rainfall interception, characterized by a storage capacity of $0.2LAI$ (Noilhan and Planton, 1989). E_{bs} is the bare soil evaporation, E_g is the grass transpiration, $E_{t,s}$ is the tree transpiration from the surface soil layer, Et,r is the tree transpiration from the fractured rock layer (with tree transpiration, $Et = E_{t,s} + (1 - \xi_t) E_{t,r}$), ξ_t is the percentage of tree root water uptake from the surface soil layer, f_d is the daily hydraulic redistribution flux between the surface soil and the fractured rock through the tree roots, D_r is the vertical drainage, L_e is the leakage, $_{fbs}$, f_g and f_t are the fractions of bare soil, grass cover and tree cover in each cell, respectively, with $f_{bs} + f_g + f_t = 1$.

Q_{sup} is estimated using the Soil Conservation Service Curve Number (SCS-CN) method (Chow, 1971; Ponce, 1989; Service, 1986) from P, and computing the antecedent moisture conditions from the rain in the previous five days:

$$P_n = \begin{cases} 0 & P \leq I_a \\ \frac{(P-I_a)^2}{(P-I_a+S)} & P > I_a \end{cases} \tag{3.3}$$

in which I_a is the initial abstraction before ponding and is equal to cS with c constant ($= 0.2$; see Ponce (1989)), and S is the maximum soil potential retention given by:

$$S = 254 \left(\frac{100}{CN} - 1 \right) \tag{3.4}$$

where $CN (= 1 - 100)$ is the curve number parameter.

The SCS-CN method distinguishes three levels of antecedent moisture condition ($AMCI$, $AMCII$, and $AMCIII$), depending on the total rainfall in the 5 days ($P5d$) preceding a storm (Service, 1986). The original seasonal rainfall limits of the SCS-CN method for the three antecedent moisture conditions are used in the model (Ponce, 1989), distinguishing between dormant season: $AMCI$ if $P5d < 12.7mm$, $AMCIII$ if $P5d > 28mm$ and growing season $AMCI$ if $P5d < 35.5mm$, $AMCIII$ if $P5d > 53.3mm$. The values of CN for the $AMCII$ condition are tabulated by the Soil Conservation Service on the basis of the soil type and land use and calibrated the CN map (for properly predicting runoff). Then, the values of CN for $AMCI$ and $AMCIII$ are expressed in terms of CN for $AMCII$ through the following relationships (Ponce, 1989):

$$CN_I = \frac{CN_{II}}{2.3 - 0.013CN_{II}} \tag{3.5}$$

$$CN_{III} = \frac{CN_{II}}{0.43 + 0.0057CN_{II}} \tag{3.6}$$

The dreinage D_r and leakage L_e are estimated using the unit gradient assumption of gravity drainage (Albertson and Kiely, 2001) and related to soil moisture following Clapp and Hornberger (1978):

$$D_r = k_{sat,s}\left(\frac{\theta_s}{\theta_{sat,s}}\right)^{2b_s+3} \tag{3.7}$$

$$L_e = k_{sat,r}\left(\frac{\theta_r}{\theta_{sat,r}}\right)^{2b_r+3} \tag{3.8}$$

where $k_{sat,s}$ and $k_{sat,r}$ are the saturated hydraulic conductivity of the surficial soil layer and the deeper layer, respectively, b_s and b_r are the slopes of the soil retention curve of the two layers, and $\theta_{sat,s}$ and $\theta_{sat,r}$ are the saturated soil moisture of the two layers. The f_d contribution is estimated as a function of the soil moisture gradient between the surface and underlying rocky sublayer through Montaldo et al. (2021); Ryel et al. (2002):

$$f_d = a_f(\theta_r - \theta_s)^{b_f} \tag{3.9}$$

where a_f and b_f are tree root parameters.

Evapotranspiration components, (E_g, $E_{t,s}$ and $E_{t,r}$) are estimated by the Penman-Monteith equation:

$$T = \frac{1}{L_v\rho_w}\left[\frac{\Delta(R_N - G)}{\Delta + \gamma(1 + r_c/r_a)} + \frac{c_p\rho_a VPD}{\left[\Delta + \gamma\left(1 + r_c/r_a\right)\right] r_a}\right] \tag{3.10}$$

where r_c includes the limiting effects exerted by soil water potential and environmental conditions and can be expressed, for example, using the Jarvis (1976) equation:

$$r_c = r_{c,min}[f_1(\theta)f_2(T_a)f_3(VPD)]^{-1} \tag{3.11}$$

$r_{c,min}$ being the minimum canopy resistance, that can be calculated as

$$r_{c,min} = \frac{r_{s,min}}{LAI} \tag{3.12}$$

with $r_{s,min}$ in $[m \cdot s^{-1}]$ is the minimum stomata resistance and LAI is the leaf area index ie the total leaf surface relative to a unit ground area of the canopy projection, which allows for the transition from the resistance of a single stoma to that of the entire plant. The braked terms represent limitations due to soil moisture $[f_1(\theta)]$ and atmospheric conditions $[f_2(VPD)$ and $f_3(T_a)]$.

The stress functions of soil/rock moisture and air temperature are determined following

Montaldo et al. (2008) as:

$$f_1(\theta) = \begin{cases} 0 & \theta \leq \theta_{wp} \\ \frac{\theta-\theta_{wp}}{\theta_{lim}-\theta_{wp}} & \theta_{wp} < \theta \leq \theta_{lim} \\ 1 & \theta > \theta_{lim} \end{cases} \tag{3.13}$$

$$f_2(T_a) = \begin{cases} 0 & T_a \leq T_{min} \quad | \quad T_a \geq T_{max} \\ 1 - \frac{T_{opt}-T_a}{T_{opt}-T_{min}} & T_{min} < T - a < T_{max} \\ 1 & T_{opt} \leq T - a \leq T_{max} \end{cases} \tag{3.14}$$

while the stress function of VPD is given by Montaldo and Oren (2018):

$$f_3(VPD) = 1 - 0.6\log(VPD) \tag{3.15}$$

whereby θ_{wp} is the wilting point, θ_{lim} is the limiting soil moisture for vegetation, and T_{min}, T_{opt} and T_{max} are the minimum, optimal and maximum temperature for vegetation.

Bare soil evaporation is estimated as a function of soil moisture through $E_{bs} = \alpha PE$ (Parlange et al., 1999), and PE is the potential evaporation given by Penman and Keen (1948).

3.1.2 The Vegetation Dynamic Model (VDM)

The VDM computes the change in biomass over time from the difference between the rates of biomass production (photosynthesis) and loss, such as what occurs through respiration and senescence (Cayrol et al., 2000; Larcher, 2003). The VDM distinguishes trees and grass components and is derived from the models of Nouvellon et al. (2000); Montaldo et al. (2005, 2008). In the VDM of trees, four separate biomass states (compartments) are tracked: green leaves (B_g), stem (B_s), living root (B_r), and standing dead (B_d). The biomass components in $[gDM \cdot m^{-2}]$ are simulated by ordinary differential equations integrated numerically at a daily time step (Montaldo et al., 2005; Cayrol et al., 2000; Nouvellon et al., 2000; Arora and Boer, 2005):

$$\frac{dB_a}{dt} = a_{as}P_{g,s}\xi_t + a_{ar}P_{g,r}(1-\xi_t) - R_a - S_a \tag{3.16}$$

$$\frac{dB_s}{dt} = a_{ss}P_{g,s}\xi_t + a_{sr}P_{g,r}(1-\xi_t) - R_s - S_s \tag{3.17}$$

$$\frac{dB_r}{dt} = a_{rs}P_{g,s}\xi_t + a_{rr}P_{g,r}(1-\xi_t) - R_r - S_r \tag{3.18}$$

$$\frac{dB_d}{dt} = S_a - L_a \tag{3.19}$$

where P_g is the gross photosynthesis, a_{as}, a_{ar}, a_{ss}, a_{sr}, a_{rs}, and arr are allocation (partitioning) coefficients to leaves, stem and root compartments, R_a, R_s and R_r are the respiration rates from leaves, stem and root biomass, respectively, S_a, S_s and S_r are the senescence rates of leaves, stem and root biomass, respectively, and L_a is the litter fall. The equations of the terms in eq. 3.16,3.18, 3.19, 3.19 are in Table 3.1.

Ecophysiological Term	Equation
Photosynthesis	$P_g = \varepsilon_p(PAR) f_{PAR} PAR \frac{1.37r_a+1.6r_{c,min}}{1.37r_a+1.6r_c}$ $\varepsilon_p(PAR) = a_0 PAR/(1 + a_1 PAR)$ $f_{PAR} = 1 - e^{-k_e LAI}$
Allocation	For woody vegetation $a_{aj} = \frac{\zeta_a}{1+\Omega[2-\lambda-f_1(\theta_j)]}$ $a_{sj} = \frac{\zeta_s+\Omega\lambda}{1+\Omega[2-\lambda-f_1(\theta_j)]}$ $a_{rj} = \frac{\zeta_r+\Omega\lambda}{1+\Omega[2-\lambda-f_1(\theta_j)]}$ $\lambda = e^{-k_e LAI}$ $\zeta_a + \zeta_s + \zeta_r = 1$ For grass $a_a = \frac{\zeta_a}{1+\Omega[2-\lambda-f_1(\theta_s)]}$ $a_r = \frac{\zeta_r+\Omega\lambda}{1+\Omega[2-\lambda-f_1(\theta_s)]}$ $\zeta_a + \zeta_r = 1$
Respiration	$f_4(T_a) = Q_{10}^{T_a/10}$ For woody vegetation $R_a = m_a f_4(T_a) B_a + g_a[a_{a,s}P_{g,s}\xi_t + a_{a,r}P_{g,r}(1-\xi_t)]$ $R_s = m_s f_4(T_a) B_a + g_s[a_{s,s}P_{g,s}\xi_t + a_{s,r}P_{g,r}(1-\xi_t)]$ $R_r = m_r f_4(T_a) B_a + g_r[a_{r,s}P_{g,s}\xi_t + a_{r,r}P_{g,r}(1-\xi_t)]$ For grass $R_a = m_a f_4(T_a) B_a + g_a P_g$ $R_r = m_r f_4(T_a) B_r + g_r P_g$
Senescence	$S_a = \delta_a B_a$ $S_s = \delta_s B_s$ $S_r = \delta_r B_r$
Litterfall	$L_a = k_a B_d$

Table 3.1: Equations of the vegetation dynamic model components. Parameters are defined in Table

The key term of the VDM, P_g, is computed using the approach of Montaldo et al. (2005), which started from a simplified form of Fick's law applied to gas exchange in plants (Larcher, 2003; Hans Lambers, 2008) and the Nouvellon et al. (2000) model, deriving a simplified expression that estimates P_g mainly by the photosynthetically active radiation PAR, soil moisture, and other routinely monitored variables (wind velocity, and air humidity and temperature). Note that in equations 3.16,3.18, 3.19, the θ soil moisture contributors are θ_s for $P_{g,s}$ and θ_r for $P_{g,r}$.

The VDM of grass distinguishes only three biomass compartments (green leaves, roots and standing dead), and the biomass components are simulated using equations 3.16,3.18, 3.19, respectively.

Leaf area index values are estimated from the biomass through linear relationships (Montaldo et al., 2005; Nouvellon et al., 2000; Hans Lambers, 2008; Hanson et al., 1988):

$$LAI = c_a B_a \tag{3.20}$$

where c_a is the specific leaf area of the green biomass.

The SWBM is coupled with the VDM, which provides the LAI values of trees and grass daily, which are then used by the SWBM for computing the evapotranspiration partitioning, and the soil water content. The SWBM provides soil moisture and aerodynamic resistances to the VDM (see Figure 3.2).

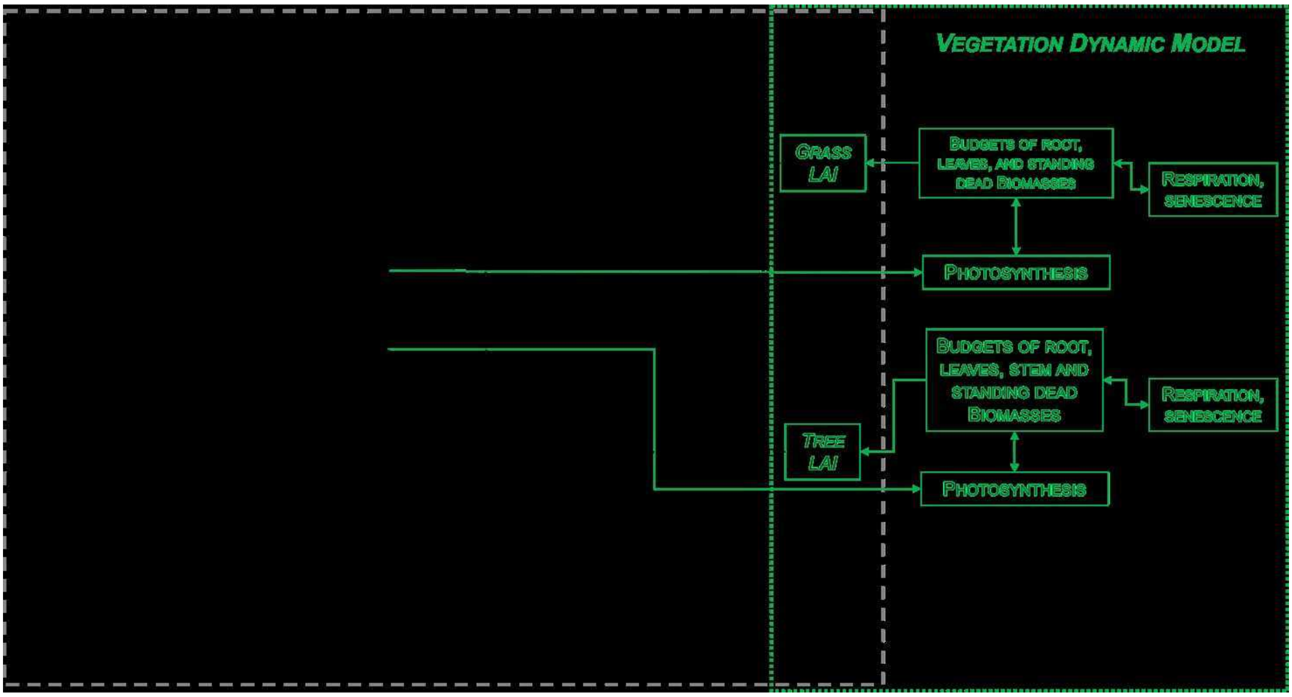

Figure 3.2: The flowchart of the distributed ecohydrological model

3.1.3 The Surface Runoff and Base Flow

In each cell of the basin, the Q_{sup} surface runoff is computed daily by the SWBM, and the total surface runoff at the basin scale is computed by summing the surface runoff contribution of the cells of the basin daily. Following Montaldo et al. (2007), the Q_b subsurface flow at the basin outlet is computed at the $j+1$ time step through a lumped conceptual approach, namely a linear reservoir method (Sorooshian, 1983):

$$Q_b^{j+1} = Q_b^j e^{-\Delta t/\kappa} + L_{e,j+1}(1 - e^{-\Delta t/\kappa}) \tag{3.21}$$

where Δt is the time step (=daily), and κ is a linear reservoir parameter. At each daily time step, the total runoff at the basin outlet (Q) is given by $Q = Q_{sup} + Q_b$.

3.2 Case Studies

The Mediterranean region is considered to be one of the most pronounced 'hot spots' in the world, highly sensitive to climate change. Sardinia is an excellent reference for ecohydrological studies on past and future climate change effects [8,11,18,47,61,62] representing typical conditions of the western Mediterranean Sea basin, and endowed with an extensive and long-term hydrological database dating back almost a century [10,47]. The island is one of the largest in the Mediterranean and is experiencing persistent negative trends in winter precipitation and even more severe ones in runoff. Runoff is a key term of basin water resources and a good indicator of water availability [12,13]. At the same time, the air temperature is increasing around the world, and the positive trend of air temperature impacts the vapor pressure deficit (VPD) trend [22,23] and consequently the vegetation dynamics. The two selected case studies represent two typical ecosystems of the Mediterranean region: a forested area included among the European Site of Community Importance (Natura 2000) and the rural area of Flumendosa, which represents the typical agro-pastoral ecosystem, with the presence of three reservoirs, it serves as the main water supply source for almost the entire southern Sardinia.

Input data

The model requires characterization of the watershed and atmospheric variables as input data.

The preliminary phase of the work primarily consists of defining the watershed of interest. This process is carried out using QGIS software, specifically with the GRASS plug-in, starting from the Digital Elevation Model (DEM) provided by the Sardinia Region at a 10m resolution(Sardinia Geoportal - Digital Elevation Model), resampled at 200m. Soil characteristics (texture, and hydrologic properties) and land cover maps are also available at the same spatial resolution in Sardinia Geoportal - Thematic maps. The soil depth map made by the Sardinian authority for agricultural scientific research and technological innovation (AGRIS) (Aru et al., 1991) at 100 m spatial resolution that was up-scaled at 200 m by averaging the 100 m data. More detailed data are also provided by the Regional Forestry Management Authority (Fo.Re.S.T.A.S.) for Marganai Forest.

Enviromental variables timeseries are provided by the Sardinian Regional Hydrographic Service. Daily rainfall, temperature, and hydrometric stations data have been available since the 1920s (more details will be provided for each basin in the paragraphs 3.2.1 and 3.2.2). Data for the other atmospheric variables have been available since more recent periods (the 1960s for wind and the 2000s for Rsw and RH). Observed data has been gap-filled using database from European Centre for Medium-Range Weather Forecasts (ECMWF): ERA20C (data from 1924 to 1939, Poli and Brunel (2018)) and the ERA5 (data from 1940 to 2023), (Hersbach et al., 2020, 2023), which have been successfully validated using 13 years of data of wind velocity from the Orroli station (RMSE = 1 $m \cdot s^{-1}$), 13 years of incoming solar radiation data from the Orroli station (RMSE = 35 $W \cdot m^{-2}$), and 5 years of data of relative humidity from the Orroli station (RMSE = 10%) (Montaldo and Corona, 2024).

Comparisons and Statistical Data Analysis

Data were analyzed at monthly, seasonal and yearly time scales. For annual computations, the hydrologic year, that begin in Sardinia in October was used. The runoff coefficient (Q/P, runoff/precipitation) was used for relating the runoff amount to the incoming precipitation amount, and an index of wetness (P/PE, precipitation/potential evaporation) was used for distinguishing annual meteorological conditions.

Model 'goodness-of-fit' was evaluated by comparing modeling results with observations and using the following statistics: mean (μ, standard deviation (SD), root mean square error ($RMSE$), correlation coefficient ρ, and the Nash–Sutcliffe model efficiency coefficient (NSE)).

Trends of the data are computed using the Mann–Kendall non-parametric test Kendall (1938); Helsel et al. (2020). The Mann–Kendall τ measures the monotonic relationship between two x and y variables (in this study, the time, e.g., year, and the hydrological variable, e.g., precipitation), and it is less sensitive to outliers and missing data values. In the method, all data pairs are ordered by increasing x and analyzing how y varies; τ value will be positive if y values increase more often than they decrease, while τ will be negative if y values decrease more often than they increase. To evaluate τ, a parameter D has been evaluated as follows:

$$D = NP - M \tag{3.22}$$

where NP is the "number of pluses", the number of times y increases as x increases, and M is the "number of minuses", the number of times y decreases as x increases. Defining n as the number of elements of the time series and n(n - 1)/2 as the number of possible comparisons, the Mann–Kendall τ coefficient is defined as follows:

$$\tau = \frac{D}{\frac{n(n-1)}{2}} \tag{3.23}$$

To verify the significance of the τ value, it is necessary for the null hypothesis to be rejected; for$n \leq 10$, an exact Mann–Kendall test is computed, while if $n > 10$, the test is modified to be approximated by a normal distribution (Helsel et al., 2020).

The Theil–Sen slope method is used to estimate the slope linear trends (Theil, 1950; Sen, 1968). The estimator is also called the "median of pairwise slope". Generally, this estimator is frequently applied in climatology and for the analysis of the hydrometeorological time series to define the rate of change. The β sign represents the direction of change, and its value indicates the steepness of change.

The Theil–Sen method and the Mann–Kendall test are strongly connected; the β slope estimator is related to the Mann–Kendall τ test statistic, such that if $\tau < 0$, then $\beta \leq 0$, and if $\tau > 0$, then $\beta \geq 0$ because τ is equivalent to the number of positive D (Equation 3.23) minus the number of negative

D, and β is the median of these D. This estimator is widely used in hydrologic applications (Hirsch et al., 1982; Mohsin and Gough, 2010; Hu et al., 2012; Amirabadizadeh et al., 2015) because it is quite resistant to the effect of extreme values in the data.

3.2.1 The Rio Fluminimaggiore Basin and the Marganai Forest

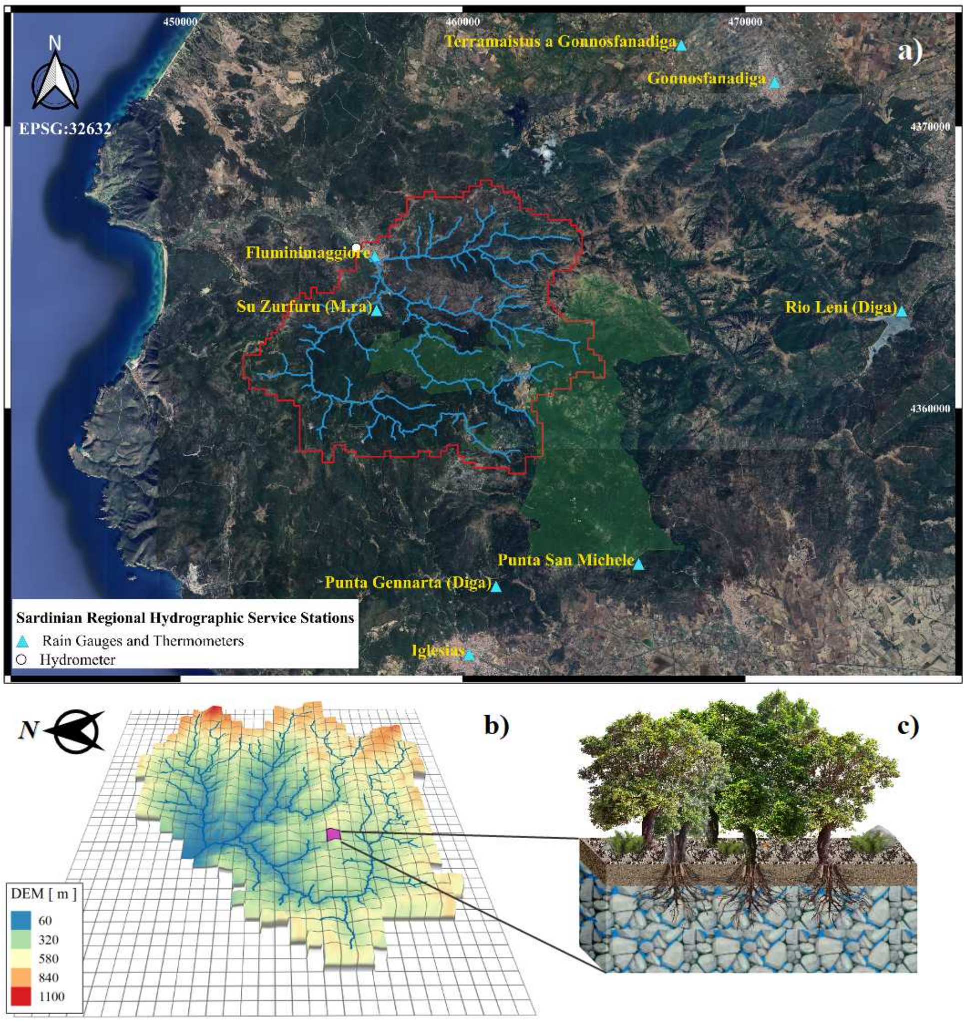

Figure 3.3: The Rio Fluminimaggiore river: a) basin with the river network and the position of the meteorological stations and hydrometer; b) digital elevation model (DEM) of the basin; c) model scheme of the soil layers and vegetation for each basin cell.

The case study is in the Rio Fluminimaggiore basin (area 83 km2), which is located in the southwest of Sardinia (Italy) (Figure 3.3) and includes the Marganai Forest, a Long–Term Ecosystem Research (LTER) Italian site and a European Site of Community Importance (Natura 2000).

The basin is predominantly mountainous (89% of the basin with height up to 200 m a.s.l.), with a mean slope of ~24°. The mountains are granitic and limestone rocks covered mainly by thin soils (mostly silty-clay) ranging from 10 to 50 cm deep. The basin is mainly natural (~97% of the basin), and the predominant land cover is forest (~55% of the basin), with half being dense *Quercus ilex* forest, and the rest typical Mediterranean maquis (*Arbutus unedo L., Phillyrea latifolia L., Euphorbia* *dendronides L., Cistus monspeliensis L., Cistus salvifolius L., Rosmarinus officinalis L.*). Typically Mediterranean basins in water-limited conditions, tree roots expand below the thin soil layer into the fractured rocky layers, looking for rock moisture (Montaldo et al., 2021).

The Fluminimaggiore basin is characterized by low urbanization conditions and low human activities, which has not changed from the past, as can be seen from the comparison of historical (1954) and recent (2016) aerial photography (Figure 3.4). The basin is still mostly natural (97% of the basin), forested (55%), and the increase in urban areas is negligible (from 0.45% to 0.79% of the basin area), the mine area (1.4%) is still present, although no longer active.

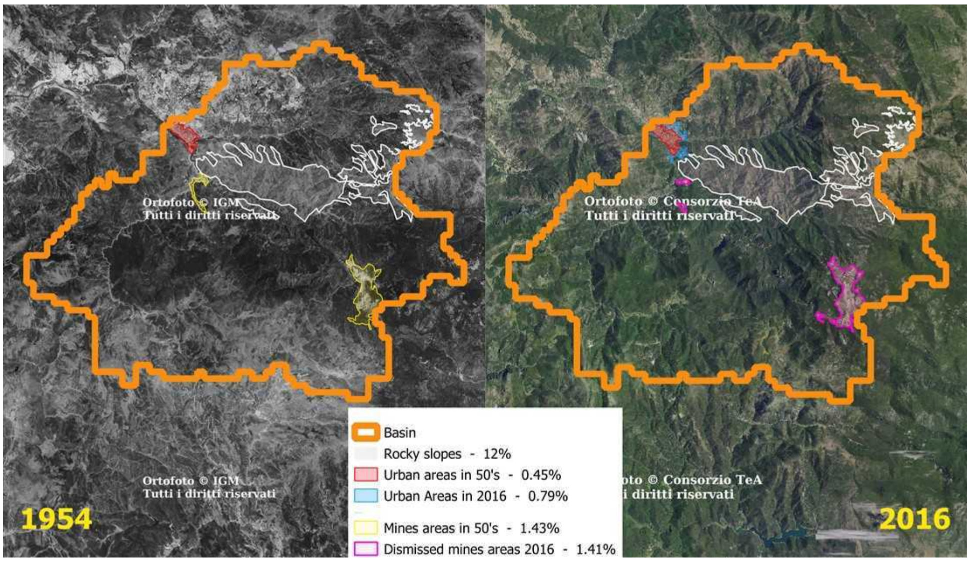

Figure 3.4: Historical comparison of the land uses (urban area, rocks, and mines area are highlighted) in the Fluminimaggiore basin: a) aerial photography of 1954, and b) aerial photography of 2016 Sardinia Geoportal - Aerial photos

The climate is typical marine Mediterranean climate type, characterized by cool and wet winters and warm and dry summers. The mean historical annual precipitation is 782 mm (1922 - 2021) with mean monthly precipitation ranging from 125 mm (in December) to 3 mm (in July). The mean annual air temperature is 16.36 °C, with mean monthly values ranging from 9.45 °C (in January) to 24.29 °C (in August).

Daily rain data from 8 stations of the Sardinian Regional Hydrographic Service are available in the area of the basin (Figure 3.3), with data from 1922 to 2021. Daily data of the hydrometric station of the Fluminimaggiore river are available from 1924 to 2021 (a record length of 97 years and 22.68% of missing data). In the following, yearly estimates of hydrologic variables are computed for the hydrologic year, which in Sardinia starts in October (when precipitation usually starts) and ends in September of the next year (when the soil is dry) (Montaldo and Oren, 2018). Data from the 8 thermometric stations of the Sardinian Regional Hydrographic Service are available, with at least 97 complete years of data (Figure 3.3), providing daily maximum and minimum air temperatures (T_{max} and T_{min}, respectively). Data from a nearby anemometric station at Capo Frasca was also used for the period since 1966 and from 2006 data from the Sardinian Enviromental Protection Agency (ARPAS) meteorological station located in Punta San Michele has been used. Incoming radiation data from two nearby meteorological station (Rio Leni and Punta Gennarta) are available since 2008, ECMWF data has been used for the previous period. RH is derived from ECMW dataset based on T_a and dew point temperature T_{dew} using Garratt (1994) eq.(A21). NDVI is estimated from red and near-infrared spectral reflectance measurements of remote sensor data. We used MODIS data at 250 m spatial resolution and 16 days of temporal resolution, available from 2000 to 2021 (Figure 1). The LAI is derived from NDVI MODIS data from Garson and Lacaze (2003) $LAI = 8.2387 \cdot NDVI + 2.9301$ for the Puchabon forest.

Historical Analysis

A long drought affected the Marganai forest in summer 2017, due to an unusual dry spring (48.37 mm of rain compared with the average 109.37 mm) that preceded a common dry summer. At the end of August 2017, the south - facing *Quercus ilex* trees turned red due to the critical state (Figure 3.5 b), while usually, they were still green at the end of the summer (Figure 3.5 a). The state of the trees was clearly identified by Sentinel 2 images (Figure 3.5 c,d) due to their high spatial resolution (10 m). However, the use of the coarse MODIS images still allowed us to capture the lower NDVI of the tree cover at the end of August 2017 (mean NDVI ~0.7), compared to the end of August 2016 (mean NDVI ~0.8; Figure c,d). Looking at the long MODIS NDVI time series of the Marganai forest, in summer 2017, the NDVI actually reached the minimum value (~0.7) in the last 13 years; however, in the first 8 years of the investigated 2000 - 2021 period, the NDVI decreased to 0.7 another five times (Figure 3.5 g); highlighting it was more common for trees to reach critical conditions in the first decade of the twenty - first century. However, 2017 was characterized by a longer and unusual drought (from spring) that caused a longer series of very low NDVI values (from April; Figure 3.5 g).

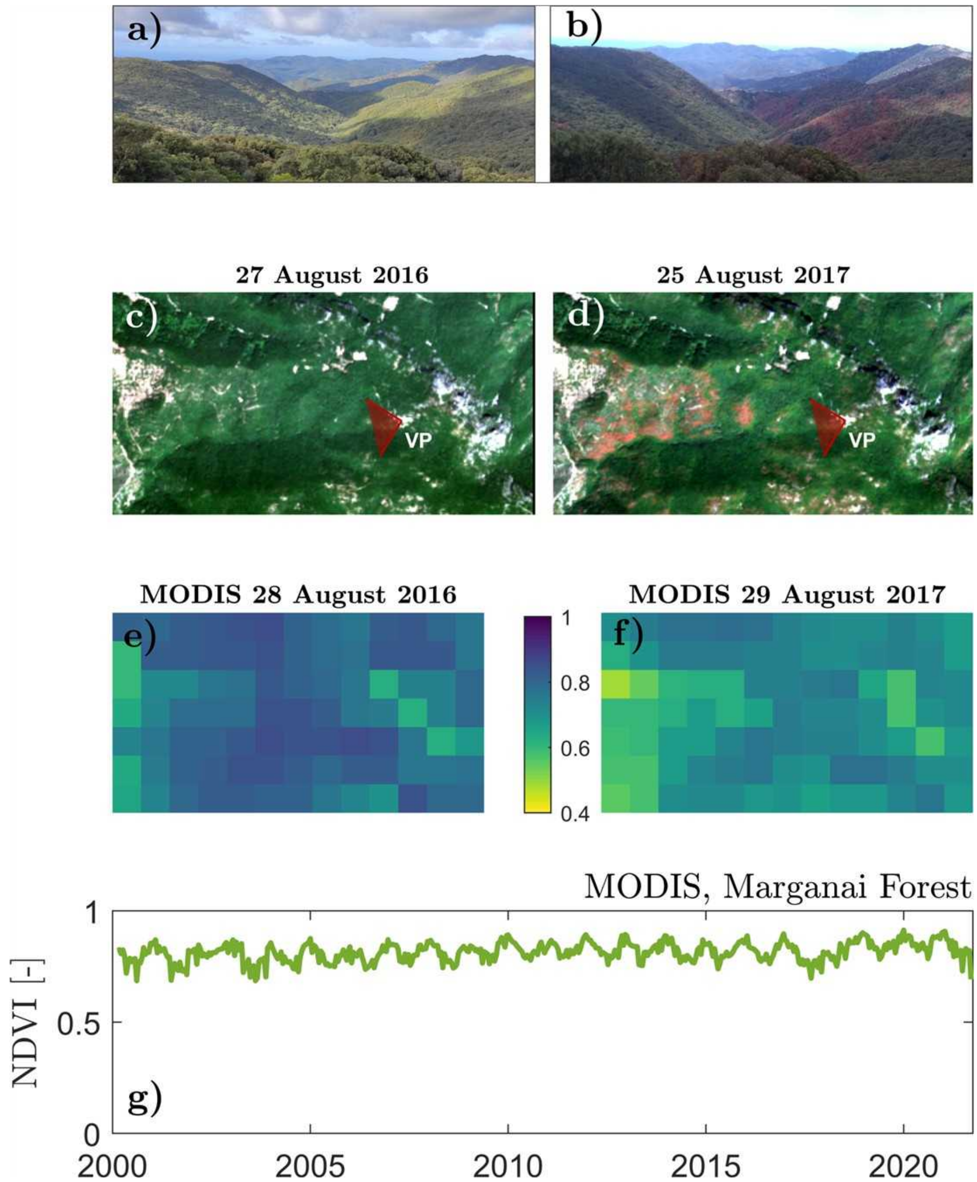

Figure 3.5: Comparison of the state of the Marganai forest in summer 2017 with that in the previous summer: a),b) pictures of the forest from the VP sight point shown in panels c),d) in summer 2016 and summer 2017, respectively; c),d) images of Sentinel 2 satellite at 10 m spatial resolution (VP is the view point of the pictures in a),b)); e),f) NDVI maps from MODIS images at 250 m spatial resolution; g) time series of the forest average NDVI (16 day temporal resolution) from MODIS data.

The analysis of the historical precipitation and temperature data at the basin scale pointed out that the yearly precipitation trend is negative but not significant (Mann - Kendall $\tau = -0.065$ with $p = 0.345$, Theil - Sen $\beta = -0.596[mm/year]$; Figure 3.6a), while the yearly air temperature is increasing significantly (Mann - Kendall $\tau = 0.300$ with $p < 0.001$, Theil - Sen $\beta = 0.010[°C/year]$; Figure 3.6b).

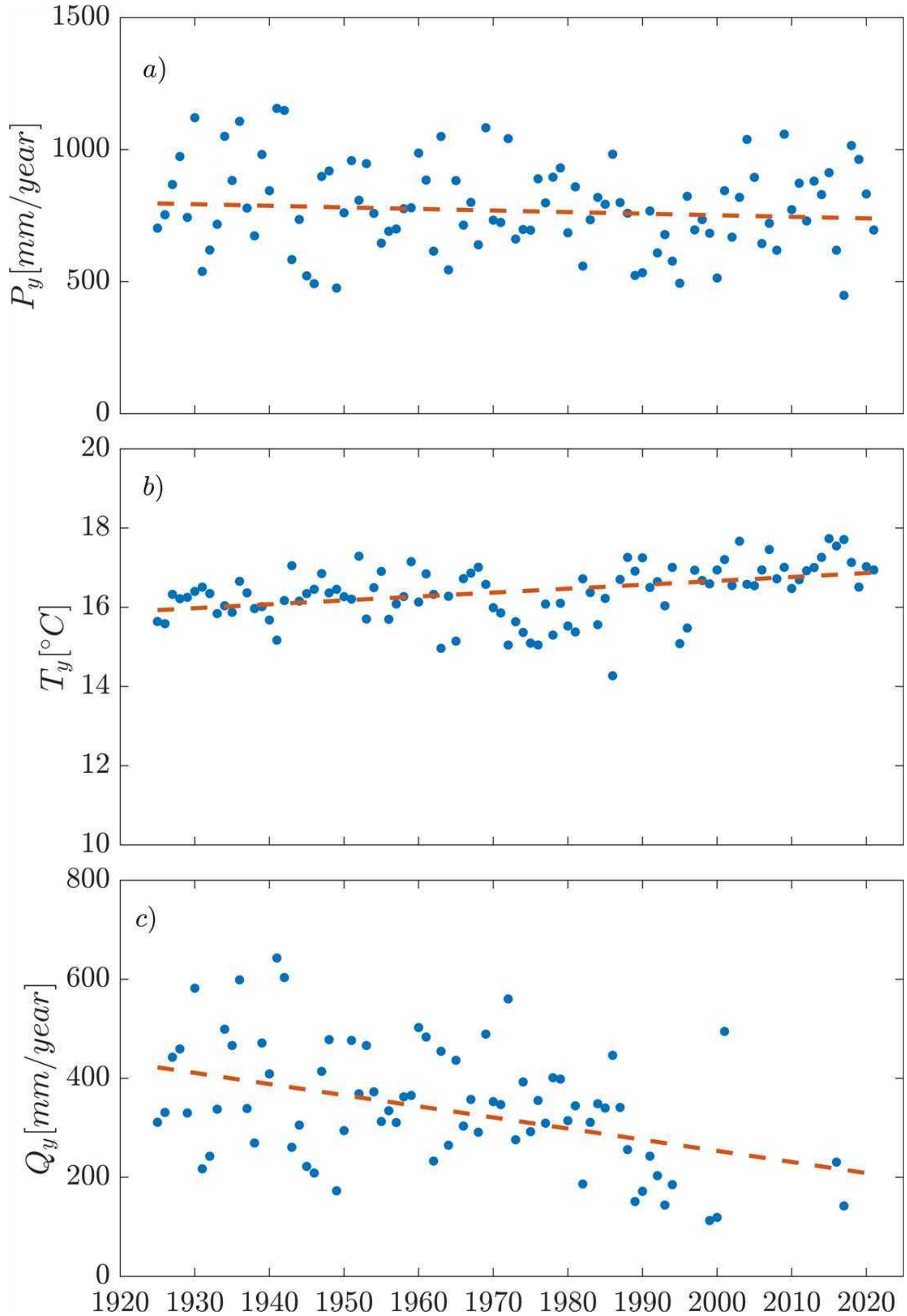

Figure 3.6: For the Fluminimaggiore basin, historical annual time series of: a) precipitation (P_y), b) air temperature (T_y), and c) runoff (Q_y). The slopes of the trend lines (red dashed) are estimated using the Theil-Sen method.

Due to the precipitation regime of the basin (Figure 3.7a), precipitation is mainly concentrated in the autumn and winter months, with mean monthly precipitation ranging from 72 mm in March to 125 mm in December (Figure 3.7a), and the decrease in precipitation was significant in winter (Mann - Kendall $\tau = -0.15$ with $p < 0.05$, and Theil - Sen $\beta = -0.26[mm/year]$; Figure 3.7 b,c).

Conversely, the air temperature increase was higher in the spring and summer months (Mann-Kendall $\tau > 0.26$ in summer; Figure3.7b,c), when the air temperature was already much higher (up to 25 °C on average in summer; Figure 3.7a). Due to the positive air temperature trend, the mean annual VPD increased significantly (Mann-Kendall $\tau = 0.13$ with $p = 0.06$, Theil-Sen $\beta = 0.01[hPa/year)$. The negative trend of observed annual runoff was significant and higher than the negative trend of annual precipitation, reaching a Mann-Kendall $\tau = -0.26$ ($p = 0.001$) and a Theil-Sen $\beta = -2.206[mm/year]$(Figure 3.6c). In the 1990s, annual runoff was very low, with values lower than $100[mm/year]$ for three years (Figure 3.6c).

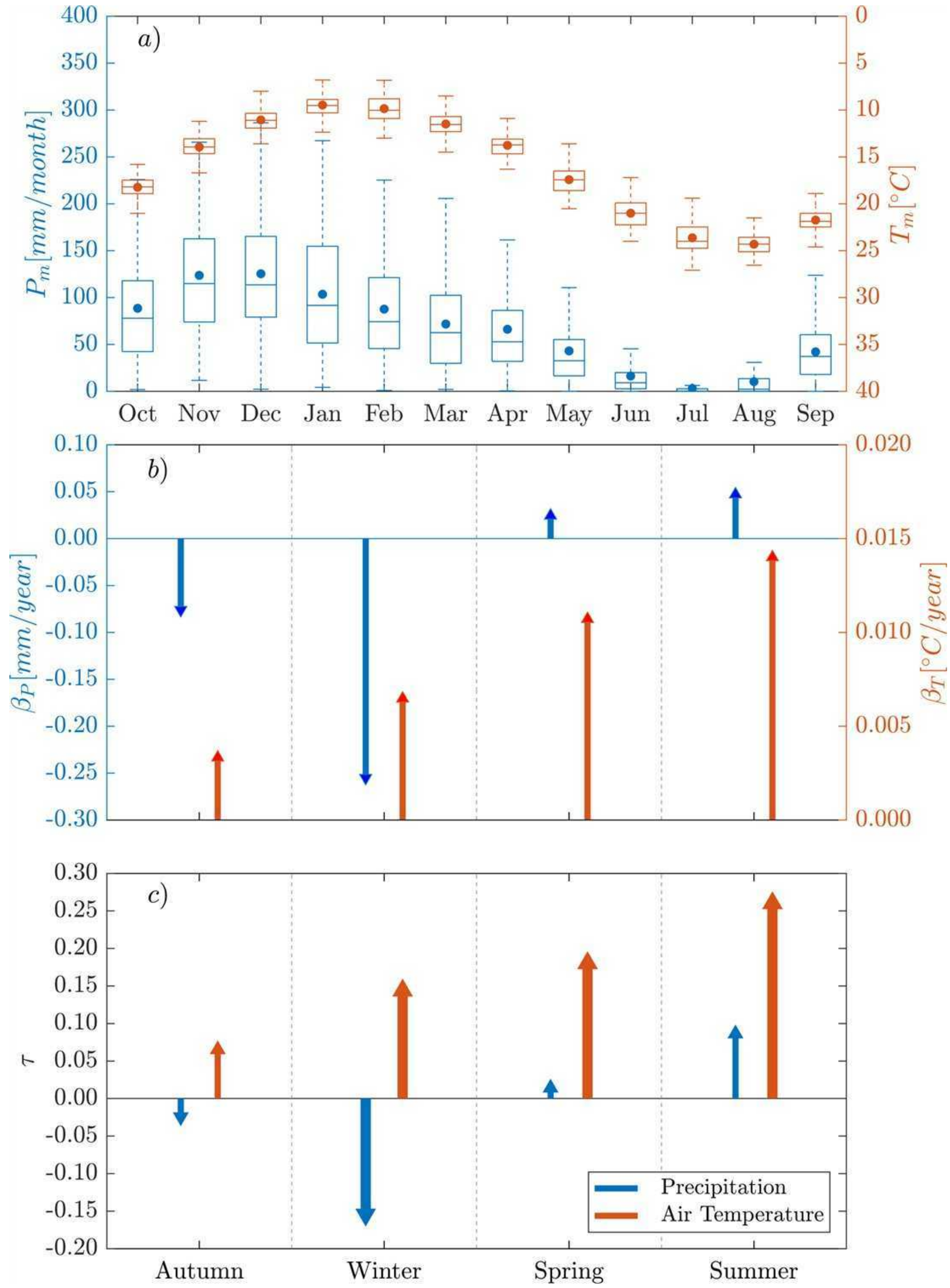

Figure 3.7: Historical climate at the Fluminimaggiore basin: a) monthly precipitation (P_m) and air temperature (T_m) regimes (in each estimation box, the statistics of the 1924 - 2021 period are shown: filled circles indicate the means, the horizontal lines the median, the box and whiskers represent quartiles, and outliers are depicted individually); b) the Theil-Sen β of the seasonal mean precipitation and air temperature trends; (c) the Mann-Kendall τ of the seasonal mean precipitation and air temperature trends (thicker arrows when $p < 0.05$).

Other Field Experimental Sites for Testing Model Components

In the Fluminimaggiore basin, measurements of some key outputs of the SWBM, such as evapotranspiration of the main tree species, *Quercus ilex*, and the soil water balance for shallow soils with trees, a typical feature of the Marganai forest, are not available. For testing these model components, data from two other case studies has been used, the Castelporziano and Orroli sites, which are still in Mediterranean climate conditions, and for which the required measurements are available. Castelporziano is a forest with the same species as the Marganai forest, while the Orroli site is characterized by a long dataset of soil moisture and micrometeorological data (Detto et al., 2006; Montaldo et al., 2020), a similar morphological soil type with a key role of the hydraulic redistribution and the water uptake by the tree roots from the underlying fractured rocks, and is located in Sardinia, 65 km from the Fluminimaggiore basin. The Castelporziano Estate is located in Lazio, central Italy (41.70°, 12.36°, 19 m elevation), and is a Long-Term Ecological Research site with data available on the FLUXNET2015 Dataset (Pastorello et al., 2020), (site ID: IT-Cp2). The site is located in a coastal area and covers about 6000 ha (Fares et al., 2014; Conte et al., 2019). The climate is typical Mediterranean semi-arid with a mean annual precipitation of 805 mm, similar to the Fluminimaggiore basin, and a mean annual temperature of 15.2°C (Fares et al., 2014; Conte et al., 2019). The soil is a sandy-loam with a mean depth of 45 cm. Vegetation is mainly composed of *Quercus ilex* with a percentage cover ~60% (Fares et al., 2014; Conte et al., 2019). This site is equipped with an eddy covariance tower for measuring evapotranspiration, CO_2, and energy fluxes and in particular, the latent heat flux has been used to calibrate the vegetation parameter.

In Orroli seven frequency domain reflectometer probes (FDR, Campbell Scientific Model CS-616) were inserted in the soil close to the tower (3.3-5.5 m away) to estimate moisture at half-hourly intervals in the thin soil layer, FDR calibration and the other instrumentation of the field site are described in Montaldo et al. (2020). This data has been used to calibrate the dynamic between the upper shallow soil layer and the deeper fractured rock layer.

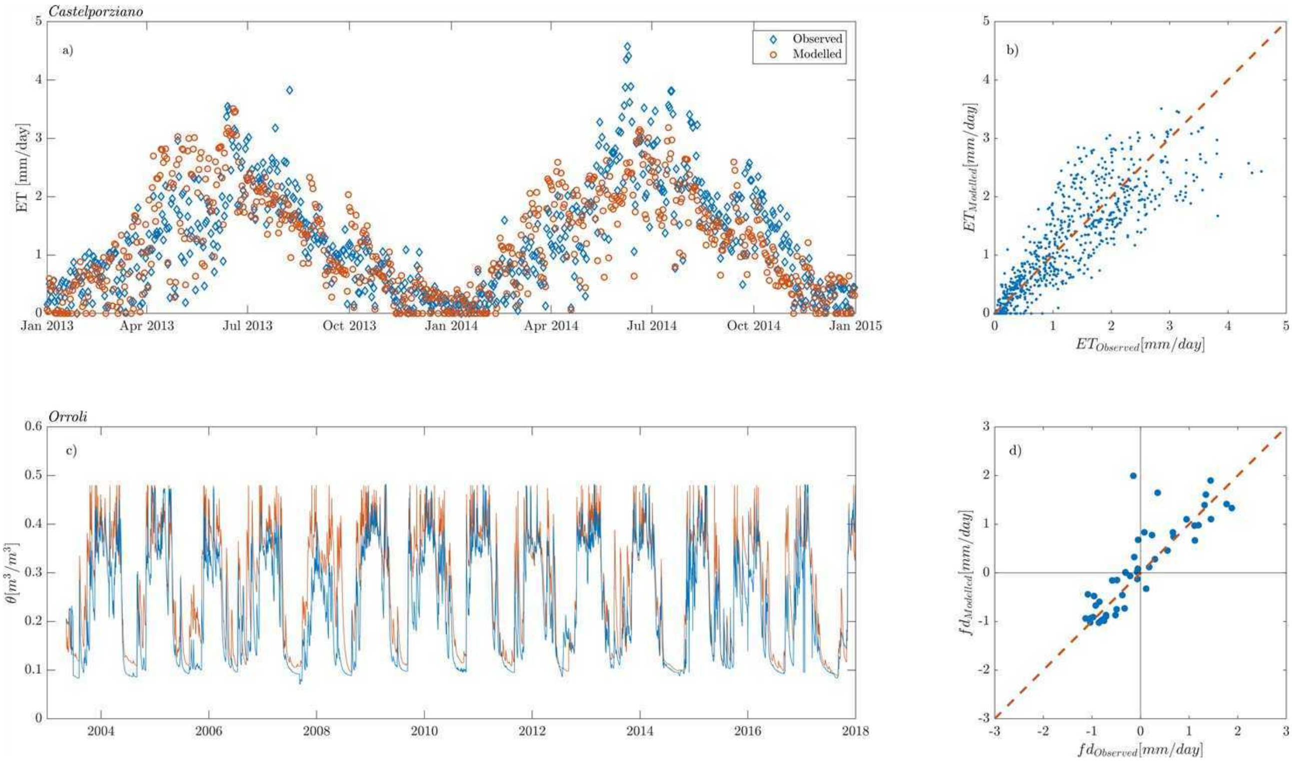

Figure 3.8: Model results at the two further experimental sites: a) and b) comparison of observed and predicted evapotranspiration (ET) at the Castelporziano site; c) comparison between observed and predicted soil moisture (θ) at the Orroli site in Sardinia; d) comparison between seasonal predicted and observed hydraulic redistribution flux between the surface soil and the underlying fractured rock through the tree roots (f_d) at the Orroli site.

Model calibration and its predictions for the past period

The model component for the evapotranspiration estimate of *Quercus ilex* was successfully tested using the 2-year Castelporziano ET observations ($RMSE = 0.039[mm/d]$, $R^2 = 0.73$ and $p < 0.05$; Figure3.8 a,b), and the model well predicted the seasonal variability of ET, which reached 4 mm/d in summer (Figure3.8a). Firstly, the model components were tested locally at the two experimental sites without considering surface and subsurface flows. The ET model components were tested using data of the Castelporziano site. The VDM parameter values are in Table 3.2. The model component for the evapotranspiration estimate of *Quercus ilex* was successfully tested using the 2-year Castelporziano ET observations ($RMSE = 0.039[mm/d]$, $R^2 = 0.73$ and $p < 0.05$; Figure3.8 a,b),. The model well predicted the seasonal variability of ET, which reached 4 mm/d in summer (Figure 3.8a). Soil moisture and $f_d(a_f = 169.83$, $b_f = 8.61$ in Equation 3.9; $\xi_t = 0.3$ if $\theta_s \geq 0.2$, otherwise $\xi_t = 0.1)$ are successfully tested using the long data base (15 years) of the Orroli site ($RMSE = 0.067$, $R^2 = 0.78$ and $p < 0.05$ for soil moisture prediction;$RMSE = 0.48$; $R^2 = 0.74$ and $p < 0.05$ for seasonal f_d; Figure 3.8c,d). The model well predicted the strong seasonal variability of soil moisture, ranging from dry (~0.1 in summer) to saturated (~0.5 in winter) conditions (Figure 3.8c).

Parameter	Description	Grass	Forest
$r_{s,min}[sm^{-1}]$	Minimum stomatal resistance	150	290
$\theta_{wp}[-]$	Wilting point	0.08	0.05
$\theta_{lim}[-]$	Limiting soil moisture for vegetation	0.20	0.18
$T_{min}[K]$	Minimum temperature	279.15	268.15
$T_{opt}[K]$	Optimal temperature	293.15	288.15
$T_{max}[K]$	Maximum temperature	299.15	304.15
$c_a[m^2gDM^{-1}]$	Specific leaf areas of the green biomass	0.01	0.0065
$c_d[m^2gDM^{-1}]$	Specific leaf areas of the dead biomass	0.01	0.0062
$k_e[-]$	PAR extinction coefficient	0.5	0.5
$\zeta_a[-]$	Parameter controlling allocation to leaves	0.6	0.55
$\zeta_s[-]$	Parameter controlling allocation to stem	0.1	0.1
$\zeta_r[-]$	Parameter controlling allocation to roots	0.4	0.35
$\Omega[-]$	Allocation parameter	0.8	0.1
$m_a[d^{-1}]$	Maintenance respiration coefficients for aboveground biomass	0.032	0.0001
$g_a[-]$	Growth respiration coefficients for aboveground biomass	0.32	0.85
$m_r[d^{-1}]$	Maintenance respiration coefficients for root biomass	0.007	0.0003
$g_r[-]$	Growth respiration coefficients for root biomass	0.1	0.1
$Q_{10}[-]$	Temperature coefficient in the respiration process	2.5	3
$d_a[d^{-1}]$	Death rate of aboveground biomass	0.023	0.0019
$d_r[d^{-1}]$	Death rate of root biomass	0.005	0.0001
$k_a[d^{-1}]$	Rate of standing biomass pushed down	0.23	0.35
$Q_N[-]$	Soil respiration coefficient related to temperature	1.2	
R_{10} $[mmolCO_2/m^2s]$	Reference respiration at 10 °C	2.54	
$z_{om,v}[m]$	Vegetation momentum roughness length	0.05	0.5
$z_{ov,v}[m]$	Vegetation water vapor roughness length	$z_{om}/7.4$	$z_{om}/2.5$
$z_{om,bs}[m]$	Bare soil momentum roughness length	0.015	
$z_{ov,bs}[m]$	Bare soil water vapor roughness length	$z_{om}/10$	

Table 3.2: Model parameters of the vegetation components calibrated using the model at field scale on the Castelporziano site.

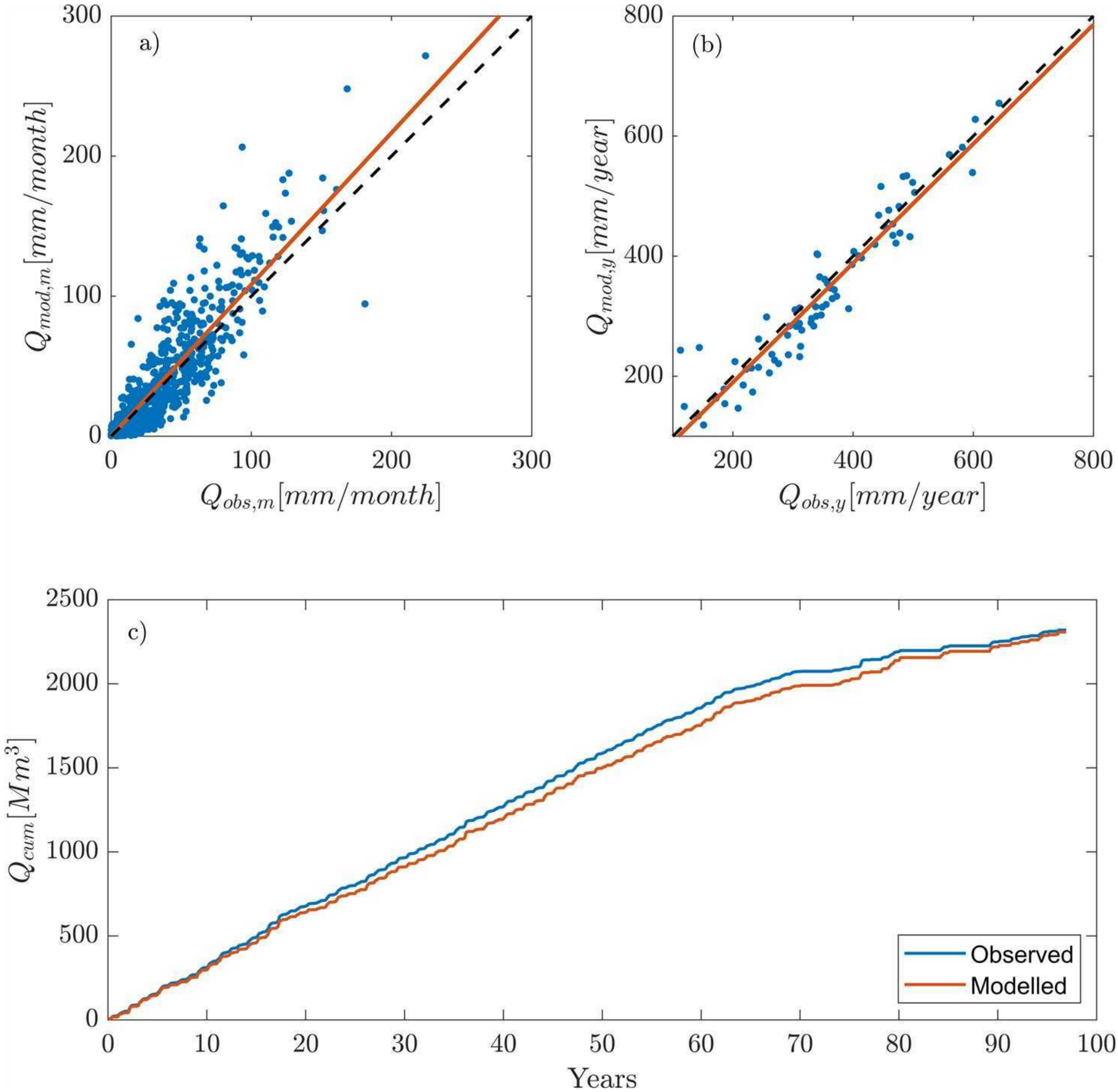

Figure 3.9: For the historical period, the comparison between observed and modeled runoff of the Rio Fluminimaggiore basin at a) monthly timescale (regression line in orange with slope of 1.08; $R^2 = 0.83$; $p \leq 10^{-5}$) and b) yearly time scale (regression line in orange with slope of 0.99; $R^2 = 0.90$; $p \leq 10^{-5}$) c) cumulative runoff (Q_{cum}, missing observed values are also not considered in the model time series; values are expressed in millions of cubic meters [Mm^3]).

The distributed version of the ecohydrological model was then applied at the Fluminimaggiore basin comparing the modeled and observed runoff for the long 1924-2020 historical period (Figure 3.9). We first used the 1924-1975 period for calibration (calibrated parameters are reported in Table 3.3) and last the 1976-2020 period for validation. Both monthly and yearly runoff predictions were tested successfully (Figure 3.9; for monthly runoff:$RMSE = 14.85mm/month$ and $R^2 = 0.94$ and $p < 0.001$ in calibration, and $RMSE = 17.76mm/month$ and $R^2 = 0.84$ and $p < 0.001$ in validation; for yearly runoff: $RMSE = 36.38mm/year$ and $R^2 = 0.98$ and $p < 0.001$ in calibration, and $RMSE = 48.51mm/year$ and $R^2 = 0.90$ and $p < 0.001$ in validation), and the total predicted runoff of the whole observed period (~28 m) matched well to the total observed runoff (difference of 0.02%; Figure 3.9 c).

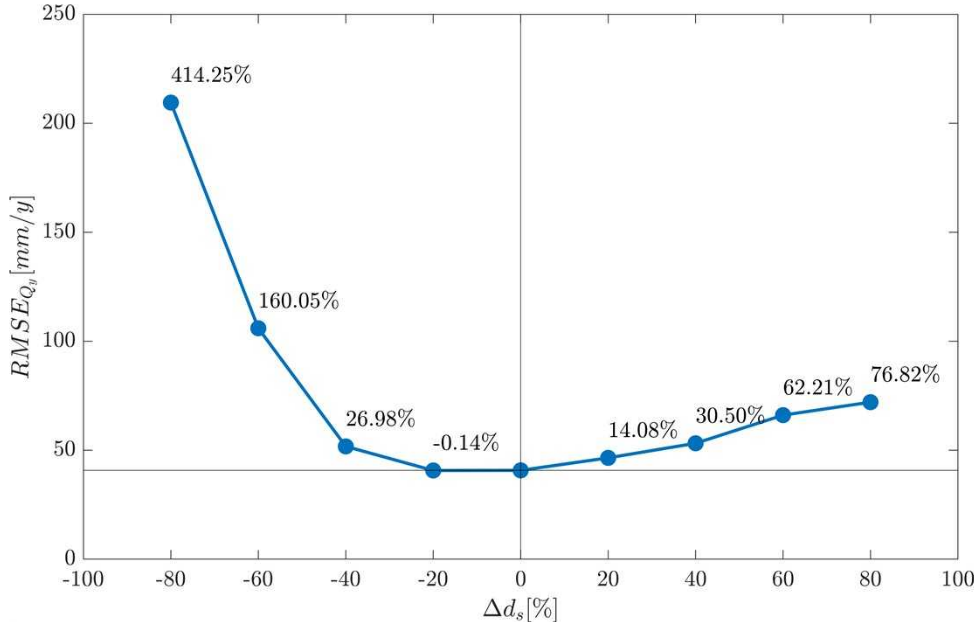

Figure 3.10: Performance of the model testing the run-off varing the shallow layer soil depth. The points labels are the values of $100 \cdot (RMSE - RMSE_{\Delta d_s=0})/RMSE_{\Delta d_s=0}$

A sensitivity analysis of the model to the soil depths was also performed (Figure 3.10). We varied the basin soil depths uniformly with respect to the reference soil depth map (provided by AGRIS) in a wide range (increasing up to +80% and decreasing up to −80%). The runoff predictions were mainly sensitive to the decrease in the soil depths (for values lower than −40%), due to the high increase in predicted runoff (which increased up to 58%, and RMSE increased up to 210 $mm/year$). Using more realistic scenarios of soil depths (variations from −40% to 40% with respect to the reference soil depth map), the model results have low sensitivity to the soil depth variations (RMSE always lower than 53 $mm/year$), confirming the robustness of the model results.

Parameter	Description	Mean	Range
CN	Curve Number of the Soil Conservation Service method	89.7	$80 - 99$
$\theta_s[-]$	Saturated soil moisture	0.44	$0.41 - 0.46$
$b_s[-]$	Slope of the retention curve in the surface soil	10.28	$7.75 - 11.40$
$k_{sat,s}[m/s]$	Saturated hydraulic conductivity	$2.82 \cdot 10^{-7}$	$10^{-8} - 10^{-6}$
$d_s[m]$	Soil layer depth	0.36	$0.20 - 0.85$
$q_{sat,r}[-]$	Saturated rock moisture	0.48	$0.45 - 0.50$
$b_r[-]$	Slope of the retention curve in the fracture rock layer	7	
$k_{sat,r}[m/s]$	Saturated hydraulic conductivity in the fracture rock layer	$1.41 \cdot 10^{-7}$	$5 \cdot 10^{-9} - 5 \cdot 10^{-7}$
$d_r[m]$	Fractured rock depth	1.5	

Table 3.3: Soil-related parameters of the model.

The VDM predicted the annual LAI estimated from MODIS NDVI quite well. We successfully tested the basin-averaged LAI predictions ($RMSE = 0.10$, $R^2 = 0.69$, $mean\ ratio = 0.99$), and the mean LAI predictions of the forest ($RMSE = 0.18$, $R^2 = 0.72$, $mean\ ratio = 0.99$, Figure 3.11). The basin average yearly ET predictions has been tested with ET estimates derived from runoff and precipitation observations. In semiarid regions at an annual scale, the runoff is roughly equal to the precipitation minus ET from the basin water balance, assuming negligible changes of the basin soil water storage (Montaldo and Oren, 2018; Zhang et al., 2004), so that annual ET estimates can be derived as the difference between observed runoff and observed precipitation. The annual ET model predictions well matched by the annual ET estimates ($RMSE = 3.93\ mm/year$; $R^2 = 0.98$, $p \leq 0.05$), confirming the model's reliability at the basin scale. At the basin scale, a nonsignificant negative trend of annual ET was predicted for the past (Mann-Kendall $\tau = -0.09$ with $p = 0.22$, Theil-Sen $\beta = -0.19$ $[mm/year]$, Figure 3.11 a), while the negative trend is significant for tree transpiration (Mann-Kendall $\tau = -0.16$ with $p = 0.02$, Theil-Sen $\beta = -0.26$ $[mm/year]$, Figure 3.11 b), and even more for tree LAI (Mann-Kendall $\tau = -0.24$ with $p < 10^{-3}$, Theil-Sen $\beta = -0.005$, Figure 3.11c).

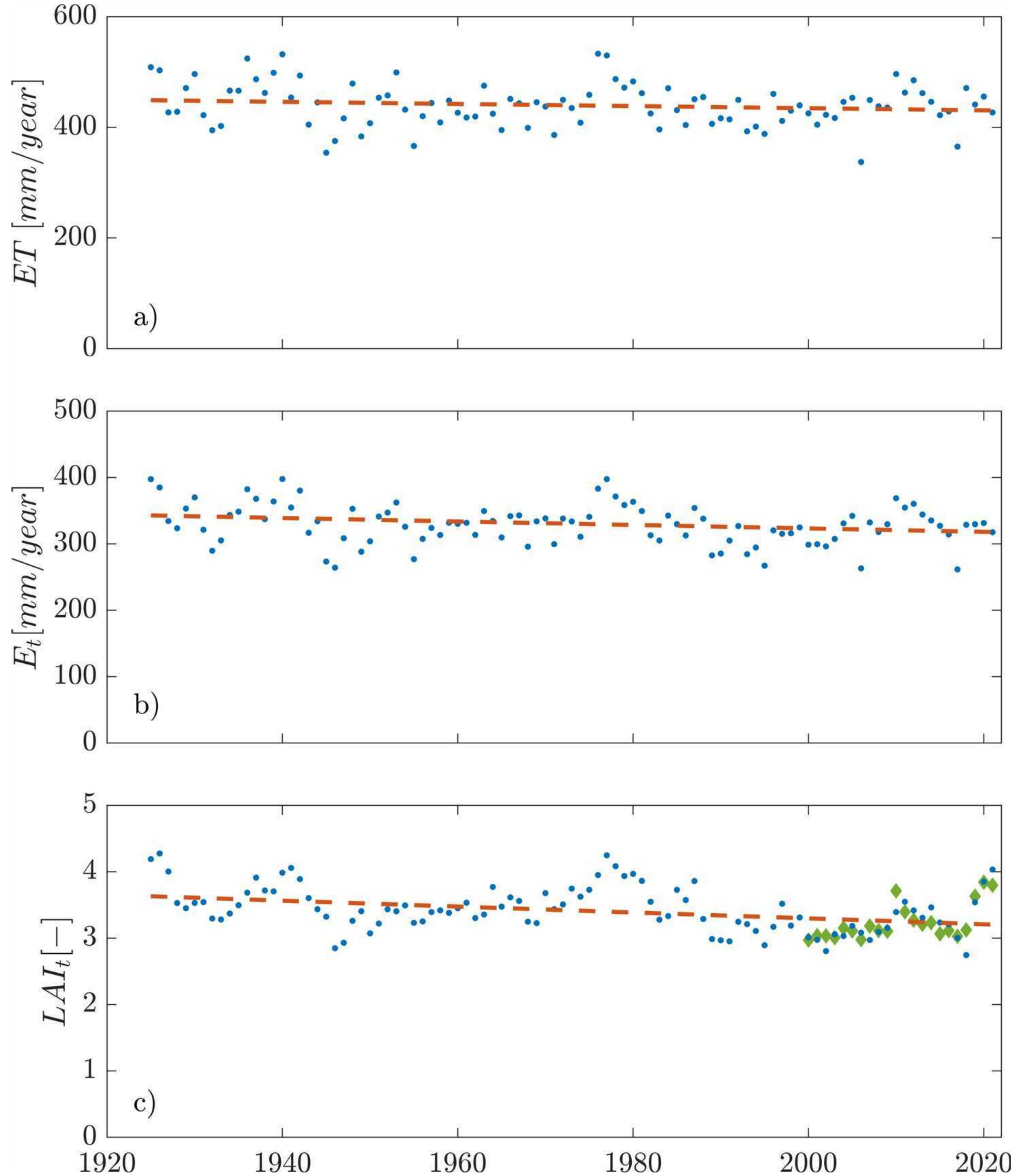

Figure 3.11: a) Evapotranspiration (ET), b) tree transpiration (E_t), and c) tree LAI (LAI_t) predictions using the meteorological observations of the Sardinian meteorological network (up to 2021). The slopes of the trend lines (orange dashed) are estimated by the Theil-Sen method. For LAI_t, green diamonds are the estimated values from NDVI of the MODIS remote sensor using Garson and Lacaze (2003).

3.2.2 The Flumendosa basin

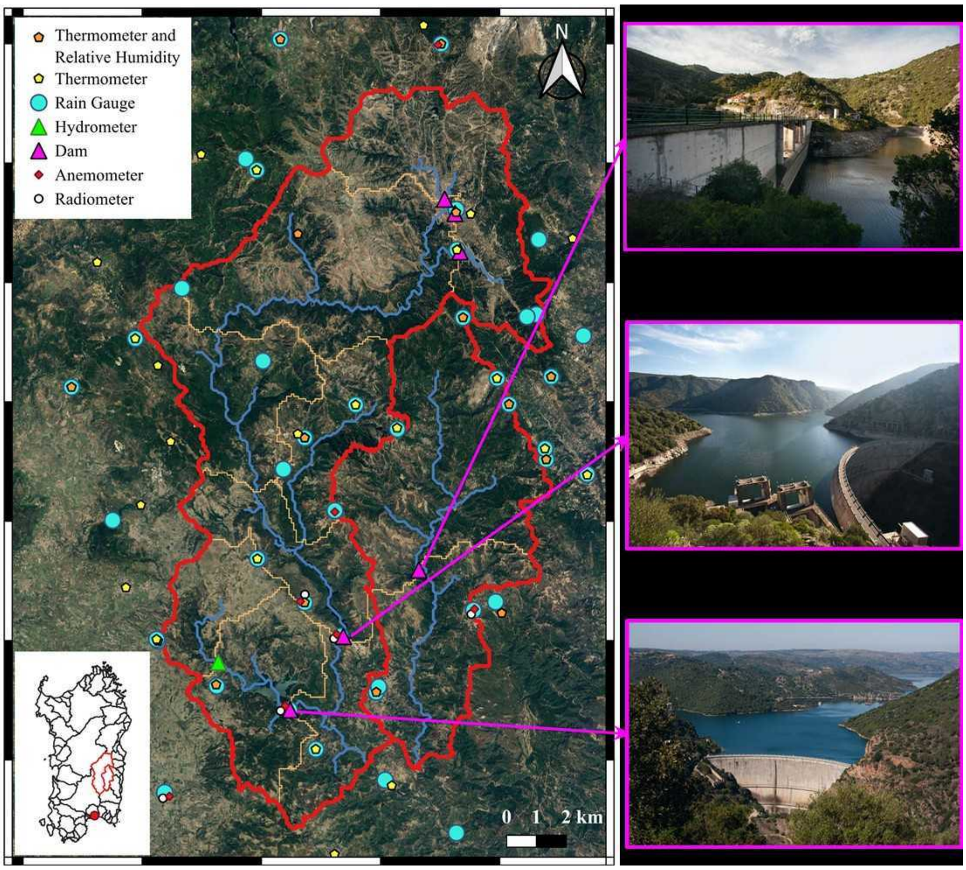

Figure 3.12: Left panel: map of the Flumendosa basin with the positions of meteorological stations, hydrometers, and dams. On the right panel: pictures of the three interconnected dams, from the top to the bottom there are Capanna Silicheri, Nuraghe Arrubiu and Monte su Rei (Images sourced from: ENAS-multisectoral regional water system and Di Felice and Salgo (2011)).

The Flumendosa basin, located in central-eastern Sardinia (9.33°E, 39.8°N), is the second longest river of the region with a length of 127 km (Figure 3.12), a mean elevation of 721 m a.s.l., a mean slope of 11%, and an area of 1017 km^2 at the Monte Scrocca section. The northern part of the basin is mountainous with steep hillslopes and higher rainfall compared to the southern part. The reservoir system includes two large dams, the Flumendosa dam at Nuraghe Arrubiu (reservoir capacity of $300 \cdot 10^6 m^3$) and the Mulargia dam at Monte Su Rei (reservoir capacity of $320 \cdot 10^6 m^3$) and a small dam in Rio Flumineddu at Capanna Silicheri (reservoir capacity of $1.44 \cdot 10^6 m^3$) (Figure 3.12). The three reservoirs are interconnected by an underground conduit to increase the collection of the runoff coming from the Nuraghe Arrubiu dam basin (751$km^2$2), which is much larger than the Mulargia basin (180km^2) and Capanna Silicheri (251km^2). The total capacity of the reservoir system is about $620 \cdot 10^6 m^3$, one of the largest reservoir capacities in Europe. Due to its key role in the Sardinian water resource system, the Flumendosa basin became an experimental basin of the University of Cagliari (Corona et al., 2018; Montaldo et al., 2008, 2013; Detto et al., 2006), resulting in an extensive hydrological database.

The climate regime is typically Mediterranean, the mean annual precipitation is 885 mm, and the mean annual air temperature is 14.21 °C. The thickness of the soil in the basin generally ranges from 5-200 cm with an average depth of 44 cm, with deeper soils in the valley and thin soil in steep slopes; the texture of the soil is mainly silt loam soils in the valley with the mountainous part dominated by exposed rocks. Land use is also inhomogeneous, with forested and natural areas predominant in the north and agricultural activities and grazing areas in the south (downstream) due to thicker soils. Urbanization is negligible (~2.31%) in the basin, while forested areas are predominant (= 57%). The spatial distribution of tree cover in the basin (spatial resolution of 200 m) was estimated from Sentinel 2 remote sensing data, using the Scene Classification Mask (SCL) product.

Daily precipitation data from 41 rain gauge stations, in and surrounding the Flumendosa basin, and monthly runoff data at the basin outlet were collected for the period 1923 – 2022 (Figure 3.12). Data have been collected from the Sardinian Environmental Protection Agency and the Sardinian water resources authority. Data have been processed and the linear regression method was used for gap-filling (using the data collected at the gap time in another consistent station). Runoff data are also available for the Mulargia section for a shorter period (2003-2007). Air temperature data from 13 stations are available at the daily scale (Figure 3.12) from 1924, and air temperature and relative humidity data from 16 stations are available from 2011, at 30 minute intervals. Incoming short wave radiation data are available from 2007 (from 5 stations at 30 minute intervals) and wind speed data are available from 1973, at a hourly timescale at 4 stations. Data from two eddy-covariance based micrometeorological stations at Orroli and Nurri are also available (Montaldo et al., 2013). The second site is at Nurri (39°41'11.51" N, 9°12'57" E). The soil is mainly silty clay loam (17.7% sand, 52.2 % silt, 30.3 % clay) and the soil depth is more than 1.5 m. The site is located in an alluvial plain valley of the Mulargia river. It is a C3 grass site, with a maximum height of 70 cm during the spring season. Data are available for the April 17th 2003-September 30^{th} 2005 period only. For an historical hydrological analysis from 1923, data of relative humidity, wind velocity and incoming so-lar radiation were collected from the ERA5 European Centre for Medium-Range Weather Forecasts (ECMWF) atmospheric reanalysis datasets (Hersbach et al., 2020, 2025), which have been successfully validated using 13 years of data of wind velocity from the Orroli station ($RMSE = 1\,m/s$), 13 years of incoming solar radiation data from the Orroli station ($RMSE = 35\,W/m^2$), and 5 years of data of relative humidity from the Orroli station ($RMSE = 10\%$).

Historical Analysis

The annual rainfall in the Flumendosa basin significantly decreased in the last century (Mann-Kendall $\tau = -0.247$, $p < 0.005$, and Theil-Sen slope $\beta = -2.50\,mm/y$), with mean annual precipitation reducing from 922 mm/y to 764 mm/y (Figure 3.13a). The decrease in rainfall is even higher, if we consider that the winter precipitation is the key to the water resources management system.

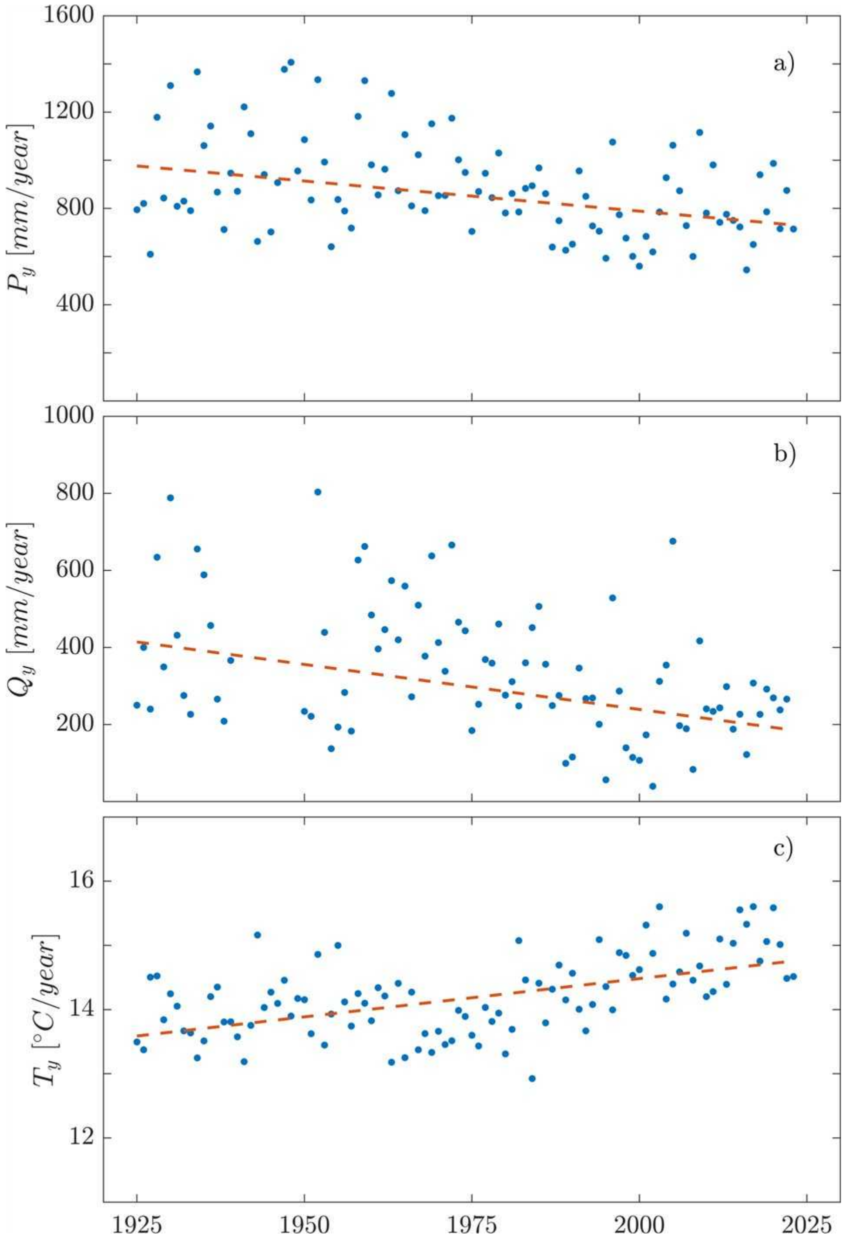

Figure 3.13: Annual series and trends of a) precipitation (P_y), b) runoff (Q_y), and c) air temperature (T_y) at the Flumendosa basin. The slopes of the trend lines (orange dashed) are estimated using the Theil–Sen method.

Due to the precipitation regime in the basin (Figure 3.14a), precipitation is mainly concentrated in the autumn and winter months, with mean monthly precipitation ranging from 86 mm in March and 134 mm in December to 15 mm in July (Figure 3.14a); the decrease in precipitation was significant in winter (Mann-Kendall $\tau = -0.271$ with $p < 0.005$, and Theil-Sen $\beta = -0.52\,mm/y$; Figure 3.14b). On the other hand, the increase in air temperature was higher in the spring and summer months (Mann-Kendall τ up to 0.26 in summer; Figure 3.14c), when the air temperature was already much higher (up to 24 °C on average in summer; Figure 3.14a), in contrast with the colder winters (7.1 °C, on average in January). The negative trend of observed annual runoff was significant and higher than the negative trend of annual precipitation, reaching a Mann-Kendall $\tau = -0.276$ ($p = 0.001$)

and a Theil–Sen $\beta = -2.337\,mm/y$ (Figure 3.14b). In the 1990s and the first decades of the 2000s, annual runoff was very low, with values lower than 100 mm/y for three years (1995, 2002, and 2018) (Figure 3.13b). In contrast, the mean annual air temperature of the basin increased in the last century (Mann-Kendall $\tau = 0.37$, $p < 0.005$ and Theil-Sen slope $\beta = +0.011\,°C/y$), highlighting warmer conditions in the last decade, with an increase in air temperature of +0.55 °C (Figure 3.13c).

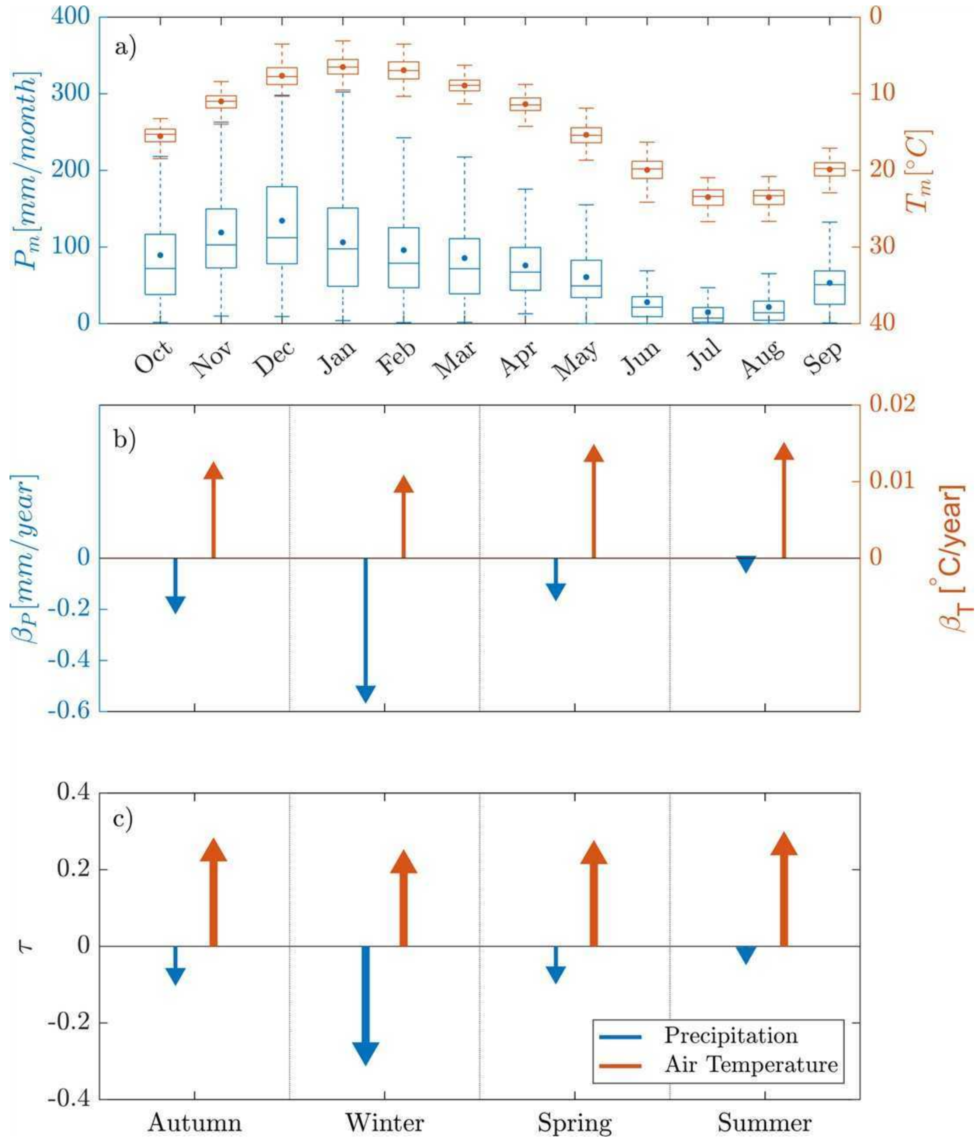

Figure 3.14: . Historical climate at the Flumendosa basin: a) monthly precipitation (P_m) and air temperature (T_m) regimes (the statistics of the 1924–2022 period are shown in each estimation box: filled circles indicate the means, the horizontal lines show the median, the box and whiskers represent quartiles, and outliers are depicted individually); b) the Theil–Sen β of the seasonal mean precipitation (β_P) and air temperature (β_T) trends; c) the Mann–Kendall τ of the seasonal mean precipitation and air temperature trends (thicker arrows when $p < 0.05$).

Model calibration

The distributed ecohydrological model was calibrated and validated at the Flumendosa basin (at Monte Scrocca), comparing the modelled and observed runoff for the longer 1925-2022 period (Figure 3.15a).

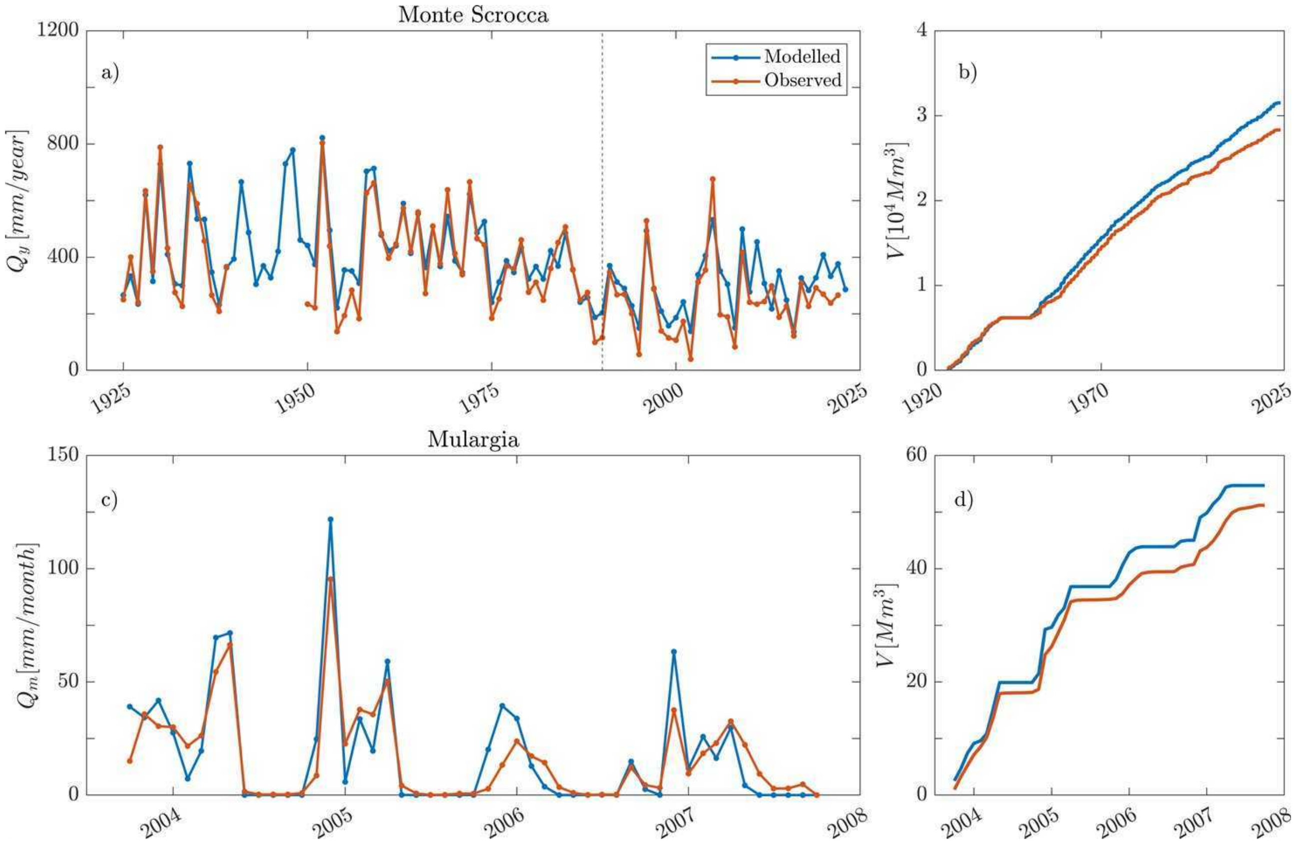

Figure 3.15: For the historical period, the comparison between observed and modeled runoff of the Flumendosa basin at a) yearly timescale, and b) the corresponding cumulative runoff, and of the Mulargia subbasin at c) monthly time scale and d) the corresponding cumulative runoff (values are expressed in millions of cubic meters [Mm^3]).

Table 3.4 and Table 3.5 report the values of the calibrated parameters: the CN of the SCS-CN method (the key parameter for the runoff modeling) was equal to 84 on average, ranging from 42-99. CN map was first derived from the map of the whole Sardinia Island (made by the Regional environmental authority), and then calibrated comparing runoff predictions and observations. We used the first 65 years (1925-1989) for calibration (Table 3.6) and the last 33 years for validation. The warm-up period was one year. Yearly runoff predictions were tested successfully (Figure 3.15 and Table 5; $RMSE = 66.01\,mm/year$, $R^2 = 0.87$, and $p < 0.001$ in calibration, while $RMSE = 87.52\,mm/year$, $R^2 = 0.72$, and $p < 0.001$ in validation. The total predicted runoff of the whole period only had a difference of 10% from that observed). The predicted runoff coefficient was 0.28 on average, ranging from 0.63 in the winter months to 0.20 in dry months, which is close to that observed ($RMSE = 0.40$, $R^2 = 0.52$, and p < 0.005). The model was also validated at a monthly timescale in the Mulargia subbasin for a shorter period, due to the avail-bility of the hydrometer data for the 2003-2007 period only, confirming the model's reliability (Figure 3.15 c and d; $RMSE = 10.42\,mm/month$, $R^2 = 0.84$, and $p < 0.001$; total predicted runoff of the whole period with a difference of 6.8% from the observed one). The model parameters for ET predictions were derived from literature data (Sirigu and Montaldo, 2022; Montaldo and Corona, 2024). Indeed, we also tested the ET predictions with the

ET observations from the two eddy-covariance stations at Orroli and Nurri, confirming the model's robustness ($RMSE = 1.12\, mm/day$ at the Nurri site, and $RMSE = 0.68\, mm/day$ at the Orroli site; the difference of the total evapotranspiration measured and modelled at a daily timescale is 5.22% at the Orroli site and 4.86% at the Nurri site). The historical trend of predicted basin average ET was not significant (Mann Kendall $\tau = -0.01$, $p = 0.84$), while the predicted tree transpiration decreased significantly (Mann Kendall $\tau = -0.14$, $p < 0.05$). The predicted F_c carbon assimilation decreased significantly (Mann Kendall $\tau = -0.15$ and $p = 0.01$) and the predicted LAI decreased significantly (Mann Kendall $tau = -0.41$ and $p < 0.05$) in the last century. An univariate sensitivity analysis has been performed of predicted runoff and evapotranspiration to vegetation model parameters for tree and grass ($r_{s,min}$, θ_{lim}, θ_{wp}) and soil model parameter (CN), varying parameter values in a range of ±50% of the calibrated values (which are in Table 1). When we varied the CN parameter we found the largest effects on runoff prediction (from -20% to 115% of the runoff), while varying the vegetation parameters the largest effects were on ET predictions although lower (from -17% to 15%).

height**Parameter**	**Description**	**Grass**	**Forest**	**Other Woody Vegetation**
$r_{s,min}[sm^{-1}]$	Minimum stomatal resistance	150	290	280
$\theta_{wp}[-]$	Wilting point	0.08	0.05	0.03
$\theta_{lim}[-]$	Limiting soil moisture for vegetation	0.20	0.18	0.15
$T_{min}[K]$	Minimum temperature	279.15	268.15	272.15
$T_{opt}[K]$	Optimal temperature	293.15	288.15	292.15
$T_{max}[K]$	Maximum temperature	299.15	304.15	318.15
$c_a[m^2 gDM^{-1}]$	Specific leaf areas of the green biomass	0.01	0.0065	0.005
$c_d[m^2 gDM^{-1}]$	Specific leaf areas of the dead biomass	0.01	0.0062	0.005
$k_e[-]$	PAR extinction coefficient	0.5	0.5	0.5
$\zeta_a[-]$	Parameter controlling allocation to leaves	0.6	0.55	0.55
$\zeta_s[-]$	Parameter controlling allocation to stem	0.1	0.1	0.1
$\zeta_r[-]$	Parameter controlling allocation to roots	0.4	0.35	0.35
$\Omega[-]$	Allocation parameter	0.8	0.1	0.8
$m_a[d^{-1}]$	Maintenance respiration coefficients for aboveground biomass	0.032	0.0001	0.0009
$g_a[-]$	Growth respiration coefficients for aboveground biomass	0.32	0.85	0.45
$m_r[d^{-1}]$	Maintenance respiration coefficients for root biomass	0.007	0.0003	0.002
$g_r[-]$	Growth respiration coefficients for root biomass	0.1	0.1	0.1
$Q_{10}[-]$	Temperature coefficient in the respiration process	2.5	3	2
$d_a[d^{-1}]$	Death rate of aboveground biomass	0.023	0.0019	0.0045
$d_r[d^{-1}]$	Death rate of root biomass	0.005	0.0001	0.005
$k_a[d^{-1}]$	Rate of standing biomass pushed down	0.23	0.35	0.35
$Q_N[-]$	Soil respiration coefficient related to temperature	1.2		
R_{10} $[mmolCO_2/m^2s]$	Reference respiration at 10 °C	2.54		
$z_{om,v}[m]$	Vegetation momentum roughness length	0.05	0.5	0.5
$z_{ov,v}[m]$	Vegetation water vapor roughness length	$z_{om}/7.4$	$z_{om}/2.5$	$z_{om}/2.5$
$z_{om,bs}[m]$	Bare soil momentum roughness length	0.015		
$z_{ov,bs}[m]$	Bare soil water vapor roughness length	$z_{om}/10$		

Table 3.4: Ecohydrological model parameters for the Flumendosa basin.

Parameter	Description	Mean	Range
CN	Curve Number of the Soil Conservation Service method	84	$42 - 99$
$\theta_{sat,s}[-]$	Saturated soil moisture	0.49	$0.41 - 0.60$
$b_s[-]$	Slope of the retention curve in the surface soil	10.28	$7.75 - 11.40$
$k_{sat,s}[m/s]$	Saturated hydraulic conductivity	$1.06 \cdot 10^{-6}$	$5 \cdot 10^{-8} - 4 \cdot 10^{-6}$
$d_s[m]$	Soil layer depth	0.45	$0.17 - 2$
$\theta_{sat,r}[-]$	Saturated rock moisture	0.50	
$b_r[-]$	Slope of the retention curve in the fracture rock layer	8	
$k_{sat,r}[m/s]$	Saturated hydraulic conductivity in the fracture rock layer	$8 \cdot 10^{-8}$	
$d_r[m]$	Fractured rock depth	3	

Table 3.5: Soil-related parameters of the model.

	Monte Scrocca		Mulargia
	Calibration	Validation	Validation
R^2	0.87	0.72	0.84
p	<0.0005	<0.0005	<0.0005
RMSE	66.01 [mm/y]	87.79 [mm/y]	10.42 [mm/m]
NSE	0.84	0.52	0.72
ΔV	11%		6.80%

Table 3.6: Runoff prediction evaluation for the calibration and validation periods (RMSE: root mean square error, NSE: Nash–Sutcliffe model efficiency coefficient,ΔV: the variation of the total cumulative runoff volume).

3.3 Conclusions

In this chapter, an eco-hydrological model has been presented, balancing complexity and parsimony to simulate the hydrological and vegetational dynamics ecosystems typical of the Mediterranean area. The adopted approach integrates key hydrological and vegetation distribution processes, including hydraulic redistribution by roots, that rapresent an important part of water supply for vegetation in water-limited ecosystems, while maintaining a low computational cost. The model was validated on two sites with different climatic and hydrological characteristics, allowing its robustness to be tested across variable conditions. While the first site is characterized by higher water availability and more stable vegetation dynamics, the second site presents drier conditions, where hydraulic redistribution plays a more critical role in vegetation maintenance. The results indicate that the model can represent the long-term water balance in different hydrological context, and it el was validated on two sites with different climatic and hydrological characteristics, allowing its robustness to be tested across variable conditions In the Flumendosa basin, the analysis of a long-term hydrological time series (1922–2022) revealed a significant decrease in winter precipitation and a 50% reduction in annual runoff over the past century. At the same time, an increase in mean annual temperature was observed. These climatic changes have compromised the sustainability of reservoir-based water resources in the basin. In the Marganai forest, the application of a distributed eco-hydrological model allowed us to simulate the evolution of the water balance and vegetation dynamics under the influence of climate change. The results showed a reduction in water resources and changes in vegetation dynamics, indicating a decrease in the ecosystem's resilience. In summary, the combined analysis of these two studies emphasizes the importance of using advanced eco-hydrological models to understand and predict the impact of climate change on water resources and terrestrial ecosystems. These tools are essential for developing adaptive management strategies aimed at mitigating the negative effects of climate change and ensuring the sustainability of natural resources. In the next chapter, the potential applications of this model in the sustainable management of water resources and the prediction of climate change impacts will be explored in more detail.

4 Impact of future climate change scenarios on basin water resources

In the previous chapter, the importance of an ecohydrological model as a tool for evaluating past climate change impacts was discussed. This chapter focuses on the application of ecohydrological models to predict future scenarios. In Mediterranean ecosystems, where water availability is a key constraint, declining precipitation directly affects both natural environments, such as forests, and water availability for civil and agricultural needs. Forests, which play a crucial role in carbon sequestration, erosion control, and biodiversity conservation (Guerra et al., 2016; Zhang et al., 2001), are increasingly vulnerable to these climatic shifts. At the same time, irrigated agriculture—accounting for approximately 85–90% of global water consumption—faces significant challenges due to climate-induced reductions in water availability, particularly in regions like Sardinia, southeastern Spain, and Greece (Qin et al., 2019; Eekhout et al., 2024; Lyra and Loukas, 2023). Future climate projections, based on global circulation models (GCMs) from IPCC reports (Flato et al., 2013; Taylor et al., 2012; CMIP5, 2013; Swart et al., 2019b), indicate increasingly severe hydrological conditions in Mediterranean regions.

The combination of future GCM climate scenarios with ecohydrological models, which integrate hydrologic and vegetation dynamics at the basin scale, provides a crucial approach for assessing the consequences of climate change on water and vegetation resources. These models enable predictions of forest health and runoff, which represents the primary water source for distribution systems in regions like Sardinia.

The sustainability of current water resource systems is under growing pressure due to climate change and increasing demands. In Sardinia, an artificial reservoir system developed over the past century has played a key role in supporting economic growth, particularly in agriculture and tourism. However, recent droughts and projected drier conditions threaten its ability to meet rising water demands. The Flumendosa reservoir system, with its extensive hydrological database and crucial role in supplying both agricultural and urban areas, serves as an ideal case study for evaluating past climate impacts and predicting future water resource scenarios.

To address these challenges, this study integrates a distributed ecohydrological model, a water resource management optimization model (WARGI), and IPCC climate projections to predict future water availability and use, as well as to assess the impact of land cover change strategies on water resource sustainability.

4.1 Future scenarios

4.1.1 IPCC Furture Projection

For future climate scenarios, the IPCC scenarios in the Fifth Assessment and Sixth Assessment report, focusing on the Atmosphere–Ocean General Circulation Models (AOGCMs) of Flato et al. (2013); CMIP5 (2013); Swart et al. (2019b); Service (2022).

Global Climate Models (GCMs) are advanced computational tools used to simulate the Earth's climate system. Based on the equations of fluid dynamics and the physics of the atmosphere, oceans, and land surface, GCMs allow for the analysis of interactions between different climate components, including greenhouse gas emissions and aerosols. These models are employed to study past, present, and future climate variations, contributing to projections of climate change on a global scale. The utility of GCMs is crucial for understanding climate dynamics and supporting political and economic decisions in areas such as water resource management, agriculture, and urban planning. Thanks to these models, it is possible to assess the impacts of global warming and develop adaptation and mitigation strategies. However, GCMs operate at a relatively low spatial resolution, typically on the order of hundreds of kilometers, which limits their applicability at the local level.

To overcome this limitation, spatial downscaling techniques are used, which allow for obtaining high-resolution climate data on a regional or local scale. There are two main approaches to downscaling:

- Dynamic Downscaling: This involves using Regional Climate Models (RCMs) which, by incorporating detailed information on topography, land use, and local atmospheric processes, refine GCM data to produce more accurate simulations on a smaller scale, although not all GCMs are used as boundary conditions for RCMs.;

- Statistical Downscaling: This is based on statistical relationships between the low-resolution data of GCMs and local climate variables. This method uses regression techniques and other statistical analyses to predict future climate conditions on a local scale.

Both approaches have advantages and limitations, but their combined use allows for obtaining more detailed and reliable climate forecasts, which are fundamental for addressing the challenges related to climate change.

The Multivariate Bias Correction - N (MBCn) proposed by Cannon (2018) is an advanced method for adjusting biases in climate model simulations, ensuring that not only individual variables are corrected but also that their relationships remain consistent with observed data. The process begins with a univariate correction using the Quantile Mapping method, which aligns the distribution of simulated variables with that of observed data. Next, all variables are standardized to have zero mean and unit standard deviation, making it easier to handle their interdependencies. At this point, a transformation based on orthogonal rotation of principal components is applied, allowing the correction of the correlation structure between variables without altering their individual distributions. After this phase, the data are transformed back to their original values by reversing the standardization. The entire process is iterated until both the distribution of variables and their interdependence align with real-world data. This method is particularly useful in applications such as hydrological modeling, agriculture, and energy, where maintaining coherence between temperature, precipitation, and other climate variables is crucial for obtaining reliable local-scale predictions.

GCMs for future scenarios has been selected scenarios after comparing the model outputs of air temperature and precipitation with the observed data in two case studies and then downscaled using the multivariate bias correction. Due to the fact that the GCMs have a low resolution, in those models it rains almost every day in opposite of what happened in observed data, to homogenize the rainfall series so that they have the same number of dry days, as Ahmed et al. (2013) suggest, before applying the bias correction,all the rainfall value of the GCMs lower then a threshold has been set to 0; this threshold is defined as the precipitation that in the GCMs has the same Probability P_0 of the 0 value in the observed data, see Figure 4.1 .

After that the multivariate bias correction was applied to the set of data, using a random sample of the 70% of the data as calibration period and the remain 30% as validation sample, an example of the result of the procedure is shown in Figure 4.2.

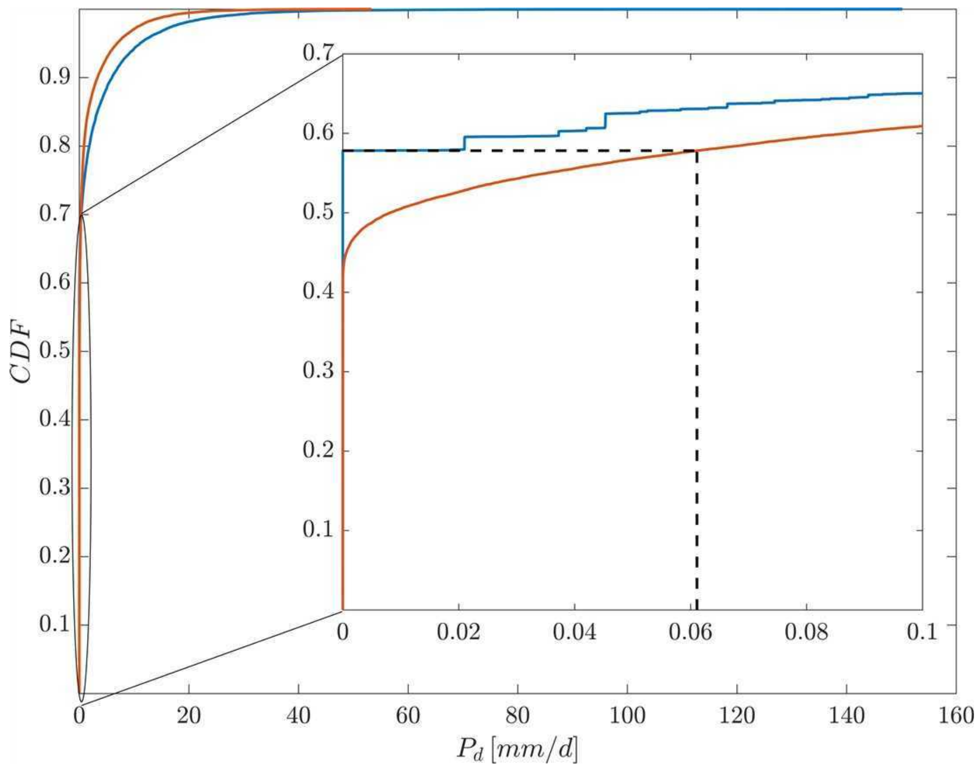

Figure 4.1: Example of the definition of the threshold precipitation value: the observed rainfall is plotted in blue line, the orange line represent the precipitation provided by the GCM for the cell where the rain-gauge is located. The child axes are a zoom of the CDF function presented in the parent plot. The horizontal black dashed line marks the P_0 and the vertical one marks the rainfall threshold value.

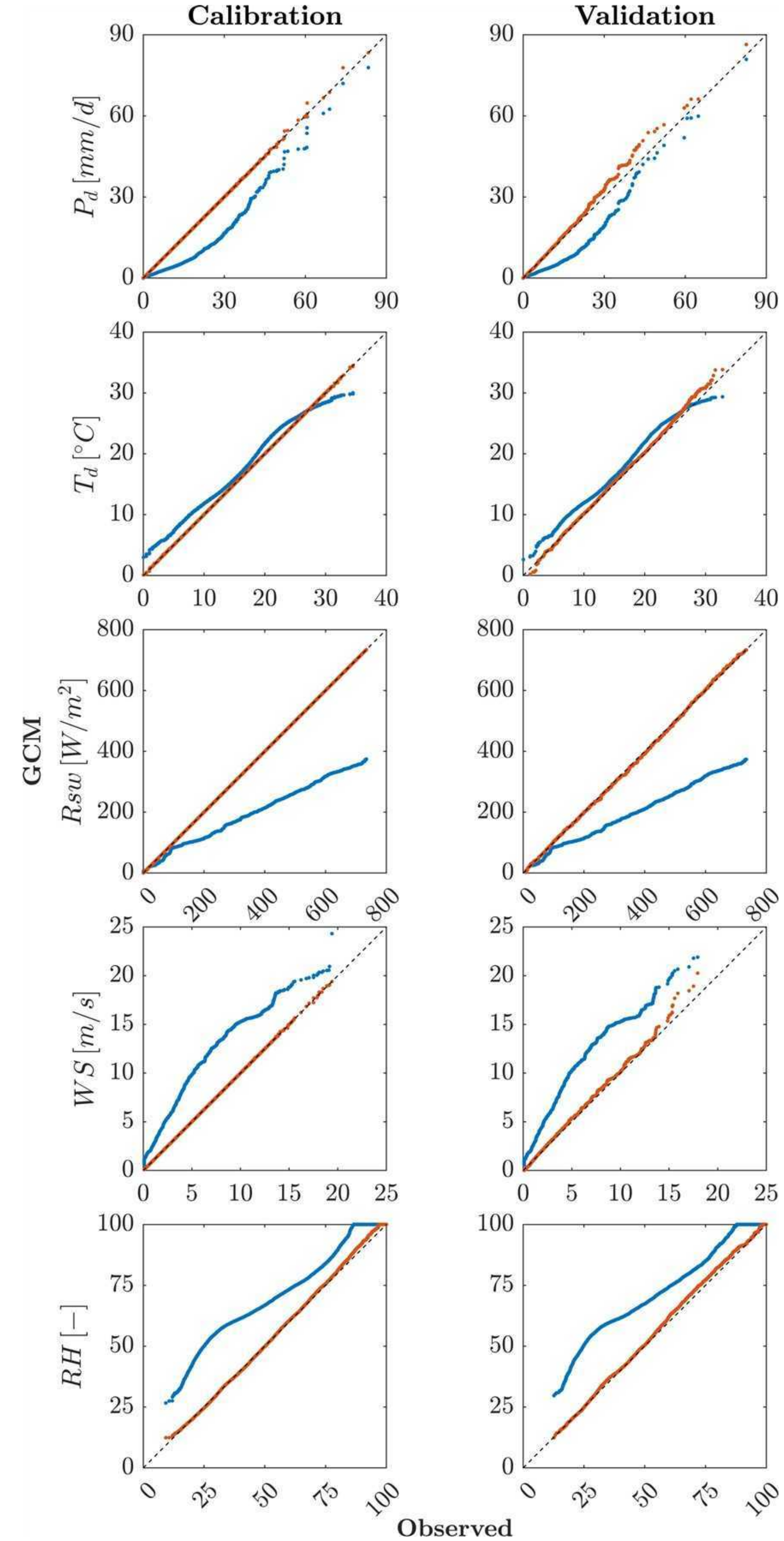

Figure 4.2: Example of the application of the MBC to a GCM to downscale data at higher resolution:in each plot the blue dots represent the QQ plot of the variable before the downscaling, the orange dots are the results of the downscaling procedure and the black dashed line is the 1:1 slope line.

4.1.2 Land Use scenarios

For investigating the impact of land cover change strategies (e.g., increase/decrease in tree cover distribution) on soil water and runoff in future climate scenarios, we developed two opposite land cover strategies: an afforestation process and a deforestation process. The afforestation was predicted in those land areas of the basin where, due to human activities, the forested areas were removed in the past, particularly in the plain areas. The impact of vegetation fraction variation on runoff was quantified by modifying the Curve Number (CN) as a function of the increase or decrease in vegetation cover. The variation in CN (ΔCN) was determined based on the morphological and hydrological characteristics of the basin, using reference maps of vegetation cover, hydrological soil classification, and CN values under intermediate moisture conditions (CN_{II}).

To estimate the relationship between vegetation fraction and CN, the vegetation cover was categorized into intervals with an increment of 10% for each hydrological soil class (e. Subsequently, the average CN value was calculated for each category, and a regression line was obtained by interpolating these values. The slope of the regression line, expressed as $\Delta CN/\Delta f_{wv}$, represents the increase in CN per unit variation of vegetation fraction, thus providing a quantitative measure of the effect of vegetation cover on the hydrological response of the basin.

4.1.3 Water resources management model

WARGI is a Decision Support System that was developed by Sechi et al. (2013, 2004); Sechi and Sulis (2009) to provide a tool to analyze the behavior and performance of a complex water resource system. It was developed to manage the requirements of multi-reservoir systems under water scarcity conditions, as frequently occur in Mediterranean regions (Sulis and Sechi, 2013; Sechi and Zucca, 2014). Water allocation in the WARGI is retrieved via user-defined preferences for supply sources and priorities for demand centers; the water flows in the system are evaluated by considering an optimal path search procedure. Additionally, the user can define reserved storage in reservoirs, the withdrawal of water from which is managed to satisfy user-selected higher-priority demands. The water resource system can be viewed as a physical network where the nodes and arcs are as follows:

- Reservoir nodes: These represent surface water resources with storage capacity. In these nodes, losses by evaporation can be considered.

- Demand nodes: These nodes represent water demand for irrigation, civil, and industrial purposes, among others.

- Hydroelectric nodes: These are non-consumptive nodes associated with hydroelectric units.

- Confluence nodes: These include river confluences, withdrawal connections for demand satisfaction, etc.

- Aquifer nodes: These nodes represent groundwater resources with storage capacity.
- Natural stream arcs: These represent the natural runoff along rivers or river beds.
- Conveyance work arcs: These are artificial channels, such as ditches, pipes, etc.
- Water pumping facility arcs: These are arcs with a pumping plant.
- Emergency transfer arcs: These arcs allow water transfers to alleviate shortages.
- Recharge facility arcs: These allow the direct injection of surface water from a connection node into an aquifer.

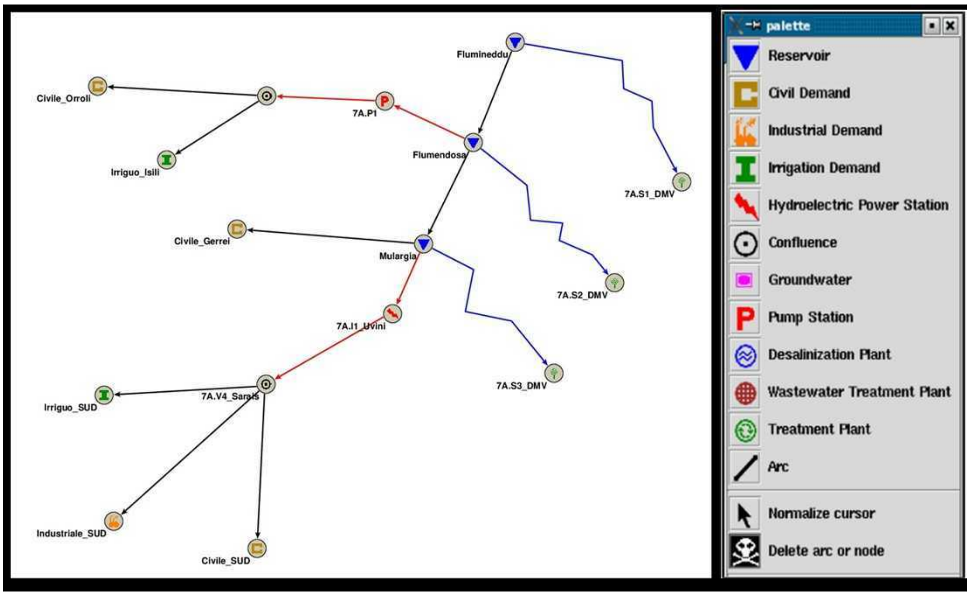

Figure 4.3: Example of graph in WARGI with the feature for graph creation

Some of the operational management issues to consider in the problem can be easily modeled using graph structures as follows:

- Priorities in the stored water level of reservoirs.
- Priorities in demand satisfaction of demand nodes.
- Penalty on shortage and emergency transfers.
- Water quality aspects related to storage conditions.

.

4.2 Future climate change impact in Maganai Forest and Fluminimaggiore Basin

Selection of Climate Models and Downscaling Approach

For future climate scenarios, the IPCC scenarios in the Fifth Assessment report has been considered, focusing on the Atmosphere–Ocean General Circulation Models (AOGCMs) of Flato et al. (2013). Following Montaldo and Oren (2018), data from the 9 AOGCMs that simulate all the variables that can be used as model inputs (CMCC-CMS, CNRM-CM5, GFDL-ESM2G, HadCM3, HadGEM2-CC, HadGEM2-ES, HadGEM2-AO, NorESM1-M, NorESM1-ME), then predictions for the past period (1951-1975 vs 1976-2000) for mean annual precipitation and temperature have been calculated and compared to the observed climate in the Fluminimaggiore basin (see Figure 4.4).

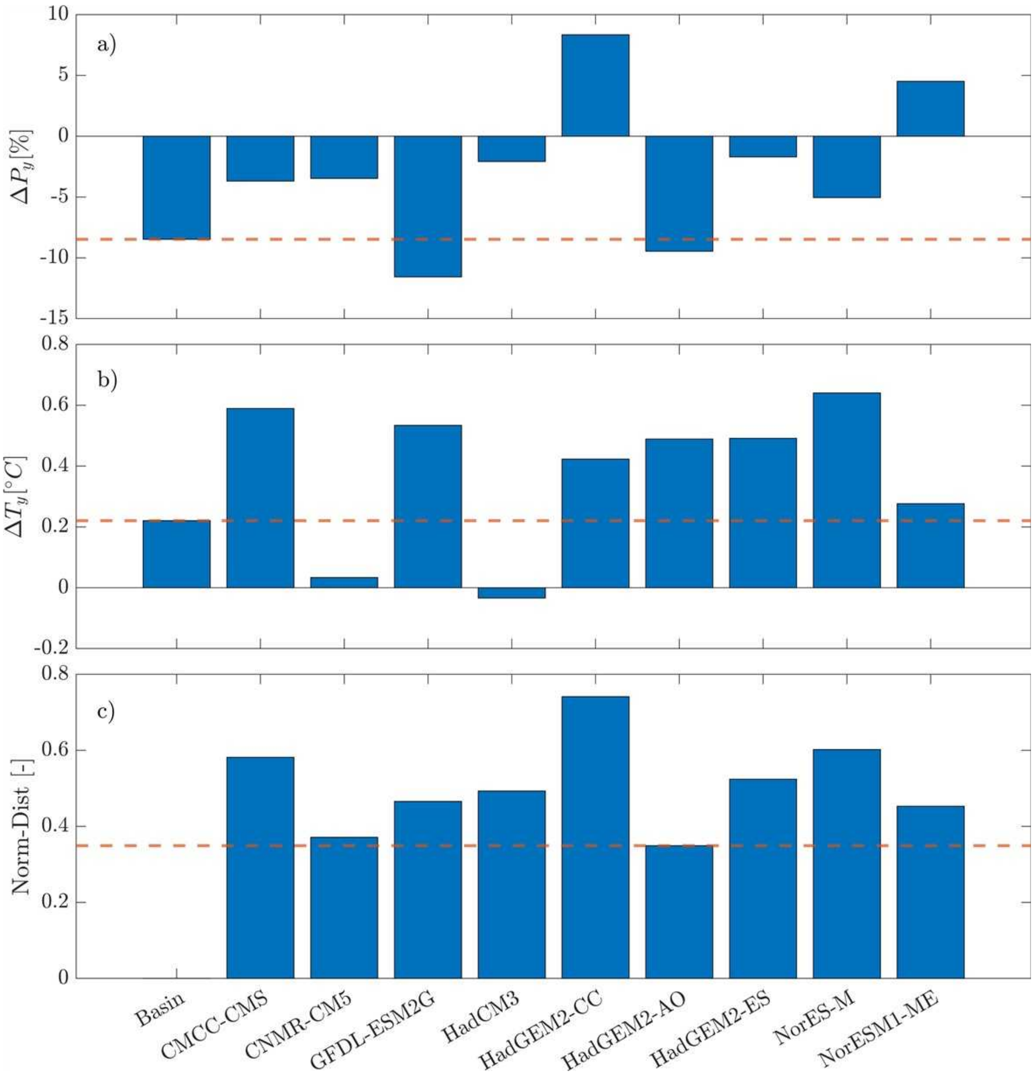

Figure 4.4: Comparison of climate model outputs. a) Changes in mean annual precipitation (ΔP_y) for the period 1976–2000 relative to 1951–1975; b) changes in mean annual temperature (ΔT_y) for the period 1976–2000 relative to 1951–1975; c) normalized distance metric $Norm - Dist$, computed as the mean of the normalized absolute differences between precipitation and temperature changes with respect to the basin-scale reference.

The model HadGEM2-AO has been selected because it predicted better than the others the observed past changes of precipitation and air temperature. The HadGEM2-AO model was able to capture past climate changes, with differences in predicted changes of winter precipitation of less than 2% of the observed changes (less than 4% for yearly data), and with low differences (˜$0.1°C$) in yearly changes of air temperature.

Future climate scenarios are generated up to 2100 for the Fluminimaggiore basin from HadGEM2-AO predictions through the multivariate bias correction technique (Cannon, 2018), downscaling data from a spatial resolution of 1.25° latitude and 1.87° longitude (~150 km) to the basin spatial scale. The reference period is from 1950 to 2005 due to the availability of solar radiation and wind speed data in the GCM timeseries. The stations with land-observed data are in Figure 3.3, and basin areal averages are computed using the Thiessen method. The temporal resolution of the HadGEM2-AO predictions is the same as the model time step (daily). Four representative concentration pathways (RCP) of HadGEM2-AO are considered (RCP 26, RCP 45, RCP 6, RCP 85).

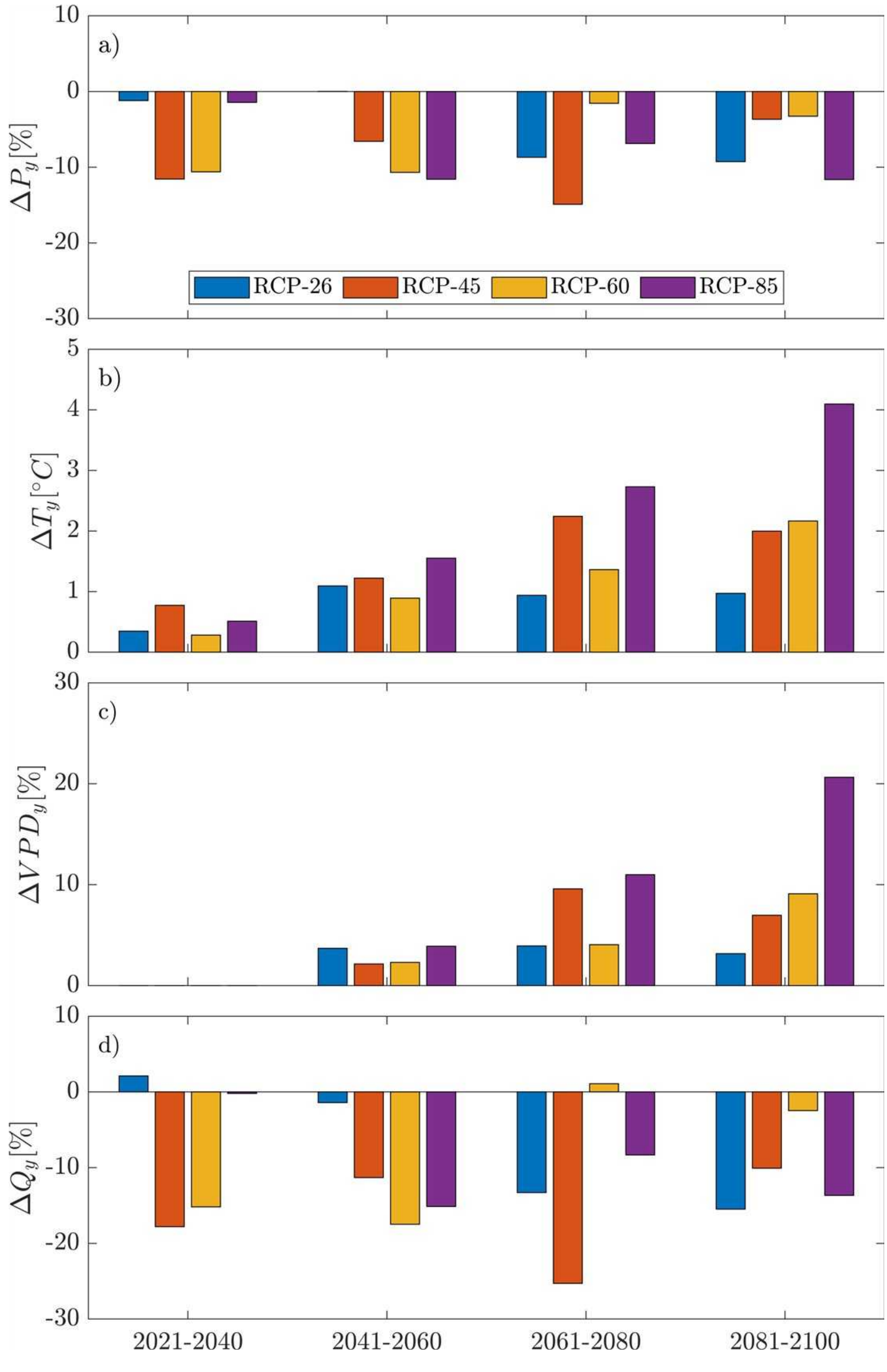

Figure 4.5: . In the Rio Fluminimaggiore basin, mean predicted changes in the future with respect to the historical 2000-2020 period of: a) annual precipitation (ΔP_y), b) annual air temperature (ΔT_y), c) annual vapor pressure deficit (ΔVPD_y) and d) annual runoff (ΔQ_y).

Future projection

Future scenarios of HadGEM2-AO predicted a decrease in annual precipitation for all the representative concentration pathways, reaching a decrease of 14% for the 2061-2080 period and RCP 45, and 12% for the farther scenario (2081-2100) and the worst RCP 85 (Figure 4.5 a) when compared with the recent 2000-2020 period. Annual air temperature is predicted to increase in future scenarios by up to 4 °C in RCP 85 and the 2081-2100 period (Figure 4.5 b), impacting VPD, which is predicted to increase starting from 2041, by up to 20% in RCP 85 and in the 2081-2100 period (Figure 4.5 c). Using the calibrated distributed ecohydrological model, the yearly runoff is predicted to further decrease in the future for most of the scenarios, mainly amplifying the rain changes (Figure 4.5 d), and reaching the highest decrease of 26% for the RCP 45 configuration and the 2061-2080 period. The warmer future scenarios (2022-2100) impacted the evapotranspiration, the trend of which is predicted to remain negative in the future, although not significantly ($\tau = -0.03$, $p = 0.68$, $\beta = -0.04mm/year$; Figure 4.6 a), and even more so for tree transpiration, the decrease of which is predicted to be higher and significant in the future ($\tau = -0.22$, $p = 0.004$, $\beta = -0.23mm/year$; Figure 4.6 b). The most alarming decreasing trend is for tree LAI ($\tau = -0.62$, $p < 0.001$, $\beta = -0.01mm/year$; Figure 4.6 c), for which the average reduction is predicted to be 31% at the end of the predicted period when compared to its value at the start of the investigated period (Figure 4.6c).

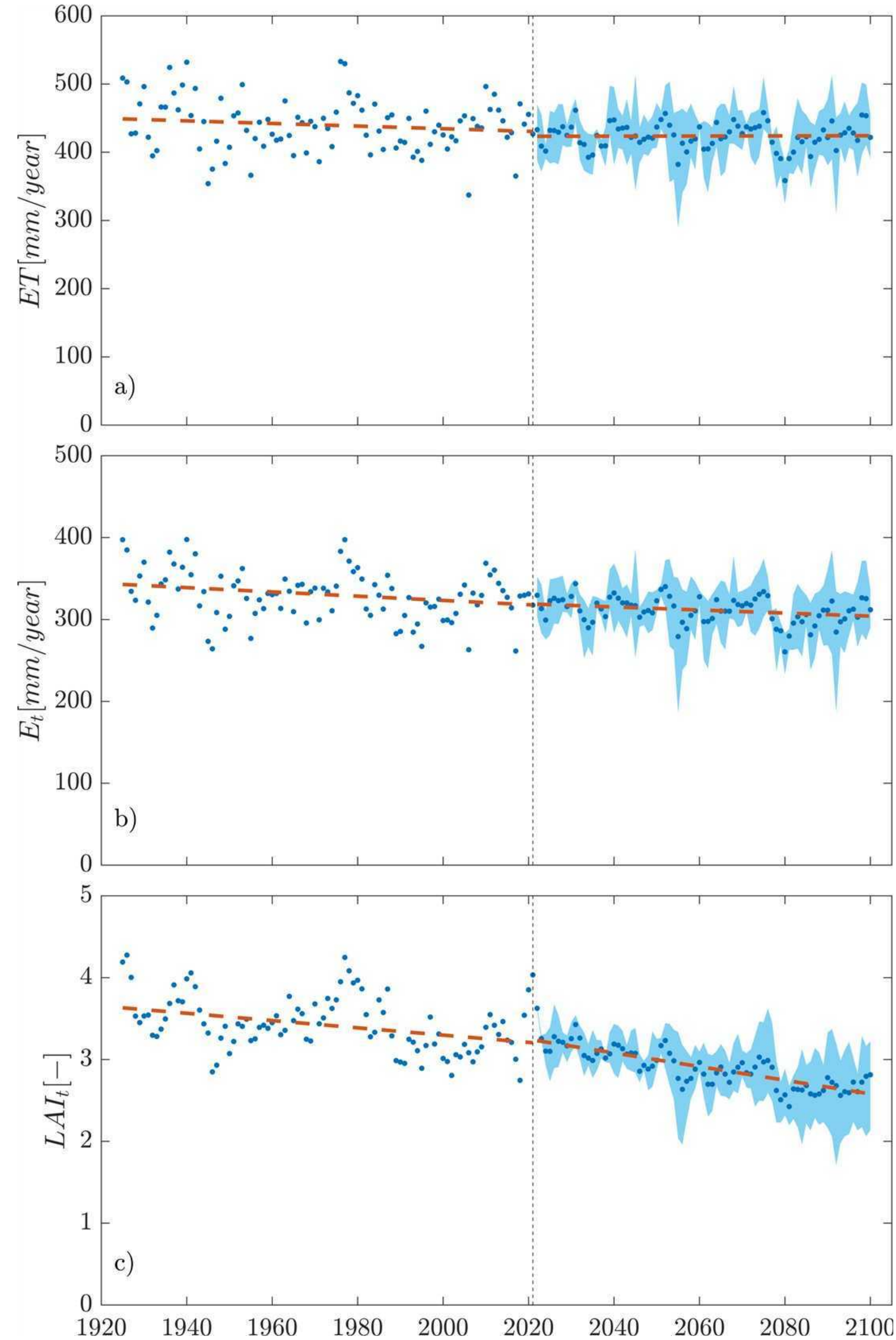

Figure 4.6: a) Evapotranspiration (ET); b) tree transpiration (E_t); and c) tree LAI (LAI_t) predictions using the meteorological observations of the Sardinian meteorological network (up to 2021), and the future climate scenarios of the HadGEM2-AO model (up to 2100). The slopes of the trend lines (orange dashed) are estimated by the Theil-Sen method. For the future period, blue dots represent the mean of the four representative concentration pathways (RCP 26, RCP 45, RCP 60, RCP 85), and the shaded light blue areas around the mean bound the minimum and maximum values of the scenarios.

The decrease in tree LAI is related more to the rise in air temperature (by 89%) than to the decline in precipitation, due to the impact of air temperature on VPD, which is a main climate control of the vegetation growth in these Mediterranean ecosystems (Yuan et al., 2019; Park Williams et al., 2013b), to test this effects, two simulation has run alternating a timeseries of precipitation and temperature generated with a stochastic weather generator using the statistics of the observed data (Figure 4.7).

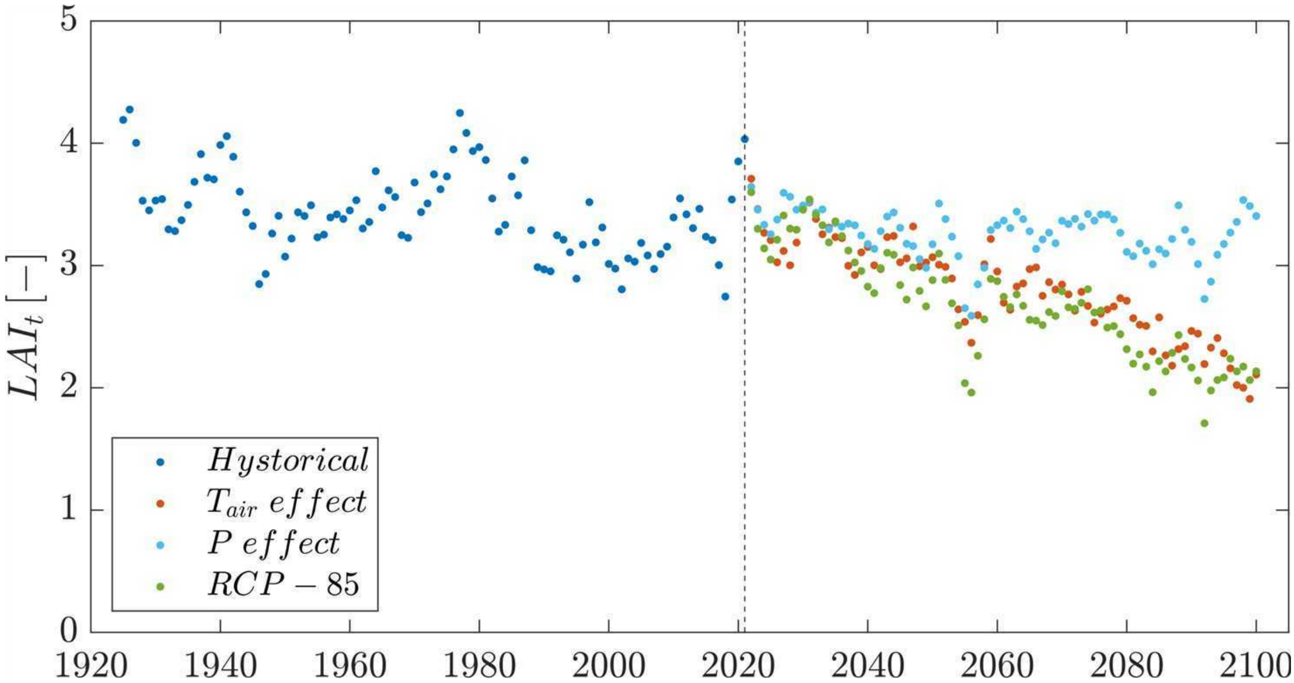

Figure 4.7: Annual mean LAI_t simulated under different climatic conditions. The dark blue points represent the simulation based on observed atmospheric variables. The green points show the results for simulation under an RCP 8.5 climate change scenario characterized by increasing temperatures and decreasing precipitation. The orange points correspond to the simulation where the scenario precipitation series was replaced with a stochastically generated series that preserves the statistical properties of past observed precipitation. Finally, the light blue points represent the simulation in which the scenario temperature series was replaced with a stochastic series maintaining the statistical properties of past observed temperatures. The dashed line marks the transition between the historical period and future projections.

In Figure 4.8a), the comparison of the extreme analysis for the reference period 1950-2005 is illustrated, with observed data in blue and downscaled GCM data in orange. The cumulative distribution of the three time series has been fitted using a Generalized Extreme Value (GEV) distribution (the goodness of fit for the three distributions is listed in the Table 4.1). The $RMSE$ between the observed cumulative distribution and the downscaled GCM cumulative distribution is 1.914 mm, indicating that the $MBCn$ procedure effectively corrected even the extreme values. This is further confirmed in panel b), where the rainfall intensity-return periods of the observed and downscaled time series closely align. Panels c) and d) extend this analysis to the entire historical period (1924-2021) and the future scenario under RCP 8.5, based on the $HadGEM2 - AO$ climate model.

The results suggest that extreme rainfall events in the Fluminimaggiore basin could increase by up to 10%, as depicted in Figure 4.8d), and it will be characterized by less annual runoff but at the same time more extreme runoff events, as suggested by a frequency analysis of daily runoff extremes in Figure 4.9 (the statistics of the Kolmogorov–Smirnov and Chi-squared tests are in Table 4.1) with an increase of daily runoff up to 34% for return periods of 100 years for the future climate scenarios.

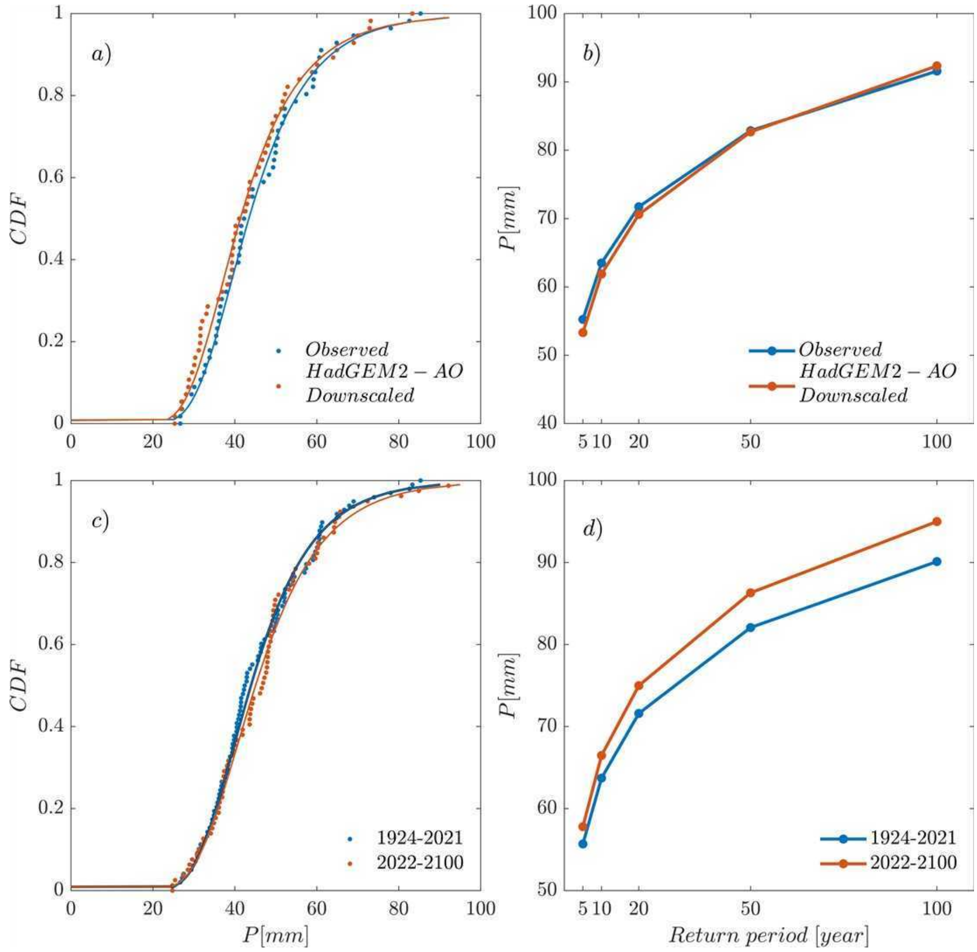

Figure 4.8: In the Rio Fluminimaggiore basin, the changes of daily precipitation extremes under climate change: a) cumulative distribution fitting estimated using the Generalized Extreme Event (GEV) for the downscaling references period (1950-2005); b) precipitation values corresponding to different return periods for the period 1950-2005 estimated using the GEV distribution; c) cumulative distribution fitting estimated using the GEV distribution fits to historical observed data (1924–2021), and future climate scenario predictions (2022–2100, using HAdGEM2-AO predictions under RCP 85 concentration pathway); d) precipitation values corresponding to different return periods for the historical observed data (1924-2021) and the RCP 85 future scenario (2022–2100).

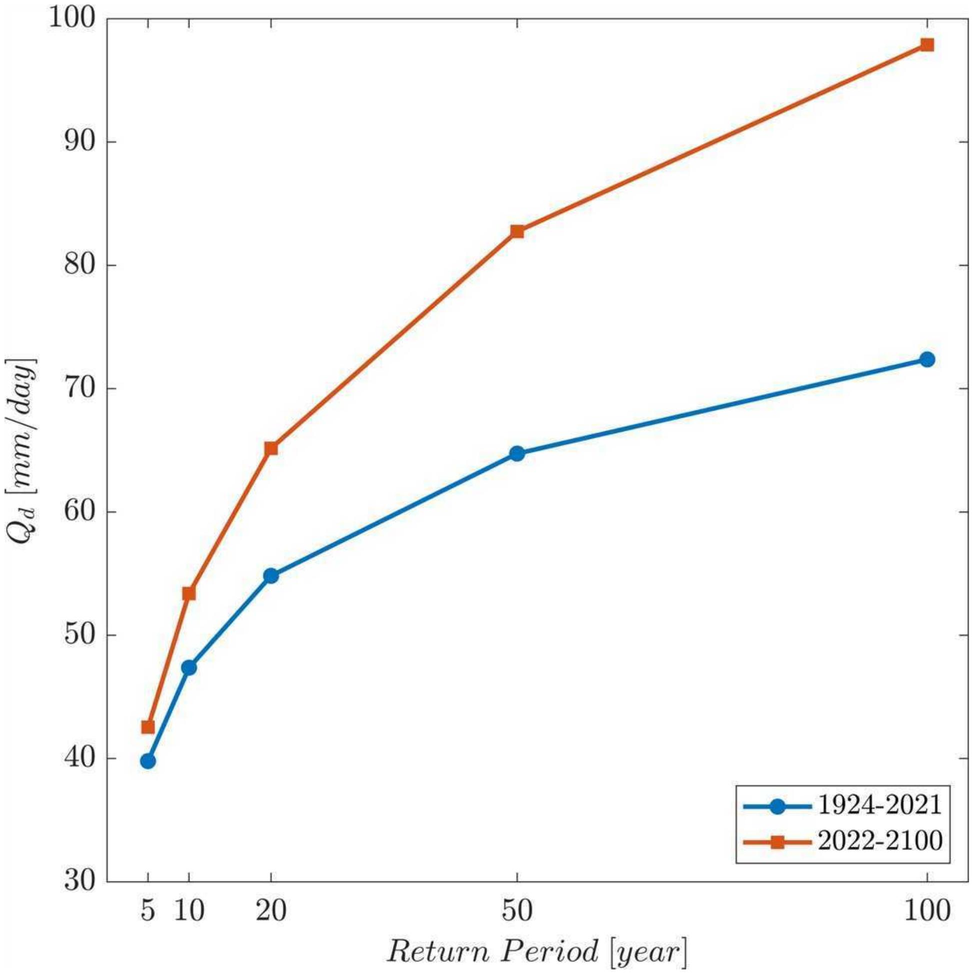

Figure 4.9: In the Rio Fluminimaggiore basin, the changes of daily runoff extremes under climate change: runoff values corresponding to different return periods estimated using the Generalized Extreme Event (GEV) distribution fits to historical observed data (1924–2021), and future climate scenario predictions (2022–2100, using $HAdGEM2 - AO$ predictions under RCP 85 concentration pathway.

		Period	Kolmogorov-Smirnov	χ^2
Precipitation	Observed	1950-2005	0.0703 (0.1782)	1.201 (11.070)
	GCM downscaled	1950-2005	0.0849 (0.1782)	1.009 (11.070)
	Observed	1924–2021	0.0622 (0.1354)	5.552 (14.67)
	Future Scenario (RCP 85)	2022–2100	0.0710 (0.1505)	6.590 (11.070)
Runoff	Observed	1924–2021	0.0721 (0.1354)	4.2951 (5.991)
	Future Scenario (RCP 85)	2022–2100	0.0783 (0.1505)	5.1175 (5.991)

Table 4.1: Results of the statistical tests (Chi-square and Kolmogorov-Smirnov tests) of the Generalized Extreme Value distribution fitting to the annual maximum daily precipitation and runoff time series of the Fluminimaggiore basin for the past (1950-2005 and 1924–2021) and the future climate scenario (2022–2100), predicted using HadGEM2-AO data in the RCP 85 configuration. Statistics of the Chi-square and Kolmogorov-Smirnov tests for normality, applied to the series, have 5% significance level.

Land Use Scenarios

In the context of climate change adaptation and mitigation strategies, different forest management scenarios were evaluated to assess their potential effects on ecosystem dynamics.

Considering the most critical climate scenario, an initial analysis explored the impact of modifying vegetation cover, either through a forced reduction or through afforestation interventions. Specifically, the fraction of vegetation, treated as a constant parameter within the model, was systematically varied by ±50% to examine its influence on ecosystem functioning.

A second approach focused on evaluating the potential effects of replacing *Quercus ilex* with alternative tree species exhibiting greater drought resistance. A review of the literature (Bartlett et al., 2016) identified species with enhanced physiological adaptations to water stress, including *Quercus garryana* and *Juniperus communis*, which are characteristic of temperate ecosystems such as the Mediterranean, and *Acacia greggii*, a species adapted to semi-arid and semi-desert environments that align more closely with the future climatic conditions projected for the Mediterranean under the selected IPCC scenario.

The results of the simulated LAT_t under these intervention scenarios are presented in the following figure.

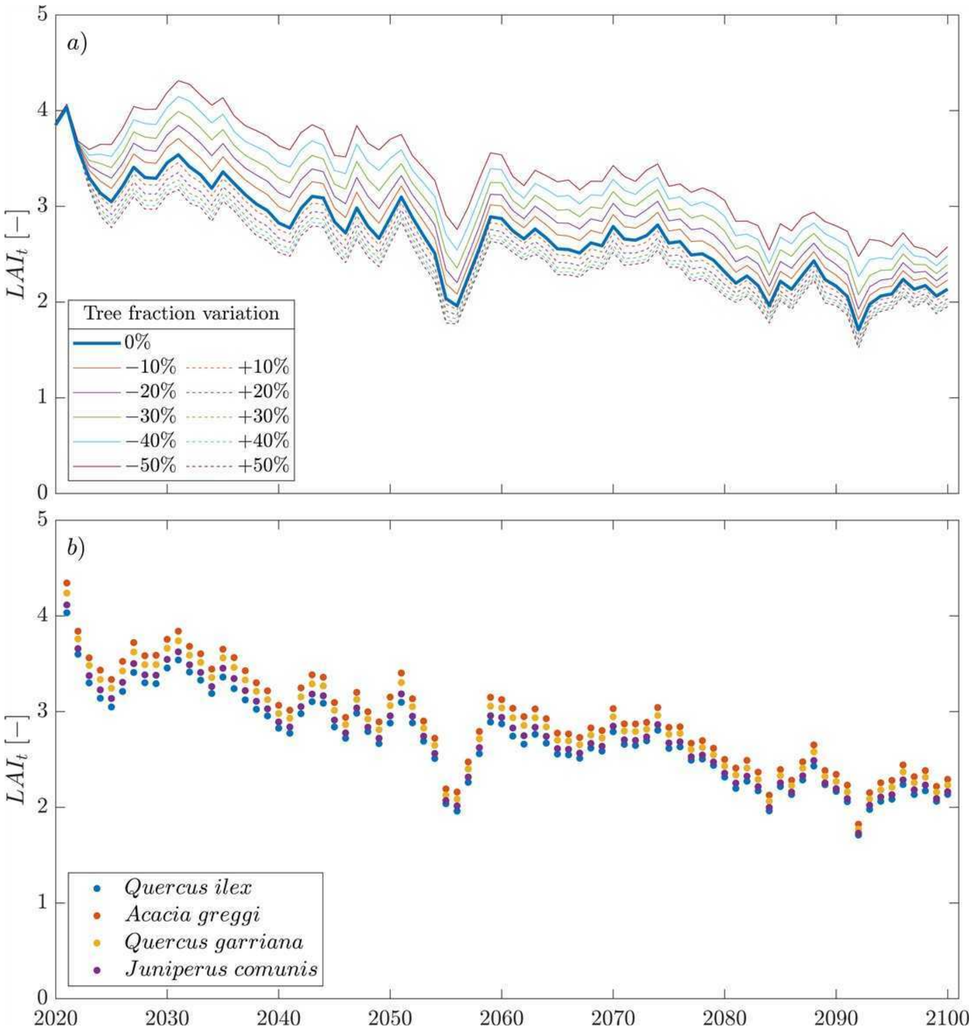

Figure 4.10: Land use scenarios: a) hypothesis of decreasing or increasing the tree cover; b) hypothesis of changing the vegetation species.

Figure 4.10 a) highlights that a reduction in vegetation cover leads to an increase in LAI, likely due to decreased competition for soil water resources among individual plants. In contrast, an increase in vegetation density results in a decrease in LAI, suggesting a stronger competition effect under limited water availability. Figure 4.10 b) illustrates the outcomes of species substitution, demonstrating that more drought-tolerant species would experience a less pronounced decline in LAI. Nevertheless, the substantial temperature increase projected in the selected scenario would still exert a significant influence on vegetation dynamics.

4.3 Future climate change impact in Flumendosa Basin

Selection of Climate Models and Downscaling Approach

For future climate scenarios, the IPCC scenarios in the Sixth Assessment report has been considered of Eyring et al. (2016); Service (2022). Historical time series of precipitation and air temperature from 17 Global Climate Models (GCMs) are tested comparing the mean annual variation of the two variables for the period 1983–2014 compared to the period 1950–1982. The model $MPI-ESM1-2-LR$ had been selected, which better represented the historical period (historical variation of the Flumendosa mean annual precipitation: $\Delta P_{y,Flumendosa} = -14.16\%$, $\Delta P_{y,MPI-ESM1-2-LR} = -8.70\%$, historical variation of the Flumendosa mean annual air temperature: $\Delta T_{y,Flumendosa} = +0.40°C$, $\Delta T_{y,MPI-ESM1-2-LR} = +0.36°C$), compared to other 16 GCMs (Figure 4.11), and provided complete datasets of precipitation, temperature, relative humidity, wind velocity, and incoming solar radiation. We considered two future scenarios of high emissions (MPI-ESM1-2-LR SSP3-RCP7.0, MPI-ESM1-2-LR SSP5-RCP8.5).

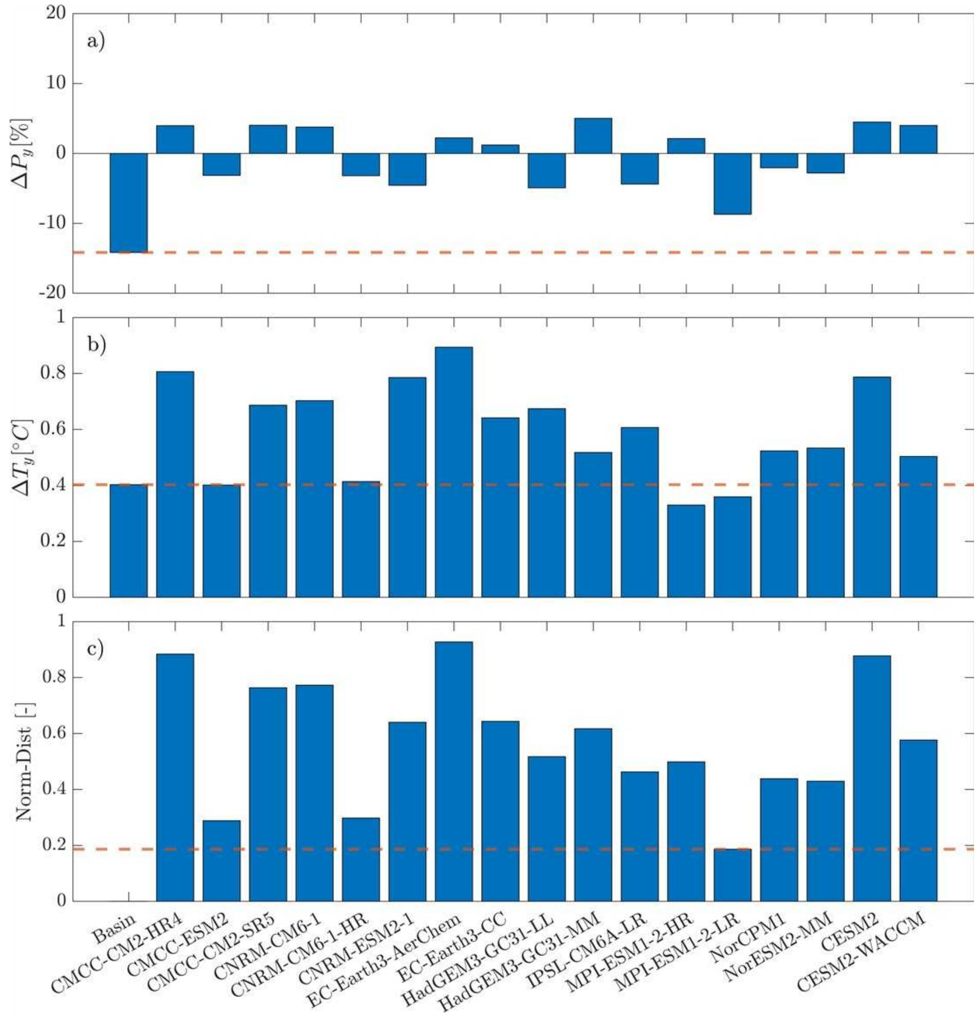

Figure 4.11: The comparison of 17 Global Climate Models (GCMs) historical predictions with the historical time series of yearly precipitation (P_y) and air temperature (T_y). The mean annual variation of the two variables for the period 1983-2014 are compared to the period 1950-1982.

Future projection

Future climate scenarios were generated for the Flumendosa basin up to the year 2100 from the GCM predictions through the multivariate bias correction technique (Cannon, 2018) using the series 1925 to 2014 as reference period. Future scenarios of MPI-ESM1-2R-LR predicted a decrease in annual precipitation for the representative concentration pathways SSP3-RCP7.0 and SSP5-RCP8.5, reaching a decrease of 17.62% for the SSP3-RCP7.0, and 14.10% for the SSP5-RCP8.5 for the period 2076–2100, when compared with the 2001–2025 period and an increase between ~1% and ~3% e 1(Figure 4.12a). For future scenarios in the 2076–2100 period, annual air temperature is predicted to increase by ~0.05 °C for the SSP1-RCP2.6, ~1.3 °C for the SSP2-RCP4.5, ~3 °C for the SSP3-RCP7.0 and ~3.7 °C for the SSP5-RCP8.5 (Figure 4.12b) and decrease by ~-0.47 °C for the SSP1-RCP1.9 scenario. Using the calibrated distributed ecohydrological model, the yearly runoff is predicted to further decrease in most future scenarios, mainly amplifying the rain changes (Figure 4.12c), reaching the highest decrease of 26% for the SSP3-RCP7.0 configuration in the 2076–2100 period, with a strong decrease in the number of dry days in the year, up to 13% for the SSP5-RCP8.5 and the 2076–2100 period (Figure 4.12). Combining the effects of the decreasing precipitation and the increasing temperature, the model also predicted a drastic decrease in carbon assimilation: up to ~-10% for the SSP3-RCP7.0 scenario and ~-17% for the SSP5-RCP8.5 scenario (for the period 2076–2100). LAI is also predicted to decrease (~-21% for the SSP3-RCP7.0 scenario and (~-30% for the SSP5-RCP8.5 scenario for the period 2076–2100). The predicted future conditions were similarly observed in other Mediterranean basins (García-Ruiz et al., 2011), a Turkish basin (Gorguner and Kavvas, 2020), and Sardinian basins (Sirigu and Montaldo, 2022; Pulighe et al., 2021). The soil water balance will be modified, with a decrease in infiltration (-8%), soil water content (-4% in the sublayer), and evapotranspiration (-7%). The runoff will further decrease by about 18% (up to 31% for the SSP3-RCP7.0 scenario and the 2076–2100 period) (Figure 4.12). Water resource planning needs to take these future conditions into account, which highlight a depletion of the basin's water resources that need to match the water demands in the future to maintain sustainability in the system. Two future scenarios of high emissions: SSP3-RCP7.0 and SSP5-RCP8.5, have been used to predict the behavior of the water resources management system.

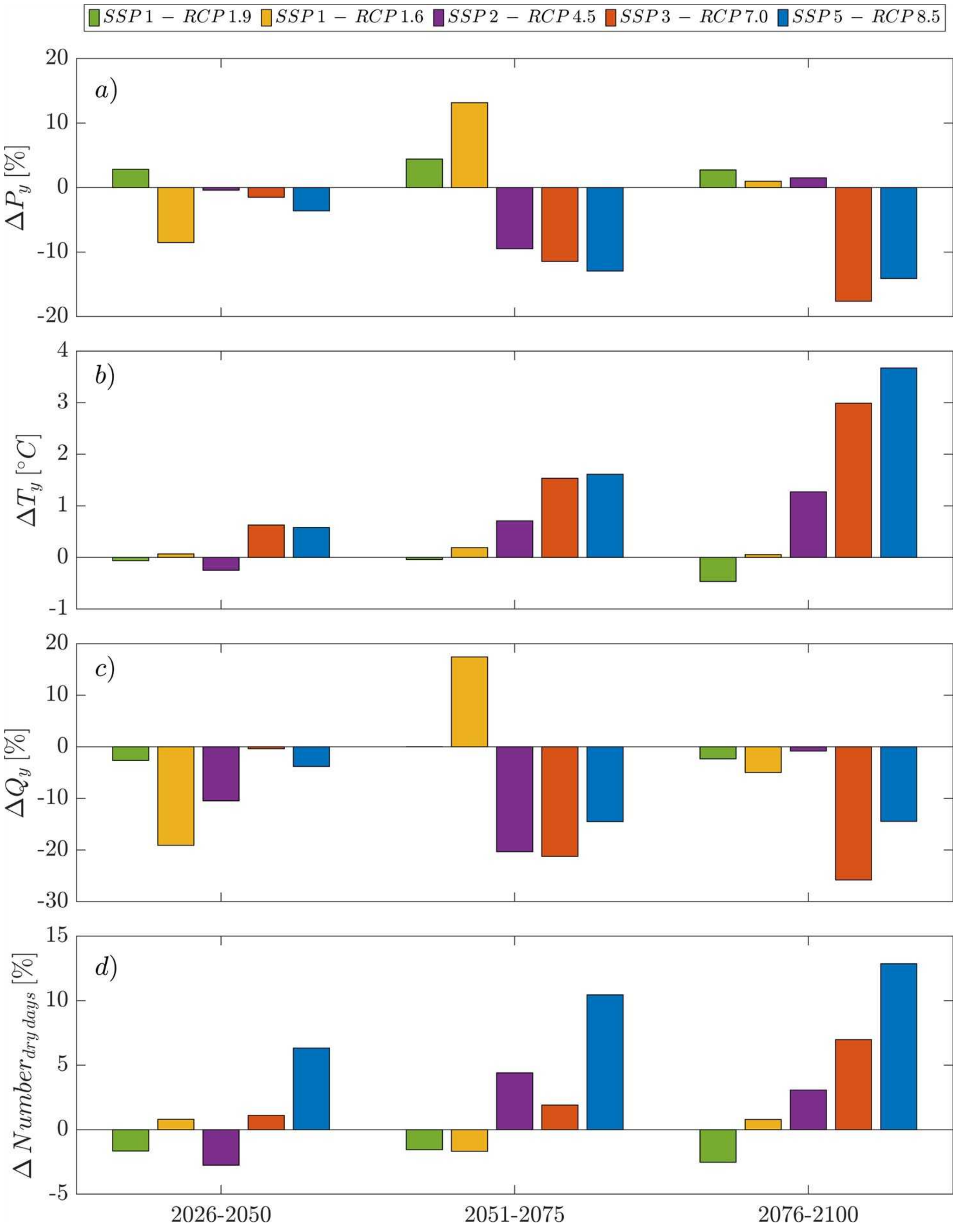

Figure 4.12: In the Flumendosa basin, mean predicted changes in the future with respect to the historical period of a) annual precipitation (ΔP_y); b) annual air temperature (ΔT_y); c) annual runoff (ΔQ_y); and d) number of dry days in the year ($\Delta Number_{dry\ days}$).

WARGI model of the Flumendosa basin

WARGI was applied to the Flumendosa water resources system, including 14 nodes, 13 arcs, 3 reservoirs, 4 demands (urban, industrial, irrigation, and environmental), and 2 confluences.

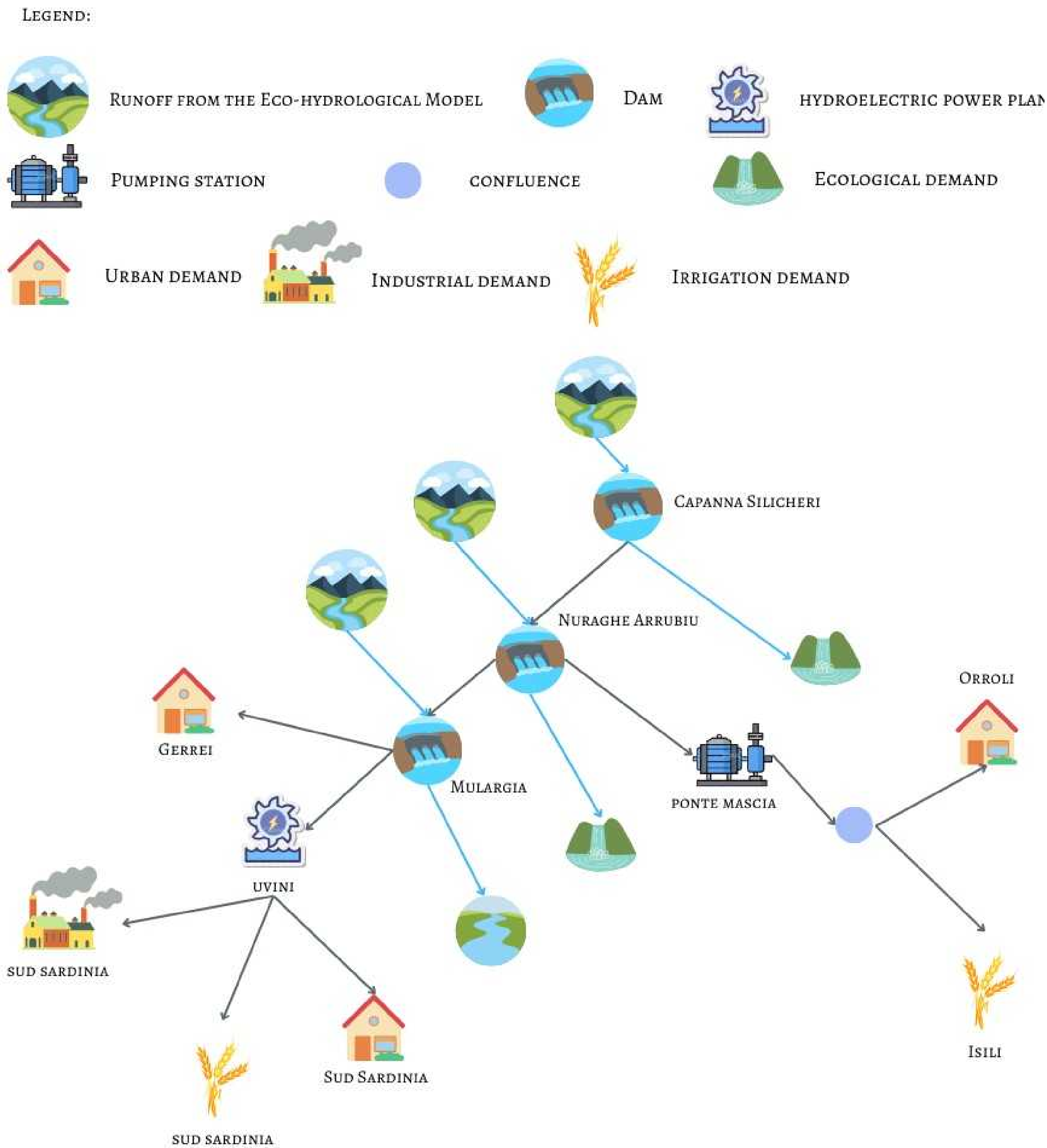

Figure 4.13: Graph for the Flumendosa water management system.

WARGI is the actual water resource management system of the Sardinian water resources authority (Sulis and Sechi, 2013). In the Flumendosa water resources system, the total annual demand is an average of ≈ 240 million cubic meters, with predominantly irrigation (48%) and civil uses (31%). In Table 4.2, the WARGI rules of priority for water use, in the case of water restrictions in the

Flumendosa reservoir system, are reported; first priority is given to civil demands, then industrial demands, which are, however, lower than civil and irrigation demands. These rules are the official rules for the Flumendosa water resources system, managed by the Sardinian water authority (ENAS), and have been preserved in our study.

Class	Civil	Industrial	Irrigation	Ecological
I	50			
II	30	80		
III	20	20	50	50
IV			50	
V				50

Table 4.2: The rules of priority classification of water uses in the Flumendosa reservoir system

Future Scenarios of the Water Resources System

Considering the potential socio-economic growth scenarios of Sardinia, mainly related to the growth of agricultural water usage, three future water use scenarios have been identified based on historical water demands (Table 4.3): scenario A ($242.1 \cdot 10^6 m^3$), which confirmed the mean water demands of the 2019–2021 period; scenario B ($279.6 \cdot 10^6 m^3$), which assumed a demand equal to the maximum annual water demands of the 2012–2021 period; and scenario C ($364.0 \cdot 10^6 m^3$), with further higher water demands. Irrigation demands are predominant and increased in all three scenarios (48% for scenario A, 49% for scenario B, and 61% for scenario C; Table 4.3).

Demand Scenario	Total Demand	Civil Demand				Industrial Demand	Irrigation Demand			Ecological Demand
		South Sardinia	Orroli	Gerrei	TOTAL Demand		South Sardinia	Isili	TOTAL Demand	
	$[Mm^3/y]$	$[Mm^3/y]$	$[Mm^3/y]$	$[Mm^3/y]$	$[Mm^3/y]$	$[Mm^3/y]$	$[Mm^3/y]$	$[Mm^3/y]$	$[Mm^3/y]$	$[Mm^3/y]$
A	242.1	73.1	0.5	0.9	74.5	12.2	115	1	116.2	
B	279.6	86.6	0.8	1	88.4	14.5	136.2	1	137.5	10% of the runoff
C	364	86.6	0.8	1	88.4	14.5	220.6	1	221.9	

Table 4.3: Yearly water demands of civil, industrial, irrigation, and ecological uses for water demand scenarios A, B, and C.

Water demands are highly seasonal, and they increase in summer months due to the increase in water usage required for irrigation and civil (including touristic) demands and the highest water demands coincide with the driest months of the year (Figure 3.14a),while industrial activities are not significantly growing in Sardinia and are not considered a beneficial development choice.

The WARGI model was set to predict the volume of water stored in the reservoir system on a monthly timescale to represent this seasonality, so monthly distributions of these water demands have been estimated from historical data and showed an increase in civil demands during summer months, a strong increase in the demand for irrigation during summer months (up to 22%), an almost constant industrial demand (average 9%) and an increase in ecological water demands in winter months (Figure 4.14).

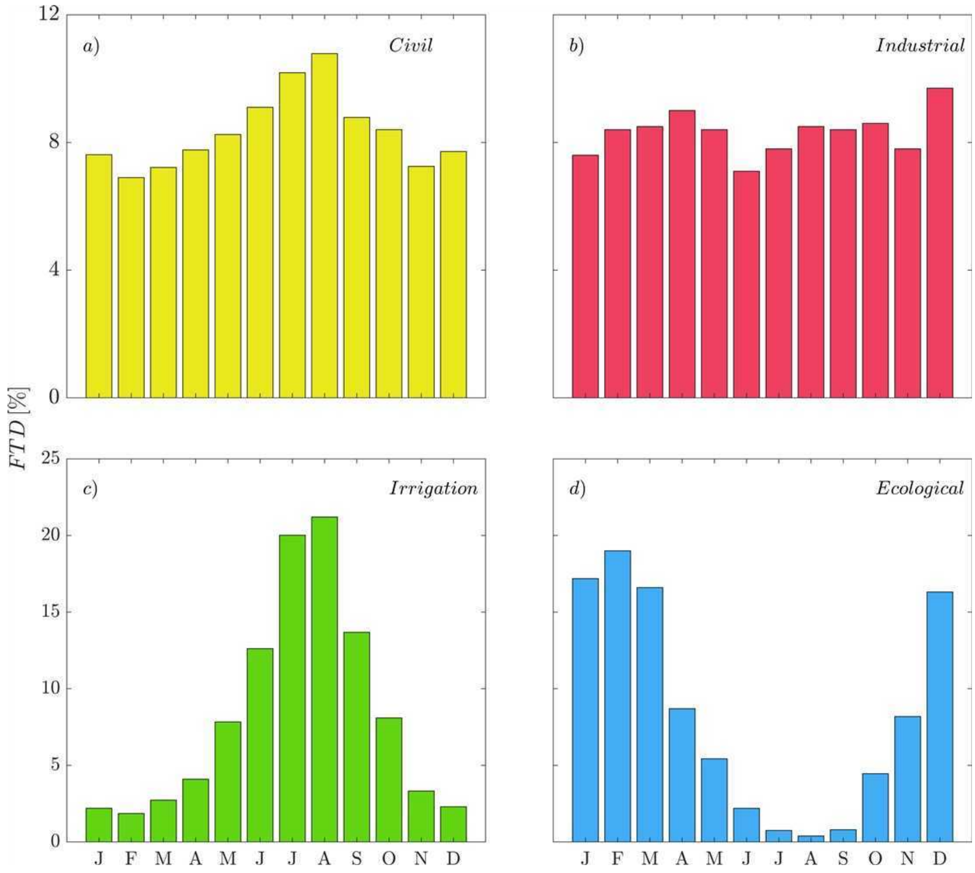

Figure 4.14: Mean monthly water demands in the Flumendosa dam system for civil, industrial, irrigation and ecological uses.

The WARGI model predicted the water volume stored in the reservoir system for the two future climate scenarios and used the three water demand scenarios (Figure 4.15). With the SSP3-RCP7.0 scenario, the reservoir volume decreased below the reserved volume for civil and industrial demands over several years, which means that irrigation demands could not be satisfied in those months, especially for irrigation scenario C. The number of years of irrigation deficit increases when the SSP5-RCP8.5 scenario is considered, with extremely low values of stored volume at the end of the 21st century, reaching the strategic volume of the dam system for scenario C. This means that, in that dramatic year, domestic water demands will not be satisfied (Figure 4.15).

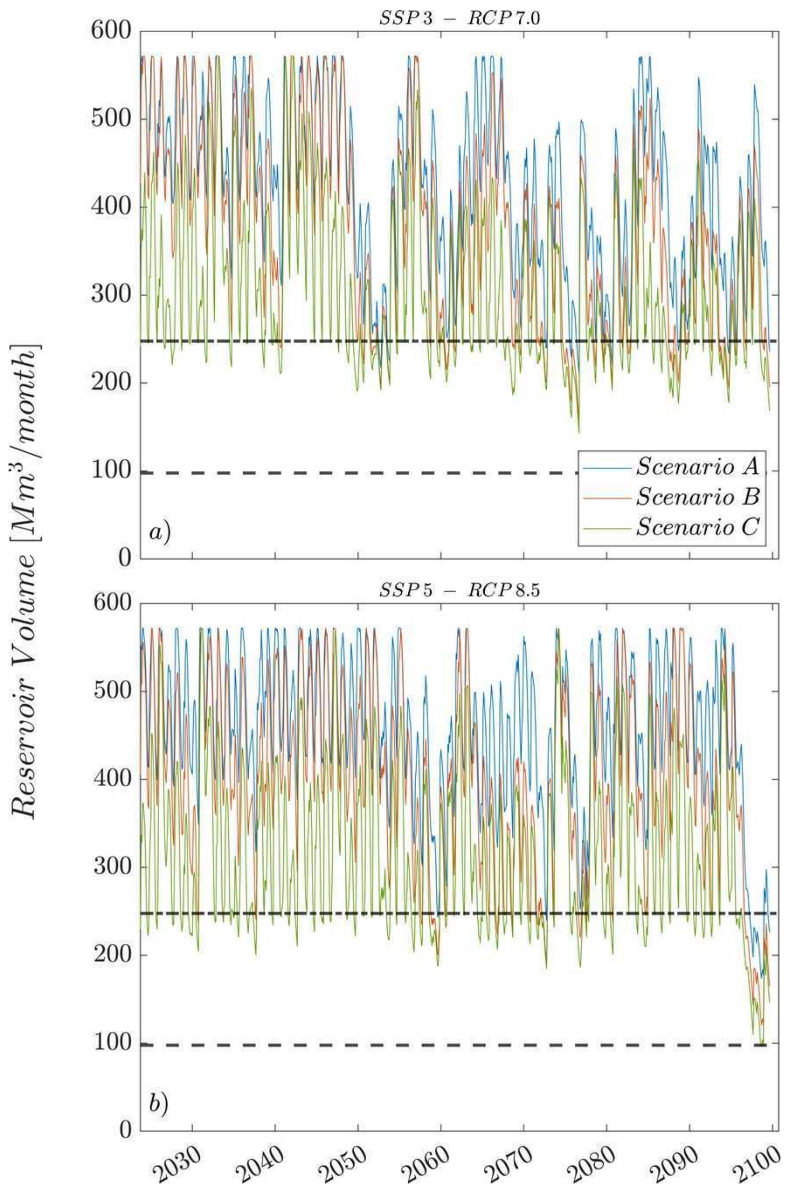

Figure 4.15: WARGI model predictions of the water volume stored in the reservoir system using the three water demand scenarios for the a) SSP3-RCP 7.0 future emission scenario and b) SSP5-RCP 8.5 future emission scenario. Dash-dot lines indicate the reserved water volume for civil and industrial water demands, and the dashed lines indicate the strategic water volume that cannot be reached.

Figure 4.16 summarizes the results, distinguishing the number of years of deficit and the mean deficit for each water demand use for the two future scenarios. Irrigation water demands are often not satisfied, up to 74% of years of deficit for the SSP5-RCP8.5 scenario C and up to 26% for the scenarios SSP3-RCP7.0 scanrio B,and the ecological water demands (the minimum water flow) even less so (Figure 4.16).

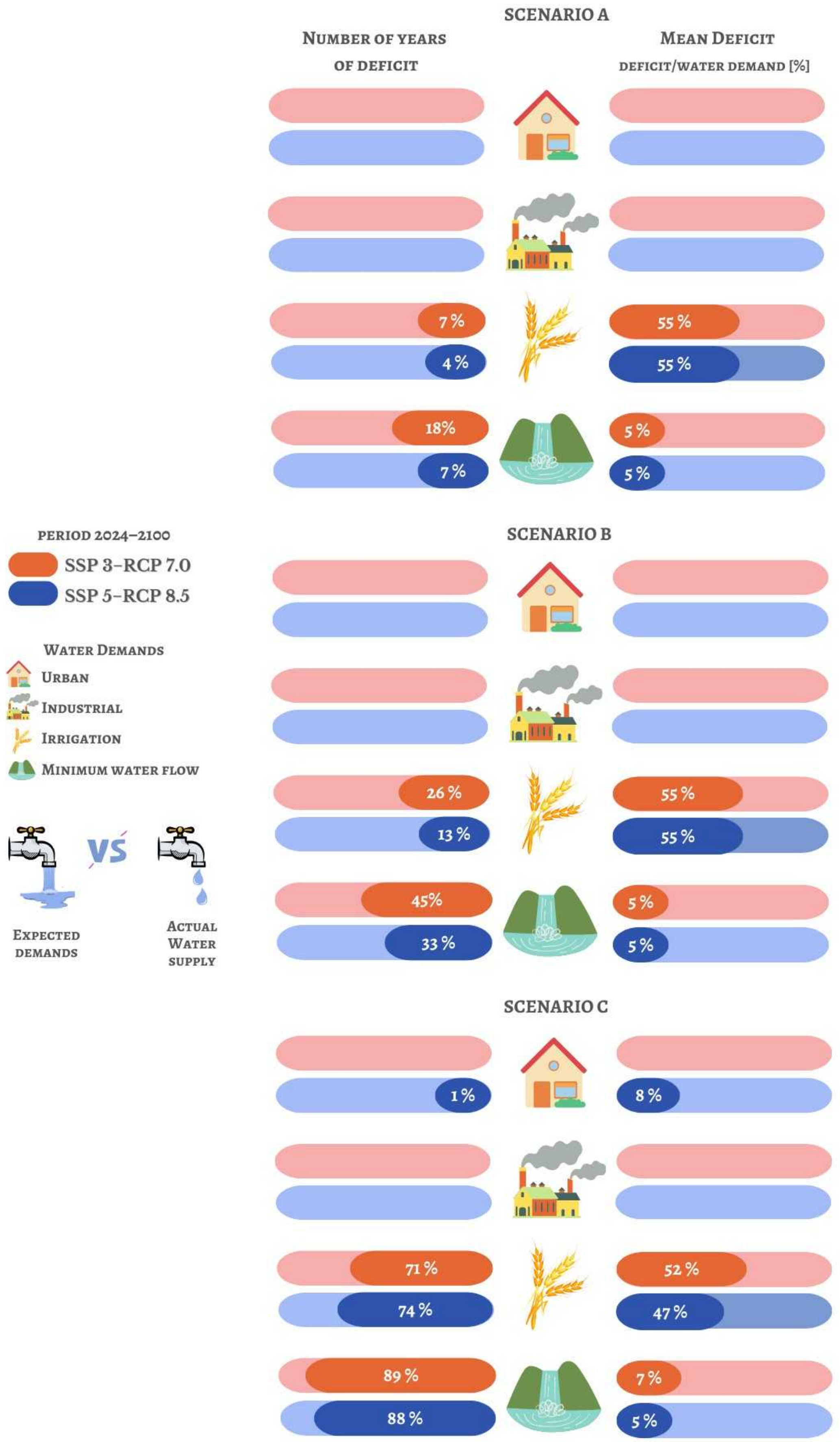

Figure 4.16: . The predicted water deficit for urban, industrial, irrigation, and ecological demands under future emissions scenarios (SSP3-RCP7.0 and SSP5-RCP8.5)(Table 4.3). Note that a year of deficit is when the water demand is not satisfied for more than 15%.

Land Cover Scenarios

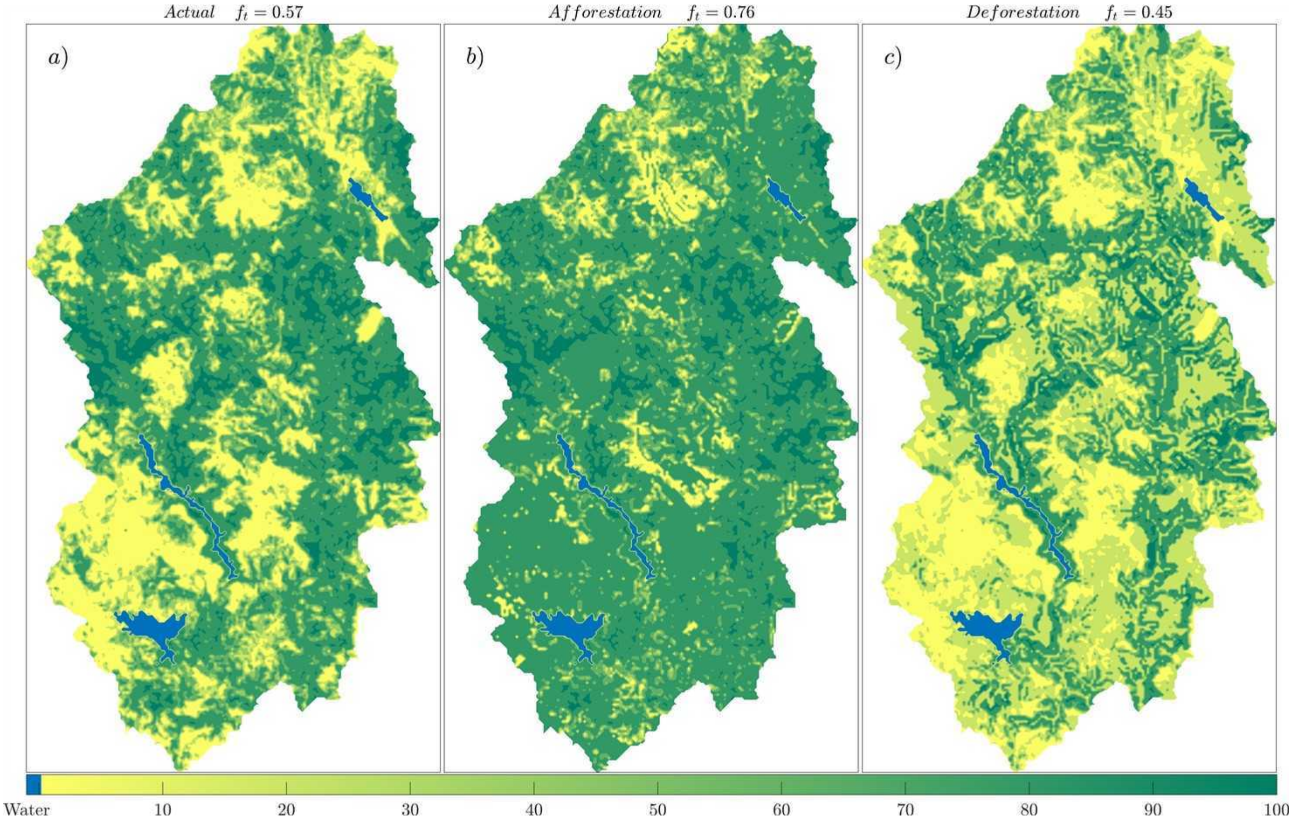

Figure 4.17: Land cover change scenarios: maps of the fraction of tree vegetation for the: a) actual basin state; b) afforestation scenario; and c) deforestation scenario. The fraction of tree cover (f_t) is reported for each map.

Two land cover strategies, afforestation and deforestation investigated, has been investigated (see Figure 4.17) and for the two future emission scenarios under water demand scenario C (Figure 4.18). The afforestation and deforestation land cover strategies increased and decreased the fraction of tree cover of the basin by 33% and 21%,respectively. It is evaluated the variation of the runoff for the three future reference periods (2026–2050, 2051–2075, and 2076–2100) and the two future emission scenarios characterized by a decrease in mean annual wetness conditions, estimating a decrease in runoff with decreasing wetness conditions for the actual cover conditions (Figure 4.18a). Runoff increased for the future scenarios with basin deforestation, while afforestation activity brought a further decrease in runoff, up to 31% for the SSP5-RCP8.5, SSP3-RCP7.0 scenario in the period 2076–2100 (Figure 4.18a). In contrast, the afforestation will produce a lower decrease in carbon assimilation despite the predicted drier conditions of both future scenarios. During deforestation, the decrease in carbon assimilation will be much higher, up to 40% for the SSP5-RCP8.5 scenario in the period 2076–2100 (Figure 4.18b). With the deforestation case, WARGI predicted a decrease in the number of deficit years for irrigation, in contrast with the increase in the number of deficit years for irrigation for the afforestation case (Figure 4.18c).

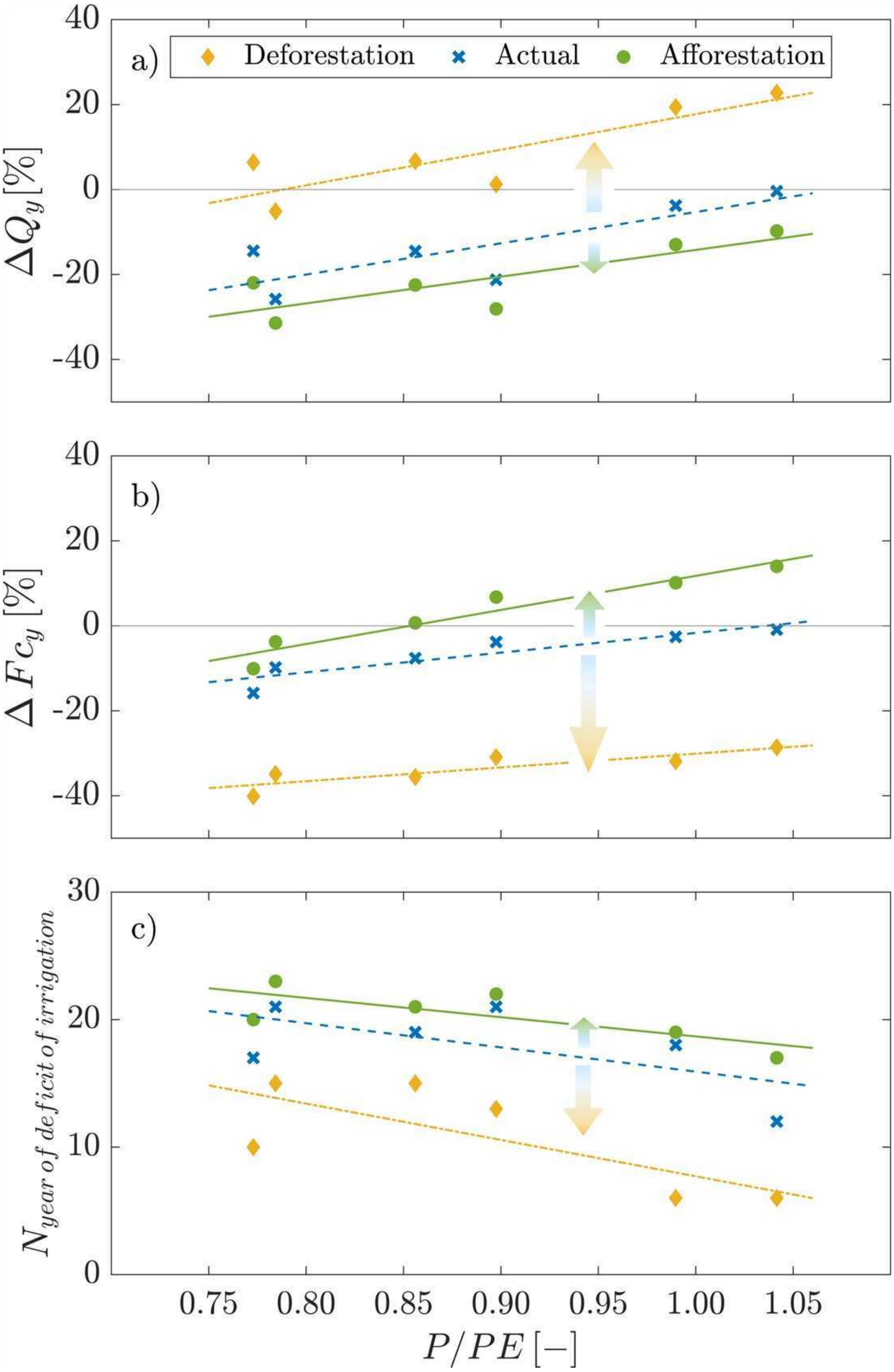

Figure 4.18: a) The impacts of the land cover change scenarios on runoff (Q_y), b) carbon assimilation (Fc_y), and c) irrigation (number of years of deficit of irrigation) for the different mean annual wetness index (P/PE) of the two future emission scenarios (SSP3-RCP7.0 and SSP5-RCP8.5) and the three future reference periods (2026-2050, 2051-2075, and 2076-2100) under water demand scenario C (Table 4.3)

Finally, it is predicted the number of deficit years for irrigation for three water demand scenarios, one conservative water demand scenario (scenario A), an optimistic water demand scenario (Scenario B), and the C scenario with the highest water demands, considering three land cover planning strategies (afforestation, deforestation, and actual land cover), and under two future emission scenarios

(SSP3-RCP7.0 and SSP5-RCP8.5). The full set of strategies under future climate change scenarios provided directions on water demand and land cover planning strategies (Figure 4.19), with few years of deficit of irrigation (from 4 to 8 years for the actual land cover conditions) for the conservative scenario of water demand, while with much more years of deficit of irrigation for the B scenario (up to 26 years of deficit of irrigation) and the C scenarios (up to 42 years).

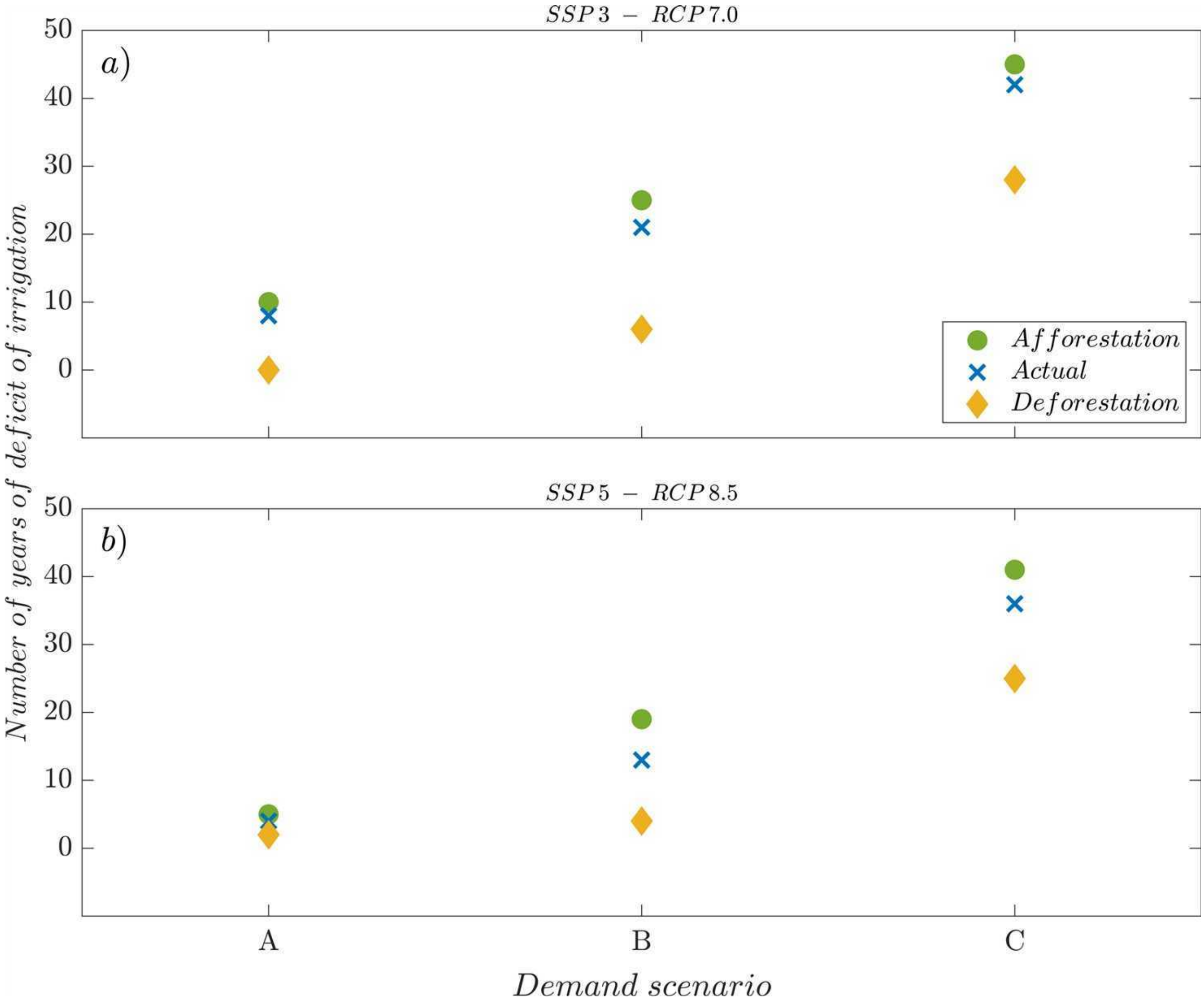

Figure 4.19: The number of years of deficit of irrigation for the three future water demand scenarios (A, B, and C, details in Table 4.3), for the future reference period (2051-2100), for three land cover planning strategies (afforestation, actual conditions, and deforestation) under the two future emission scenarios (SSP3-RCP7.0 and SSP5-RCP8.5)

The Flumendosa basin is hydrological sensitive to forest changes ($\Delta Q_y/\Delta f_t$, Hou et al. (2023)) with values of 0.4–1.4, which are in agreement with Hou et al. (2023) results for water-limited wa-tersheds of small areas. Paradoxically, an extreme land cover change strategy of deforestation could help to increase the availability of water resources in future scenarios (Figure 4.18) because the decrease of 21% of the forested cover of the basin will lead to an increase in runoff (~7%) and a decrease of 20% of the number of years of irrigation deficit for scenario C. These results agree with several studies (Ellison et al., 2012; Andréassian, 2004) at a small scale, showing that afforestation reduces runoff. Moreover, deforestation will have a substantial impact on the carbon assimilation in the basin, which will decrease by up to 37%; this is definitely not compatible with policies of climate change mitigation and adaptation. Furthermore, in a larger regional and global context, afforestation supplies the atmospheric moisture that becomes precipitation in the hydrologic cycle, increasing water yield.

4.4 Conclusions

The analysis of climate change impacts on the Sardinian basins, Flumendosa and Fluminimaggiore, highlights critical challenges for future water resource management and forest sustainability. Using ecohydrological and water management models, the study projects significant reductions in soil moisture, infiltration, and evapotranspiration, leading to decreased runoff—by up to 31% in the late 21st century for Flumendosa and 26% for Fluminimaggiore in worst-case scenarios. This will exacerbate irrigation deficits, with up to 74% of future years experiencing water shortages, particularly under expansionist irrigation policies.

The Flumendosa basin's hydrology is highly sensitive to land cover changes, where deforestation could enhance water availability but at the unacceptable cost of carbon assimilation reduction and ecosystem degradation. Conversely, afforestation would enhance carbon sequestration but further reduce runoff. Similarly, in the Fluminimaggiore basin, the Marganai forest is already experiencing drought stress, leading to systematic reductions in tree LAI, a trend expected to worsen with rising air temperature and vapor pressure deficit (VPD). By 2100, tree LAI could be halved, threatening forest health and resilience.

These findings emphasize the urgent need for climate-adaptive water and forest management strategies in Sardinia, balancing environmental preservation with resource sustainability. While climate change is a global phenomenon, its local impacts demand targeted planning to mitigate risks, especially for Mediterranean basins facing increasing water scarcity and ecosystem stress.

5

Conclusions

This doctoral research project has addressed the complex and interrelated dynamics of ecohydrological processes in Mediterranean environments, characterized by seasonal drought, heterogeneous vegetation patterns, and shallow soils over fractured bedrock. Through an integrated experimental and modeling approach, the work explored how terrestrial ecosystems in these regions respond to increasing climatic stress, particularly in relation to water availability and vegetation resilience. The Mediterranean basin has long been identified as a climate change hotspot (Giorgi, 2006), and the empirical and modeling efforts presented in this thesis reinforce that designation. Across the study sites, particularly Orroli and Marganai in Sardinia, the combination of experimental monitoring (eddy covariance, sap flux, soil moisture, and remote sensing) with advanced process-based distributed modeling has yielded new insights into water fluxes, vegetation dynamics, and the broader hydrological balance of the ecosystem. One of the key findings emerging from the integrated analysis is the central role played by rock moisture that is, water stored in fractured bedrock below shallow soil layers. As demonstrated in the study "Rock Water as a Key Resource for Patchy Ecosystems on Shallow Soils" (Montaldo et al., 2021), deep-rooted evergreen tree species such as wild olive (*Olea sylvestris*) access this hidden reservoir during the dry season, maintaining transpiration and photosynthetic activity when surface soil moisture is depleted. Importantly, this rock moisture is not solely exploited by the trees themselves: through nighttime hydraulic redistribution, it subsidizes the water needs of surrounding seasonal herbaceous vegetation during spring, establishing a facilitative interaction that sustains the mosaic-like ecosystem configuration typical of Mediterranean landscapes (Scholes and Archer, 1997; Breshears, 2006; Montaldo et al., 2013). This dynamic equilibrium is fragile. Simulation scenarios within the Orroli site, combining sap flux measurements, eddy covariance flux partitioning, and soil water balance models, indicate that increasing drought severity expressed as higher potential ET to precipitation ratios could disrupt this delicate interdependence. The absence of access to deep water would lead to a significant reduction in growing season length and photosynthetic capacity, particularly for the herbaceous layer. This reveals that any land-use policy aiming to modify vegetation structure either by increasing tree cover (to enhance carbon sequestration) or by reducing it (to enhance water yield) must carefully consider these hidden hydrological interactions to avoid unintended ecological consequences. Tree clumps play a key role in supporting the overall functionality of the ecological mosaic, not only by accessing deep water reserves in the rocky substrate but also by contributing to the redistribution of moisture to the upper soil layers during the night (hydraulic lift). The modeling applications and field validations carried out in this research have confirmed that these interactions are not only ecologically significant but also quantifiable and predictable. In particular, through the combined use of eddy covariance measurements, sap flow monitoring, and soil moisture observations, the model was calibrated to account for the complex flux dynamics and the vertical partitioning of water sources. The experimental challenges posed by such heterogeneous terrain, including issues of eddy covariance energy balance closure and the impact of topography on turbulent fluxes, have also been addressed through novel analytical techniques. In particular, the findings reported in Sirigu et al. (2025) demonstrate how terrain-induced anisotropy can affect the interpretation of flux-variance similarity and energy balance closure, leading to corrections necessary for accurate upscaling and modeling of ecosystem-level fluxes. These results confirm that even in complex environments, careful statistical treatment and understanding of turbulence structure can allow for robust micrometeorological inference. Moreover, the work "Spectral Distortions to Momentum and Scalar Exchanges by Non-Turbulent Motion and Patchy Landscape Variability" accepted in *Agricultural and Forest Meteorology* explores the spectral signatures of turbulence and scalar transport across patchy Mediterranean landscapes, highlighting how landscape heterogeneity and low-frequency non-turbulent motions distort co-spectra and scalar variance. While the conclusions of this particular study are more methodological, they support the broader thesis argument: accurate quantification of water and energy fluxes in Mediterranean ecosystems requires the integration of fine-scale spatial and temporal variability, both in measurements and in model structure. The modeling applications conducted in the Flumendosa basin, documented in the article "Long-Term Climate and Water Resource Trends in a Mediterranean Island Basin" (Montaldo et al., 2024), further contextualize these ecohydrological insights within a basin-wide perspective. The integration of historical precipitation data, runoff trends, and land cover change with climate projections (CMIP6 scenarios) and reservoir operation models underscores the increasing vulnerability of water supply systems. Simulations reveal that if current trends continue, irrigation needs will remain unmet in a growing proportion of years up to 74% with an average deficit of over 50%. This has profound implications for agriculture, especially in regions where economic and social resilience is tightly coupled to irrigation-based food production. The Marganai forest study, covered in the article "Climate Change Impacts on the Water Resources and Vegetation Dynamics of a Forested Sardinian Basin through a Distributed Ecohydrological Model" (Sirigu and Montaldo, 2022), adds another dimension by examining the structural vulnerability of Mediterranean forests under climate change. Projected reductions in LAI (Leaf Area Index) of up to 50% by the end of the century reflect both physiological stress and potential shifts in species composition. These findings, consistent with increased VPD levels and lower soil moisture availability, indicate that evergreen broadleaf species, while drought-resistant, are not immune to prolonged and recurrent climate extremes. Furthermore, hydrological simulations point to a paradoxical increase in flood risks despite overall drying due to more intense and concentrated precipitation events. The ecohydrological model developed and calibrated throughout this thesis extending traditional land surface models by explicitly including vegetation dynamics and deep water access has proven to be a powerful predictive tool. It enables the simulation of coupled water–vegetation–climate interactions under various management and climate scenarios. Importantly, the model's modular architecture allows for adaptation to new sites and contexts, including the incorporation of different vegetation types, land cover mosaics, and reservoir management rules. From a policy and planning perspective, the outputs generated by this research have direct applicability. Scenario analyses can be used by water authorities and land managers to test the effectiveness of different strategies aimed at mitigating the impacts of climate change. These include afforestation or reforestation policies, irrigation planning, and reservoir operation optimization. By providing a platform to evaluate trade-offs between ecosystem services such as water yield, carbon sequestration, and biodiversity conservation the model can support integrated and adaptive decision-making. In a broader scientific context, this thesis contributes to the growing body of literature that seeks to merge ecohydrology with Earth system science. It emphasizes the necessity of capturing below-ground hydrological processes, such as root water uptake from fractured rock, which are often neglected in global models but critical for water-limited regions. The concept of the "ecohydrology of roots in rocks," proposed by Schwinning (2010), becomes not only relevant but operationally important in Mediterranean-type systems. Looking forward, several avenues for future research emerge. First, improving the representation of vegetation functional types, and carbon assimilation processes would enhance the model's realism and scope. Second, the integration of remote sensing data, particularly from new high-resolution platforms, offers promising opportunities for model calibration and validation over broader areas. Third, linking ecohydrological models with socio-economic models could allow for more comprehensive assessments of land-use and water policy impacts. In conclusion, this thesis offers a detailed and operational framework for understanding and managing Mediterranean ecohydrosystems under climate stress. Through the coupling of field experiments, hydrological theory, and distributed modeling, it advances the capacity to diagnose current vulnerabilities and project future trajectories of ecosystem services, with a focus on sustainability, resilience, and adaptability.

6 Appendix

6.1 Micrometeorological Measurements with the Eddy Covariance Method

he direct application of the aforementioned equation in cases of turbulent flow, such as flows in the lowest part of the atmospheric boundary layer, can only be approached statistically in terms of average flows.

Imagining the airflow as a horizontal stream of many rotating vortices, each with three components u, v (horizontal plane) and w (vertical direction), and assuming flat, uniform terrain and negligible variations in air density, the average flow F of a quantity X is given by (Burba, 2022):

$$F = \overline{\rho w x} \tag{6.1}$$

The Eddy Covariance method is based on applying Reynolds decomposition to the relevant quantities:

$$x = \overline{x} + x', \quad w = \overline{w} + w' \tag{6.2}$$

By developing and considering the properties of the averaging operator and the assumption of negligible air density fluctuations, we obtain:

$$F = \rho \cdot \overline{w'x'} \tag{6.3}$$

Recalling the definition of covariance between two quantities x_1 and x_2:

$$\mathrm{cov}(x_1, x_2) = \overline{(x_1 - \overline{x}_1)(x_2 - \overline{x}_2)} = \overline{x_1' x_2'} \tag{6.4}$$

The right-hand term of the equation represents the covariance between the vertical velocity component w and the quantity x.

Applying the method to the flows mentioned earlier, we obtain:

$$F_c = \rho \cdot \overline{w'c'} \tag{6.5}$$

$$LE = \rho \cdot \lambda \cdot \overline{w'q'_v} \tag{6.6}$$

$$H = \rho \cdot c_p \cdot \overline{w'T'} \tag{6.7}$$

$$\tau_{uw} = \rho \cdot \overline{u'w'} \tag{6.8}$$

$$\tau_{vw} = \rho \cdot \overline{v'w'} \tag{6.9}$$

Here, q_v [Kgvap m^{-3} air] represents absolute humidity, i.e., the mass of vapor in a unit volume of air.

The values of turbulent stresses are used in data processing to assess atmospheric thermal stability and identify the lowest layer of the atmosphere where the method's assumptions hold. This is done using the Monin-Obukhov parameter ζ [-]:

$$\zeta = \frac{z - d_0}{L} \tag{6.10}$$

Where:

- z is the measurement height [m];
- d_0 is the average reference height of the ground [m], depending on vegetation height and density, often taken as a function of vegetation height h_v [m]:

$$d_0 = 0.67 \cdot h_v \tag{6.11}$$

- L is the Obukhov length (Brutsaert, 1982), interpreted as the height above which turbulence caused by wind's mechanical action dominates over that caused by thermal exchanges (sublayer of dynamic turbulence):

$$L = -\frac{u_*^3 \cdot T}{kg \cdot \overline{w'T'}} \tag{6.12}$$

- u_* is the friction velocity:

$$u_* = \sqrt{\sqrt{\overline{u'w'}^2 + \overline{v'w'}^2}} \tag{6.13}$$

- k is the Von Kármán constant;
- g is gravitational acceleration [m/s^2].

Measurement Instruments

The Eddy Covariance method requires high-resolution sampling (10 Hz or higher) of the turbulent component of wind speed and atmospheric gas concentration, using instruments rugged enough for long-term field operation.

Currently, the suitable instruments are ultrasonic anemometers and optical gas analyzers.

Ultrasonic Anemometer Thermometers (SATs)

Operating Principle

A SAT measures wind speed v_d and the speed of sound in air c_s along the line (path) between two transducers. The path length ranges from 0.05 to 0.20 m depending on the model. Each sensor contains an acoustic transmitter. The signal is transmitted in both directions. From the travel times t_{AB} and t_{BA}, the following can be calculated:

$$v_d = \frac{d}{2}\left(\frac{1}{t_{AB}} - \frac{1}{t_{BA}}\right) \tag{6.14}$$

$$c_s = \frac{d}{2}\left(\frac{1}{t_{AB}} + \frac{1}{t_{BA}}\right) \tag{6.15}$$

$$T_v = \frac{c_s^2}{\gamma R} \tag{6.16}$$

Wind speed v_d is derived by subtracting the inverse of both formulas.

Types of SATs

Commonly used SATs are 3D-SATs, with three sensor pairs to measure wind speed components u, v, w. Unlike 1D anemometers, they allow momentum flux calculations, coordinate transformation in post-processing, and virtual temperature corrections for cross-wind effects.

Types of 3D-SATs:

- **Vertical path:** One vertical and two horizontal sensor pairs.
- **Slanted path:** Three sensor pairs arranged in a triangular pattern.

These can be further categorized as:

- **Omnidirectional sensors** (e.g., R.M. Young 81000): symmetric and less prone to distortion except under horizontal or upward wind.
- **C-Clamp sensors** (e.g., Campbell Scientific C-SAT 3): non-omnidirectional, more prone to distortion (>30%).

Optical Gas Analyser

Various methods exist to measure gas concentration in air—chemical, electrical, optical. Eddy Covariance uses optical sensors for high-frequency sampling.

Operating Principle

The system emits a broadband infrared beam filtered to allow only 4.26 μm and 2.59 μm wavelengths, directed at a detector that measures the intensity. These are absorbed by CO_2 and H_2O respectively. The intensity is a nonlinear function of gas molecule numbers and is converted using calibration coefficients.

Types of Gas Analyzers

- **Closed-path:** Larger, weather-protected; air is pumped to a chamber near the tower base. Requires filters, cannot be cleaned in the field.
- **Open-path:** Compact, with sensor and control box. Susceptible to H_2O interference (cross-sensitivity), temperature, and pressure fluctuations. Requires WPL corrections.

The case study uses a LICOR-7500A (Open-path) by Licor Biosciences with post-processing corrections.

6.2 Supflux measurament

The measurement of transpiration is an essential element for understanding plant physiology and water transfer dynamics in an ecosystem.

Transpiration is the flow of water vapor released through plant leaves into the atmosphere.

Transpiration is greater during daylight hours because, during the process of photosynthesis, the opening of the stomata necessary for the absorption of carbon dioxide also allows the water present in the cells to evaporate into the drier atmosphere.

This loss generates a water lift that transports water from the soil to the leaves through the xylem channels (sapwood).

There are various techniques to estimate transpiration; one of the simplest, most indicative, and economical is the Granier method (Granier, 1987).

Measuring Instruments – Granier Probes

The method allows the calculation of the intensity and, potentially, the direction of water flow in the trunk and roots, through the insertion of probes that penetrate the sapwood layer.

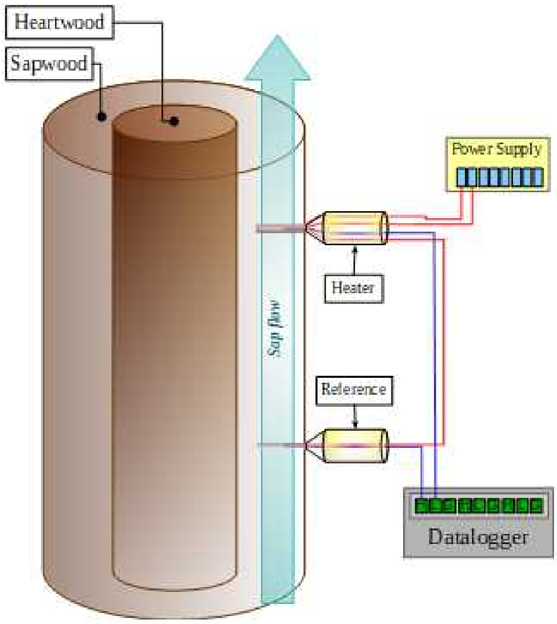

Figure 6.1: Stem Sapflow probe installation

The probes consist of type T thermocouples (Copper-Constantan), in varying numbers depending on the sensor to be installed, one of which is heated using the Joule effect via a constant current source.

The basic hypothesis of the method is that in thermal equilibrium conditions of the sensor-wood/sap system and under steady flow conditions, the heat generated by the Joule effect equals the heat dissipated by convection and conduction on the cylindrical surface external to the heated probe.

When the sap flow moves, it intercepts the heated probe, cooling it and thus reducing the measured temperature. This enables the measurement of the potential difference triggered by the temperature difference itself.

In the case study, three different types of sensors based on the Granier method were used:

- Stem Sapflow probes, which allow calculation of the unidirectional flow intensity through the tree trunk;
- Bi-Directional Root Sapflow probes, which allow measurement of the intensity and direction of flow through the tree roots;
- Directional Sapflow probes, which evaluate the direction of flow in the roots.

Stem Sapflow Probe

The sensors installed in the trunks consist of two thermocouples inserted in two 2 cm long hypodermic needles, 15 cm apart, penetrating the sapwood and connected together (Figure 6.1).

Sensors should be installed at a height of 40 cm from the ground, on carefully selected trunks that must be free of irregularities and areas formed by scar tissue, which could compromise measurement accuracy (Smith and Allen, 1996).

The probe installed below the flow direction measures ambient temperature and acts as the reference probe, while the one above is heated (Heater) via an electrical circuit.

The average radial flow J_s [g m^{-2} s^{-1}] is calculated through calibration for different species:

$$J_s = 119 \cdot 10^{-6} K^{1.231} \tag{6.17}$$

where:

$$K = \left(\frac{\Delta V_0 - \Delta V}{\Delta V} \right) \tag{6.18}$$

K is dimensionless and depends on ΔV_0 [°C] and ΔV [°C], which are the temperature differences between the two probes under zero flow and positive flow conditions, respectively.

The total trunk flow F [m^3 s^{-1}] is calculated as:

$$F = J_s \cdot A_{sw} \tag{6.19}$$

where A_{sw} is the Sapwood Area, the cross-sectional area of the sapwood, determined as described in the next paragraph.

The spatial distribution of the vegetation, composed of clusters of numerous wild olive specimens, complicates determination of the active xylem area, as it would require sampling an excessively large number of plants. To overcome this problem, the measured value is scaled from sapwood area to crown area using the following relation (Oren et al., 1999):

$$E_c = \frac{J_s \cdot A_{sw}}{A_g} \tag{6.20}$$

Where E_c is the transpiration rate per unit time, A_{sw} the sapwood area, and A_g the projection of the crown onto the field plane.

Bi-Directional Root Sapflow Probe

Water normally flows from the soil to the trunk through the roots. During periods of hydraulic redistribution, however, it can flow back to the soil through the same roots.

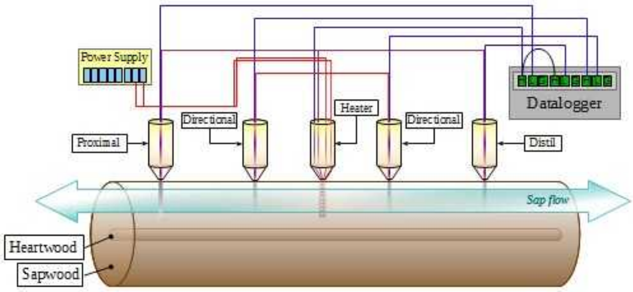

Figure 6.2: bi-directional root sapflow installation diagram

To quantify this bidirectional flow, as part of the INFER QATP Task 4: Water Uptake, Storage, and Distribution project (see bi-directional sap manual), an operational procedure was developed extending the use of Granier probes, originally designed only for measuring sap flow in trunks, with some system modifications.

The full bidirectional sensor consists of a symmetric system of two reference probe pairs centered around the heated probe (Figure6.2). Needle lengths are 2 or 1 cm depending on the monitored root diameter.

The first pair of probes is placed 10 cm to the left and right of the heated probe and are called: proximal (closer to the trunk) and distal (further away).

A second reference probe pair is placed about 7 mm upstream and downstream from the heated probe.

The probe measures three different temperature differences or potentials:

- ΔV_1: temperature difference between the heated probe and the distal;
- ΔV_2: temperature difference between the heated probe and the proximal;
- ΔV_3: temperature difference between the pair closest to the heater, indicating flow direction.

The flow is calculated with the following equation:

$$J_s = d \cdot 119 \cdot 10^{-6} K^{1.231} \tag{6.21}$$

where:

- J_s is the radial flow [g m^{-2} s^{-1}];
- d is the directional multiplier derived from ΔT_3: positive if towards the plant, negative if towards the soil;
- K is dimensionless and calculated as:

$$K = \left(\frac{\Delta V_0 - \Delta V_1}{\Delta V_1} \right) \tag{6.22}$$

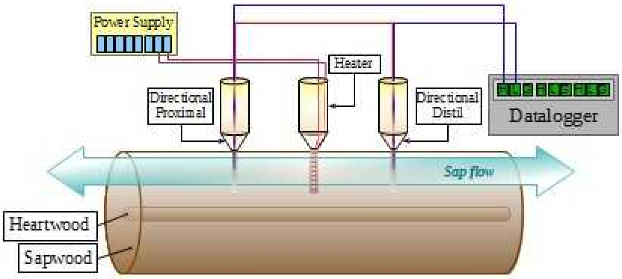

Figure 6.3: Directional root sapflow installation diagram

if flow is positive (d = +1)

$$K = \left(\frac{\Delta V_0 - \Delta V_2}{\Delta V_2}\right) \tag{6.23}$$

if flow is positive (d = -1)

As in the previous case, total flow F [m^3 s^{-1}] is obtained by scaling the radial flow u over the Sapwood Area A_{sw}:

$$F = J_s \cdot A_{sw}$$

Directional Sapflow Probe

This sensor is a simplified variant of the bi-directional root sapflow sensor, using only the reference pair that provides direction (Figure 6.3).

In the case study, eight of these sensors were mounted to sample actual direction reversals during nighttime periods.

Sapwood Area Determination

The sapwood layer area is determined by staining the cross-section with an iodine contrast solution, based on sampling trunks and roots of various diameters.

The sapwood area A_{sw} of trunks and A_{swr} of roots is obtained from the following expression (Oishi et al., 2008): $A_s w = \pi \left(\frac{D}{2} - S_b\right)^2 - \pi \left(\frac{D}{2} - S_b - S_s w\right)^2$

where:

- D: outer diameter of the trunk or root sample;
- S_b: bark thickness;
- S_{sw}: thickness of the xylem circular crown.

Construction of Sapflow Sensors

As previously mentioned, the sensors are made of type T thermocouples, with copper and constantan conductors (an alloy of 60% copper and 40% nickel), operating over a -200°C to 350°C range, with a sensitivity of 40.5 mu V/°C.

The thermocouples are made from a 16 cm segment of copper-constantan coil, with ends stripped, twisted, and soldered with tin for about 5 mm.

The structure is made by cutting a 20G hypodermic needle (0.9 x 40 mm) at a 45° angle at 20 mm or 10 mm from the barrel.

Each thermocouple is inserted into the probe structure through the barrel, so the junction is centered in the needle.

For heated probes, a hole is drilled in the barrel to mount the heating coil (constantan wire, 0.12 mm diameter, 50 cm for 20 mm probes, 30 cm for 10 mm), then covered with a 2.38 mm aluminum sheath.

Finally, epoxy resin is injected into the barrels to fix the wires.

Each constantan wire is powered by a circuit supplying constant voltage. Each heated sensor receives a current of 0.115 A, corresponding to a power of 0.2 W and a resistance of 15 Ω.

6.3 Spectra analysis theory

6.3.1 Definitions

The Cartesian coordinate system used defines x, y, and z along the longitudinal, lateral, and vertical directions, respectively with $z = 0$ being the ground surface and the longitudinal direction is aligned along the mean wind direction. The instantaneous velocity components along x, y, and z directions are labeled as u, v, and w, respectively and overline defines time averaging over a period T_p. The $\overline{U}$ represents the mean velocity over T_p. Three scalars are considered - air temperature T, water vapor concentration Q, and carbon dioxide concentration C. For convenience, variable s is used to indicate a general scalar ($s = T, Q, C$). Turbulent fluctuations from their time-averaged values are indicated by lower case primed quantities. The $\overline{w'u'}$ is the dominant kinematic shear stress representing the vertical turbulent flux of longitudinal momentum at z, and $\sigma_u = \sqrt{\overline{u'u'}}$, $\sigma_v = \sqrt{\overline{v'v'}}$, and $\sigma_w = \sqrt{\overline{w'w'}}$ are the root-mean squared velocity fluctuations along the x, y, and z directions, respectively. Likewise, the scalar variance is defined as $\sigma_s = \sqrt{\overline{s's'}}$ and the covariance with w' is $\overline{w's'}$. The spectra and co-spectra satisfy the normalizing property:

$$\sigma_u^2 = \int_0^\infty F_{uu}(n)dn; \; \sigma_w^2 = \int_0^\infty F_{ww}(n)dn; \; \sigma_s^2 = \int_0^\infty F_{ss}(n)dn \tag{6.24}$$

$$\overline{w'u'} = \int_0^\infty F_{wu}(n)dn; \; \overline{w's'} = \int_0^\infty F_{ws}(n)dn, \tag{6.25}$$

where n is the natural frequency (cycles per period), $F_{uu}(n)$, $F_{ww}(n)$, $F_{ss}(n)$ are the spectra of the longitudinal, vertical, and scalar quantities, and $F_{wu}(n)$, $F_{ws}(n)$ are the co-spectra for the momentum and scalar fluxes, respectively (Kaimal and Finnigan, 1994). In atmospheric surface layer turbulence studies, it is convenient to define the so-called dimensionless frequency $f = n(z-d)/\overline{U}$, where d is the zero-plane displacement. Likewise, a one-dimensional (longitudinal) wavenumber in space $k_x = 2\pi n/\overline{U}$ can also be derived from Taylor's frozen turbulence hypothesis (Taylor, 1938). The n, f, and k_x are used interchangeably depending on whether the context is time, space, or dimensionless frequencies. To be clear, spectral theories for turbulence are usually derived in wavenumber (or k-) space but tower measurements provide data in the time or frequency domain. The two spaces are assumed to be linked through $\overline{U}$ using Taylor's frozen turbulence hypothesis, which is applicable under certain conditions. Common corrections to Taylor's frozen turbulence hypothesis simply adjust the magnitude of the spectrum or co-spectrum using the turbulent intensity but do not alter the relation between time (or frequency) and k_x (Wyngaard and Clifford, 1977; Hsieh and Katul, 1997). Finer corrections that utilize the so-called elliptic approximation can simultaneously adjust for magnitude and wavenumber distortions due to the use of Taylor's frozen turbulence hypothesis, but those corrections require closely aligned multiple towers (Everard et al., 2021) and cannot be implemented here. Still, comparisons between one-dimensional (longitudinal) ensemble-averaged spatial velocity spectra (both u' and w') measured with particle-image velocimeter or PIV and those inferred from cross-probes using Taylor's hypothesis in wind tunnels show excellent agreement for scales up to 6 times the boundary layer depth (Deshpande et al., 2023). These findings suggest that Taylor's hypothesis without any modification may be reasonable for spectral analysis as long as the turbulent intensity is not large, which is likely to be the case for near-neutral conditions explored here.

Turbulent flows in the near-neutral atmospheric surface layer are dominated by eddies with wide ranging time scales. The large eddies tend to scale with the boundary layer height

$$\delta = C_\delta \frac{u_*}{f_o}, \tag{6.26}$$

where f_o=1×10^{-4} s^{-1} is the Coriolis parameter, u_* is the friction velocity defined by $u_* = (\overline{w'u'}^2 + \overline{w'v'}^2)^{1/4}$, and $C_\delta = 0.08 - 0.2$ is a similarity constant (Clarke, 1970; McBean, 1976; Arya, 1981; Zilitinkevich and Baklanov, 2002). The finest scales of turbulence are in the regime where the action of kinematic viscosity ν becomes significant compared to the turbulent viscosity and those scales are referred to as the Kolmogorov micro-scale eddies given by

$$\eta = \left(\frac{\nu^3}{\overline{\epsilon}}\right)^{1/4}, \tag{6.27}$$

where $\overline{\epsilon}$ is the mean turbulent kinetic energy dissipation rate, and ν is the kinematic viscosity (Tennekes and Lumley, 1972). Eddies attached to the ground are presumed to be responsible for diffusive exchanges as well as turbulent kinetic energy production and they scale as $l_m = \kappa(z-d)$, where $\kappa = 0.4$ is the von Kármán constant (Prandtl, 1952). The aforementioned three length scales can now be used to determine dominant time scales associated with turbulent motion. These time scales (or inverse frequencies) are: (i) the Kolmogorov micro-scale time $\sqrt{\nu/\epsilon}$ being the smallest (or highest frequency), (ii) the attached eddy or mean flow vorticity given by $[\partial\overline{U}/\partial z]^{-1} = \kappa(z-d)/u_*$ being intermediate, and (iii) the inactive eddy advection time scale $(u_*/\overline{U})(C_\delta/f_o)$ being the largest (or lowest frequency for turbulent motion). For order of magnitude estimates of these scales, the case where z=10 m, d=0.67h_c, h_c=5 m being the canopy height, $C_\delta = 0.2$ (upper value for near-neutral conditions), u_*=0.1 m s^{-1}, and $\overline{U}$=1 m s^{-1} are used. For these assumed values, η =1.7 mm (orders of magnitude smaller than the path-averaging of typical sonic anemometers used in micro-meteorology), the concomitant Kolmogorov micro-time scale is 0.2 s, the attached eddy time scale 27 s, $\delta = 200$ m resulting in the largest eddy time scale of 200 s. In these calculations, it was assumed that

$$\overline{\epsilon} = u_*^2 \frac{d\overline{U}}{dz} = \frac{u_*^3}{\kappa(z-d)}, \tag{6.28}$$

or mechanical production balances the mean turbulent kinetic dissipation rate, a reasonable choice for near-neutral conditions in stationary and planar homogeneous flow with no subsidence (Charuchittipan and Wilson, 2009; Katul et al., 2011; Salesky et al., 2013; Saddoughi and Veeravalli, 1994). For these reasons, a spectral cut-off filter set to 300 s (or 5 min) is used to separate the largest turbulent scale from non-turbulent low frequency motion. The precise numerical value of this filter cutoff is not essential for near-neutral conditions provided it varies between 5 to 10 min. This insensitivity to the precise cutoff value was examined in a number of studies summarized below:

- In flux-variance analysis, how to separate turbulent from non-turbulent motion was explored using high frequency data from the National Ecological Observatory Network (NEON) database. It was shown that for 39 sites (spanning short crops to forests) and multiple years per site, a 5 min cutoff recovered flux-variance relations and similarity constants reasonably well when compared to standard values (Waterman et al., 2022).

- In partitioning evapotranspiration into evaporation and transpiration, a low frequency cutoff that varied from 5-10 min was necessary to achieve acceptable convergence given the use of flux-variance similarity in these schemes (Zahn et al., 2022; Scanlon and Sahu, 2008; Scanlon and Kustas, 2010).

- In studies of mass, energy, and momentum transporting eddies over heterogeneous forested sites, it was reported that the time scale associated with the largest eddy was few minutes (Thomas et al., 2006) suggestive that eddies much longer than this time scale were surrogates to non-stationarity (i.e. non-turbulent).

- In ogive analysis for momentum and scalar fluxes at a few sites, more than 90% of total fluxes was shown to carried by time scales smaller than 5 min in the near-neutral limit (Sakai et al., 2001).

These are some reasons why a 5 min spectral cutoff was deemed plausible and employed here to separate turbulent from non-turbulent motion in near-neutral conditions. The outcomes are to be contrasted to the original (de-mean but not de-trended or filtered) time series.

6.3.2 Spectral and co-Spectral shapes: An overview

The mathematical form of the reference pre-multiplied spectra and co-spectra for a uniform planar homogeneous flow over a flat-terrain and near-neutral conditions are briefly reviewed and are given as (Kaimal and Finnigan, 1994):

$$\frac{nF_{uu}(n)}{\overline{u'u'}} = \frac{a_{uu}f}{(1+b_{uu}f)^{5/3}};\ \frac{nF_{ww}(n)}{\overline{w'w'}} = \frac{a_{ww}f}{(1+b_{ww}f)^{5/3}};\ \frac{nF_{ss}(n)}{\overline{s's'}} = \frac{a_{ss}f}{(1+b_{ss}f)^{5/3}}; \tag{6.29}$$

$$\frac{nF_{wu}(n)}{\overline{w'u'}} = \frac{a_{wu}f}{(1+b_{wu}f)^{7/3}};\ \frac{nF_{ws}(n)}{\overline{w's'}} = \frac{a_{ws}f}{(1+b_{ws}f)^{7/3}}, \tag{6.30}$$

where a_{uu}, a_{ww}, a_{ss}, a_{wu}, a_{ws}, b_{uu}, b_{ww}, b_{ss}, b_{wu}, b_{ws} are coefficients to be determined for the site here. These coefficients are to be compared to those for the ideal sites such as those featured in the Kansas experiment(Kaimal and Finnigan, 1994) after adjusting for differences in the normalization. For the Kansas experiment, these adjusted coefficients are: $a_{uu} = 19.24$, $a_{ww} = 3.11$, a_{ss}=9.37, $a_{wu} = 45.18$, $a_{ws} = 29.53$ for $n \leq 1$ and $a_{ws} = 3.41$ for $n \geq 1$, b_{uu}=25.48, b_{ww}=4.06, b_{ss}=13.7, b_{wu}=6.25, and $b_{ws} = 4.23$ for $n \leq 1$ and $b_{ws} = 1.23$ for $n \geq 1$. Note that equations 6.30 are normalized by the local variances and fluxes instead of u_*^2 or other scalar flux normalizing variables as in the original Kansas references. In adjusting these Kansas coefficients to the normalization employed here, we used the flux-variance coefficients for σ_u, σ_v, σ_w, and σ_s derived from the Kansas experiment for near-neutral conditions. The above spectral formulations also recover the Kolmogorov spectra (Kolmogorov, 1991) for large f (or small scales), where the flow is presumed to have attained local isotropy. The Kolmogorov spectra are derived by assuming the eddy sizes are much smaller than the integral scale of the flow but much larger than the micro-scales. This range of scales is referred to as the inertial subrange, and the velocity spectra are often written in wavenumber space as

$$F_{uu}(k_x) \text{ or } F_{ww}(k_x) \propto \overline{\epsilon}^{2/3} k_x^{-5/3}. \tag{6.31}$$

Local isotropy, however, is incompatible with finite co-spectra because finite shear $d\overline{U}/dz$ and finite mean scalar gradients $d\overline{S}/dz$ act across all turbulent scales (including the inertial subrange). It has been demonstrated that scaling laws describing spectra and co-spectra appear insensitive to the local isotropy assumptions (Saddoughi and Veeravalli, 1994; Katul et al., 2019).

In some studies, the co-spectra were reported to decay slower than the classical $f^{-7/3}$, with an f^{-2} exponent better describing the data (Su et al., 2004; Horst, 1997; Massman, 2000). Theoretical justification as to why an f^{-2} scaling occurs instead of the $f^{-7/3}$ have been proposed (Bos et al., 2004; Cava and Katul, 2012; Li and Katul, 2017) and can be accommodated in such formulation by revising the exponents in the denominator of the co-spectral equations.

A pre-multiplied spectral representation is also convenient because the spectral and co-spectral peaks occur at frequencies that match the integral time scale Γ (Kaimal and Finnigan, 1994). The definition of Γ is

$$\Gamma = \int_0^\infty \rho(\tau) d\tau, \tag{6.32}$$

where τ is the time lag and $\rho(\tau)$ is the autocorrelation function of any stationary flow variable. The integral time scale is routinely used as a measure of the memory or de-correlation time of a stochastic process (Tennekes and Lumley, 1972). For a zero-mean and unit variance stochastic process, the energy spectrum $F_{\alpha\alpha}(n)$ is the Fourier transform of $\rho(\tau)$ and is given by

$$F_{\alpha\alpha}(n) = \frac{1}{2\pi} \int_{-\infty}^{\infty} \rho(\tau) \exp(-in\tau) d\tau, \tag{6.33}$$

where i^2=-1. It follows that

$$F_{\alpha\alpha}(0) = \frac{1}{2\pi} \int_{-\infty}^{\infty} \rho(\tau) d\tau = \frac{\Gamma}{\pi} \tag{6.34}$$

when using $\rho(-\tau) = \rho(\tau)$. Spectral analysis of finite time series cannot estimate $F_{\alpha\alpha}(0)$ as this estimate requires an infinite sampling duration. A pre-multiplied spectrum of the form

$$nF_{\alpha\alpha}(n) = \frac{a_1 f}{(1 + a_2 f)^\beta} \tag{6.35}$$

has a maximum or peak at $f_p = [a_2(\beta - 1)]^{-1}$. Moreover, the variance $\sigma^2_{\alpha\alpha} = 1$ can be derived by integrating $F_{\alpha\alpha}(n)$ over all n to give

$$\sigma^2_{\alpha\alpha} = 1 = \int_0^\infty F_{\alpha\alpha}(n) dn = \frac{a_1}{a_2(\beta - 1)} = a_1 f_p. \tag{6.36}$$

Noting that the actual (not the pre-multiplied) spectrum can be evaluated at $n = 0$, the following outcomes emerge:

$$F_{ss}(0) = a_1 = \frac{\sigma^2_{ss}}{f_p} = \frac{1}{f_p} = \frac{\Gamma}{\pi}. \tag{6.37}$$

That is, the integral time scale of a flow variable can be readily determined from f_p using $\Gamma = \pi/f_p$

provided $\beta > 1$ (Kaimal and Finnigan, 1994). For $\beta = 1$, the variance is unbounded. Hereafter, the integral time scale for any flow variable s is indicated by Γ_s.

While the empirical shapes in equation 6.29 are convenient to use, they miss a number of features associated with the physics of turbulence at large scales (i.e. scales larger than $z-d$) and fine scales (i.e. those commensurate with η). A summary of the established shapes of the spectra at low frequencies (or low wavenumbers) for canonical boundary layers is summarized below:

(i) It has been known for some time now that the $F_{uu}(k_x)$ exhibits an k_x^{-1} scaling predicted from Townsend's attached eddy hypothesis (Townsend, 1976; Marusic and Monty, 2019). It is usually expressed in wavenumber space as

$$F_{uu}(k_x) = C_{uu} u_*^2 k_x^{-1}, \tag{6.38}$$

where C_{uu} is a similarity coefficient that varies between 0.9 and 1.0 (Kader and Yaglom, 1991; Katul et al., 1995; Katul and Chu, 1998; Huang and Katul, 2022). This scaling has been extensively studied in pipe and open channel flows, and atmospheric boundary layers (Kader and Yaglom, 1991; Katul and Chu, 1998; Banerjee and Katul, 2013; Marusic et al., 2013; Nikora, 1999; Nickels et al., 2007; Chamecki et al., 2017; Huang and Katul, 2022). The $F_{ww}(k_x)$ usually exhibit an extended 'energy splashing' (randomization) region (i.e. $E_{ww}(k_x) \sim k_x^0$) for eddies larger than $z-d$ due to the presence of a solid boundary (Mortarini et al., 2023; Katul et al., 1998). Thus, the direct implication of Townsend's attached eddy hypothesis is that a spectral peak associated with Γ_u may not be defined or delineated from data when determined from $fF_{uu}(f)$. However, Γ_w is well defined because of the energy splashing transitioning from f^{+1} to a $f^{-2/3}$ at high frequency or small scales in pre-multiplied form.

(ii) As $n \to 0$ (i.e. $k_x\delta < 1$), there are a number of theories and constraints that must be satisfied. Two theories that describe the shape of the spectrum within those constraints as this zero-frequency limit is approached stand out in studies of turbulence. Both theories commence with homogeneous-isotropic turbulence described by the Karman-Howarth equation (Karman and Howarth, 1938; Panchev, 1971) but differ in the specification of L_u as initial conditions to the solution. The first is attributed to Saffman (Saffman, 1967) and it predicts an $F_{uu}(k_x)$ exhibiting an k_x^{+2} scaling (Pope, 2000). The second is known as the Batchelor-Proudman theory (Batchelor and Proudman, 1956) and it predicts a k_x^{+4} scaling. For $L_u > 0$, the Saffman spectrum is recovered but for $L_u = 0$, the Batchelor-Proudman spectrum emerges. The k_x^{+2} scaling is congruent with other spectral budgets recently proposed for such a limit but in unbounded domains (Porporato et al., 2020). That $F_{uu}(k_x)$ decays for small k_x is necessary for a spectral gap to exist to enable separation of the flow variables into a mean state and a fluctuating state. Returning to the usage of these theoretical results for correcting the low frequency limits of the Kansas spectra, one possible adjustment to $F_{uu}(k_x)$, which is widely used in wind engineering, is the so-called von Kármán spectrum (Pope, 2000). When expressed in wavenumber space, this spectrum yields

$$F_{uu}(k_x) = C_u \epsilon^{2/3} L_u^{5/3} \frac{(k_x L_u)^4}{(1+(k_x L_u)^2)^{17/6}}, \tag{6.39}$$

where $L_u = \Gamma_u \overline{U}$ is the integral scale of the flow, $C_u = 0.5$ is the Kolmogorov constant, and $k_x = 2\pi n/\overline{U}$ is the wavenumber (or inverse scale). This spectrum recovers a k_x^4 scaling (i.e. Batchelor-Proudman) for $k_x L_u << 1$ (or small n) and a $k_x^{-5/3}$ scaling for $k_x L_u >> 1$ (i.e. Kolmogorov's spectrum (Kolmogorov, 1991)). Using similar arguments, it is possible to derive a spectral form that recovers the Saffman theory in the limit of $k_x L_u \to 0$ given by

$$F_{uu}(k_x) = C_u \epsilon^{2/3} L_u^{5/3} \frac{(k_x L_u)^2}{(1+(k_x L_u)^2)^{11/6}}, \tag{6.40}$$

where the Saffman limit and the Kolmogorov limits are recovered.

(iii) As $k_x \to \infty$, $F_{\alpha\alpha}(k_x) \to 0$ when using the Kansas spectral shapes. The presence of a viscous cutoff, which is ignored by the Kansas spectral shapes, in reality ensures a much steeper decay with increasing k_x compared to conventional inertial subrange scaling (i.e. $k_x^{-5/3}$). This fine-scale limit is not resolved by current sonic anemometery. The viscous effects often extend to spatial scales (or eddy sizes) commensurate with 10η (Pope, 2000; Meyers and Meneveau, 2008; Katul et al., 2015). In some spectral studies, the viscous effects can be represented as an exponential cutoff to the inertial subrange scaling and are usually expressed as (Pope, 2000)

$$F_{uu}(k_x) = \left[C_o(\bar{\epsilon})^{2/3} k_x^{-5/3}\right] \exp\left[-\beta_d(k_x \eta)\right], \tag{6.41}$$

where $\beta_d = 5.2$ is a constant (Pope, 2000; Porporato et al., 2020). The inclusion of this exponential cutoff limit correction may be overlooked (as was done in the Kansas experiment) given the high Reynolds number flows expected here. A 'spectral' interpretation of a high Reynolds number here is a large scale separation between $z-d$ and η, or $(z-d)/\eta \gg 1$. Because of such large separation between $z-d$ and η, and because of the rapid decay of the spectrum with decreasing scale, a small amount of energy and turbulent flux is expected at scales smaller than 10η (Katul et al., 2013).

Spectral and co-spectral measurements in the roughness sublayer above tall and dense forests experience additional modifications to the Kansas spectra (Raupach et al., 1996; Brunet, 2020; Mortarini et al., 2023). The main modification is a shift in the peak length scale from $z-d$ to αh_c, where $\alpha \leq 1$ is a constant that depends on the foliage distribution (Finnigan, 2000; Mortarini et al., 2023). Recent experiments and Large Eddy Simulation runs suggest that the scaling laws for the longitudinal and vertical velocity at low wavenumbers are not as impacted. In particular, the k_x^{-1} scaling in $F_{uu}(k_x)$ and the k_x^0 in the $F_{ww}(k_x)$ at $k_x h_c < 1$ have been reported in a large corpus of experiments (Katul and Chu, 1998; Mortarini et al., 2023; Dupont and Patton, 2022). Likewise for the co-spectral shapes of scalars (Katul et al., 1998) with the prevalence of an f^{-2} decay in the inertial subrange better describing some data sets (Su et al., 2004).

Bibliography

Ahmed, K. F., Wang, G., Silander, J., Wilson, A. M., Allen, J. M., Horton, R., and Anyah, R. (2013). Statistical downscaling and bias correction of climate model outputs for climate change impact assessment in the us northeast. *Global and Planetary Change*, 100:320–332.

Albertson, J. and Kiely, G. (2001). On the structure of soil moisture time series in the context of land surface models. *Journal of Hydrology*, 243(1):101–119.

Allen, M. F. (2009). Bidirectional water flows through the soil-fungal-plant mycorrhizal continuum. *New Phytologist*, pages 290–293.

Amirabadizadeh, M., Huang, Y. F., and Lee, T. S. (2015). Recent trends in temperature and precipitation in the langat river basin, malaysia. *Advances in Meteorology*, 2015(1):579437.

Andréassian, V. (2004). Waters and forests: from historical controversy to scientific debate. *Journal of hydrology*, 291(1-2):1–27.

Arnau-Rosalén, E., Calvo-Cases, A., Boix-Fayos, C., Lavee, H., and Sarah, P. (2008). Analysis of soil surface component patterns affecting runoff generation. an example of methods applied to mediterranean hillslopes in alicante (spain). *Geomorphology*, 101(4):595–606.

Arnold, J., Muttiah, R., Srinivasan, R., and Allen, P. (2000). Regional estimation of base flow and groundwater recharge in the upper mississippi river basin. *Journal of Hydrology*, 227(1):21–40.

Arora, V. K. and Boer, G. J. (2005). A parameterization of leaf phenology for the terrestrial ecosystem component of climate models. *Global Change Biology*, 11(1):39–59.

Aru, A. P. B., Vacca, A., Delogu, G., Dessena, M. A., S. Madrau, R. T. M., , and Vacca, S. (1991). *Nota illustrativa alla carta dei suoli della Sardegna.*

Arya, S. (1981). Parameterizing the height of the stable atmospheric boundary layer. *Journal of Applied Meteorology and Climatology*, 20(10):1192–1202.

Baldocchi, D. D. (2003a). Assessing the eddy covariance technique for evaluating carbon dioxide exchange rates of ecosystems: past, present and future. *Global change biology*, 9(4):479–492.

Baldocchi, D. D. (2003b). Assessing the eddy covariance technique for evaluating carbon dioxide exchange rates of ecosystems: past, present and future. *Global Change Biology*, 9(4):479–492.

Banerjee, T. and Katul, G. (2013). Logarithmic scaling in the longitudinal velocity variance explained by a spectral budget. *Physics of Fluids*, 25(12):125106.

Bartlett, M. K., Klein, T., Jansen, S., Choat, B., and Sack, L. (2016). The correlations and sequence of plant stomatal, hydraulic, and wilting responses to drought. *Proceedings of the National Academy of Sciences*, 113(46):13098–13103.

Bashford, K. E., Beven, K. J., and Young, P. C. (2002). Observational data and scale-dependent parameterizations: explorations using a virtual hydrological reality. *Hydrological Processes*, 16(2):293–312.

Batchelor, G. K. and Proudman, I. (1956). The large-scale structure of homogenous turbulence. *Philosophical Transactions of the Royal Society of London. Series A, Mathematical and Physical Sciences*, 248(949):369–405.

Beven, K. J., Kirkby, M. J., Freer, J. E., and Lamb, R. (2021). A history of topmodel. *Hydrology and Earth System Sciences*, 25(2):527–549.

Bos, W., Touil, H., Shao, L., and Bertoglio, J.-P. (2004). On the behavior of the velocity-scalar cross correlation spectrum in the inertial range. *Physics of Fluids*, 16(10):3818–3823.

Breshears, D. D. (2006). The grassland–forest continuum: trends in ecosystem properties for woody plant mosaics? *Frontiers in Ecology and the Environment*, 4(2):96–104.

Breshears, D. D., Myers, O. B., and Barnes, F. J. (2009). Horizontal heterogeneity in the frequency of plant-available water with woodland intercanopy–canopy vegetation patch type rivals that occuring vertically by soil depth. *Ecohydrology: Ecosystems, Land and Water Process Interactions, Ecohydrogeomorphology*, 2(4):503–519.

Brunet, Y. (2020). Turbulent flow in plant canopies: historical perspective and overview. *Boundary-Layer Meteorology*, 177(2):315–364.

Brunetti, M., Maugeri, M., Nanni, T., and Navarra, A. (2002). Droughts and extreme events in regional daily italian precipitation series. *International Journal of Climatology: A Journal of the Royal Meteorological Society*, 22(5):543–558.

Burba, G. (2022). *Eddy covariance method for scientific, regulatory, and commercial applications.* LI-COR Biosciences.

Caloiero, T. and Veltri, S. (2019). Drought assessment in the sardinia region (italy) during 1922–2011 using the standardized precipitation index. *Pure and Applied Geophysics*, 176(2):925–935.

Cannon, A. J. (2018). Multivariate quantile mapping bias correction: an n-dimensional probability density function transform for climate model simulations of multiple variables. *Climate dynamics*, 50(1):31–49.

Cava, D. and Katul, G. (2012). On the scaling laws of the velocity-scalar cospectra in the canopy sublayer above tall forests. *Boundary-Layer Meteorology*, 145:351–367.

Cayrol, P., Chehbouni, A., Kergoat, L., Dedieu, G., Mordelet, P., and Nouvellon, Y. (2000). Grassland modeling and monitoring with spot-4 vegetation instrument during the 1997–1999 salsa experiment. *Agricultural and Forest Meteorology*, 105(1):91–115.

Chamecki, M., Dias, N. L., Salesky, S. T., and Pan, Y. (2017). Scaling laws for the longitudinal structure function in the atmospheric surface layer. *Journal of the Atmospheric Sciences*, 74(4):1127–1147.

Charuchittipan, D. and Wilson, J. (2009). Turbulent kinetic energy dissipation in the surface layer. *Boundary-Layer Meteorology*, 132(2):193–204.

Choi, K.-S. and Lumpley, J. L. (2001). The return to isotropy of homogeneous turbulence. *Journal of Fluid Mechanics*, 436:59–84.

Chow, V. (1971). *Applied hydrology.* McGraw-hill.

Clapp, R. B. and Hornberger, G. M. (1978). Empirical equations for some soil hydraulic properties. *Water Resources Research*, 14(4):601–604.

Clarke, R. (1970). Observational studies in the atmospheric boundary layer. *Quarterly Journal of the Royal Meteorological Society*, 96(407):91–114.

CMIP5, C. M. I. P. P. . (2013). Cmip5 multi-model ensemble.

Conte, A., Fares, S., Salvati, L., Savi, F., Matteucci, G., Mazzenga, F., Spano, D., Sirca, C., Marras, S., Galvagno, M., et al. (2019). Ecophysiological responses to rainfall variability in grassland and forests along a latitudinal gradient in italy. *Frontiers in Forests and Global Change*, 2:16.

Corona, R., Montaldo, N., and Albertson, J. D. (2018). On the role of nao-driven interannual variability in rainfall seasonality on water resources and hydrologic design in a typical mediterranean basin. *Journal of Hydrometeorology*, 19(3):485 – 498.

Deng, C., Liu, P., Wang, D., and Wang, W. (2018). Temporal variation and scaling of parameters for a monthly hydrologic model. *Journal of Hydrology*, 558:290–300.

Deshpande, R., de Silva, C. M., and Marusic, I. (2023). Evidence that superstructures comprise self-similar coherent motions in high Reynolds number boundary layers. *Journal of Fluid Mechanics*, 969:A10.

Detto, M., Katul, G., Mancini, M., Montaldo, N., and Albertson, J. (2008). Surface heterogeneity and its signature in higher-order scalar similarity relationships. *agricultural and forest meteorology*, 148(6-7):902–916.

Detto, M., Montaldo, N., Albertson, J. D., Mancini, M., and Katul, G. (2006). Soil moisture and vegetation controls on evapotranspiration in a heterogeneous Mediterranean ecosystem on Sardinia, Italy. *Water Resources Research*, 42(8):W08419.

Di Felice, M. L. and Salgo, R. (2011). *DIGHE DELLA SARDEGNA*, volume 1. Poliedro.

Dohn, J., Dembélé, F., Karembé, M., Moustakas, A., Amévor, K. A., and Hanan, N. P. (2013). Tree effects on grass growth in savannas: competition, facilitation and the stress-gradient hypothesis. *Journal of Ecology*, 101(1):202–209.

Domec, J.-C., King, J. S., Noormets, A., Treasure, E., Gavazzi, M. J., Sun, G., and McNulty, S. G. (2010). Hydraulic redistribution of soil water by roots affects whole-stand evapotranspiration and net ecosystem carbon exchange. *New Phytologist*, 187(1):171–183.

Drobinski, P., Carlotti, P., Newsom, R. K., Banta, R. M., Foster, R. C., and Redelsperger, J.-L. (2004). The structure of the near-neutral atmospheric surface layer. *Journal of the Atmospheric Aciences*, 61(6):699–714.

Dupont, S. and Patton, E. G. (2022). On the influence of large-scale atmospheric motions on near-surface turbulence: Comparison between flows over low-roughness and tall vegetation canopies. *Boundary-Layer Meteorology*, 184(2):195–230.

Eekhout, J. P., Delsman, I., Baartman, J., van Eupen, M., Van Haren, C., Contreras, S., Martínez-López, J., and De Vente, J. (2024). How future changes in irrigation water supply and demand affect water security in a mediterranean catchment. *Agricultural Water Management*, 297:108818.

Eliades, M., Bruggeman, A., Lubczynski, M. W., Christou, A., Camera, C., and Djuma, H. (2018). The water balance components of mediterranean pine trees on a steep mountain slope during two hydrologically contrasting years. *Journal of Hydrology*, 562:712–724.

Ellison, D., N. Futter, M., and Bishop, K. (2012). On the forest cover–water yield debate: from demand-to supply-side thinking. *Global change biology*, 18(3):806–820.

Estrada-Medina, H., Graham, R. C., Allen, M. F., Jiménez-Osornio, J. J., and Robles-Casolco, S. (2013). The importance of limestone bedrock and dissolution karst features on tree root distribution in northern yucatán, méxico. *Plant and soil*, 362:37–50.

Everard, K., Katul, G., Lawrence, G., Christen, A., and Parlange, M. (2021). Sweeping effects modify Taylor's frozen turbulence hypothesis for scalars in the roughness sublayer. *Geophysical Research Letters*, 48(22):e2021GL093746.

Eyring, V., Bony, S., Meehl, G. A., Senior, C. A., Stevens, B., Stouffer, R. J., and Taylor, K. E. (2016). Overview of the coupled model intercomparison project phase 6 (cmip6) experimental design and organization. *Geoscientific Model Development*, 9(5):1937–1958.

Fares, S., Savi, F., Muller, J., Matteucci, G., and Paoletti, E. (2014). Simultaneous measurements of above and below canopy ozone fluxes help partitioning ozone deposition between its various sinks in a mediterranean oak forest. *Agricultural and Forest Meteorology*, 198-199:181–191.

Fatichi, S., Vivoni, E. R., Ogden, F. L., Ivanov, V. Y., Mirus, B., Gochis, D., Downer, C. W., Camporese, M., Davison, J. H., Ebel, B., et al. (2016). An overview of current applications, challenges, and future trends in distributed process-based models in hydrology. *Journal of Hydrology*, 537:45–60.

Finnigan, J. (2000). Turbulence in plant canopies. *Annual Review of Fluid Mechanics*, 32:519–571.

Flato, G., Marotzke, J., Abiodun, B., Braconnot, P., Chou, S., Collins, W., Cox, P., Driouech, F., Emori, S., Eyring, V., Forest, C., Gleckler, P., Guilyardi, E., Jakob, C., Kattsov, V., Reason, C., and Rummukainen, M. (2013). Evaluation of climate models. In Stocker, T., Qin, D., Plattner, G.-K., Tignor, M., Allen, S., Boschung, J., Nauels, A., Xia, Y., Bex, V., and Midgley, P., editors, *Climate Change 2013: The Physical Science Basis. Contribution of Working Group I to the Fifth Assessment Report of the Intergovernmental Panel on Climate Change*, pages 741–866. Cambridge University Press, Cambridge, United Kingdom and New York, NY, USA.

Franks, S., Beven, K., Quinn, P., and Wright, I. (1997). On the sensitivity of soil-vegetation-atmosphere transfer (svat) schemes: equifinality and the problem of robust calibration. *Agricultural and Forest Meteorology*, 86(1):63–75.

García-Ruiz, J. M., López-Moreno, J. I., Vicente-Serrano, S. M., Lasanta–Martínez, T., and Beguería, S. (2011). Mediterranean water resources in a global change scenario. *Earth-Science Reviews*, 105(3):121–139.

Garratt, J. (1994). *The Atmospheric Boundary Layer*. Cambridge Atmospheric and Space Science Series. Cambridge University Press.

Garson, D. C. and Lacaze, B. (2003). Monitoring leaf area index of mediterranean oak woodlands: Comparison of remotely-sensed estimates with simulations from an ecological process-based model. *International Journal of Remote Sensing*, 24(17):3441–3456.

Giorgi, F. and Lionello, P. (2008). Climate change projections for the mediterranean region. *Global and Planetary Change*, 63(2):90–104. Mediterranean climate: trends, variability and change.

Gorguner, M. and Kavvas, M. L. (2020). Modeling impacts of future climate change on reservoir storages and irrigation water demands in a mediterranean basin. *Science of The Total Environment*, 748:141246.

Granier, A. (1987). Evaluation of transpiration in a douglas-fir stand by means of sap flow measurements. *Tree Physiology*, 3(4):309–320.

Guerra, C. A., Maes, J., Geijzendorffer, I., and Metzger, M. J. (2016). An assessment of soil erosion prevention by vegetation in mediterranean europe: Current trends of ecosystem service provision. *Ecological Indicators*, 60:213–222.

Hans Lambers, F. Stuart Chapin, T. L. P. (2008). *Plant Physiological Ecology*. Springer.

Hanson, J., Skiles, J., and Parton, W. (1988). A multi-species model for rangeland plant communities. *Ecological Modelling*, 44(1):89–123.

Helsel, D. R., Hirsch, R. M., Ryberg, K. R., Archfield, S. A., and Gilroy, E. J. (2020). *Statistical Methods in Water Resources*, volume book 4, chapter A3 of *Techniques and Methods*. U.S. Geological Survey. Supersedes USGS Techniques of Water-Resources Investigations, book 4, chapter A3, version 1.1.

Hersbach, Hans, Bell, Bill, Berrisford, Paul, Hirahara, Shoji, Horányi, A., Muñoz-Sabater, J., Nicolas, J., Peubey, C., Radu, R., Schepers, D., Simmons, A., Soci, C., Abdalla, S., Abellan, X., Balsamo, G., Bechtold, P., Biavati, G., Bidlot, J., Bonavita, M., De Chiara, G., Dahlgren, P., Dee, D., Diamantakis, M., Dragani, R., Flemming, J., Forbes, R., Fuentes, M., Geer, A., Haimberger, L., Healy, S., Hogan, R. J., Hólm, E., Janisková, M., Keeley, S., Laloyaux, P., Lopez, P., Lupu, C., Radnoti, G., de Rosnay, P., Rozum, I., Vamborg, F., Villaume, S., and Thépaut, J.-N. (2020). The era5 global reanalysis. *Quarterly Journal of the Royal Meteorological Society*, 146(730):1999–2049.

Hersbach, Hans, Bill, B., Berrisford, Paul, Biavati, Gionata, Horányi, András, Sabater, M., Joaquín, Nicolas, Julien, Peubey, C., Radu, Raluca, Rozum, Iryna, et al. (2023). Era5 hourly data on single levels from 1940 to present, copernicus climate change service (c3s) climate data store (cds)[data set].

Hersbach, H., Bell, B., Berrisford, P., Biavati, G., Horányi, A., Muñoz Sabater, J., Nicolas, J., Peubey, C., Radu, R., Rozum, I., Schepers, D., Simmons, A., Soci, C., Dee, D., and Thépaut, J.-N. (2025). ERA5 hourly data on single levels from 1940 to present.

Hirsch, R. M., Slack, J. R., and Smith, R. A. (1982). Techniques of trend analysis for monthly water quality data. *Water resources research*, 18(1):107–121.

Horst, T. (1997). A simple formula for attenuation of eddy fluxes measured with first-order-response scalar sensors. *Boundary-Layer Meteorology*, 82:219–233.

Hou, Y., Wei, X., Zhang, M., Creed, I. F., McNulty, S. G., and Ferraz, S. F. (2023). A global synthesis of hydrological sensitivities to deforestation and forestation. *Forest Ecology and Management*, 529:120718.

House, J. I., Archer, S., Breshears, D. D., Scholes, R. J., and Participants, N. T. I. (2003). Conundrums in mixed woody–herbaceous plant systems. *Journal of Biogeography*, 30(11):1763–1777.

Hsieh, C.-I. and Katul, G. G. (1997). Dissipation methods, Taylor's hypothesis, and stability correction functions in the atmospheric surface layer. *Journal of Geophysical Research: Atmospheres*, 102(D14):16391–16405.

Hu, Y., Maskey, S., and Uhlenbrook, S. (2012). Trends in temperature and rainfall extremes in the yellow river source region, china. *Climatic change*, 110(1):403–429.

Huang, K. Y. and Katul, G. G. (2022). Profiles of high-order moments of longitudinal velocity explained by the random sweeping decorrelation hypothesis. *Physical Review Fluids*, 7(4):044603.

Jarvis, P. (1976). The interpretation of the variations in leaf water potential and stomatal conductance found in canopies in the field. *Philosophical Transactions of the Royal Society of London. B, Biological Sciences*, 273(927):593–610.

Kader, B. and Yaglom, A. (1991). Spectra and correlation functions of surface layer atmospheric turbulence in unstable thermal stratification. In *Turbulence and Coherent Structures*, pages 387–412. Springer.

Kaimal, J. and Finnigan, J. J. (1994). *Atmospheric Boundary Layer Flows: Their Structure and Measurement*. Oxford University Press.

Karman, T. and Howarth, L. (1938). On the statistical theory of isotropic turbulence. *Proceedings of the Royal Society of London. Series A-Mathematical and Physical Sciences*, 164(917):192–215.

Katul, G. and Chu, C.-R. (1998). A theoretical and experimental investigation of energy-containing scales in the dynamic sublayer of boundary-layer flows. *Boundary-Layer Meteorology*, 86(2):279–312.

Katul, G., Geron, C., Hsieh, C., Vidakovic, B., and Guenther, A. (1998). Active turbulence and scalar transport near the land-atmosphere interface. *Journal of Applied Meteorology*, 37:1533–1546.

Katul, G., Konings, A., and Porporato, A. (2011). Mean velocity profile in a sheared and thermally stratified atmospheric boundary layer. *Physical Review Letters*, 107(26):268502.

Katul, G., Li, D., and Manes, C. (2019). A primer on turbulence in hydrology and hydraulics: the power of dimensional analysis. *Wiley Interdisciplinary Reviews: Water*, 6(2):e1336.

Katul, G. G., Chu, C. R., Parlange, M. B., Albertson, J. D., and Ortenburger, T. A. (1995). Low-wavenumber spectral characteristics of velocity and temperature in the atmospheric surface layer. *Journal of Geophysical Research: Atmospheres*, 100(D7):14243–14255.

Katul, G. G., Manes, C., Porporato, A., Bou-Zeid, E., and Chamecki, M. (2015). Bottlenecks in turbulent kinetic energy spectra predicted from structure function inflections using the von kármán-howarth equation. *Physical Review E*, 92:033009.

Katul, G. G., Porporato, A., Manes, C., and Meneveau, C. (2013). Co-spectrum and mean velocity in turbulent boundary layers. *Physics of Fluids*, 25(9):091702.

Katul, G. G., Porporato, A., Shah, S., and Bou-Zeid, E. (2014). Two phenomenological constants explain similarity laws in stably stratified turbulence. *Physical Review E*, 89(2):023007.

Kendall, M. G. (1938). A new measure of rank correlation. *Biometrika*, 30(1-2):81–93.

Kolmogorov, A. N. (1991). The local structure of turbulence in incompressible viscous fluid for very large Reynolds numbers. *Proceedings of the Royal Society of London. Series A: Mathematical and Physical Sciences*, 434(1890):9–13.

Larcher, W. (2003). *Physiological Plant Ecology: Ecophysiology and Stress Physiology of Functional Groups*. Physiological Plant Ecology: Ecophysiology and Stress Physiology of Functional Groups. Springer.

Li, D. and Katul, G. G. (2017). On the linkage between the $\mathrm{k}^{-5/3}$ spectral and $\mathrm{k}^{-7/3}$ cospectral scaling in high-Reynolds number turbulent boundary layers. *Physics of Fluids*, 29(6):065108.

Li, X.-Y., Contreras, S., Solé-Benet, A., Cantón, Y., Domingo, F., Lázaro, R., Lin, H., Van Wesemael, B., and Puigdefábregas, J. (2011). Controls of infiltration–runoff processes in mediterranean karst rangelands in se spain. *Catena*, 86(2):98–109.

Lionello, P. and Scarascia, L. (2018). The relation between climate change in the mediterranean region and global warming. *Regional Environmental Change*, 18:1481–1493.

Lumley, J. L. (1979). Computational modeling of turbulent flows*1this work supported in part by the u.s. national science foundation, meteorology program under grant number atm77-22903, and in part by the u. s. office of naval research, fluid dynamics branch. it is a pleasure to acknowledge fruitful discussion with b. brumley, and the computational help of d. hatziavromidis. volume 18 of *Advances in Applied Mechanics*, pages 123–176. Elsevier.

Luo, X., Liang, X., and Lin, J.-S. (2016). Plant transpiration and groundwater dynamics in water-limited climates: Impacts of hydraulic redistribution. *Water Resources Research*, 52(6):4416–4437.

Lyra, A. and Loukas, A. (2023). Simulation and evaluation of water resources management scenarios under climate change for adaptive management of coastal agricultural watersheds. *Water Resources Management*, 37(6):2625–2642.

Marusic, I., Monty, J., Hultmark, M., and Smits, A. (2013). On the logarithmic region in wall turbulence. *Journal of Fluid Mechanics*, 716.

Marusic, I. and Monty, J. P. (2019). Attached eddy model of wall turbulence. *Annual Review of Fluid Mechanics*, 51:49–74.

Massman, W. (2000). A simple method for estimating frequency response corrections for eddy covariance systems. *Agricultural and Forest Meteorology*, 104(3):185–198.

McBean, G. (1976). Scaling turbulence in the planetary boundary layer. *Atmosphere*, 14(4):254–267.

McCole, A. A. and Stern, L. A. (2007). Seasonal water use patterns of juniperus ashei on the edwards plateau, texas, based on stable isotopes in water. *Journal of Hydrology*, 342(3-4):238–248.

Meyers, J. and Meneveau, C. (2008). A functional form for the energy spectrum parametrizing bottleneck and intermittency effects. *Physics of Fluids*, 20(6):065109.

Mohsin, T. and Gough, W. A. (2010). Trend analysis of long-term temperature time series in the greater toronto area (gta). *Theoretical and applied climatology*, 101:311–327.

Montaldo, N., Albertson, J. D., and Mancini, M. (2008). Vegetation dynamics and soil water balance in a water-limited mediterranean ecosystem on sardinia, italy. *Hydrology and Earth System Sciences*, 12(6):1257–1271.

Montaldo, N. and Corona, R. (2024). Hydrologic sustainability of a mediterranean tree-grass ecosystem under climate change. *Journal of Hydrology*, 641:131772.

Montaldo, N., Corona, R., and Albertson, J. D. (2013). On the separate effects of soil and land cover on mediterranean ecohydrology: Two contrasting case studies in sardinia, italy. *Water Resources Research*, 49(2):1123–1136.

Montaldo, N., Corona, R., Curreli, M., Sirigu, S., Piroddi, L., and Oren, R. (2021). Rock water as a key resource for patchy ecosystems on shallow soils: Digging deep tree clumps subsidize surrounding surficial grass. *Earth's Future*, 9(2):e2020EF001870. e2020EF001870 2020EF001870.

Montaldo, N., Curreli, M., Corona, R., and Oren, R. (2020). Fixed and variable components of evapotranspiration in a mediterranean wild-olive - grass landscape mosaic. *Agricultural and Forest Meteorology*, 280:107769.

Montaldo, N., Mancini, M., and Rosso, R. (2004). Flood hydrograph attenuation induced by a reservoir system: analysis with a distributed rainfall-runoff model. *Hydrological Processes*, 18(3):545–563.

Montaldo, N. and Oren, R. (2018). Changing seasonal rainfall distribution with climate directs contrasting impacts at evapotranspiration and water yield in the western mediterranean region. *Earth's Future*, 6(6):841–856.

Montaldo, N., Ravazzani, G., and Mancini, M. (2007). On the prediction of the toce alpine basin floods with distributed hydrologic models. *Hydrological Processes*, 21(5):608–621.

Montaldo, N., Rondena, R., Albertson, J. D., and Mancini, M. (2005). Parsimonious modeling of vegetation dynamics for ecohydrologic studies of water-limited ecosystems. *Water Resources Research*, 41(10).

Montaldo, N. and Sarigu, A. (2017). Potential links between the north atlantic oscillation and decreasing precipitation and runoff on a mediterranean area. *Journal of Hydrology*, 553:419–437.

Montaldo, N., Sirigu, S., Zucca, R., Ruiu, A., and Corona, R. (2024). Hydrological sustainability of dam-based water resources in a mediterranean basin undergoing climate change. *Hydrology*, 11(12):200.

Montaldo, N., Toninelli, V., Albertson, J. D., Mancini, M., and Troch, P. A. (2003). The effect of background hydrometeorological conditions on the sensitivity of evapotranspiration to model parameters: analysis with measurements from an italian alpine catchment. *Hydrology and Earth System Sciences*, 7(6):848–861.

Mortarini, L., Katul, G. G., Cava, D., Dias-Junior, C. Q., Dias, N. L., Manzi, A., Sorgel, M., Araújo, A., and Chamecki, M. (2023). Adjustments to the law of the wall above an Amazon forest explained by a spectral link. *Physics of Fluids*, 35(2):025102.

Nickels, T., Marusic, I., Hafz, S., Hutchins, N., and Chong, M. (2007). Some predictions of the attached eddy model for a high Reynolds number boundary layer. *Philosophical Transactions of the Royal Society of London*, 365:807–822.

Nikora, V. (1999). Origin of the “- 1” spectral law in wall-bounded turbulence. *Physical Review Letters*, 83(4):734.

Noilhan, J. and Planton, S. (1989). A simple parameterization of land surface processes for meteorological models. *Monthly weather review*, 117(3):536–549.

Nouvellon, Y., Rambal, S., Lo Seen, D., Moran, M., Lhomme, J., Bégué, A., Chehbouni, A., and Kerr, Y. (2000). Modelling of daily fluxes of water and carbon from shortgrass steppes. *Agricultural and Forest Meteorology*, 100(2):137–153.

Oishi, A. C., Oren, R., and Stoy, P. C. (2008). Estimating components of forest evapotranspiration: a footprint approach for scaling sap flux measurements. *agricultural and forest meteorology*, 148(11):1719–1732.

Panchev, S. (1971). *Random Functions and Turbulence.* Pergamon Press, New York.

Park Williams, A., Allen, C. D., Macalady, A. K., Griffin, D., Woodhouse, C. A., Meko, D. M., Swetnam, T. W., Rauscher, S. A., Seager, R., Grissino-Mayer, H. D., et al. (2013a). Temperature as a potent driver of regional forest drought stress and tree mortality. *Nature climate change*, 3(3):292–297.

Park Williams, A., Allen, C. D., Macalady, A. K., Griffin, D., Woodhouse, C. A., Meko, D. M., Swetnam, T. W., Rauscher, S. A., Seager, R., Grissino-Mayer, H. D., et al. (2013b). Temperature as a potent driver of regional forest drought stress and tree mortality. *Nature climate change*, 3(3):292–297.

Parlange, M. B., Albertson, J. D., Eichinger, W. E., Cahill, A. T., Jackson, T. J., Kiely, G., and Katul, G. G. (1999). *Evaporation. Use of fast-response turbulence sensors, raman lidar, and passive microwave remote sensing.*, page 260–278. Oxford University Press, Oxford.

Pastorello, G., Trotta, C., Canfora, E., Chu, H., Christianson, D., Cheah, Y.-W., Poindexter, C., Chen, J., Elbashandy, A., Humphrey, M., et al. (2020). The fluxnet2015 dataset and the oneflux processing pipeline for eddy covariance data. *Scientific data*, 7(1):225.

Penman, H. L. and Keen, B. A. (1948). Natural evaporation from open water, bare soil and grass. *Proceedings of the Royal Society of London. Series A. Mathematical and Physical sciences*, 193(1032):120–145.

Poli, P. and Brunel, P. (2018). Assessing reanalysis quality with early sounders nimbus-4 iris (1970) and nimbus-6 hirs (1975). *Advances in Space Research*, 62(2):245–264.

Ponce, V. (1989). *Engineering Hydrology: Principles and Practices.* Prentice Hall.

Pope, S. (2000). *Turbulent Flows.* Cambridge University Press, Cambridge, UK.

Porporato, A., Hooshyar, M., Bragg, A. D., and Katul, G. (2020). Fluctuation theorem and extended thermodynamics of turbulence. *Proceedings of the Royal Society A*, 476(2243):20200468.

Prandtl, L. (1952). *Essentials of fluid dynamics with applications to hydraulics, aeronautics, meteorology, and other subjects.* Hafner Publishing Company.

Pulighe, G., Lupia, F., Chen, H., and Yin, H. (2021). Modeling climate change impacts on water balance of a mediterranean watershed using swat+. *Hydrology*, 8(4).

Qin, Y., Wang, C., Zhao, Z., Pan, X., and Li, Z. (2019). Climate change impacts on the global potential geographical distribution of the agricultural invasive pest, bactrocera dorsalis (hendel)(diptera: Tephritidae). *Climatic Change*, 155:145–156.

Raupach, M. R., Finnigan, J. J., and Brunet, Y. (1996). Coherent eddies and turbulence in vegetation canopies: the mixing-layer analogy. In *Boundary-Layer Meteorology 25th anniversary volume, 1970–1995*, pages 351–382. Springer.

Rempe, D. M. and Dietrich, W. E. (2018a). Direct observations of rock moisture, a hidden component of the hydrologic cycle. *Proceedings of the national academy of sciences*, 115(11):2664–2669.

Rempe, D. M. and Dietrich, W. E. (2018b). Direct observations of rock moisture, a hidden component of the hydrologic cycle. *Proceedings of the National Academy of Sciences*, 115(11):2664–2669.

Rodriguez-Iturbe, I. (2000). Ecohydrology: A hydrologic perspective of climate-soil-vegetation dynamies. *Water Resources Research*, 36(1):3–9.

Ryel, R., M., C., C., Y., D., O., and A., L. (2002). Hydraulic redistribution in a stand of artemisia tridentata: evaluation of benefits to transpiration assessed with a simulation model. *Oecologia*, 130:173–184. Springer.

Saddoughi, S. and Veeravalli, S. (1994). Local isotropy in turbulent boundary layers at high Reynolds number flow. *Journal of Fluid Mechanics*, 268:333–372.

Saffman, P. (1967). The large-scale structure of homogeneous turbulence. *Journal of Fluid Mechanics*, 27(3):581–593.

Sakai, R. K., Fitzjarrald, D. R., and Moore, K. E. (2001). Importance of low-frequency contributions to eddy fluxes observed over rough surfaces. *Journal of Applied Meteorology*, 40(12):2178–2192.

Salesky, S. T., Katul, G. G., and Chamecki, M. (2013). Buoyancy effects on the integral length scales and mean velocity profile in atmospheric surface layer flows. *Physics of Fluids*, 25(10):105101.

Sankaran, M., Hanan, N. P., Scholes, R. J., Ratnam, J., Augustine, D. J., Cade, B. S., Gignoux, J., Higgins, S. I., Le Roux, X., Ludwig, F., et al. (2005). Determinants of woody cover in african savannas. *Nature*, 438(7069):846–849.

Scanlon, T. M. and Kustas, W. P. (2010). Partitioning carbon dioxide and water vapor fluxes using correlation analysis. *Agricultural and Forest Meteorology*, 150(1):89–99.

Scanlon, T. M. and Sahu, P. (2008). On the correlation structure of water vapor and carbon dioxide in the atmospheric surface layer: A basis for flux partitioning. *Water Resources Research*, 44(10):W10418.

Scholes, R. J. and Archer, S. R. (1997). Tree-grass interactions in savannas. *Annual review of Ecology and Systematics*, 28(1):517–544.

Schwinning, S. (2010). The ecohydrology of roots in rocks. *Ecohydrology: Ecosystems, land and water process interactions, Ecohydrogeomorphology*, 3(2):238–245.

Sechi, G., Sulis, A., and Zuddas, P. (2004). Wargi: Water resources system optimization aided by graphical interface. In Blain, W. and Brebbia, C., editors, *Hydraulic Engineering Software*, pages 109–120. WIT Press.

Sechi, G. and Zucca, R. (2014). *Applying the WARGI DSS to optimise water supply systems under drought conditions: Analysis of the South Sardinia water system.* CRC Press.

Sechi, G. M. and Sulis, A. (2009). Water system management through a mixed optimization-simulation approach. *Journal of Water Resources Planning and Management*, 135(3):160–170.

Sechi, G. M., Zucca, R., and Zuddas, P. (2013). Water costs allocation in complex systems using a cooperative game theory approach. *Water Resources Management*, 27:1781–1796.

Sen, P. K. (1968). Estimates of the regression coefficient based on kendall's tau. *Journal of the American Statistical Association*, 63(324):1379–1389.

Service, C. C. C. (2022). CMIP6 climate projections.

Service, S. C. (1986). *National engineering handbook, section 4: hydrology.* US Soil Conservation Service, USDA, Washington, DC. USDA, Department of Agriculture, Washington DC.

Sirigu, S., Katul, G., Montaldo, N., and Corona, R. (2025). Biosphere-atmosphere water vapor and heat fluxes from a forested ecosystem situated on complex terrain: Similarity, anisotropy, and the energy balance closure. Technical report, Copernicus Meetings.

Sirigu, S. and Montaldo, N. (2022). Climate change impacts on the water resources and vegetation dynamics of a forested sardinian basin through a distributed ecohydrological model. *Water*, 14(19).

Sorooshian, S. (1983). Surface water hydrology: On-line estimation. *Reviews of Geophysics*, 21(3):706–721.

Stiperski, I., Calaf, M., and Rotach, M. W. (2019). Scaling, anisotropy, and complexity in near-surface atmospheric turbulence. *Journal of Geophysical Research: Atmospheres*, 124(3):1428–1448.

Stiperski, I., Katul, G. G., and Calaf, M. (2021). Universal return to isotropy of inhomogeneous atmospheric boundary layer turbulence. *Phys. Rev. Lett.*, 126:194501.

Su, H.-B., Schmid, H. P., Grimmond, C., Vogel, C. S., and Oliphant, A. J. (2004). Spectral characteristics and correction of long-term eddy-covariance measurements over two mixed hardwood forests in non-flat terrain. *Boundary-Layer Meteorology*, 110:213–253.

Sulis, A. and Sechi, G. M. (2013). Comparison of generic simulation models for water resource systems. *Environmental modelling & software*, 40:214–225.

Swart, N. C., Cole, J. N., Kharin, V. V., Lazare, M., Scinocca, J. F., Gillett, N. P., Anstey, J., Arora, V., Christian, J. R., Jiao, Y., et al. (2019a). Cccma canesm5 model output prepared for cmip6 cmip picontrol. *(No Title)*.

Swart, N. C., Cole, J. N., Kharin, V. V., Lazare, M., Scinocca, J. F., Gillett, N. P., Anstey, J., Arora, V., Christian, J. R., Jiao, Y., Lee, W. G., Majaess, F., Saenko, O. A., Seiler, C., Seinen, C., Shao, A., Solheim, L., von Salzen, K., Yang, D., Winter, B., and Sigmond, M. (2019b). Cccma canesm5 model output prepared for cmip6 c4mip.

Tabari, H., Abghari, H., and Hosseinzadeh Talaee, P. (2012). Temporal trends and spatial characteristics of drought and rainfall in arid and semiarid regions of iran. *Hydrological processes*, 26(22):3351–3361.

Tague, C. L. and Band, L. E. (2004). Rhessys: Regional hydro-ecologic simulation system—an object-oriented approach to spatially distributed modeling of carbon, water, and nutrient cycling. *Earth interactions*, 8(19):1–42.

Taylor, G. I. (1938). The spectrum of turbulence. *Proceedings of the Royal Society of London. Series A-Mathematical and Physical Sciences*, 164(919):476–490.

Taylor, K. E., Stouffer, R. J., and Meehl, G. A. (2012). An overview of cmip5 and the experiment design. *Bulletin of the American Meteorological Society*, 93(4):485 – 498.

Tennekes, H. and Lumley, J. (1972). *A First Course in Turbulence*. MIT Press, Cambridge, MA.

Theil, H. (1950). A rank-invariant method of linear and polynomial regression analysis. *Indagationes mathematicae*, 12(85):173.

Thomas, C., Mayer, J.-C., Meixner, F. X., and Foken, T. (2006). Analysis of low-frequency turbulence above tall vegetation using a Doppler sodar. *Boundary-Layer Meteorology*, 119:563–587.

Townsend, A. (1976). *The structure of turbulent shear flow*. Cambridge University press.

Ward, E. J., Domec, J.-C., King, J., Sun, G., McNulty, S., and Noormets, A. (2017). Tracc: an open source software for processing sap flux data from thermal dissipation probes. *Trees*, 31:1737–1742.

Waterman, T., Bragg, A. D., Katul, G., and Chaney, N. (2022). Examining parameterizations of potential temperature variance across varied landscapes for use in earth system models. *Journal of Geophysical Research: Atmospheres*, 127(8):e2021JD036236.

Wood, A. W., Maurer, E. P., Kumar, A., and Lettenmaier, D. P. (2002). Long-range experimental hydrologic forecasting for the eastern united states. *Journal of Geophysical Research: Atmospheres*, 107(D20):ACL–6.

Wyngaard, J. and Clifford, S. (1977). Taylor's hypothesis and high–frequency turbulence spectra. *Journal of Atmospheric Sciences*, 34(6):922–929.

Wyngaard, J. C. (2010). *Turbulence in the Atmosphere*. Cambridge University Press.

Yan, Y., Dai, Q., Jin, L., and Wang, X. (2019). Geometric morphology and soil properties of shallow karst fissures in an area of karst rocky desertification in sw china. *CATENA*, 174:48–58.

Yu, K. and D'Odorico, P. (2015). Hydraulic lift as a determinant of tree–grass coexistence on savannas. *New Phytologist*, 207(4):1038–1051.

Yuan, W., Zheng, Y., Piao, S., Ciais, P., Lombardozzi, D., Wang, Y., Ryu, Y., Chen, G., Dong, W., Hu, Z., Jain, A. K., Jiang, C., Kato, E., Li, S., Lienert, S., Liu, S., Nabel, J. E., Qin, Z., Quine, T., Sitch, S., Smith, W. K., Wang, F., Wu, C., Xiao, Z., and Yang, S. (2019). Increased atmospheric vapor pressure deficit reduces global vegetation growth. *Science Advances*, 5(8):eaax1396.

Zahn, E., Bou-Zeid, E., Good, S. P., Katul, G. G., Thomas, C. K., Ghannam, K., Smith, J. A., Chamecki, M., Dias, N. L., Fuentes, J. D., et al. (2022). Direct partitioning of eddy-covariance water and carbon dioxide fluxes into ground and plant components. *Agricultural and Forest Meteorology*, 315:108790.

Zégre, N., Skaugset, A. E., Som, N. A., McDonnell, J. J., and Ganio, L. M. (2010). In lieu of the paired catchment approach: Hydrologic model change detection at the catchment scale. *Water Resources Research*, 46(11).

Zhang, L., Dawes, W., and Walker, G. (2001). Response of mean annual evapotranspiration to vegetation changes at catchment scale. *Water resources research*, 37(3):701–708.

Zhang, L., Hickel, K., Dawes, W. R., Chiew, F. H. S., Western, A. W., and Briggs, P. R. (2004). A rational function approach for estimating mean annual evapotranspiration. *Water Resources Research*, 40(2).

Zilitinkevich, S. and Baklanov, A. (2002). Calculation of the height of the stable boundary layer in practical applications. *Boundary-Layer Meteorology*, 105:389–409.